Proceedings ICSBM 2019 Volume 3 - Greened materials

Document status and date:
Published: 01/11/2019

Document Version:
Publisher's PDF, also known as Version of Record (includes final page, issue and volume numbers)

Please check the document version of this publication:

• A submitted manuscript is the version of the article upon submission and before peer-review. There can be important differences between the submitted version and the official published version of record. People interested in the research are advised to contact the author for the final version of the publication, or visit the DOI to the publisher's website.
• The final author version and the galley proof are versions of the publication after peer review.
• The final published version features the final layout of the paper including the volume, issue and page numbers.

Link to publication

PROCEEDINGS ICSBM 2019
VOLUME 3 - Greened Materials

2nd International Conference on Sustainable Building Materials

August 12-15, 2019 - Eindhoven, The Netherlands
Editors: V. Caprai and H.J.H. Brouwers

ICSBM 2019, Conference proceedings

Front page image: V. Caprai

Editors: V. Caprai and H.J.H. Brouwers

Organizing committee:

Conference Chairman: Prof. H.J.H. (Jos) Brouwers, Eindhoven

Conference Co-Chairman: Prof. Wen Chen, Wuhan

Conference Secretary: Mrs V. (Veronica) Caprai and Dr. M.V.A. (Miruna) Florea, Eindhoven

Dr. Qiu Li, Wuhan

Dr. Bo Yuan, Wuhan

Dr. Q. Yu, Eindhoven

Dr. F. Gauvin, Eindhoven

Dr. K. Schollbach, Eindhoven

Mr. Y. Chen, Eindhoven

Mrs. L.T.J. Harmsen, Eindhoven

Mrs. N.L. Rombley, Eindhoven

Table of Contents

Volume 3

Greened materials

Sustainability of Durable Concrete Reinforced with Aluminum Metal

H. Justnes

SINTEF Building and Infrastructure, Trondheim, Norway. Contact: harald.justnes@sintef.no.

Abstract - Aluminium metal cannot be used to reinforce regular concrete since the high hydroxyl ion concentration will attack the metal and evolve hydrogen gas. However, it has been shown the aluminium metal rods alloyed with 5% magnesium is stable in concrete where 55% of the regular cement is replaced with calcined, natural clay in the concrete mix. Replacing high fraction of clinker burnt at 1450°C, and with high CO_2 emission from decomposition of limestone in the raw meal, with a clay calcined at 850°C obtainable by bio-fuel gives obvious savings in energy and CO_2 emissions. Furthermore, since aluminium can withstand carbonation and chlorides a cover of only 20 mm for mechanical interaction with reinforcement is needed resulting in a smaller volume of concrete. The binder with 55% calcined clay has been shown to be sulphate resistant, and no chance of AAR is expected due to lower pH and no remaining calcium hydroxide in the system. Hence, the only degradation mechanism left, is freeze-thaw action that can be avoided by proper air entrainment. Thus, in theory an infinite service life without maintenance may be at hand for aluminium metal reinforced concrete.

Instead of overshooting strength by making an impermeable concrete to protect steel reinforcement using low w/c, and often excess cement, the design criterion can now be the strength itself with a higher w/c enabling fast carbonation of the concrete guaranteeing a stable reinforcement in the long run. After all, > 80% of the concrete market is covered by a design strength of < 30 MPa in compression.

Aluminium metal is weaker than iron with 1/3 of the E-modulus and ¼ tensile strength of the pure metals, but density is also 1/3 of iron. However, the tensile strength level of steel can be met by alloying (e.g. 10% Mg). The E-modulus is of the same level of FRP rods used for construction, but the failure is ductile unlike FRP rods with a brittle failure. Ductile failure is important for safety with concrete crack warning. Aluminium metal rods can be made from scrap metal in an electricity powered screw extrusion without heating.

Keywords: Aluminium, calcined clay, durability, reinforcement, sustainability.

1. Introduction

Cement is a key binder component of concrete production in the building industry. It is a complex hydraulic binder, made up of four main clinker components; alite (Ca_3SiO_5), belite (Ca_2SiO_4), tricalcium aluminate ($Ca_3Al_2O_6$) and ferrite (Ca_2AlFeO_5), which are milled together with gypsum to regulate setting time. In recent years, the production of cement has been identified as the third largest emitters of carbon dioxide (CO_2), accounting for approximately 5 to 8% of the total global anthropogenic emissions, with 60% coming from decomposition of limestone in the raw meal and 40% from fuel to reach clinkerization temperatures of 1450°C for a pure Portland clinker. Four main methods are currently in place to mitigate this challenge; i) switching from fossil fuels to alternative fuels, ii) increase efficiencies in factories, iii) implementation of supplementary cementitious materials (SCMs) replacing cement clinker [1] and iv) carbon capture and

storage (CCS) [2]. Among which, clinker partially replaced by SCMs is the most promising on a short term [1], whereby significant reduction in CO_2 emission could be expected depending on how much emission is associated with the SCM (transport, activation energy etc.). Replacing cement with SCM will also reduce the amount of raw meal needed per unit cement and increase the cement production volume of a cement plant. Most of the cement produced today has clinker replaced with SCMs with an average global clinker factor of 0.65 in 2014 [3], but higher clinker replacement with a greater variety of SCMs is expected in the future. The potential SCMs of the future include combustion ashes, slag, calcined clay and limestone. Fly ash is commonly employed in current cements with replacement of 20% in Norway. Calcined clay and marl are new and upcoming SCMs due to their abundance as increased clinker replacement demands large volumes of available SCMs. Additionally, previous studies displayed that calcined marl is a potential SCM up to a replacement level of 50% in terms of equal 28 day strength according to Justnes [1], but generally it is limited to < 35% replacement if sufficient alkalinity is to be maintained to protect steel from corroding in the long run.

The most common reinforcement for structural concrete is rebars made of steel. At the same time the most common degradation mechanism of reinforced concrete is corrosion of the steel initiated by carbonation (i.e. CO_2 from the air diffuse in and lower the pH by neutralization) or by chlorides exceeding a critical limit in spite of maintained pH. Thus, there is a need for concrete reinforcement that will not corrode, but at the same time being composed of common chemical elements like aluminium (8.1% of earth's crust [4]) since a gross volume of 10^{10} m³ concrete is produced annually world-wide. "Stainless steel" exists that will not corrode, but the typical 16-20% chromium (0.014% of earth's crust [4]) and 8-14% nickel (0.009% of earth's crust [4]) content makes it rather pricy. Some efforts have been made to make rebars out of fibre reinforced plastic (FRP), but these tend to have a brittle failure unlike metals being ductile and cannot be bent in place at site. Karlsson [5] made a review and evaluation of alternative concrete reinforcement. Naturally, aluminium was not a part of this evaluation since it will be degraded by the high pH of regular concrete and can only function in a sufficiently low pH concrete.

The main durability design of concrete today is in relation to preventing the steel reinforcement from corroding. The major degradation mechanisms; chloride ingress and carbonation, does not jeopardize the integrity of the concrete binder itself. Steel needs the high pH of conventional concrete to be passive towards corrosion while aluminium metal will be corroded by high pH and develop hydrogen gas. Environmentally friendly concrete is often designed by either using blended cement where maximum 35% of the clinker is replaced by supplementary cementitious materials (SCMs) to secure the presence of calcium hydroxide over time that will buffer a pH of 12.5 passivating steel, or by replacing cement in concrete mixes with corresponding amounts of SCM. In order to secure long service life for steel reinforced concrete, low w/c is used for low permeability often leading to much higher strength and even higher cement content than required. Low w/c can also create complications in the construction phase as lower workability is calling for use of super-plasticizing admixtures. Using more cement to attain low w/c can create higher temperature and subsequent thermal cracking risk generated by hydration heat as well as chemical shrinkage. The required compressive strength for the bulk of concrete today is still in the range of 25-30 MPa (B25).

The new concept is to make environmentally friendly concrete with > 50% cement replacement by a combination of SCMs where some are so pozzolanic active that all calcium hydroxide formed by cement hydration is consumed and the pH is kept so low that the concrete can be reinforced with aluminium metal rods without formation of hydrogen gas. The w/c can then be so high that it is only determined by required compressive strength for construction. Then workability should not be a problem and neither hydration generated heat. Permeability is not important as aluminium metal is resilient to atmospheric CO_2 and chlorides (when alloyed with 5% Mg), and high initial permeability is in fact beneficial for the concrete to

carbonate as fast as possible to reduce the carbon footprint further and lower the pH further for the long run. The concrete cover over the reinforcement can be made much thinner (20 mm) than today (50-70 mm) reducing weight and further improving the carbon footprint by using less concrete. Justnes [6] discussed the options of making a concrete with lower pH than usual ranging from large cement replacement (>50%) to calcium sulphoaluminate-belite cement systems with a smaller content of pozzolana.

2.   Methodology

2.1   Materials

The aluminium reinforcement used in the experimental part was alloyed with 5% magnesium. The cement was a CEM I with composition of oxides as listed in Table 1. The cement Blaine value was 388 m²/kg and the equivalent sodium oxide content (Na_2O_{Eq}) was 0.61%. The clay was rich in smectite (53.5%) and contained some calcium carbonate (24.7%), mainly in the form coccolith skeletons due to its marine origin. Other minerals in the raw clay was 8.4% kaolinite, 4.4% illite, 4.3% quartz, 3.3% siderite and 1.4% pyrite. The specific surface of the calcined clay as measured by BET was 32.1 m²/g.

Table 1 – Chemical composition of cement and calcined clay as oxides as obtained by XRF

Oxide (%)	CEM I	Calcined clay
SiO_2	21.12	43.34
Al_2O_3	4.60	15.99
Fe_2O_3	3.77	8.97
CaO	63.21	10.64
K_2O	0.40	2.10
Na_2O	0.35	0.85
MgO	1.71	2.39
TiO_2	0.31	1.00
P_2O_5	0.18	0.18
Mn_2O_3	0.06	0.27
SO_3	3.39	-

2.2   Mortar and concrete

The mortar mixing was performed according to EN 196-1, however at w/p = 0.6 or 0.7 instead of 0.5 (sand/cementitious powder = 3/1). The basic powder mix was 0.45 parts CEM I and 0.55 parts calcined clay with compositions as in Table 1. The compressive strength and the flexural strength for the mortar prisms were measured according to EN 196-1. A concrete was also made with composition as in Table 2.

Table 2: Concrete composition

Component	Mass (kg/m³)
CEM I	143.9
Calcined marl	175.9
Free water	223.9
Adsorbed water	5.7
0-8 mm Granite sand	970.9
8-16 mm Granite gravel	702.4
SIKA Viscocrete RMC-315	1.92

3.   Results and discussion

As a proof of concept, two paste mixes with w/c = 0.60 were made with 100% ordinary Portland cement and 50% calcined marl [7] replacing cement. These pastes were poured into a plastic cup and an aluminium plate placed in each of them as shown in Fig. 1. The paste of pure cement separated and after a few minutes

hydrogen gas started to bubble vigorously along the aluminium plate as seen from the top image of Fig. 1, while for the mix with 50% calcined marl some water was added on top for better visualization, but only a few small bubbles were observed. After the pastes had hardened, the samples were split and the imprints of the front and back of the aluminium plates on the pastes showed clearly much more cavities in the OPC sample next to the plate, while only a few small gas voids were seen on the interface for the paste with 50% calcined marl. One cannot rule out that these minor gas voids were due to entrained air by the high shear mixer, and the only way to find out is to capture and measure the evolved hydrogen gas volume [8]. This was done for Al/5%Mg rods placed in paste in plastic cups in confined environment. Fig. 2 shows such rods when the hardened paste is split after 28 days. The rod in the OPC paste had reacted completely to gibbsite while the rod in the OPC/calcined marl paste showed no sign of corrosion.

The purpose of the calcined marl was to consume all calcium hydroxide produced by the cement and render all alkalis as aluminate or silicate and to prevent them for regenerating as hydroxides as outlined in the alkali cycle for catalytic pozzolanic reaction exemplified principally (i.e. not necessarily correct ratio between the different oxides in the compounds) for aluminosilicate (AS) in Eq. 1.

AS (s)   +   2 (N,K)H (aq) $\rightarrow$ (N,K)SH (aq) + (N,K)AH (aq)

$\uparrow$ "alkali cycle"   + $\downarrow$ (1)

CSH (s) + CAH (s) + (N,K)H (aq) $\leftarrow$ CH (aq or s)
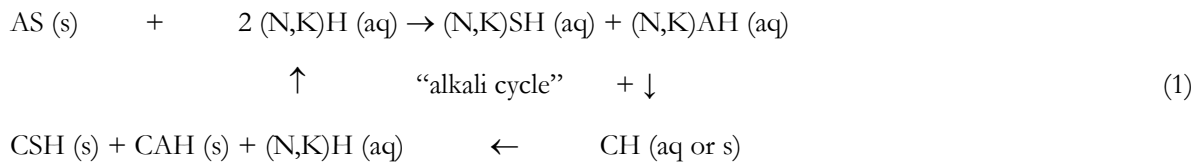
where cement chemist's short hand notation is used; $C = CaO$, $H = H_2O$, $K = K_2O$, $N = Na_2O$, $S = SiO_2$ and $A = Al_2O_3$. The alkali hydroxides dissolves alumina and silica from the aluminosilicate that react with calcium hydroxide (CH) to amorphous calcium silicate hydrate (CSH) gel and crystalline calcium aluminate hydrates (CAH) as binder. After reaction with CH the alkali hydroxides are regenerated, and the cycle continues until all calcium hydroxide is consumed and they end up as alkali silicate and alkali aluminate that in theory should not attack the aluminium metal in the rebars even though they result in a high pH. Justnes et al [7] showed that paste where cement is replaced with 50% calcined marl showed no traces of calcium hydroxide after 2 years by XRD.

Aluminium metal forms a dense layer of Al_2O_3 in contact with air that prevents further oxidation (or corrosion). This layer may dissolve by alkali hydroxides and open up for further corrosion evolving hydrogen gas;

Oxidation: Al (s) + 4 OH^- = $Al(OH)_2O^-$ + H_2O + 3 e^- (2)

Reduction: 2 H_2O + 2 e^- = H_2 (g) + 2 OH^- (3)

Total: 2Al (s) + 2OH^- + 4H_2O = 2$Al(OH)_2O^-$ + 3H_2 (g)   (4)
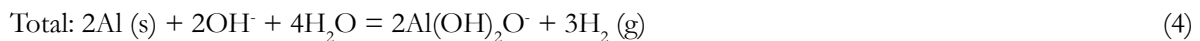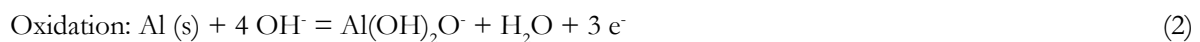
The standard electrochemical potentials of Eqs. 2, 3 and 4 are E^0 = +2.333 V, E^0 = -0.828 V and E^0 = +1.502 V, respectively. According to the total reaction in Eq. 4, there will be a net consumption of one hydroxide ion per aluminium oxidized, or none if gibbsite, $Al(OH)_3$, is precipitated rather than the dissolved aluminate anion due to lack of water as indicated in the top photo of Fig. 2 with total reaction;

2 Al (s) + 6 H_2O = 2 $Al(OH)_3$ (s) + 3 H_2 (g)   (5)

Figure 1: Aluminium metal plate placed in OPC paste (top) evolving gas and in paste where OPC is replaced with 50% calcined marl (bottom).

Figure 2: Al/5% Mg alloy rods placed in OPC paste (top) and totally converted to gibbsite after 28 days curing in moist condition, while same rod placed in paste where OPC is replaced with 55% calcined marl is in pristine condition without any corrosion products in its imprint (bottom).

Concrete was made with composition as given in Table 2, and a soluble magnesium salt (0.57% Mg^{2+} of binder mass) added to lower the initial pH. The compressive strength, splitting tensile strength and static E-modulus of cylinders (Φ 100 mm · 200 mm) was measured after 28 days curing under wet burlap and plastic wrapping to avoid drying, and the results listed in Table 3. The concrete was made in two batches and used to cast 18 cylinders and three 150·250·1100 mm beams reinforced with Φ10 mm aluminium bars alloyed with 5% magnesium. The beams were tested in a 4-point bending and the crack pattern compared to finite element calculations (not reported here). After the bending test, one of the beams were cut and split to inspect the bars for corrosion. As seen from Fig. 3, there was no sign of corrosion on the bars (top image) and the imprint in the concrete (lower image) was clean without corrosion products. Prior

to these bigger batches, a smaller trial mix was made, and a number of 10 cm cubes cast in steel moulds. The strength evolution for the trial mix versus curing age at 98% RH and 20°C is plotted in Fig. 4, and the temperature evolution in a 3.5 litre Styrofoam mould (10 mm wall thickness) was measured indicating a setting time of 4.5 h (270 min) and giving a maximum temperature increase of 6.5°C from ambient.

Table 3: Mechanical properties of concrete cylinders

Property	No. samples	Value
Density (kg/m^3)	12 from 2 batches	2328±16
Compressive strength (MPa)	8 from 2 batches	22.3±0.9
Splitting tensile strength (MPa)	4 from 2 batches	2.3±0.2
Dynamic E-modulus (GPa)	4 from 2 batches	20.3±0.9

Note that the concrete target strength was around 25 MPa and that it was deliberately made porous with a water-to-binder ratio of 0.7 so it would carbonate quickly and keep pH low over time. It could of course be made stronger by simply lowering the water content and increasing the super-plasticizer dosage a bit from the current 0.6% of binder mass. Justnes et al [9] showed that mortar where cement was replaced with 50% calcined marl and the water-to-binder ratio was 0.55 achieved the same compressive strength as mortar with 100% cement and that the compressive strength continued to increase until the last measurement at 2 years age in spite of no calcium hydroxide present at 28 days age.

The pH evolution of paste similar to the binder of the concrete with and without 6% magnesium nitrate hexahydrate is plotted in Fig. 5. The idea was that this would convert alkali hydroxides to nitrates when precipitating brucite and lower pH to 10.5;

$$2\ NaOH\ (aq) + Mg(NO_3)_2\ (aq) = 2\ NaNO_3\ (aq) + Mg\ (OH)_2\ (s) \tag{6}$$

Figure 3: Aluminium alloy round bars and T-bar (top) of beam after chiselling it open and their imprints (bottom) showing no signs of corrosion products after 40 days moist curing at 20°C.

However, as seen from Fig. 5, the pH rises back towards the level of the mix without magnesium nitrate after 7 days. The reason is probably that the nitrate ion exchange with the layered double hydroxide AFm

phases forming $Ca_3Al_2O_6\cdot Ca(NO_3)_2\cdot 11H_2O$.
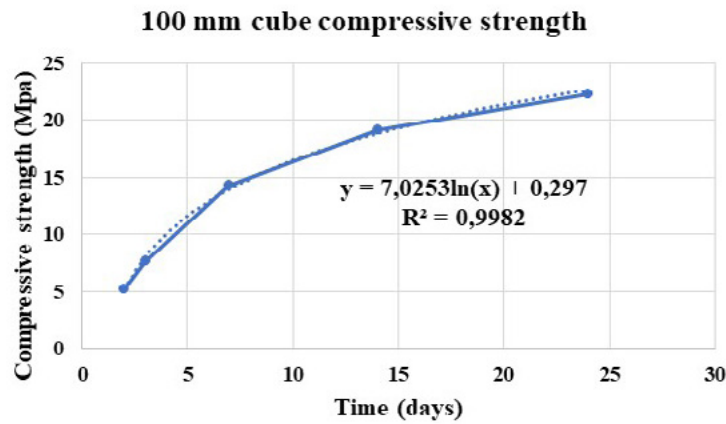
Figure 4: Compressive strength evolution versus time of the concrete cured at 98% RH and 20°C.
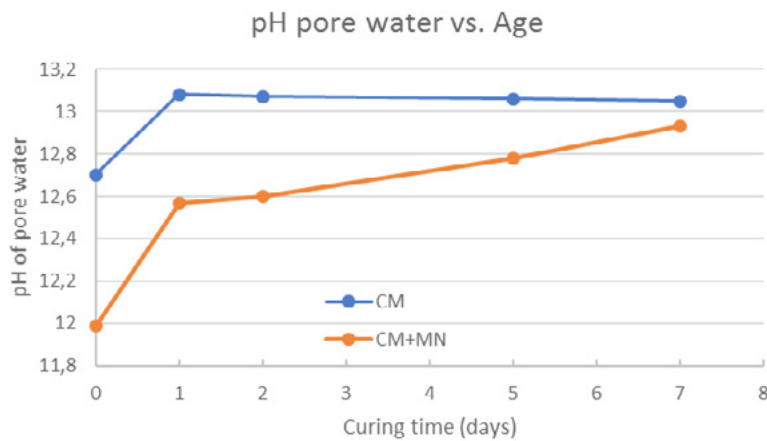
Figure 5: pH evolution as a function of sealed curing age at 20°C. CM = paste with 45% CEM I, 55% calcined marl and w/p = 0.70, while CM+MN is added additional 6% $Mg(NO_3)_2\cdot 6H_2O$ of powder mass.

The compressive strength of carbonated mortar versus non-carbonated mortar was measured to 20.2±0.2 and 23.7±0.5, respectively. The mortar composition was 0.45 parts CEM I, 0.55% calcined clay and w/p = 0.7 cured for 28 days at 90% RH and 20°C for 28 days before one set of 3 prisms were carbonated through in a 5% CO_2 chamber with 60% RH and the other set just stored at 60% RH in a closed box for same length of time. According to Justnes et al [10] the strength reduction is higher for cements blended with alumina containing SCMs than for OPC since the higher amount of calcium aluminate hydrates formed [11] will lead to a porosity increase when they carbonate, unlike calcium hydroxide leading to a volume decrease upon carbonation.

The molar volume change (ΔV_m) for ettringite carbonating to calcite, gibbsite, gypsum and liquid water;

$$Ca_3Al_2O_6\cdot 3CaSO_4\cdot 32H_2O \text{ (s)} + 3H_2CO_3 \text{ (aq)} = 3CaCO_3 \text{ (s)} + 2Al(OH)_3 \text{ (s)} + 3CaSO_4\cdot 2H_2O \text{ (s)} + 26H_2O \qquad (7)$$
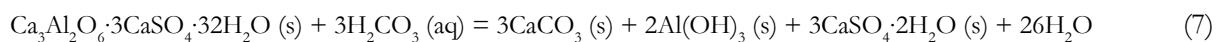
$\Delta V_m = 3\cdot 36.93 + 2\cdot 32.22 + 3\cdot 74.50 - 705.91 = -307.18 \text{ cm}^3/\text{mol AF}_t$

For calcium monosulphoaluminate hydrate carbonating to calcite, gibbsite, gypsum and liquid water;

$$Ca_3Al_2O_6\cdot CaSO_4\cdot 12H_2O \text{ (s)} + 3 H_2CO_3 \text{ (aq)} = 3 CaCO_3 \text{ (s)} + 2 Al(OH)_3 \text{ (s)} + CaSO_4\cdot 2H_2O \text{ (s)} + 10 H_2O \qquad (8)$$
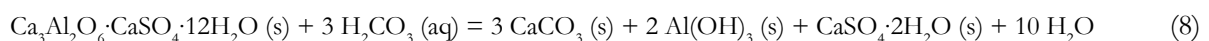
$\Delta V_m = 3\cdot 36.93 + 2\cdot 32.22 + 74.50 - 308.94 = -59.21 \text{ cm}^3/\text{mol AF}_m$

For calcium monocarboaluminate hydrate carbonating to calcite, gibbsite and liquid water;

$$Ca_3Al_2O_6 \cdot CaCO_3 \cdot 11H_2O \text{ (s)} + 3\ H_2CO_3 \text{ (aq)} = 4\ CaCO_3 \text{ (s)} + 2\ Al(OH)_3 \text{ (s)} + 11\ H_2O \qquad (9)$$

$\Delta V_m = 4 \cdot 36.93 + 2 \cdot 32.22 - 261.28 = -49.12\ cm^3/mol$ monocarboaluminate

For calcium hemicarboaluminate hydrate carbonating to calcite, gibbsite and liquid water;

$$Ca_3Al_2O_6 \cdot \tfrac{1}{2}CaCO_3 \cdot \tfrac{1}{2}\ Ca(OH)_2 \cdot 11.5H_2O \text{ (s)} + 3.5\ H_2CO_3 \text{ (aq)} = 3.5\ CaCO_3 \text{ (s)} + 2\ Al(OH)_3 \text{ (s)} + 12\ H_2O \qquad (10)$$

$\Delta V_m = 3.5 \cdot 36.93 + 2 \cdot 32.22 - 284.36 = -90.67\ cm^3/mol$ hemicarboaluminate

For mortars with binders based on 30% siliceous fly ash and 5% limestone stabilizing ettringite cured for 56 days [10], the water vapour diffusion coefficient, k_d (10^{-12} kg/Pa·m·s), increased upon carbonation (from 0.41±0.09 to 3.06±0.04) unlike mortar based on OPC (changed from 0.76±0.10 to 0.59±0.10).

The aluminium rebars are produced by an extrusion process. The screw extrusion process is patented by Werenskiold et al [12]. A prototype extruder along with fundamental knowledge of the process have been developed to a level that allows industrial implementation. Compared to the traditional process route based on re-melting and ram extrusion, direct screw extrusion of scrap material represents a significant reduction in energy consumption according to Duflou et al [13]. Moreover, this process is well suited for utilization of swarf material from material removal processes such as cutting, milling and turning that is commonly of less value than other scrap types. This is further contributing to the environmental friendliness of the overall concept of reinforcing with aluminium metal.

The E-modulus of pure aluminium metal (70 GPa) is 1/3 of steel (210 GPa), but the density of aluminium (2.70 kg/l) is also about 1/3 of iron (7.87 kg/l). The ultimate tensile strength of pure aluminium is 110 MPa, while it for steel is 400 MPa, but aluminium can be alloyed to approach steel in tensile strength. Ram extruded aluminium alloyed with 5 and 10% magnesium have tensile strengths of 274 and 395 MPa, respectively, and even higher for screw extruded rods. The challenge is the lower E-modulus, but some of this may be alleviated by designing the aluminium rebars differently. On the other hand, FRP rebars made with glass, basalt or carb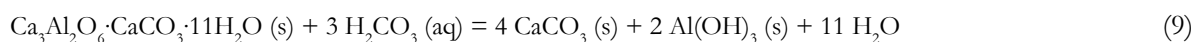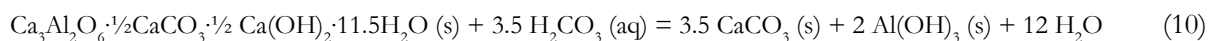on fibres have E-moduli of 45, 60 and 145 GPa and tensile strength of 700, 800 and 2000 MPa, respectively, according to Karlsson [5]. In the SEACON project [14] a bridge was built using FRP rebars demonstrating the feasibility of constructing with rebars with such lower E-modulus than steel.

Another issue is the difference in linear thermal expansion coefficient. Concrete has $6-14 \cdot 10^{-6}$ m/m·K, while pure iron and pure aluminium exhibits 10 and $22 \cdot 10^{-6}$ m/m·K, respectively. The thermal expansion of aluminium can be reduced by alloying (in particular by silicon). As comparison, glass fibre reinforced polyester has a linear thermal expansion coefficient of $25 \cdot 10^{-6}$ m/m·K. The consequence of difference in thermal dilation between reinforcement and concrete will be an issue for further research.

4.   Conclusions

A new concept of durable and environmentally friendly aluminium reinforced concrete is described where cement is replaced by high content (50-55%) of pozzolanic SCM that might lead to;

- No corrosion induced by carbonation or chloride intrusion

- Tolerable microcracks caused by drying shrinkage etc that will not jeopardize reinforcement durability

- Superior sulphate resistance when alumina containing SCMs like calcined marl is used [6]

- Applicability of alkali reactive aggregate due to alkali binding [15] or soluble aluminates from clay inhibiting silica dissolution [16, 17]

- Usability of seawater as mixing water when reinforcement is Al alloyed with e.g. 5% Mg

- Acceptance of the best strength accelerator, calcium chloride, when reinforcement is aluminium alloyed with 5% Mg (sea-water resistant aluminium used for boats)

- Much less need of cover over rebar (save 30 mm in concrete cover), probably only 20 mm needed for proper anchoring of reinforcement with concrete

- Significant lower unit weight of Al-reinforced concrete (reduced "dead-weight")

- Higher w/c allowed giving more permeable concrete leading to

- Easier to cast concrete with less plasticizers or none

- Faster carbonation leading to binding of CO_2 and further reduction of Carbon-footprint

- Less thermal movements in monolithic concrete

Hence, aluminium metal reinforced concrete may provide a system for extraordinary long service life without maintenance.

5.   Acknowledgment

6.   References

[1] Justnes, H., 2015. How to Make Concrete More Sustainable. Journal of Advanced Concrete Technology. 13:147-154.

[2] Bosoga, A., Mazek, O., Oakey, J.E., 2009. CO2 Capture Technologies for Cement Industry. Energy Procedia. 1:133-140.

[3] https://www.iea.org/publications/freepublications/publication/TechnologyRoadmapLowCarbonTransitionintheCementIndustry.pdf

[4] http://periodictable.com/Properties/A/CrustAbundance.v.log.html

[5] Karlsson, J., 2014. Alternative reinforcement approaches – Extended service life of exposed concrete structures. MSc thesis 151, Chalmers University of Technology, Department of Civil and Environmental Engineering, Gothenburg, Sweden, 117 pp.

[6] Justnes, H., 2017. Durable Aluminium Reinforced Environmentally-friendly Concrete Construction – DARE2C. Nordic Concrete Research. 56:71-81.

[7] Danner, T., Justnes, H., Norden, G., Østnor, T., 2015. Feasibility of calcined marl as alternative pozzolan. Proc. 1st Int. Conf. Calcined Clays for Sustainable Concrete, Eds. Karen Scrivener and Aurélie Favier, RILEM Book series 10:67-74. Springer.

[8] Justnes, H., 2018. Utilizing Pozzolana to Enable Aluminium Reinforced Concrete. 14th Int. Conf. Recent Advances in Concrete Technology and Sustainability Issues, Supplementary paper proceeding, Beijing, October 30-November 2, 2018.

[9] Justnes, H., Østnor, T.A., Ng, S., 2016. Applicability of Nordic clays as SCM. Proc. Int. RILEM Conf. on Materials, Systems and Structures in Civil Engineering, Conference segment on Concrete with

Supplementary Cementitious materials, 22-24 August, Technical University of Denmark, Lyngby, Denmark, RILEM Proceedings 113:331-340.

[10] Justnes, H., Skocek, J., Østnor, T.A, Engelsen, C.J., Skjølsvold, O. 2019. Microstructural changes of hydrated cement blended with fly ash upon carbonation. Reviewed but under revision for Cement and Concrete Research.

[11] De Weerdt, K., Ben Ha-Ha, M., Le Saout, G., Kjellsen, K.O., Justnes, H. and Lothenbach, B.: "Hydration mechanism of ternary Portland cements containing limestone powder and fly ash", Cement and Concrete Research, Volume 41, Issue 3, March 2011, pp. 279-291.

[12] Werenskiold, J. C., Auran, L., Roven, H. J., Ryum, N., Reiso, O., 2013. Screw extruder for continuous extrusion of materials with high viscosity. European Patent 2 086 697 B1, 01.05.2013, 8 pp.

[13] Duflou, J. R., Tekkaya, A. E., Haase, M., Welo, T., Vanmeensel, K., Kellens, K., Dewulf, W. and Paraskevas, D., 2015. Environmental assessment of solid-state recycling routes for aluminium alloys: Can solid state processes significantly reduce the environmental impact of aluminium recycling? CIRP Annals - Manufacturing Technology, 64:37–40.

[14] www.infravation.net/projects/SEACON

[15] Chappex, T., Scrivener, K.L., 2012. Alkali fixation of C–S–H in blended cement pastes and its relation to alkali silica reaction. Cement and Concrete Research, 42:1049–1054.

[16] Chappex, T., Scrivener, K.L., 2012. The influence of aluminum on the dissolution of amorphous silica and its relation to alkali silica reaction. Cement and Concrete Research, 42:1645–1649.

[17] Chappex, T., Scrivener, K.L., 2013. The Effect of Aluminum in Solution on the Dissolution of Amorphous Silica and its Relation to Cementitious Systems. J. Am. Ceram. Soc., 96:592–597.

Experimental investigation on RC one-way slabs subjected to contact explosion

Y. Hu[1], D. Song[2], Z. Jiang[2], Y. Huang[2], Z. Wu[1]

[1] College of Aerospace Science and Engineering, National University of Defense Technology, Changsha, 410073, P.R. China.

[2] Undergraduate School, National University of Defense Technology, Changsha, 410072, P.R. China.

Abstract

RC one-way slabs which have been widely used in bridge decks of bridge structures refer to reinforced concrete slabs supported by two pairs of sides or four sides and having a ratio of long side to short side greater than 3. These kinds of engineering structures may suffer from blast loads such as accidental explosions, explosive terrorist attacks, or military strikes throughout their life cycle. In this paper, four RC one-way slabs have been designed and tested under contact explosion, and the effects of charge mass have been investigated. The failure modes and damage parameters of RC one-way slabs were obtained and discussed. The results show that a smaller funneled crater in the front surface of the tested slabs under the contact explosion is observed with cracks around the funneled crater, while a larger funneled crater in the rear surface is also observed; as the amount of charge mass increases, the damage degree of RC one-way slabs also increases; when the amount of charge mass is 150 g, 225 g and 300 g, the range of damage of the front (rear) surface for the slabs is approximately equal, but the depth and the volume of the funneled craters increase; the failure mode of the above three slabs is found to be the combination of the overpressure damage of the front surface and the tensile failure of the rear surface and the slabs is collapsed without any penetration. When the amount of charge mass is 450g, the slab is penetrated under the explosion shock wave, and the failure mode of the slab is found to be punching failure.

Keywords: RC slab, Contact explosion, Failure mode, Funneled crater, Experimental investigation.

1. Introduction

Bridges have strategic significance for the development of national economic and the security of social life as an important joint of public transportation, and they may be subjected to blast loading during their life-cycle as a result of military strike, terrorist attack and accidental explosion accident. In 2007, the Sarafiya Bridge in Baghdad was attacked by a car bomb, causing heavy casualties and leading to panic among the locals, as shown in Figure 1(a) [1]. In 2013, a truck loaded with fireworks exploded in the Yichang Bridge of the Lianhuo Expressway, China, and the bridge surface collapsed immediately, as shown in Figure 1(b) [2]. The above examples show that the damage caused by blast loading may be serious, and it is especially necessary to improve the anti-explosion performance of the bridge.

RC slabs which refer to reinforced concrete slabs are the basic structures or components in building construction and various engineering structures. RC slabs are also widely used in bridge engineering, and a lot of researches were conducted on the explosion of RC slabs. Low and Hao [3-4] simulated the shear failure and bending failure of RC slab under blast loading and studied the reliability of the RC slab. Xu and

Lu [5] considered the strain rate effect of materials, and used the erosion technique to simulate the concrete cracks under different blast loads and structural conditions.

1a) The collapsed Sarafiya Bridge   1b) The collapsed Yichang Bridge

Figure 1: Cases of explosions on bridges

Luccioni et al. [6] conducted experiments and simulations on RC pavement slabs under different blast loads. Ngo et al. [7] carried out the anti-explosion test of high-strength concrete slabs. The results show that the anti-explosion performance of high-strength concrete slabs is better than that of ordinary concrete slabs, but the brittleness is enhanced and the cracking of the slabs is serious. Zhou et al. [8] used dynamic plastic damage model to reproduce the response of RC slabs under blast loading and numerical simulation analysis was also carried out. Schenker et al. [9] studied the dynamic response of concrete slabs under blast loading by field explosion test, and concluded that aluminium foam can effectively reduce the impact load of explosion. Wu et al. [10] analyzed the size of the fragments formed by concrete slabs under blast loading. Petro and Lu [11] analyzed the dynamic response and failure modes of the test-piece by the anti-explosion test of the RC square plate. Pantelides et al. [12] found that RC slabs reinforced with steel fibers have better blast resistance than other types of slabs. Thiagarajan [13] studied the damage behavior and dynamic response of high-strength concrete slabs and ordinary strength concrete slabs under blast loading through explosion test. It is concluded that the use of high-strength materials can improve the protection ability of structures under blast loading. Assadi-Lamouki and Krauthammer [14] used a modified Timoshenko beam formula including nonlinear effects of materials to re-evaluate the damage of RC slabs under blast loading, and the models were validated by 11 tests of RC slabs under blast loading. Kuang and Tsoi [15] based on the rigid plastic model and took the effects of orthotropic steel bars and asymmetric support bending constraints into account; the response and failure modes of RC slabs under blast loading are studied. Li et al. [16] conducted field explosion tests on high-strength self-compacting concrete slabs incorporating steel wire mesh. The results show that the incorporation of steel mesh effectively reduces the propagation of shock waves, and the range of concrete spalling and damage is reduced. Syed et al. [17] studied the effects of explosion pressure distribution and strength on damage and failure modes of RC slabs by far (near) field explosion tests.

In China, Yan et al. [18] used the finite element software ABAQUS to analyze the failure modes of RC slabs under blast loading. The results show that the peak pressure of the explosion is small, and the bending failure mainly occurs when the action time is long; Shear damage occurs mainly when the action time is short. Zhang et al. [19] conducted a contact explosion test on finite-thickness RC slabs, and simulated the dynamic process of plate deformation and failure. Sun [20] conducted an independent explosion test on two identical RC slabs, and studied the failure modes of RC slabs in elastic and plastic regions. Li et al. [21] used the finite element analysis software to establish the analysis method of response and failure of RC slab under blast loading, and fitted the *P-I* curve according to the simulation results, which can be used to evaluate the RC slab after explosion. Wang et al. [22] conducted a near-field explosion test on a square RC slab under unidirectional support conditions, and used the AUTODYN software to numerically

simulate the dynamic response process of the slab. The results show that with the amount of charge increasess, the failure mode of the concrete slab changes from bending failure to punching failure. Liu et al. [23] conducted a comparative test of RC two-way slabs under contact blast loading. The results show that improving the strength grade of steel and the reinforcement ratio of steel can effectively improve the anti-explosion performance of RC slabs. Chen et al. [24] experimentally analyzed the effects of steel bar type, reinforcement ratio, peak value of explosive load on the anti-explosion performance of RC slabs. In summary, most of the previous studies are focused on the anti-explosion performance of RC two-way slabs, while the research on RC one-way slabs under contact explosion is still limited. Set against this backgrounds, tests of RC one-way slabs under contact explosion are conducted, and the damage mechanism and failure characteristics of the RC one-way slabs under different blast loadings are also discussed. The test results can not only be used for engineering application of RC one-way slabs but also provide a reference for damage assessment.

2.   Specimens design and test methods

2.1   Specimens design

The RC one-way slab was designed according to "Code for Design of Concrete Structures" (GB50010-2010) in China[25]. Four specimens have the same materials and dimensions and the dimensions are 2000mm × 500mm × 100mm. The configurations of the specimens are shown in Figure 2. During the installation, the two short sides were simply supported. Four RC one-way slabs were numbered with P1-P4, and the mass of the charge (Emulsion explosive) was 150g, 225g, 300g and 450g respectively. The design concrete cube strength for pouring the RC one-way slab is 50 MPa.

2.2   Material properties

The designed ingredients and mix proportion of concrete are shown in Table 1. When pouring, the cubic specimens with the size of 150mm×150mm×150mm and the prism specimens of 150mm×150mm×300mm were reserved. After 28 days of natural curing, the cube compressive strength of concrete was measured to be 46.3 MPa, and the tensile strength was 4.0 MPa.

Table 1: Ingredients and mix proportion of concrete (kg/m3).

Cement	Sand	Aggregate	Water	Admixture
440	653	1045	140	142

Using HRB335 steel of Φ8mm and Φ6mm, the yield strength of reinforcement with (Φ8 mm) is 554MPa, the ultimate strength is 684MPa, and the reinforcement ratio of RC one-way slab is 0.628%.
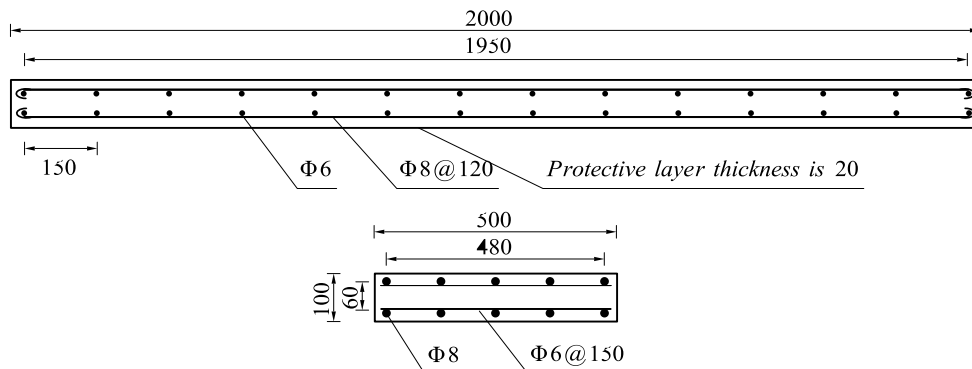
Figure 2: RC one-way slab structure diagram(Units:mm)

2.3 Explosive loading and testing

The explosion test was carried out by means of electric detonator detonating emulsion explosive. A cylindrical charge was 75g and the charge mass of specimens P1-P4 in the test design is composed of several cylindrical charges, as shown in Figure 3 (a). The explosive was placed at the center of the top surface of the slabs with contact explosion. The detonation direction was the width direction of the slabs, as shown in Figure 3(b). During the test, in order to make the bottom surface of the slabs in the free surface, the site was levelled before the test, and the brick support was fixed firmly. The contact parts of the specimens and the support were padded with oil felt to form a simple support structure, and the installation are shown in Figure 3(c). After the test, the macroscopic phenomena such as the failure mode and crack distribution of the RC one-way slabs were observed, and the specific parameters such as the size and depth of the local failure feature were measured to evaluate the damage degree of the RC one-way slabs under blast loading.

150g   225g   300g   450g

3a) Bundled explosive

3b) Charge method

3c) Installation diagram
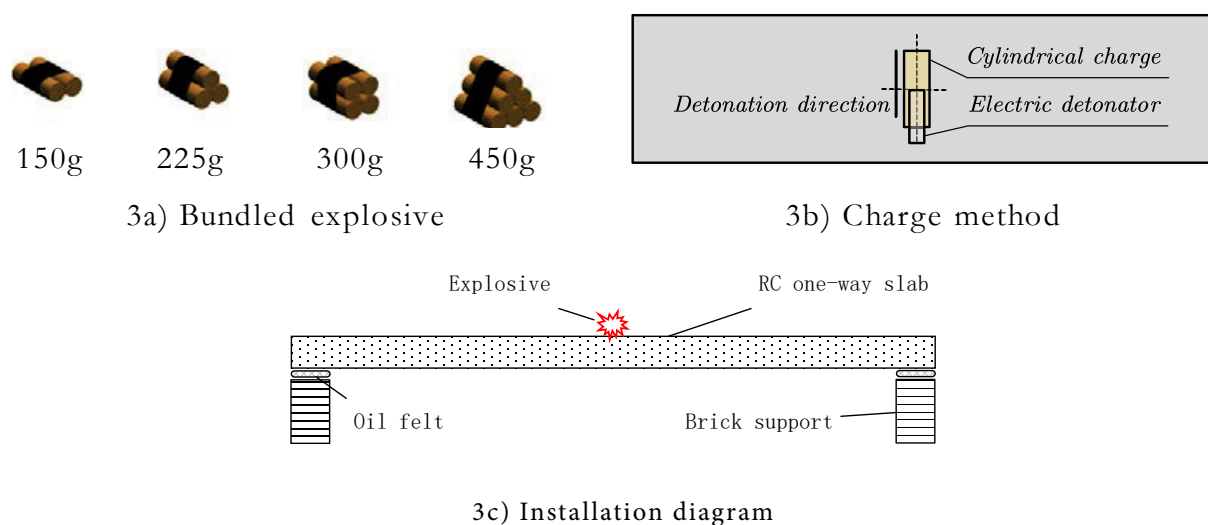
Figure 3: Specimens installation and loading method

3. Test results

According to the specifications of the specimens designed in Section 2.1 and the test conditions proposed in Section 2.3, the anti-explosion tests of the RC one-way slabs were carried out. Figure 4 shows the failure modes of the top and bottom surface of the specimen P1-P4. In order to facilitate the observation of the extent and shape of the specimens after test, the concrete of slabs were divided into 5cm*5cm grids by ink cartridges. After the test, the macroscopic damage phenomena of the blasting concrete on the top surfac and bottom surfaces are listed in Table 2. It can be seen from Fig. 4 that the failure modes of P1, P2 and P3 are similar, there are a small amount of concrete caving on the top surface, and concrete cracking phenomenon of the bottom surface is remarkable, a tensile spalling crater appears on the bottom surface of the slab. The amount of concrete caving increases with the increase of explosive equivalent, the range and depth of the spalling crater increase, and there is a phenomenon that the steel are bare. The failure mode of P4 is that the concrete spalling crater on the bottom surface and the spalling crater on the top surface form a breach, and the bottom surface has the phenomenon of transverse steel fracture. In addition to the concrete caving on the top surface and the spalling crater on the bottom surface, a large number of radial cracks generated near the explosion point and the transverse (longitudinal) cracks away from the explosion point are also the failure modes of the RC one-way slabs.

1) The top surface   2) the bottom surface

4a) P1

1) The top surface   2) the bottom surface

4b) P2

1) The top surface   2) the bottom surface

4c) P3

1) The top surface   2) the bottom surface

4d) P4
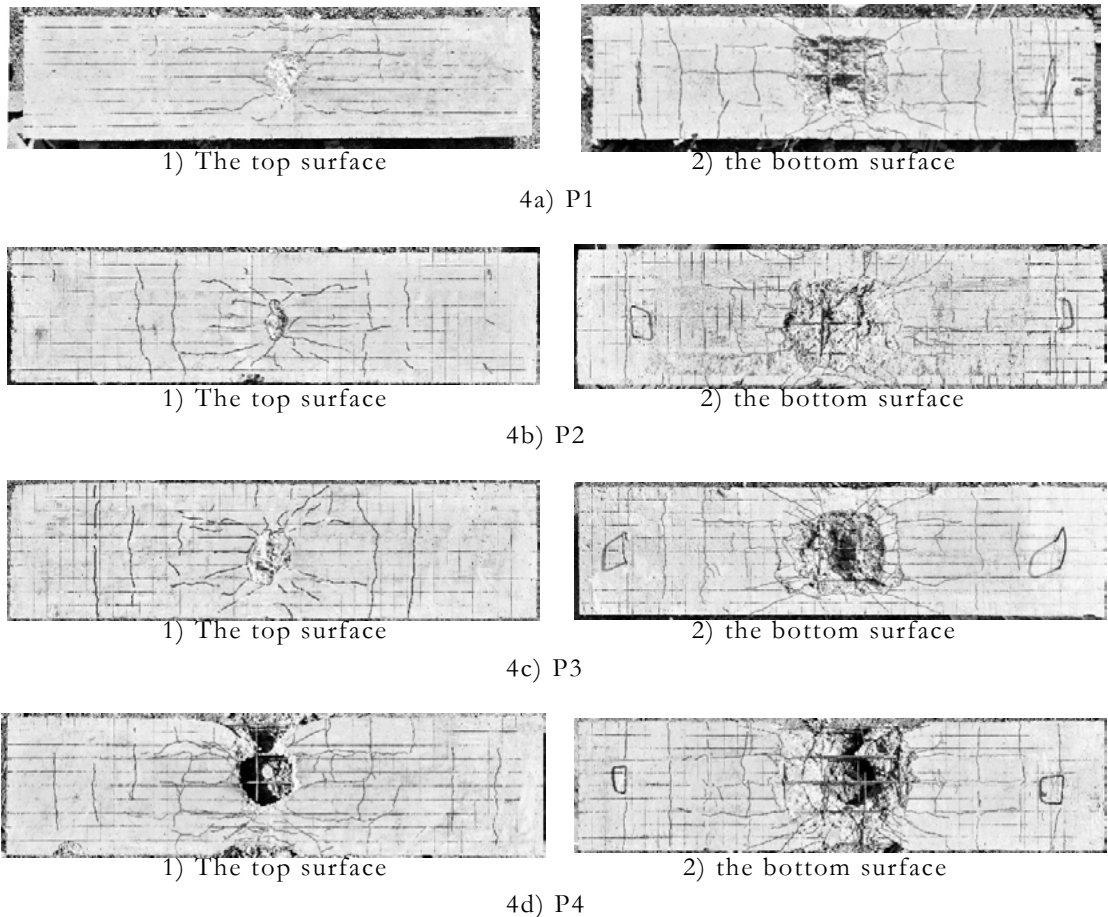
Figure 4: Explosion surface (back explosion surface) damage form

Therefore, the macroscopic characteristics of the RC one-way slabs are: the top surface (the bottom surface) spalling crater + radial cracks at the explosion point + transverse (longitudinal) cracks away from the explosion point. The damage of P4 also includes the collapse of the side concrete, while the concentrated charge and the detonation direction cause the pressure distribution in the concrete to be uneven, furthermore the concrete displacement on the side of the concrete slab is not coordinated, resulting in concrete peeling.

Table 2: RC one-way slab failure mode

Specimens number	Test condition	The top surface damage	The bottom surface damage
P1	150g emulsion explosive	A small amount of concrete collapsed, no steel bare	Tensile spalling crater, 2*2 (Longitudinal * transverse) bare steel exposed
P2	225g emulsion explosive	A small amount of concrete collapsed, no steel bare	Tensile spalling crater, 3*2 (Longitudinal * transverse)bare steel exposed
P3	300g emulsion explosive	A small amount of concrete collapsed, no steel bare	Tensile spalling crater, 3*2 (Longitudinal * transverse)bare steel exposed
P4	450g emulsion explosive	Large concrete collapses, 3*1 (Longitudinal reinforcement * transverse reinforcement) steel bars are exposed	Tensile spalling crater, forming a break with the front funnel pit, 5*4(Longitudinal * transverse) steel bars, 2 steel bars broken

4.   Analysis and discussion

4.1   Damage parameters

The measurement results of the spalling crater including the plane size, depth and volume are shown in

Table 3, where d_1 and d_2 are the length of the damage range along the direction of the longitudinal and transverse reinforcements respectively, h_0 and v_0 are the depth and the volume of the spalling crater; or the bottom surface, D_1 and D_2 are the length of the damage range along the direction of the longitudinal and transverse reinforcements, h_0 and v_0 are the length of the damage range along the direction of the longitudinal and transverse reinforcements. The damage parameters are shown in Fig. 5.

Figure 5: Damage parameter
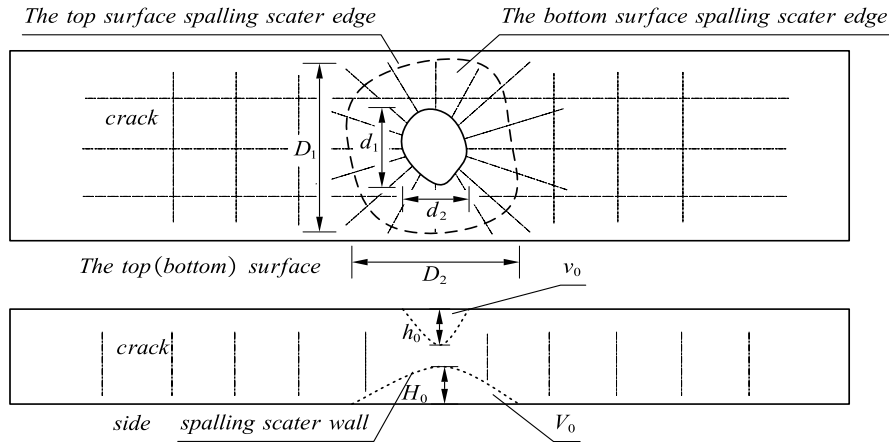
Table 3: Main damage parameters of the specimens

Specimens number	Explosive mass/g	The top surface surface				The bottom surface			
		d_1/cm	d_2/cm	h_0/cm	v_0/cm³	D_1/cm	D_2/cm	H_0/cm	V_0/cm³
P1	150	15.38	15.67	1.65	209.24	30.39	37.10	4.54	2400.26
P2	225	12.28	7.08	2.13	273.65	32.76	41.59	6.05	2566.49
P3	300	17.86	12.28	3.04	310.94	32.73	38.94	5.93	3045.79
P4	450	20.18	20.35	3.42	380.32	42.86	53.10	6.58	5676.96

4.2 Influence of parameters

It can be seen from Fig. 4 and Table 2 that the RC one-way slabs generates spalling craters on the top surface and bottom surface under the contact blast loading, and the crater size and depth increase correspondingly with the increase of explosive equivalent. Figure 6 shows the crater volume histogram of the RC one-way slab under different equivalents. It can be seen that with the increase of explosive mass, the volume of the spalling crater increases; compared with P1, the top surfaces of P2, P3 and P4 increased by 31.1%, 48.8% and 81.8%. For the bottom surface, the volume of the spalling crater of P2, P3 and P4 increased by 6.92%, 26.91% and 136.54% in compared with P1, respectively.
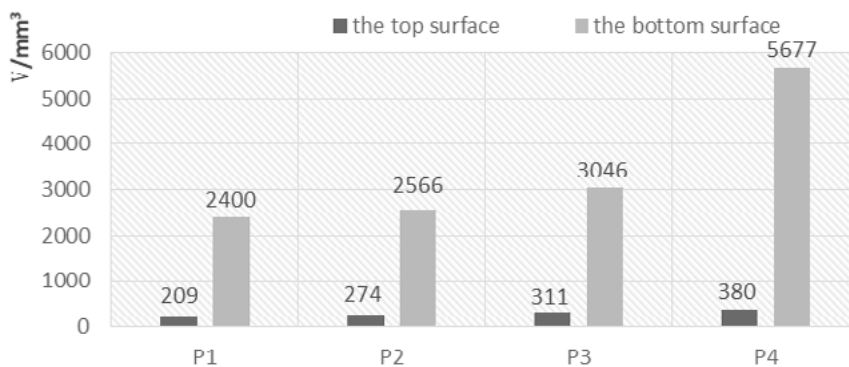
Figure 6: Explosion surface, back explosion surface funnel pit volume histogram

The obvious cracks (width≥0.1mm) are marked with red pen on the top and bottom surfaces. It can be seen that there are three types of cracks in the specimen subjected to the explosion shock: longitudinal crack, transverse cracks, and oblique cracks that radiates outward from the center of the explosion. The oblique cracks are concentrated around the fracture, and the transverse cracks and the longitudinal cracks are combined into a grid shape, which is more evenly distributed on the top and bottom sides of the specimens. The statistics of the three types of cracks are shown in Table 3.

Table 3: Number of cracks

Specimens number	The top surface crack			The bottom surface crack		
	Portrait	Landscape	Oblique	Portrait	Landscape	Oblique
P1	2	2	8	3	9	10
P2	2	5	13	2	7	15
P3	3	6	14	3	9	18
P4	3	10	13	3	9	16

With the increase of explosive mass, the number of oblique cracks and lateral cracks in the top surface increased, but the increase of longitudinal cracks was not obvious; the number of diagonal cracks on the bottom surface increased with the rise of explosives, while the number of transverse and longitudinal cracks remained almost unchanged. The spacing between two adjacent transverse cracks is about 13~15 cm, while the spacing between two adjacent longitudinal cracks is 10~13 cm, and the position of the transverse and longitudinal cracks is the location of the reinforcement. It should be pointed out that the amount of the oblique cracks is less than the amount of 300g explosive when the amount of explosive is 450g. This is because the energy is mostly concentrated in the falling concrete when the punching failure occurs, causing other parts to be affected.

The impact wave is less affected and the number of diagonal cracks is decreased.The RC slab forms a compression spalling crater on the top surface under the action of the blast loading. The concrete of the bottom surface spall to form a tensile spalling crater, the spallation penetrating and the punching failure will occur with the increase of the charge weight. For RC slabs of finite thickness under the contact explosion with a small amount of explosives, the main performance is the spallation damage. This is because the high temperature and high pressure generated in the early stage of the explosion acts on the RC one-way slab, which causes the top surface to form a crushed zone. At this time, the ultra-high pressure of the strong shock wave is mainly applied to the shock wave compression damage effect of the structure, and the crack appears to be "radial". The crushed zone has a relatively small range, but consumes a large part of the energy, as a result the shock wave is attenuated into a compressive stress wave. At this point, there is a small spalling crater on the top surface of the slab, and the bottom surface has not yet exhibited visible macroscopic damage. As stress waves travel through the concrete, the impact compression wave caused by the explosion will be reflected at the bottom surface of the concrete, thus forming a tensile wave. Since the tensile strength of concrete is much lower than its compressive strength, when the tensile wave strength causes the concrete to reach a certain yield condition, tensile failure occurs and thereby forming a tensile spalling crater on the bottom surface.

The failure modes of the P1, P2 and P3 specimens used for the tests belong to this category. In this case, the specimens has two modes of overpressure failure and tensile failure. Increase the amount of explosives, which can cause the spalling crater on the top surface and the tensile spalling crater on the bottom surface to form spallation penetrating. Just then, the specimens present mainly overpressure failure and tensile failure. As the amount of explosives continues to increase, the concrete was completely punched out before

the material has not been crushed, generating an explosion punching phenomenon. The P4 specimen in the test showed such a phenomenon, in which case the concrete member was mainly shear fracture.

5. Conclusions

In this paper, the test of four RC one-way slabs which have the same material properties under contact explosion are conducted. The four RC one-way slabs named P1-P4 and are detonated under 150g, 225g, 300g and 450g emulsion explosives respectively. The failure modes and damage parameters are analyzed, and the failure mechanism is revealed. The results show that when the explosive mass is small, the specimens are tend to be tensile failure accompanied by transverse (longitudinal) cracks and radial cracks near the explosion point. With the increase of explosive mass, the failure modes of the RC one-way slabs transfer into punching failure, which is characterized by the concrete spalling near the explosion point and a large tensile spalling crater with a large number of transverse (longitudinal) cracks and radial cracks. The volume of the spalling crater increases accordingly; compared with P1, the top surfaces of P2, P3 and P4 increased by 31.1%, 48.8% and 81.8%. For the bottom surface, the volume of the spalling crater of P2, P3 and P4 increased by 6.92%, 26.91% and 136.54% in compared with P1, respectively.

6. Acknowledgment

7. References

[1] Hao J W. Accident risk assessment and management of large bridges during operation period. 2015. (in Chinese)

[2] Li L Y. Let the safety rules go from "on paper" to "on the road". Safety and health, 2013(3):1-1. (in Chinese)

[3] Low H Y , Hao H . Reliability analysis of RC slabs under explosive loading. Structural Safety, 2001, 23(2):157-178.

[4] Low H Y , Hao H . Reliability analysis of direct shear and flexural failure modes of RC slabs under explosive loading. Engineering Structures, 2002, 24(2):189-198.

[5] Xu K , Lu Y . Numerical simulation study of spallation in RC plates subjected to blast loading. Computers & Structures, 2006, 84(5-6):431-438.

[6] Bibiana María Luccioni, Luege M . Concrete pavement slab under blast loads. International Journal of Impact Engineering, 2006, 32(8):1248-1266.

[7] Ngo T ,Mendis P , Krauthammer T . Behavior of Ultrahigh-Strength Prestressed Concrete Panels Subjected to Blast Loading. Journal of Structural Engineering, 2007, 133(11):1582-1590.

[8] Zhou X Q ,Kuznetsov V A , Hao H , et al. Numerical prediction of concrete slab response to blast loading. International Journal of Impact Engineering, 2008, 35(10):1186-1200.

[9] András Schenker, Anteby I , Gal E , et al. Full-scale field tests of concrete slabs subjected to blast loads. International Journal of Impact Engineering, 2008, 35(3):184-198.

[10] Wu C ,Nurwidayati R , Oehlers D J . Fragmentation from spallation of RC slabs due to airblast loads. International Journal of Impact Engineering, 2009, 36(12):1371-1376.

[11] Silva P F , Lu B . Blast Resistance Capacity of RC Slabs. Journal of Structural Engineering, 2009, 135(6):708-716.

[12] Pantelides C P , Garfield T T , Richins W D , et al. RC and fiber RC panels subjected to blast detonations and post-blast static tests. Engineering Structures, 2014, 76:24-33.

[13] Thiagarajan. Experimental and finite element analysis of doubly RC slabs subjected to blast loads. International Journal of Impact Engineering, 2015, 75:162-173.

[14] AssadilamoukiA , Krauthammer T . Reevaluation of RC Slabs Subjected to Blast Effects// Seismic Engineering. ASCE, 2015.

[15] J. S. KUANG,H. F. TSOI.Failure of Blast-Loaded RC Slabs.//Proceedings of the Twelfth East Asia-Pacific Conference on Structural Engineering and Construction (EASEC12), Vol.4: Hong Kong, 26-28 January 2011.2013:2658-2665.

[16] Li J , Wu C , Hao H , et al. Experimental and numerical study on steel wire mesh RC slab under contact explosion. Materials & Design, 2017, 116:77-91.

[17] Syed Z I , Raman S N , Ngo T , et al. The Failure Behaviour of RC Panels Under Far-field and Near-field Blast Effects. Structures, 2018:S2352012418300341.

[18] Yan S, Zhang L, Wang D. Failure Mode Analysis of RC Slabs under Explosive Loading. Journal of Shenyang Jianzhu University: Natural Science Edition, 2005, 21(3): 177-180. (in Chinese)

[19] Zhang XB, Yang XM, Chen YY, et al. The Collapse Effect of Explosive RC Slabs. Journal of Tsinghua University(Science and Technology), 2006, 46(6): 765-768. (in Chinese)

[20] Sun Wenbin. Experimental study on blast loading of RC slab. Journal of Liaoning Technical University, 2009, 28(2): 217-220. (in Chinese)

[21] Failure Assessment Method of RC Slabs under Explosive Loading. Journal of Building Structures, 2009, 30(6): 60-66.

[22] Wang W, Zhang D, Lu FY, et al. Near-field anti-explosion performance of square RC slab. Explosion and Shock Wave, 2012, 32(3): 251-258. (in Chinese)

[23] Liu Y, Lu HB, Zhou BK, et al. Analysis of anti-contact explosion test of high strength RC plate. Journal of the Chinese Ceramics, 2012, 11(5):571-574. (in Chinese)

[24] Chen WX, Lu HB, Hou XW, et al. Experimental study on anti-explosion performance of high strength steel RC slab. JOURNAL OF VIBRATION AND SHOCK, 2015, 34(10):135-141. (in Chinese)

[25] Prepared by the Ministry of Construction of the People's Republic of China. Code for design of concrete structures. China Building Industry Press, 2002. (in Chinese)

Electrodialytically treated MSWI fly ash use in clay bricks

L. Skevi[1/2], L. M. Ottosen[2], G. M. Kirkelund[2]

[1] School of Physics, Faculty of Sciences, Aristotle University of Thessaloniki.

[2] Department of Civil Engineering, Technical University of Denmark

Abstract

Fly ash from municipal solid waste incineration (MSWI) is classified as hazardous waste, due to high heavy metal and salt content. Thus, beneficial use is restricted, and the fly ash hazardousness should be reduced before testing reuse options. Electrodialytic treatment can remove heavy metals and soluble salts and be used to decontaminate MSWI fly ash. In Greenland, MSWI fly ash is stored at uncontrolled disposal sites, and a more sustainable solution for handling fly ash is needed. At the same time, most construction materials are imported from Europe to Greenland, and increased use of local materials would greatly benefit the circular economy in the area. In this study, it was investigated if local Greenlandic resources could have potential in brickmaking. Two different clays; a Danish clay (used commercially in brick production) and one Greenlandic (not used commercially) and raw and electrodialytically treated MSWI fly ash from Sisimiut, Greenland were used. Small clay discs with a 0, 10, 20 and 30 % substitution of clay by MSWI fly ash were fired at $1000^{\circ}C$ for 24h. Substituting clay with fly ash generally resulted in lower technical properties of the clay discs. From this initial screening, the clay discs with electrodialytically treated fly ash and Greenlandic clay showed the lowest porosity and water absorption, which could be beneficial for use as construction material in cold climates.

Keywords: heavy metals, circular economy, secondary resources, ceramics, Arctic.

1.   Introduction

Incorporation of waste residues in building materials has been gained increased focus in the past years as a waste management practice on the one hand and a way to upgrade construction materials' properties on the other. Industrial wastes, like fly ash from coal combustion, silica fume and blast furnace slag are fine-grained materials with a high content in CaO, SiO_2, Al_2O_3 and other relative minerals, and this composition is compatible with cement-based and clay-based materials. Therefore, several studies investigate the application for partly replacement of cement and clay with these waste materials as secondary raw materials for the production of mortar, concrete and bricks [1, 2]. Ceramic materials made of clay, like bricks, are considered particularly attractive for the incorporation of wastes due to the heterogeneous composition of clay that can incorporate and stabilize various wastes in the matrix even if the wastes contain toxic substances. Also, there is a need for preservation of natural clay resources, and thus research on replacing part of clay for more sustainable brick production has been encouraged. It has, also, been demonstrated that the use of wastes as clay supplements in bricks do not affect significantly key properties of the final product [3], while in some cases they can even contribute to the enhancement of several of its properties.

Municipal solid wastes (MSW) account for about 10% of the total waste production, but due to their complex composition, their treatment presents certain difficulties. A common practice for avoiding the

landfill disposal of these solids wastes and thus for minimizing the environmental risk is incineration as it greatly reduces the mass and volume of the wastes. The miscellaneous composition of MSW depends on the sources of the wastes, which can vary for different countries according to waste management regulations and policies. Household and commercial wastes are the most common sources which may include different amounts of food waste, plastic and synthetic materials, even electrical devises and batteries when these are not recycled. As a result, MSW has a large content of organic and inorganic contaminants, such as heavy metals and alkaline salts. All these toxic compounds are finally highly concentrated in the residues of the incineration process. Handling of these residual materials, like fly ash, bottom ash and air pollution control residues (APC), can be very challenging. Disposal in landfills is a widely applied solution, but imposes a danger on the environment as a result of the leaching of the soluble elements which contaminate the soil and the water resources in the area. A more sustainable approach suggests the recycling and reusing of these materials. MSWI fly ash is an ultrafine material rich in calcium, silica and aluminium oxides and therefore it could be used as a cement and clay substitution for the production of sustainable building materials. However, because it also contains heavy metals, like Pb, Cd, Cr, Mo, Zn and alkali metal salts such as K and Na chlorides and sulphates it is classified as a hazardous waste. Thus, proper treatment for reducing the hazardousness of the material in acceptable limits is essential prior considering its possible beneficial uses.

Various techniques have been proposed for reducing the concentration of heavy metals and salts in MSWI fly ash [4]. Water washing is a simple method, often used as a pre-treatment before other techniques since it is more suitable for removing salts and very mobile fractions of heavy metals. Other techniques which stabilizes heavy metals include carbonation, chemical stabilization and thermal and hydrothermal treatment. The electrodialytic treatment has been proposed as an alternative method for the removal of heavy metals and soluble salts and has been applied for the decontamination of MSWI fly ash [5,6]. The method relies on the application of an electric current to the waste material and the subsequent removal of heavy metal ions in the electric field [5]. Untreated and treated MSWI fly ashes have been tested in building materials in laboratory stage [7-10]. In [11] untreated Greenlandic MSWI fly and bottom ash were added in mortars as cement replacement, and it was concluded that up to 5% of ashes could be stabilized successfully in the mortar. In [3] it was tested if 20 % or 40% MSWI fly ash could replace clay for brick production and especially 40 % replacement resulted in deteriorating the properties of the final product and leaching of several heavy metals, especially an increase of Cr leaching was seen. There is a need to find the optimum replacement percentage of MSWI fly ash in brick products, for this application to be feasible. Removal of heavy metals and salts from the MSWI fly ash is also needed, to reduce the toxicity of the fly ash.

MSWI fly ash in Greenland is so far stored at uncontrolled disposal sites, before being shipped for end disposal abroad. Thus there is a need for a more sustainable and economically feasible solution. At the same time, most construction materials are imported from Europe to Greenland, while increased use of local materials would greatly benefit the circular economy in the area. Therefore, there is an option of using MSWI fly ash as a substitution of clay in bricks, which should stabilise the heavy metals and conserve primary resources. This study investigates the potential of brick production from Danish and Greenlandic clay that is partly substituted with MSWI fly ash, by screening the production on small clay discs. The effect of electrodialytic treatment of the fly ash in the final product is evaluated in comparison with that of the untreated waste.

2.   Methodology

2.1   Experimental materials

Two different clays were used for the clay discs; commercially available Teglværksler (denoted T) from Wienerberger, Denmark and a clay sediment sampled from Sisimiut, Greenland (denoted S). MSWI fly ash was collected from the incineration plant in Sisimiut, Greenland and was used raw (denoted R) or

electrodialytically treated in the clay discs. The electrodialytic treatment was performed in both a two- and a three-compartment cell (denoted E and D respectively), to remove heavy metals from the fly ash as a treatment method. More specific information and details about the electrodialytic treatment experiments can be found in [6]. Particle size distribution and mineralogy were determined on the separate electrodialytically treated ashes, whereas heavy metal leaching and total content were measured on a mix of the two ashes (denoted ED). All notations of the experimental materials are shown in Table 1.

Table 1: Experimental materials

Clay	Symbol
Teglværksler (Danish clay)	T
Sisimiut ler (Greenlandic clay)	S
Fly ashes	
Treated fly ash (2 compartments)	E
Treated fly ash (3 compartments)	D
Mix E and D fly ashes	ED
Untreated (Raw) Sisimiut fly ash	R

2.2 Analytical methods

The Atterberg limits (liquid and plastic limits) were determined for the two clay samples to evaluate the plastic properties of the clays. The plastic limits (W_P) were determined by the rolling method (ISO/TS 17892-12), and liquid limits (W_L) were measured using the Casagrande method (DIN 18122-1). The particle size distribution was determined for all samples with a Malvern Mastersizer 2000 laser diffractometer on dry samples. Clay and ash mineralogy was studied by X-ray powder diffraction (XRD) for identification of major crystalline phases. The instrument was a PANalytical X'Pert Pro operating at 45 mA and 40 kV applying Cu Kα radiation with a 2ΘX'Celerator detector. The samples were scanned within 4–70 2Θ for 2.5 h. The diffractograms were interpreted using the ICDD PDF-4 database for minerals. Total heavy metal concentrations were measured by Inductive Coupled Plasma – Optical Emission Spectrometry (ICP-OES) after pre-treatment according to DS 259. Heavy metal leaching was performed in a modified version of DS/EN 12457-1 (L/S 2), where 15 g ash was mixed with 30 mL distilled water (instead of 2 kg and 40 L as described in the standard) and suspended for 24 hours, before pH was measured in the suspension, filtration of the suspension and measurement of heavy metals in the eluate by ICP-OES.

2.3 Production of the discs

Twelve different clay mixtures with ash were made and compared to clay without fly ash (Table 2).

Table 2: Composition of the clay mixtures with the amount of fly ash given in wt%. The sample name follows the denotation in Table 1, and the numbers in the names of the samples refer to the percentage by weight of replaced fly ash.

Sample name	T	S	E	D	R
T0	100				
TED10	90		5	5	
TED20	80		10	10	
TED30	70		15	15	
TR10	90				10
TR20	80				20
TR30	70				30
S0		100			
SED10		90	5	5	
SED20		80	10	10	
SED30		70	15	15	
TR10		90			10
TR20		80			20
TR30		70			30

For the study, small brick specimens in the form of discs were constructed following the method that was applied in a previous study [3]. According to this method, the materials were mixed with a total weight of 2.3 g material, and distilled water was added to the material to obtain a paste-like texture. The mixture then absorbed the moisture for 24h. Next, the clay mixture was pressed into discs mechanically (Instron 6022), under a maximum load of 10 KN. The produced discs weighted approximately 2 g while their diameter and thickness (height) were around 20 mm and 3 mm respectively. Five discs of each mixture were produced, and their exact dimensions and weight was immediately measured with a micrometre scale gauge and a precision balance. The discs were then dried at 105ºC for 24h and the dimensions and weight of the dried discs were again measured. Finally, the discs were fired at 1000ºC for 24h and their dimension characteristics were again measured. The loss of mass (ML) and the linear shrinkage (LS) was determined between the wet, dry and fired condition, the total mass loss (TML) and total linear shrinkage (TLS) from wet to fired condition as described in the following equations. X is the diameter when referring to linear shrinkage and the mass when referring to the loss of mass.

$$DLS \ (or \ DML) = \frac{x_{wet} - x_{dry}}{x_{wet}} \times 100 \ \% \tag{1}$$

$$FLS \ (or \ FML) = \frac{x_{dry} - x_{fired}}{x_{dry}} \times 100 \ \% \tag{2}$$

$$TLS \ (or \ TML) = \frac{x_{wet} - x_{fired}}{x_{wet}} \times 100 \ \% \tag{3}$$

Where:

DLS – dry linear shrinkage

FLS – fired linear shrinkage

DML – dry mass loss

FML – fired mass loss

TLS- total linear shrinkage

TML- total mass loss

The open porosity, dry density and water absorption were determined according to the procedure Ti-B-25 by the Danish Technical Institute. The discs were dried at 105ºC, cooled to room temperature in a desiccator and weighed (m_{dry}). The discs were placed in a vacuum in the desiccator for 3 h, whereafter distilled water was added until the discs were submerged. The vacuum was again added for 1 h, whereafter the vacuum was released and the submerged discs were left at atmospheric pressure overnight. The water saturated discs were then weighed in water (m_{sw}) and air (m_{sa}) after being wiped for excess water. The open porosity, dry density and water absorption were then calculated as:

$$Open \ porosity = \frac{m_{sa} - m_{dry}}{m_{sa} - m_{sw}} \cdot 100\% \tag{4}$$

$$Dry \ density = \frac{m_{dry} \cdot \rho_w}{m_{sa} - m_{sw}} \cdot 100\% \tag{5}$$

$$Water \ absorption = \frac{m_{sa} - m_{dry}}{m_{dry}} \cdot 100\% \tag{6}$$

Where ρ_w is the water density at room temperature.

Mineralogy (XRD) and heavy metal leaching were also performed on crushed clay discs.

3. Results and discussion

3.1 Characteristics of experimental materials

Geotechnical properties of the clays are shown in Table 3 and the particle size distribution of the raw materials, clays and treated fly ashes is shown in Figure 1. The plasticity index (I_p) can be used to evaluate the span between the plastic and liquid limits. Both clays used in this study present low plasticity, especially Sisimiut clay, which has a very low plastic index (<10). This agrees with results found by [3]) and indicate that their moulding range is very limited. Belmonte et al. [3] found higher plasticity index for mixtures of clay with fly ash than the clay itself, and the moulding of the clay discs with fly ash was not more difficult in practice than the clay itself. The two treated fly ashes, E and D, have similar particle size distribution as it is shown in the graph above. Also, their particles' size presents similar distribution with the one of the Sisimiut clay, although this the Sisimiut clay to have a slightly higher fraction of finer particles. Teglværks clay (T), on the other hand, has a larger volume percentage of coarse particles than the fly ashes and the Sisimiut clay. According to the Unified Soil Classification System (USCS) (ASTM D2487-17) both clays are classified as fine-grained soils (silt and clay) as more than 50% of their volume contains particles with fraction d<75 µm. For both clays, the clay fraction (<2 µm) was about 10% of their total volume, while approximately 45% of the volume of Teglværks and 65% of Sisimiut clay consisted of silt. The rest of their volume consisted of sand, 45% and 25% for Teglværks and Sisimiut clay, respectively. Finally, the raw untreated fly ash (R) consisted of finer particles than the treated fly ashes (E and D) and the two clays (T and S).

Taking into consideration the liquid limit (W_L) and plasticity index (I_p) of the clays as well as their particle size distribution according to the Casagrande plasticity chart [12], Teglværks clay is characterized as sandy lean clay, while Sisimiut clay as lean clay with sand.

Table 3: Geotechnical properties of the clays. Plasticity Index $I_p = W_L - W_p$.

Clays	Plastic Limit	Liquid Limit	Plasticity Index
	W_p (%)	W_L (%)	I_p (%)
T	15.2	28.5	13.3
S	14.2	22.5	8.3
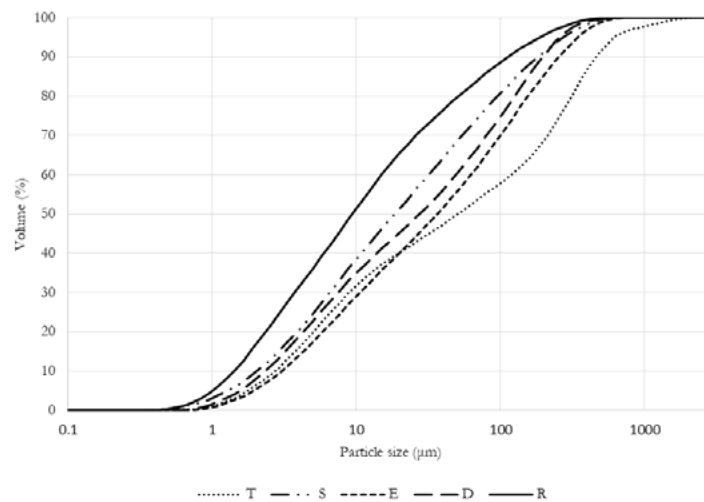
Figure 1: Particle Size Distribution of Teglværksler (T), Sisimiut clay (S), treated fly ashes (E&D) and raw fly ash (R)

The XRD diffractograms of clays and fly ashes are shown in Figure 2.
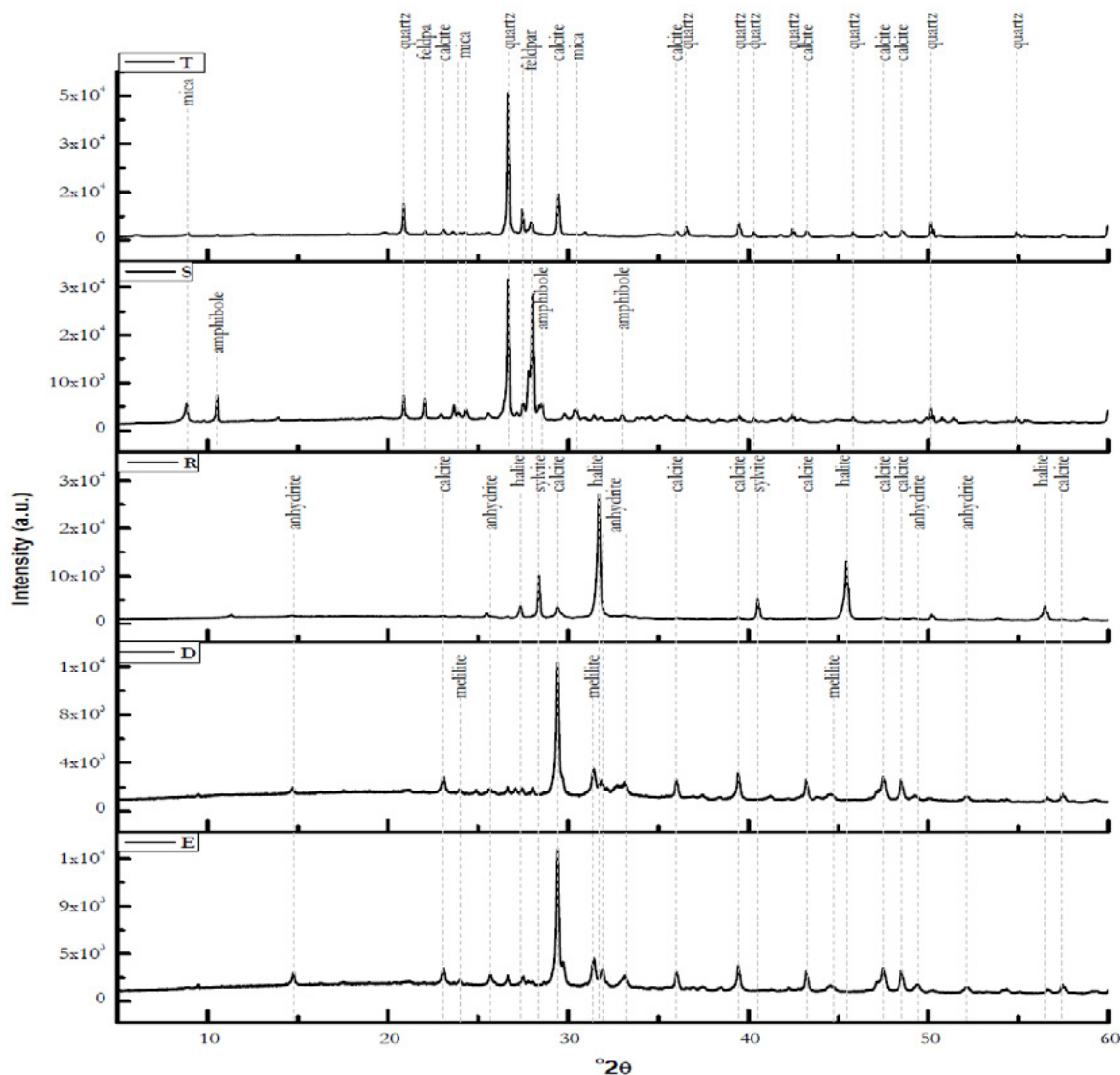
Figure 2: X-ray diffractograms of the experimental materials Teglværksler (T), Sisimiut clay (S), treated fly ashes (E&D) and raw fly ash (R)

As shown in the diffractogram, of Teglværks clay (T), this clay sample was dominated by quartz (SiO_2) and calcite ($CaCO_3$), and it also consisted of feldspars (albite ($NaAlSi_3O_8$) and microcline ($KAlSi_3O_8$) as well as micas (muscovite ($KAl_2(AlSi_3O_{10})$)). Sisimiut clay (S), on the other hand, mainly consisted of quartz and did not contain calcite. Instead, the second most dominant mineral phase in the Sisimiut clay was feldspars (albite, microcline and anorthite ($CaAl_2Si_2O_8$)), followed by amphibole (magnesiohornblende) and Fe – rich mica (phlogopite). This explains the light grey colour of Danish clay due to calcite, in comparison with the dark grey of the Greenlandic clay (photos of clays not shown). As for the fly ashes, the untreated raw fly ash (R) was dominated by salts: halite (NaCl) and sylvite (KCl). It also contained calcite and anhydrite ($CaSO_4$) as minor mineral phases. The two electrodialytically treated fly ashes (D and E) present identical mineralogy. As shown from their diffractograms they were calcareous but, unlike the untreated fly ash, they did not contain salts. Also, the phase of anhydrite (basanite) intensified in the electrodialytically treated ashes compared to the raw fly ash and traces of melilite mineral phases (gehlenite) were identified. It shows that the electrodialytic treatment is responsible for the removal of the salts in fly ashes D and E. Based on

the similar particle size distribution and mineralogy, it was determined to mix the two electrodialytically treated ashes in for the further experiments.

Total heavy metal concentration and leaching of heavy metals, chloride and sulphate were measured for raw fly ash (R) and the mixture of the two treated fly ashes (ED). The results are shown in Table 4, in which the pH of the fly ashes is also given. The values are compared to the limits given by the Danish Ministry of Environment for use in geotechnical applications [13], as no limits exist for the use of waste in construction materials. The total metal concentrations show a significant reduction in the total content of heavy metals due to the electrodialytic treatment, but the leaching of As, Cr, Ni and Zn increased, also to above the Category 3 limit. There was a significant reduction in the chloride and sulphate leaching, linked to the removal of chloride and sulphate containing mineral during the electrodialytic treatment.

Table 4: Total heavy metal concentration and leaching of the fly ashes.

	Raw ash	ED ash	Category 3
Total concentration (mg/kg)	Average	Average	
As	277	29	>20
Cd	162	132	>0.5
Cr	109	71	>500
Cu	1,350	667	>500
Ni	32	73	>30
Pb	8,770	2,170	>40
Zn	21,600	8,680	>500
Leaching (µg/l)			
As	91	600	8-50
Cd	1560	2	2-40
Cr	550	1190	10-500
Cu	120	33	45-2000
Ni	46	125	10-70
Pb	397	35	10-100
Zn	109	340	100-1500
Cl	$155 \cdot 10^6$	$1.7 \cdot 10^6$	$1.5 \cdot 10^6 - 3.0 \cdot 10^6$
SO$_4$	$3.04 \cdot 10^6$	$0.75 \cdot 10^6$	$2.5 - 3.0 \cdot 10^6$
pH	10.3	9.8	

3.2   Characteristics of the clay discs

The produced discs are shown in Figure 3, in the left the Teglværks clay discs and in the right the Sisimiut clay discs, both containing different amounts of substitution with fly ashes, treated (ED) and raw (R). It is seen in Figure 3 that as the amount of the fly ashes increases the colour of the discs gets lighter, both for the Danish (Teglværksler) and the Greenlandic (Sisimiut) clay mixtures. The stronger red colour of the Sisimiut S0 disc is probably linked to the Fe-minerals that were identified in this clay. There was a difference in the colour of the discs with raw fly ash and electrodialytically treated fly ash. This was more dependent on the clay used than the ash since the disc with electrodialytically treated fly ash in Teglværksler were darker than with raw fly ash, but the discs with Sisimiut clay were darkerst with raw fly ash.
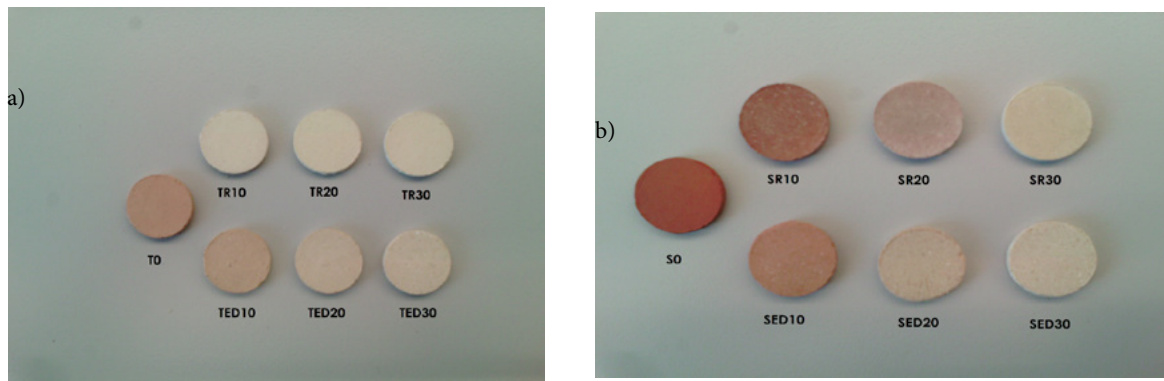
Figure 3: Colours of discs with substitution of clay with different amounts (0%, 10%, 20%, 30%) fly ash (R – raw, ED – treated. a) Teglværks (T) clay discs, b) Sisimiut (S) clay discs

The total loss of mass, total linear shrinkage, total volume change, porosity, dry density and water absorption of the produced discs are given in Figure 4. The total volume change of the discs containing raw fly ash (R) was negative for both types of clays, meaning that these discs expanded instead of shrinking as the other discs did, and their expansion was larger as the amount of fly ash increased. This can be attributed to a bloating effect due to gas from the decomposition of sulphates or carbonate [3]. On the contrary, the addition of more treated fly ash (ED) resulted in lower volume change for both clay discs, since sulphates are removed by electrodialytic treatment [5].

A lower mass loss but a higher linear shrinkage were seen for the Sisimiut clay discs compared to Teglværksler discs and increasing the amount of electrodialytically treated fly ash increased the volume change. This is clearly linked to the results of porosity, dry density and water absorption show in Figure 4. The porosity and water absorption increased by the addition of fly ash for both clay and fly ash types. Teglværks clay discs showed the highest porosity for substitution with raw fly ash, which is also linked to the higher mass loss for these clay discs compared to the Sisimiut clay discs. For the Sisimiut clays discs, the porosity was highest when treated fly ash was added, with corresponding lower densities of the discs and a higher water absorption, even if bloating occurred for the Sisimiut clay discs with raw ash.

The water absorption was lower for all Sisimiut clay discs than for the Teglværksler clay discs, also linked to the porosity. In bricks used in the building industry, typical ranges are: dry densities 1610-2120 kg/m^3 [14, 15]; open porosities 18.8-39 % [15] and water absorption 22-37 % [16]. Only the water absorption is lower for some of the samples in this study, especially for the discs with Sisimiut clay and raw fly ash.

For the discs with electrodialytically treated fly ash, there was a difference when using Teglværksler or Sisimiut clay. The performance of the discs was lower with Teglværksler than the Sisimiut clay, which is also linked to the properties of the clays themselves. The low porosity, high density and low water absorption for the Sisimiut clay discs indicate good performance in cold climates. However, the pore size should be studied further to evaluate the possibility of resisting frost/thaw cycles.
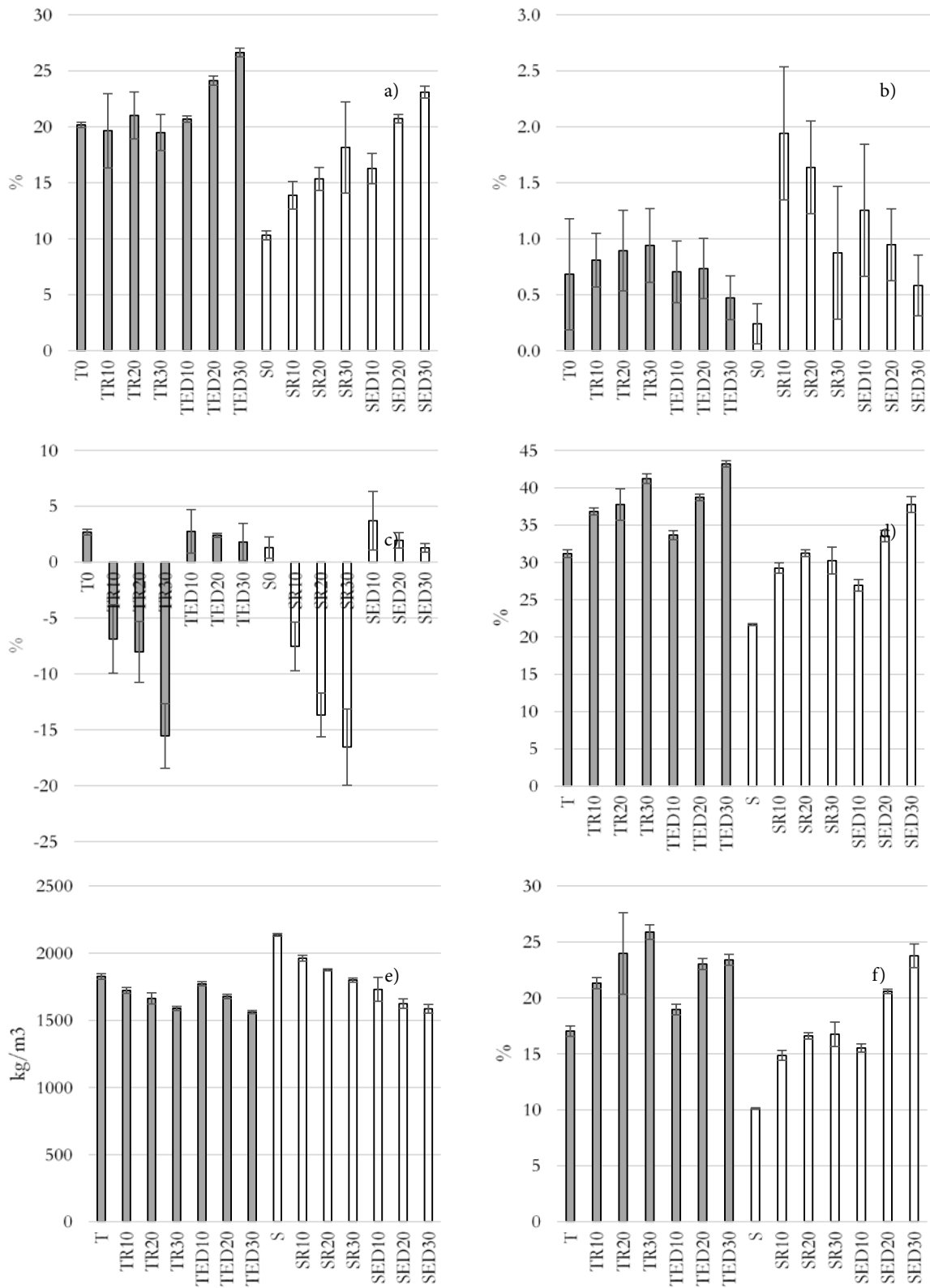
Figure 4: Physical properties of the clay discs: a) total mass loss, b) total linear shrinkage, c) total volume change, d) porosity, e) dry density, e) water absorption

The diffractograms of discs made of Teglværks (T) clay and treated fly ash (ED) in different proportions

is shown in Figure 5 and for discs made of Sisimiut clay in Figure 6.
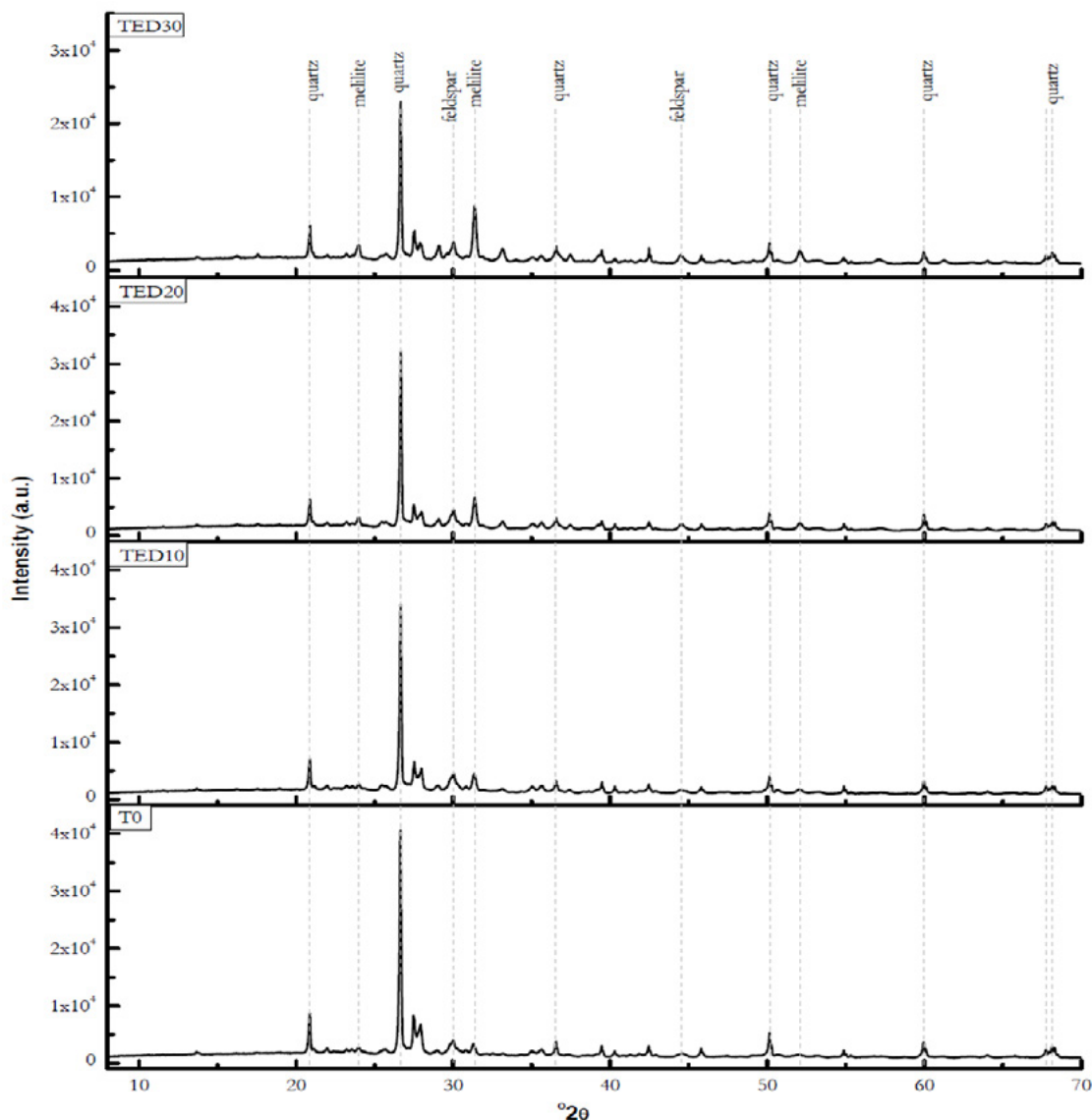
Figure 5: Diffractogram of Teglværks (T) clay discs with treated fly ash substitution of clay at 0%, 10%, 20% and 30%.

The reference discs with Teglværks clay, without the addition of fly ash, mainly contained quartz and feldspars (albite, microcline) as well as traces of melilite. As the amount of treated fly ash increases in the Teglværksler discs, the peak of quartz decreased significantly while that of melilite becomes more intense. In the discs with Sisimiut clay quartz was also the dominant mineral but feldspars (albite and microcline) were also abundant. Moreover, pyroxene was found in the control sample and increased by the addition of fly ash.

On the other hand, hematite that appeared in the control sample showed decreased peaks as the amount of fly ash increased. The occurrence of hematite in the Sisimiut discs, especially the control sample, justifies the red colour of the Sisimiut clay discs, unlike the yellowish colour of the Teglværks clay discs where there was no presence of an iron-based mineral.
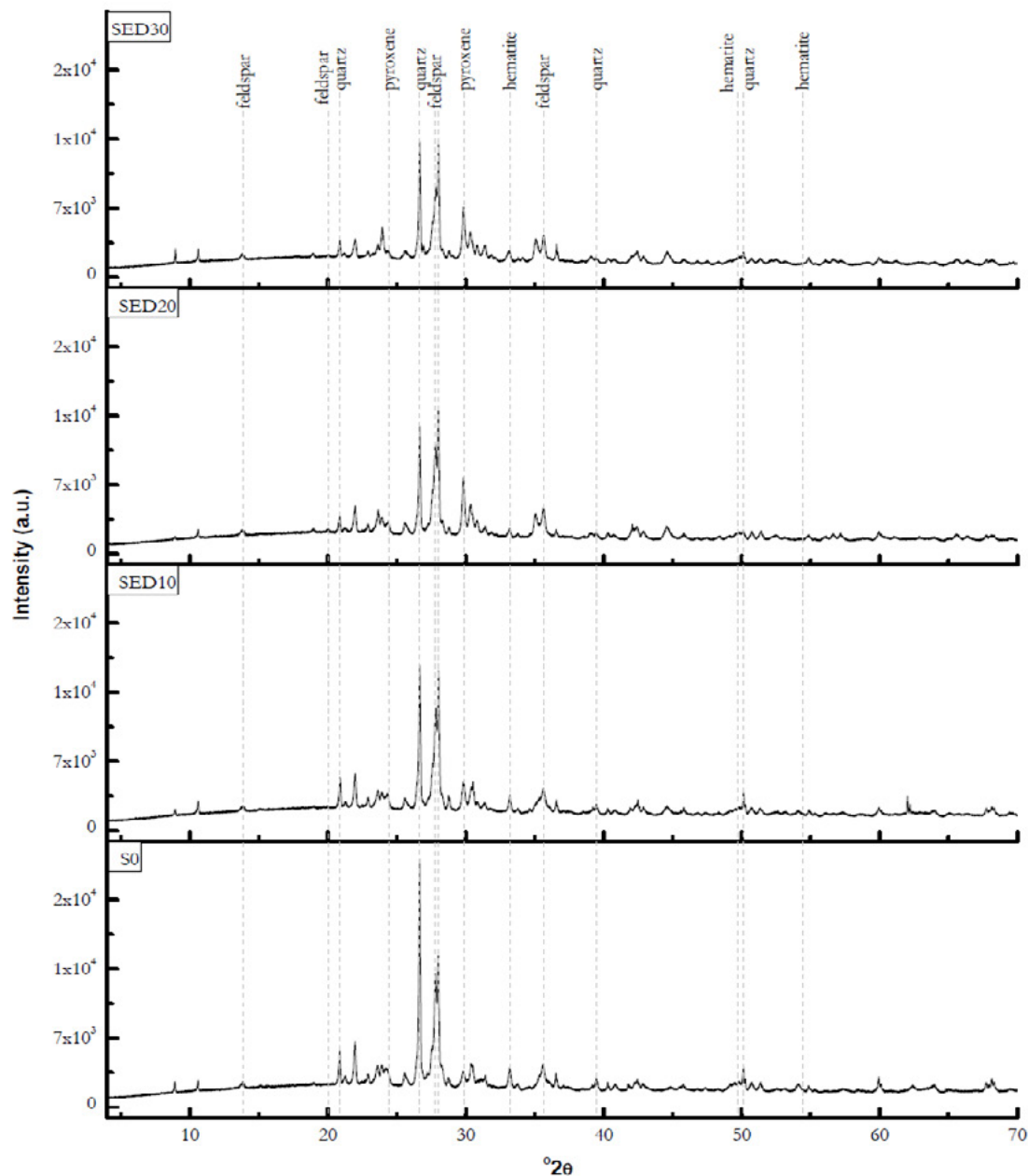
Figure 6: Diffractogram of Sisimiut (S) clay discs with treated fly ash substitution of clay at 0%, 10%, 20% and 30%.

Table 5 shows the leaching properties of the brick discs. There is no clear pattern in increased metal leaching with increasing addition of fly ash. However, these leaching results are from only one replicate, and there could be large uncertainties in the leaching values because of this. As leaching from most of the clay discs and Cr leaching from the TED10 sample was above the Category 3 guideline. The mobility of the metals was calculated, showing the extent of the immobilization of the metals when added in the bricks in comparison with the metals' leaching from the fly ashes. Belmonte et al. [3] observed increased mobility of As and Cr in clay discs containing 20 % and 40 % pre-treated MSWI fly ash by washing and electrodialytic treatment. The contrary was observed in this study, were all samples showed immobilization in the clay matrix, except for the sample TED10, where Cr leaching increased compared to the initial leaching of the ED fly ash. Wan et al. [10] studied the incorporation of MSWI fly ash in 5×5×5 cm^3 bricks and found that leaching of heavy metals both in batch leaching (determined by DS/EN 12457-1) and total leachability (determined by the Dutch leaching test at pH 4) was below the regulatory standards for these tests. This

could indicate that producing such a small number of the specimen as in this study should be used with care for conclusive studies of leaching properties and also that the leaching properties should be investigated further.

Table 5: Leaching of Teglværks and Sisimiut clay discs

Sample	pH	As (µg/l)	Cd (µg/l)	Cr (µg/l)	Cu (µg/l)	Ni (µg/l)	Pb (µg/l)	Zn (µg/l)
T0		115	<20	354	51	<20	<20	53
TR10	10.1	<20	<20	53	<20	<20	<20	<20
TR20	9.9	<20	<20	46	<20	<20	<20	<20
TR30	9.8	47	<20	74	<20	<20	<20	<20
TED10	11.2	50	<20	3240	33	<20	<20	31
TED20	10.7	75	<20	102	23	<20	<20	40
TED30	9.9	80	<20	<20	<20	<20	<20	80
S0		64	<20	<20	<20	<20	<20	39
SR10	10.1	<20	<20	<20	<20	<20	<20	<20
SR20	9.7	279	<20	<20	<20	<20	<20	<20
SR30	9.4	52	<20	<20	<20	<20	<20	<20
SED10	9.9	100	<20	<20	<20	<20	<20	33
SED20	9.7	64	<20	<20	<20	<20	<20	36
SED30	9.6	94	<20	<20	<20	<20	<20	38

4.   Conclusions

The commercial clay consisted mainly of the minerals quartz, calcite, feldspars and mica, whereas the Sisimiut clay consisted of quartz, feldspars, amphibole and mica. The MSWI fly ashes consisted mainly of calcite and anhydrite and the raw fly ash also of halite and sylvite. The clay discs with Sisimiut clay presented a reddish colour compared to commercial clay, which gave white/greyish colour. Hematite was detected in the clay discs with Sisimiut clay, although increasing the fly ash proportion resulted in lighter colours. Leaching of Cr of untreated and treated fly ash exceeded the limits of Danish regulation for wastes in construction but was lower than for disposal at non-hazardous waste disposal sites. Apart from this, treated fly ash presented much lower heavy metal concentration than the untreated fly ash. Most heavy metals were incorporated into the clay disc matrix, and the mobility of metals decreased after firing. Expansion of the discs occurred for the samples containing raw fly ash, caused by bloating due to gas formation from the decomposition of minerals during firing. The expansion increased with the increased amount of fly ash in the clay discs. The porosity and water absorption increased with the addition of more fly ash while dry density decreased. The clay discs with Sisimiut clay showed the lowest porosity and water absorption, which will be beneficial for use in the cold climates. As the electrodialytically treated MSWI fly ash showed better environmental performance than raw fly ash in the clay discs, there is a potential for using these Greenlandic raw materials in bricks, to support local production of construction materials.

5.   Acknowledgement

6.   References

[1]   Muñoz Velasco, P., Morales Ortíz, M.P., Mendívil Giró, M.A., and Muñoz Velasco, L. (2014). Fired clay bricks manufactured by adding wastes as sustainable construction material - A review. Construction and Building Materials *63*, 97-107.

[2]   Raut, S.P., Ralegaonkar, R.V., and Mandavgane, S.A. (2011). Development of sustainable construction material using industrial and agricultural solid waste: A review of waste-create bricks. Construction and Building Materials *25*, 4037-4042.

[3]   Belmonte, L.J., Ottosen, L.M., Kirkelund, G.M., Jensen, P.E., and Vestbø, A.P. (2018). Scree of heavy metal containing waste types for use as raw material in Arctic clay-based bricks. Environmental Science and Pollution Research *25*, 32831-32843.

[4]   Quina, M.J., Bordado, J.C., and Quinta-Ferreira, R.M. (2008). Treatment and use of air pollution control residues from MSW incineration: An overview. Waste Management *28*, 2097-2121.

[5]   Gunvor M. Kirkelund, C.M., Paula Guedes, Pernille E. Jensen, Alexandra B. Ribeiro, Lisbeth M. Ottosen (2015). Electrodialytic removal of heavy metals and chloride from municipal solid waste incineration suspension – test of a new two compartment experimental cell. In Electrochimica Acta, Volume 181. pp. 73–81.

[6]   Kirkelund, G.M., and Jensen, P.E. (2018). Electrodialytic treatment of Greenlandic municipal solid waste incineration fly ash. Waste Management *80*, 241-251.

[7]   Quina, M.J., Bontempi, E., Bogush, A., Schlumberger, S., Weibel, G., Braga, R., Funari, V., Hyks, J., Rasmussen, E., and Lederer, J. (2018). Technologies for the management of MSW incineration ashes from gas cleaning: New perspectives on recovery of secondary raw materials and circular economy. Science of the Total Environment *635*, 526-542.

[8]   Aubert, J.E., Husson, B., and Sarramone, N. (2006). Utilization of municipal solid waste incineration (MSWI) fly ash in blended cement Part 1: Processing and characterization of MSWI fly ash. J Hazard Mater *136*, 624-631.

[9]   Huang, T.Y., and Chuieh, P.T. (2015). Life Cycle Assessment of Reusing Fly Ash from Municipal Solid Waste Incineration. Procedia Engineering *118*, 984-991.

[10]   Chen, W., Klupsch, E., Kirkelund, G., Jensen, P., Ottosen, L., and Dias-Ferreira, C. (2017). Recycling of MSWI fly ash in clay bricks—effect of washing and electrodialytic treatment.

[11]   Kirkelund, G.M., Ottosen, L.M., Jensen, P.E., and Goltermann, P. (2016). Greenlandic waste incineration fly and bottom ash as secondary resource in mortar. International Journal of Sustainable Development and Planning *11*, 719-728.

[12]   Casagrande, A (1948). Classification and identification of soils, Transactions of the American Society of Civil Engineers, *113,* 103-112.

[13]   BEK nr 1672 15/12/2016. Bekendtgørelse om anvendelse af restprodukter, jord og sorteret bygge-og anlægsaffald. Ministry of Environment and Food in Denmark.

[14]   Dondi, M., Principi, P., Raimondo, M., Zanarini, G. (2000). The thermal conductivity of bricj produced with Italian clays. L'industria dei Laterizi, *65*, 309-320.

[15]   Dondi, M., Mazzanti, F., Principi, P., Raimondo, M., Zanarini, G. (2004). Thermal conductivity of clay bricks. Journal of Materials in Civil Engineering, *16*, 8-14.

[16]   Domone, P., Illlson, J. (2010). Construction materials: their nature and behaviour. London and New York, Spon Press.

Experimental Studies on Fly Ash Gypsum Slurry

V.Revathi[1], S.Jayanthi[2]

[1]K.S.R.College of Engineering, Tiruchengode, Tamilnadu

[2]Government College of Engineering, Bodinayakannur, Tamilnadu

E-mail: [1]revthiru2002@yahoo.com; hodcivil@ksrce.ac.in;   2gcebodi@gmail.com

Abstract

This study aimed to examine the performance of fly ash gypsum slurry in relation to the properties of its ingredients. Experiments were carried out to arrive at an optimum proportion of various ingredients for Fly ash-Gypsum slurry (F-G) mixtures having 150 mm, 300 mm, 375 mm, 425 mm and 500 mm flows. The designed mixtures were tested for flowability, density and compressive strength. The results show that even a small variation in water content drastically affected the flowablity of F-G slurry. While flowablity is mainly governed by water, observations indicated that flowablity depends on the composition of the mixture ingredients and its properties. It is understood that the minimum volume of water required for the slurry having higher flows of more than 300 mm flow is 50%. Also, it is found that almost all FG mixtures show considerable compressive strength suitable for backfilling and structural filling applications.

Key words: Fly ash, Gypsum, flowablity, Flowable Slurry, backfilling, structural filling

1.   Introduction

Generally, soil backfilling is adopted to strengthen and support the foundation of a structure. Proper compaction is required more to ensure uniform and rigid filling than original soil. However, in many cases, the material is dumped into the trench, leading to poor compaction. This made the researchers use a low strength flowable material which does not require compaction. Flowable slurry or Controlled Low Strength Material (CLSM), an alternative to compacted soil fill, has been used increasingly in the construction industry as it has numerous advantages such as easy to place, strong, durable, free from settlement, free from compaction, excavatability and allows fast return to traffic. Flowable slurry is a self compacting cementitious material and it has a compressive strength of 8.3 MPa or less at the age of 28 days. Flowable slurry is mainly used in the areas of backfilling, structural filling, mining and underground construction, erosion control and pavement base. The chief benefit is that it makes use of industrial by-products [1]. *The properties of flowable slurry lie between soil and concrete.* The materials used, production and placing is similar to concrete. In service properties exhibits the characteristics of soil. Both fresh and hardened properties need to be considered to use flowable slurry for various applications.

In 1964, the U.S. Bureau of Reclamation documented the first known use of controlled low-strength material. It is perhaps the most novel material which found one of its earliest applications in the year 1964 as the bedding material for the 515 km long pipe line in the Canadian River Aqueduct project by the US Bureau of Reclamation. The use of CLSM reduced the project cost by 40% compared to that of conventional soil fill (Brewer 1994).

Flowablity is the exclusive property of flowable slurry, which facilitates the materials to be self-leveling - to flow into and fill a void and be self-compacting without the need of compacting equipment. Flowablity can be varied from stiff to fluid, depending upon the requirements. The flowable slurry is quantitatively described by its spread of flow. Similar to concrete/mortar, flowable slurry is a composite material. But it flows like a liquid. Flowablity of flowable slurry mixtures is influenced by its ingredients, quantity, and the properties of the ingredients. When flowable slurry mixtures were developed with foundry sand and fly ash, proper amount of fly ash was required to obtain desired flowablity [2-3]. Gandham indicated that flowablity mainly depends on fly ash and water content in the mixture and phospho gypsum alone does not contribute to a satisfactory flowablity [4]. Another study carried out by Nataraja et al showed that the mixture containing fly ash achieved the desired flowablity with a lower w/c ratio, compared to mixture containing rice husk ash [5]. The mixture containing quarry dust achieved the desired flowablity with lower w/c ratio compared to the mix containing sand. Use of cement kiln dust increased the water demand of flowable slurry to achieve a specific flowablity [6-7].

Jason et al. carried out an experimental study using recycled crumb rubber and native silty sand to produce lightweight, soil-based, rubberized flowable slurry for a bridge approach repair. A Fluidizing agent was added to the mixtures to improve flowablity and control bleeding. For the backfilling of a small bridge abutment, 200 mm flow was recommended, as it does not require to flow a significant distance [8]. Pierce et al pointed out that mixtures that flowed for more than 600 mm are considered unacceptable for flowable fill because the crumb rubber was segregated during the test. Rubberized flowable slurry is not flowable without the addition of sand. Fully rubberized CLSM provided poor workability [9].

FHWA (Federal Highway Administration) specifies that the density of high fly ash is in the range of 1460 kg/m³ to 1945 kg/m³ [10]. Charles et al reported that density of less than 800 kg/m³ can be obtained with the use of a foaming agent for flowable fly ash slurry [11]. It has been observed that the compressive strength depends on the quantity of the cement and its water content. A cement content of about 90 kg/m³ was required to produce a compressive strength greater than 0.345 N/mm² at the age of 28 days. As the water content increased compressive strength probably got reduced [11-15]. It could be said that flowablity of flowable slurry, not only depends on the amount of water but also on the composition of ingredients.

Generally, 5% of OPC and 95% of fly ash is used as a binder in flowable slurry. Amitava Roy et al and Poon et al have mentioned that ordinary Portland cement can be completely replaced by alkalies and sulphates (industrial by-product/reagent grade) to obtain a binder with similar properties. The activated fly ash by industrial by-products as a binder in CLSM will boost the large-scale utilization of both fly ash and industrial wastes [16-17].

Phosphogypsum (PG) is a by-product obtained from the phosphoric acid process in fertilizer manufacturing. Only 15% of PG is being utilized by the cement and gypsum industries as a setting moderator for cement and for making gypsum plaster. The remaining 85% of PG creates an environmental problem. Around 6 million tons of phosphogypsum, available annually in India, can be used as a resource to activate fly ash so as to conserve natural resources, protect the environment and save energy([18-19].

In this context, the present work aims to develop flowable slurry using industrial waste by-products such as fly ash and gypsum. The study examined the performance of fly ash gypsum slurry in relation to the properties of ingredients which had not been addressed in the earlier work.

2. Methodology

2.1 Materials

2.1.1 Fly Ash

Fly ash obtained from Neyveli Lignite Corporation (NLC) was used in this study. The physical and chemical properties of the fly ash were carried out using the procedure prescribed by IS 1727-1967 (R2004) and the results are presented in Tables 1 and 2.

Table 1: Physical properties of fly ash

Sl. No.	Test Conducted	Observed Values	Required As Per IS 3812 - 2003
1	Specific Gravity	2.47	-
2	Initial Setting Time (min)	45	-
3	Final Setting Time (min)	280	-
4	Consistency (%)	35	-
5	Blain's Fineness (cm²/gm)	3550	3200 min
6	Lime Reactivity (MPa)	7.1	4.5 min

Table 2: Chemical properties of fly ash

Sl. No.	Test Conducted	Observed Values (%)	Required As Per IS 3812 - 2003
1	Loss on Ignition LOI	3.74	5 % max
2	Silica as SiO_2	35.87	25 % min
3	Iron as Fe_2O_3	4.00	--
4	Alumina as Al_2O_3 + SiO_2	34.14	50 min
5	Calcium as CaO	14.25	--
6	Magnesium as MgO	3.64	5 % max
7	Sulphate as SO_3	3.4	3 % max
8	Sodium as Na_2O	0.90	1.5 % max
9	Potassium as K_2O	0.06	--
10	Chloride	--	0.05 % max

2.1.2 Gypsum

The Phospho-gypsum used in this study was obtained from TANFAC (a fluoride industry), Cuddalore. Its specific gravity was found to be 2.70. The chemical properties of gypsum are shown in Table 3.

Table 3: Chemical properties of gypsum

Sl.No.	Chemical Composition	Observed Values (%)
1	Loss on Ignition	1.63
2	Insoluble Residue	0.5
3	Alumina as Al_2O_3	0.75
4	Iron as Fe_2O_3	0.82
5	Calcium as CaO	44.99
6	Magnesium as MgO	1.02
7	Sulphate as SO_3	48.84
8	Purity	99.4

2.2 Mixture Proportion for Flowable F-G Slurry

For the experimental investigation, five different flow series of flowable slurry mixtures were considered. The mixtures were proportioned for the flow of 150 ± 50 mm, 300 ± 50 mm, 375 ± 25 mm, 425 ± 25mm and 500 ± 25 mm. All the mixtures were proportioned to obtain flowable slurry as defined by ACI Committee 229R (2005). The gypsum content in the binder was 10% by mass of fly ash. The water content

was arrived at by trial and error method in order to obtain the desired flowablity. The details of mixtures are presented in Table 4. The F-G mixtures are designated as A, B, C, D and E.

Table 4: Mixture proportions of F-G slurry and fresh slurry properties

| Sl. No | Flow Range (mm) | Mixture Designation | Mixture Ingredients | | | | Flow/ Spread (mm) |
			Fly ash (kg/m³)	Gypsum (kg/m³)	Water (kg/m³)	W/ (FA+ G)	
1	500 ± 25 flow	A	898.1	89.8	642.0	0.65	481.0
2	425 ± 25 flow	B	941.3	94.2	621.2	0.60	420.0
3	375 ± 25 flow	C	1053.4	105.3	579.4	0.50	391.0
4	300 ± 50 flow	D	1188.2	118.8	522.8	0.40	274.0
5	150 ± 50 flow	E	1366.6	136.7	451.0	0.30	185.0

2.3 Preparation and Testing

The calculated quantity of fly ash and gypsum were mixed in dry condition for about five minutes. The required quantity of water was slowly added and mixing was continued for another five minutes. Flow test as per ASTM D 6103 was carried out and fresh slurry density determined. The freshly prepared F-G slurry was tested for wet density. Cube specimen of 50 mm was used for determining the density of hardened F-G slurry. Cubes were de-moulded after 24 hours and humidity cured, until testing. Twelve specimens were prepared, cured and tested for each mixture. The test was carried out using 2000 kN compression testing machine. The load was applied on each specimen till its failure. The Ultimate load applied over a specimen that caused failure was noticed and recorded. The compressive strength was estimated using the equation

$$\text{Compressive strength} = P/A \qquad (1)$$

where, P = Ultimate load in kN;

A = Cross sectional area of cube in mm^2

3. Results and discussion

Fly ash gypsum slurry is characterized by its properties like flow, density and compressive strength. This part presents the results of the laboratory investigations and the observations made thereof.

3.1 Flow Test of F-G Slurry Mixtures

Flow of fly ash gypsum (F-G) slurry is an important property. Therefore, it is essential to understand the influence of F-G slurry ingredients on flow behaviour. Water is the predominant ingredient which influences the spread of the slurry. The quantity of water required to obtain a desired flow depends primarily on the quantity of fly ash, and gypsum in the mixture. The attempt made to understand the relationship between volume of solids and flowablity is presented below.

F-G slurry consists of fly ash, gypsum and water. It is considered as a system consisting of only two prominent phases, namely, solids and liquid. Totally, five mixtures were made with flowability values of 150 mm, 300 mm, 375 mm, 425 mm and 500 mm. Experiments were carried out to arrive at the optimum proportions of ingredients for each mixture. The quantity of water required, relative ratios (RR) as well as successive relative ratio (SRR) of each flow are presented in Table 5. It is evident from the Table that the RR value of flow varies in the range of 1 to 1.42. However, the RR value of water varies from 1 to 1.42. It is evident that the RR value of F-G slurry with 500 mm flow increased three fold while the relative ratios

(RR) of water increased only 42%. This indicates that the flow of slurry is highly sensitive even to the little variations in water content. Also, it has been substantiated with computed successive relative ratios of flow and water. The SRR of flow varies in the range of 1.13 to 2.0, while corresponding values for water requirement varies in the range of 1.03 to 1.16. It is also observed that mixtures with higher flow are more sensitive to even marginal variation in water content than mixtures with low flow.

Also, for better understanding rheology of slurry, quantities of ingredients such as fly ash, gypsum and water are converted from mass to volume and presented in Table 6. It is inferred that the minimum volume of water required for the slurry having higher flows (more than 300 mm flow) is 50%. It is obvious that the water requirement increases with increase in flowability and thereby the content of solids gets reduced in the mixture.

Table 5: Water requirement of F-G slurry mixtures

| Sl. No | Mixture Designation | Flow Range (mm) (x_1) | Flow Variation | | Water Requirements | | |
			Relative Ratio ($x_1/150$)	Successive Relative Ratio	lit / m³ (y_1)	Relative Ratio (RR)*	Successive Relative Ratio**
1	A	500	3.33		642	1.42	
2	B	425	2.83	1.17	621	1.37	1.03
3	C	375	2.5	1.13	579	1.28	1.07
4	D	300	2	1.25	523	1.16	1.1
5	E	150	1	2	451	1	1.16

* RR = y1 / water requirements of corresponding filler having 150 mm flow

**SRR- 1.42/1.37=1.03 and so on..

Table 6: Phase system in F-G slurry mixtures

Sl.No	Mixture Designation	Flow Range (mm)	Volume of Fly Ash (%)	Volume of Gypsum (%)	Volume of Total Solids (%)	Volume of Water (%)
1	A	500	35	3.2	38.2	61.8
2	B	425	36.8	3.3	40.1	59.9
3	C	375	40.8	3.6	44.4	55.6
4	D	300	45.9	4.1	50	50
5	E	150	52.4	4.7	57.1	42.9

3.2 Density of F-G Slurry

The density of slurry depends on the type of ingredients present and their proportions. Generally, it will have a bearing on the yield, strength, durability and also shrinkage. Density of fresh slurry (wet density) and hardened slurry of all mixtures were determined and presented in Table 7. The wet density of F-G slurry is varying from 1620 kg/m³ to 1920 kg/m³., whereas, the dry density is in the range of 1600 kg/m³ to 1900 kg/m³. It is obvious that density increases both in fresh as well as hardened slurry with the increase in the volume of solids. A marginal reduction in density of wet slurry is noticed, on hardening. It is due to the evaporation of water from slurry during the hardening process. However, the loss of water has resulted in only a marginal reduction in yield of slurry. The yield of slurry is the hardened unit mass of the flowable slurry that could be obtained after the slurry settles and hardens at the ambient temperature. The results are in conformity with the reported density of slurry [10-14]. The reported density is in the range of 1460 kg/m³ to 1945 kg/m³.

Table 7: Density of fresh and hardened F-G slurry mixtures

Sl. No	Mixture Designation	Flow Range (mm)	Volume of Total Solids (%)	Wet Slurry Density (kg/m³) (x)	Hardened Slurry Density (kg/m³) (y)	Yield of the Slurry, (y/x) * 100
1	A	500	38.2	1620	1600	98.8
2	B	425	40.1	1730	1700	98.3
3	C	375	44.4	1850	1800	97.3
4	D	300	50	1900	1890	99.5
5	E	150	57.1	1920	1900	99

x - Wet Slurry Density (kg/m³); y - Hardened Slurry Density (kg/m³)

Also, an attempt has been made to compare the observed and the computed density of FG. The Density of the slurry in the hardened state is essential to compute the quantity of the materials required for a particular application. In order to compute optimum quantity of water required for the slurry for a specific application, an attempt has been made to arrive at an expression. Generally, dry density is computed using the following expression (1).

$$Dry\ Density\ (\gamma_d) = \frac{\gamma}{1+w} \tag{2}$$

where γ_d – dry density in kg/m³

γ – wet density in kg/m³

w–water content (ratio of the weight of water to the weight of solids)

The above expression has been modified based on several laboratory trials to obtain **the** computed hardened density. The modified expression is presented below (2):

$$Computer\ Hardened\ Density\ (\gamma_{cd}) = \frac{\gamma}{1+w/100} \tag{3}$$

where γ_{cd} – dry density in kg/m³

γ – wet density in kg/m³

w–water binder ratio (ratio of **the** weight of water to the weight of binder)

The computed and observed densities are presented in Table 8. It is observed that the computed density of hardened slurry is in agreement with the measured densities. The maximum deviation of computed density from measured density is only 2%. The above expression can be used effectively to arrive at the optimum quantities of materials to obtain the required hardened density.

Table 8: Comparison between the observed and the computed hardened density of F-G slurry mixtures

Sl. No	Mixture Designation	Flow Range (mm)	Wet Slurry Density (kg/m³)	Observed Hardened Slurry Density (kg/m³) (x)	Water/ Binder Ratio W/(FA+ G)	Computed Hardened Density (y)	Computed / Observed Hardened Density (y/x)
1	A	500	1620	1600	0.65	1609.5	1.01
2	B	425	1730	1700	0.6	1719.7	1.01
3	C	375	1850	1800	0.5	1840.8	1.02
4	D	300	1900	1890	0.4	1892.4	1.00
5	E	150	1920	1900	0.3	1914.3	1.01

x - Wet Slurry Density (kg/m³); y - Hardened Slurry Density (kg/m³)

3.3   Compressive Strength of F-G Slurry

The cured specimens of various F-G slurry mixtures were tested for compressive strength at the age of

3, 7, 28 and 56 days. The test results are furnished in Table 9. The compressive strength mainly depends on the type of binder and the mixture proportion of ingredients used in slurry. ACI 229 R 2005 specified a compressive strength of maximum 8.3 MPa or less at the age of 28 days for controlled low strength material (CLSM). However, it has been reported in the literature that fly ash gypsum flowable slurry was made even with 10 MPa compressive strength (Gandham et al 1996). At the same time, fly ash slurry was also made with a compressive strength as low as 0.34 MPa (Naik et al 1990). The minimum compressive strength of 0.34 MPa can be used when later age excavatabilty of the flowable slurry is predicted. It shows that fly ash slurry can be produced with a wide range of strengths depending on requirements.

The compressive strength of F-G slurry is varying from 1.7 MPa to 5.61 MPa at the age of 28 days. Hence, the F-G slurry produced in the present study can be considered as controlled low strength material. It is noticed that the compressive strength at all ages improved with an increase in the volume of solids. It is obvious that the increased volume of solids reduced the volume of water in slurry. This in turn improved the compressive strength of hardened slurry. The compressive strength gradually decreased with increase in the flow of slurry from 150 mm to 500 mm. Similar observations were made on flowable slurry by FHWA (1998), Krell.(1989), and Naik et al (1990, 2003). However, significant reduction in strength is noticed in the slurry having flowability greater than 375 mm. It must be due to the addition of much more water than the optimum quantity of water required for the hydration of the binder.

Table 9: Compressive strength of F-G slurry mixtures

Sl. No	Mixture Designation	Flow Range (mm)	Volume of Solids (%)	Compressive Strength at Various Ages (MPa)			
				3 days	7 days	28 days	56 days
1	A	500	38.2	1.43	2.01	2.36	2.72
2	B	425	40.1	0.36	1.41	1.70	3.10
3	C	375	44.4	2.62	3.72	5.00	5.70
4	D	300	50	2.96	4.19	5.41	5.90
5	E	150	57.1	3.20	5.60	5.61	6.50

4.   Conclusions

This article presents a study carried out to evaluate the behaviour of F-G slurry. From the results and discussion the following conclusions are drawn:

The relative ratios and successive relative ratios of flow are significantly higher than the water requirement for F-G slurry. It shows that even a small variation in the water content drastically affects the flowability of slurry. Also, the mixtures with higher flow are much more sensitive to even marginal variation in the water content than the mixtures with low flowability. Further, it is noticed that a minimum of 50% volume of water is required for F-G slurry having flowability higher than 300 mm.

The wet and hardened density of FG slurry is in the range of 1620 to 1920 kg/m³ and 1600 to 1900 kg/m³, depending on the respective quantity of solids. The marginal reduction in the density of wet slurry is noticed, on hardening, in F-G slurry. It is due to the evaporation of water from slurry during hardening process. FG slurry mixes considered in the present study can be classified as regular flowable slurry, based on their density, as the density of all of the mixtures is more than 800 kg/m³.

The compressive strength at all ages improved with the increase in the volume of solids and reduction in flowability. Also, it is found that almost all FG slurry mixtures have shown compressive strength ~~varies~~ varying from 1.7 MPa to 5.61 MPa, at the age of 28 days, depending on the flow of mixtures. However, ~~the~~ considerable reduction in strength is noticed in the slurry having flowability greater than 375 mm. It must be due to the addition of much more water than the optimum quantity of water required for the hydration

of the binder.

The strength obtained for all the mixes are below 8.3 MPa, as specified by ACI 229 R. Therefore, it satisfies the strength requirement of flowable slurry. Also, all the mixes can be used as structural fills as the strengths of the mixes are between 0.69 to 8.3 MPa.

5. References

1. ACI Committee 229 R. (2005) 'Controlled Low Strength Materials (CLSM)'– ACI Concrete International Vol. 16, No.7, pp.55-64.

2. Bhat S.T. and. Lovell C.W. (1996) 'Design of Flowable Fill: Waste Foundry Sand as a Fine Aggregate' – Transportation Research Record No. 1546, pp 70-87.

3. Bhat S.T. and. Lovell C.W. (1997) 'Mix Design for Flowable Fill', Transportation Research Record, No. 1589, pp. 26-35.

4. Charles K.N., Frances McNeal and Dean Martin (1997) 'New Foaming Agent for CLSM Applications', Concrete International, Vol. 19, No. 4, pp. 44-47.

5. FHWA-RD-97-148 (1998) 'User Guidelines for Waste and By-Product Materials in Pavement Construction', U.S. Department of Transportation, Federal Highway Administration, Turner-Fairbank Highway Research Centre.

6. Gandham S. Seals R.K. and Foxworthy Paul.T. (1996) 'Phosphogypsum as a Component of Flowable Fill' – Transportation Research Record No.1546, pp.79-87.

7. Jason Y. Wu. and Mufan. Tsai. (2009) 'Feasibility Study of a Soil-Based Rubberized CLSM' –Waste Management Vol 29, No.2 pp. 636-642.

8. Krell William C. (1989a) 'Flowable Fly ash', Transportation Research Record No. 1234, pp. 8-12.

9. Lachemi M. Hossain K.M.A. Shehata M. and Thaha W. (2007) 'Characteristics of Controlled Low-Strength Materials Incorporating Cement Kiln Dust' – Canadian Journal of Civil Engineering, Vol. 34, No 4, pp.485-495.

10. Lachemi M. Hossain K.M.A. Shehata. M. and Thaha.W. (2008) 'Controlled Low Strength Materials Incorporating Cement Kiln Dust from Various Sources' – Cement and Concrete Composites, Vol. 30, No.5, pp.381-392.

11. Naik T.R., Ramme B.W. and Kolbeck H.J. (1990) 'Filling Abandoned Underground Facilities with CLSM Fly ash Slurry', Concrete International, Vol. 12, No. 7, pp. 19-25.

12. Naik T.R., Kraus R.N., Ramme B.W., Yoon-Moon Chun and Rakesh Kumar (2006) 'High-Carbon Fly Ash in Manufacturing Conductive CLSM and Concrete', Journal of Materials in Civil Engineering, Vol. 18, No. 6, pp.743-746.

13. Nataraja M.C. and Nalanda Y. (2008) 'Performance of Industrial By-Products in Controlled Low-Strength Materials (CLSM)', Waste Management, Vol. 28, No. 7, pp. 1168-1181.

14. Pierce C.E. and Blackwell M.C (2003) 'Potential of Scrap Tire Rubber as Lightweight Aggregate in Flowable Fill' – Waste Management Vol. 23 No.3, pp.197-208.

15. Ramme B.W., Naik T.R. and Kolbeck H.J. (1994) 'Use of Fly Ash Slurry for Underground Facility

Construction', Construction and Building Materials, Vol. 8, No. 1, pp. 63-67.

16. Amitava Roy, Paul Schilling, Eaton Harvill C. and Seals Roger K. (1992) 'Alkali Activation of Class C Fly Ash', Proceedings of Utilization of Waste Materials in Civil Engineering Constructions, ASCE National Convention, New York, Sept. 13-17, pp. 104-115.

17. Poon C.S., Kou S.C. Lam L. and Lin Z.S. (2001) 'Activation of Fly Ash/Cement Systems using Calcium Sulfate Anhydrite $CaSO_4$)' – Cement and Concrete Research, Vol. 31, No. 6, pp. 873-881.

18. Mridul Garg Manjit Singh and Rakesh Kumar (1996) 'Some Aspects of the Durability of a Phosphogypsum-Lime-Fly Ash Binder' – Construction and Building Materials, Vol. 10, No. 4, pp. 273-279.

19. Manjit Singh (2007) 'Utilization of Waste Gypsum; An Indian Scenario' – Global Gypsum Magazine, pp. 22-28.

20. IS: 1727 – 1967 (R2004) Indian Standard Methods of Test for Pozzolanic Materials, The Bureau of Indian Standards, New Delhi.

21. IS 3812: Part 1: 2003 – Pulverized Fuel Ash - Specification - Part 1: For Use as Pozzolana in Cement, Cement Mortar and Concrete, The Bureau of Indian Standards, New Delhi.

Production of bioplastic from CO_2 with light energy by coupling Cupriavidus necator with inorganic photocatalysts

T. Zhang, P. Tremblay

State Key Laboratory of Silicate Materials for Architectures, Wuhan University of Technology, Wuhan 430070, PR China

School of Chemistry, Chemical Engineering and Life Science, Wuhan University of Technology, Wuhan 430070, PR China

International School of Materials Science and Engineering, Wuhan University of Technology, Wuhan 430070, P. R. China

Email of the corresponding author: tzhang@whut.edu.cn

Abstract

The cement industry is responsible for the release of 5% of worldwide anthropogenic emissions of the greenhouse gas carbon dioxide. One approach to reduce CO2 emissions by cement plants is to feed CO_2 to biocatalysts for the production of valuable chemical products such as biofuels. Ideally, CO_2-based bioproduction should be powered by a ubiquitous energy source that is easy to access, free and renewable such as solar energy.

Massive research efforts have been deployed to develop productive and energy-efficient CO_2 bioprocesses relying on natural photosynthesis such as ethanol production by sugarcane or oil production by algae or cyanobacteria. Until now, one major hurdle with these processes is that natural photosynthesis has a low solar energy-to-specific product conversion efficiency, which limits productivity and increases space required for implementation. A possible response to this challenge is the development of hybrid photosynthesis systems where sunlight is harvested by more efficient inorganic devices, which then generate energy that can be used by microbial catalysts for the production of useful chemicals.

In this project, inorganic photocatalysts were used to drive the production of polyhydroxybyturate (PHB) from CO_2 or organic carbon molecules by Cupriavidus necator. PHB is an industrially-relevant and biodegradable bioplastic generated by C. necator for energy and carbon storage purposes. Its synthesis required reducing power under the form of NADPH.

In our system, photocatalysts such as graphitic C3N4 and CdS harvest light energy to generate reducing equivalents that are used by C. necator for CO2 reduction via the Calvin-Benson-Bassham pathway as well as in the conversion of the central metabolite acetyl-CoA into PHB. Our results indicate that solar energy-to-specific product conversion efficiencies obtained by coupling inorganic photocatalysts with C. necator could easily surpass the efficiency of natural photosynthesis-based bioproduction processes.

Study on the preparation of high quality autoclaved aerated concrete made from stone-sawing mud

H. Wan[1], Y. Hu[2], G. Liu[1]*, J. Liu[2], Y. Qu[2]

[1] State Key Laboratory of Silicate Materials for Architectures, Wuhan University of Technology, Wuhan, China;

[2] School of materials science and engineering, Wuhan University of Technology, Wuhan, China.

Abstract

Stone-sawing mud is a by-product of the stone processing industry, which is difficult to be used. Testing results show that: in the stone-sawing mud, the SiO_2 content is more than 70%, particles sizes are small, specific surface area is about 375 m^2/ kg and the moisture content is about 22%. It implies that the stone-sawing mud could be directly used as siliceous raw material for preparation of the autoclaved aerated concrete (AAC) without drying-grinding, meanwhile alleviating the surrounding environmental pollution. This study mainly discusses the effect of the water materials ratio, mixing water temperature, aluminium powder content, cement content, stone-sawing mud and lime + gypsum content on the AAC properties. Experimental results show that with an increase of stone-sawing mud content and a decrease of lime content, the bulk density of AAC increases gradually, while its compressive strength firstly increases and then decreases. The maximum compressive strength of 3.60MPa and the bulk density of 606 kg/m^3 can be obtained when the water-binder ratio is 0.60, the mixing water temperature is 45°C, the aluminium powder content is 0.12%□ the stone-sawing mud content is 71% and the lime + gypsum content is 21% as well the mass ratio of them is about 4:1. The XRD and SEM results show that the crystallization of tobermorite crystals in the AAC with the stone-sawing mud grows into a leaf shape, and interleaves with each other to form a dense structure net, which makes the AAC with improved mechanical properties.

Keywords: stone-sawing mud; autoclaved aerated concrete; bulk density; strength.

1.   Introduction

Stone-sawing mud is a by-product of the stone processing industry, which is difficult to be used. It can produce a lot of stone powder containing lots of water during the stone cutting processing. After precipitation, it forms the stone-sawing mud. It was reported that the processing of each ton of rock produced about 0.1m³ of sawing mud [1]. In order to protect the saw blade, a small amount of cutting fluid was usually added to the cooling water during the process of cutting stone, which caused the stone-sawing mud paste to be weak acid and contain a small amount of phosphate and organic material, this could pollute the environment. Therefore, how to effectively utilize stone-sawing mud is an issue that relates to the protection of environment and groundwater.

The autoclaved aerated concrete (AAC) is an effective and scientific way to use the solid waste [2]. It can not only greatly reduce the cost of manufacturing new wall materials, but also consume a lot of solid waste and has high utilization rate. AAC is a kind of lightweight, porous new building material with good performance

of light weight, good thermal insulation, machinability and non-combustion. It can be made into different specifications of the block, plate and insulation products widely used in industrial and enclosure filling structure of bearing or embosom filling structure, which makes it get much attention around the world and become the building materials vigorously promoted by many countries [3].

The AAC, whose main raw materials are the siliceous materials (river sand, fly ash and tailings containing silicon, etc.) and calcium materials (lime, cement), by adding gas agent [4] (aluminium powder) and adding water mixing, then a series of independent holes being formed by chemical reactions, is a porous silicate product prepared by the processes of pouring shape, cutting, autoclaved curing and so on [5]. Through many years of research, production and application, people have basically mastered the production process of using fly ash or river sand to prepare the AAC[6][7]. Matsushita F [8] studied the durability of AAC (degree of carbonation). Narayanan N [9], Alexanderson J [10] and others also thorough researched the structure and performance of AAC. Chen YL [11] used recycled desulfurization slag to produce AAC. Huang X [12] et al used low silicon copper tailings-cement clinker-wind-accretion sand-slag powder system to prepare no lime AAC. A large number of research results have accumulated rich experience in the scale production of AAC.

This research systematically studied the effects of preparation process parameters and material compositions on the performance of AAC based on raw materials of more than 70% of the stone-sawing mud and small amounts of lime and desulfurization gypsum and technology by adding stabilized foam agent to improve gas progress. The outcome of this study can be used to guide massively using the stone-sawing mud in the AAC production. It is meaningful to save the resources and protect the environment.

2.   Experiment

2.1   Materials

2.1.1 Stone-sawing mud

The stone-sawing mud used in this study was from the stone processing factory in Hubei mountain area. Due to the geological reasons, the type of stone was mainly granite in this area, and its stone resources were extremely rich. As a result, the stone processing factory in this area had generated at least 6 million stone-sawing mud every year, which caused serious damage to the surrounding environment. The test showed that the powder of processing granite stone with higher SiO_2 content and small particle size, high water content. When used for preparing the raw materials of AAC, it doesn't need drying and grinding. The pH value of stone-sawing mud was 6.5, which was weak acidic. The moisture content of stone-sawing mud was about 22%, and sieving residue alone 80 microns was less than 15%, with an apparent density of $2.72g/cm^3$ and a surface area of $375m^2/kg$. The chemical compositions of stone-sawing mud were shown in Table 1, and its XRD analysis was shown in Figure1.

Table 1 Chemical composition of raw materials

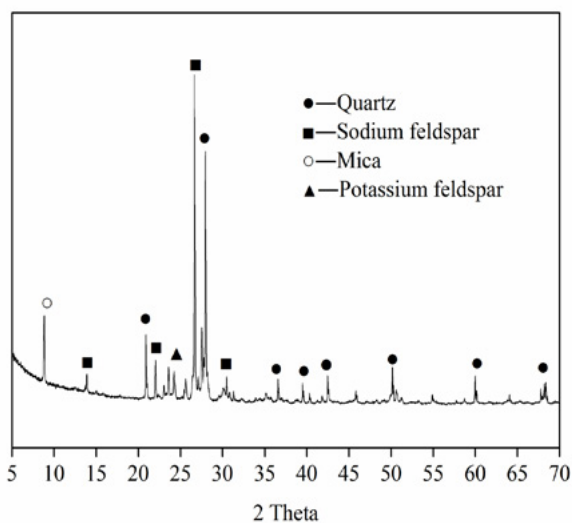| Chemical composition (%)	SiO_2	CaO	Al_2O_3	Fe_2O_3	MgO	SO_3	K_2O	Na_2O	LOI
Stone-sawing mud	72.66	1.56	15.09	1.15	0.38	-	3.58	4.54	0.42
P.O42.5 cement	20.49	61.02	5.01	3.50	2.23	2.58	0.64	0.15	3.07
Desulfurization gypsum	2.61	30.5	0.66	-	0.92	43.40	-	-	20.12

Figure 1. XRD analysis of stone-sawing mud.

2.1.2 Cement

The cement used in this study was P.O 42.5 ordinary Portland cement. Its physical properties and chemical compositions were shown in Table 1 and Table 2 respectively.

Table 2: Physical properties of Portland cement

Specific surface area (m²/kg)	Setting time (min)		Flexural strength (MPa)		Compressive strength (MPa)		Cement stability
	Initial setting time	Final setting time	3d	28d	3d	28d	
348	165	220	7.8	8.6	26.3	49.9	qualified

2.1.3 Lime

The active CaO content in the lime used in this study was more than 80%, while the content of MgO was less than 5%. The digestion time was 14 min, with the sieve residue alone 80 microns less than 10%.

2.1.4 Desulfurization gypsum

Desulphurization gypsum used in this study was discharged from coal-fired power plants. Its chemical compositions were shown in Table 1.

2.1.5 Aluminium powder and foam stabilizer

Aluminium powder used in this study was mainly used for air-making.

2.2   Sample preparation and testing

According to Yingliang Chen's study [13], the mass ratio of lime to gypsum was about 4:1, in which case it can ensure the coagulation time of the slurry and the lime digestion speed more appropriate. Then, this ratio was adopted in this study, the materials composition and proportion of the base AAC were presented

in Table 3.

Table 3. Materials composition and proportion of the base AAC (wt %).

Cement	Sawing mud	Lime + gypsum	Aluminum powder	Stable foam agent
8	70	22	0.12	0.01

The whole processes to make the AAC sample were shown as follows: firstly, mix the slurry with the temperature during 40~45 °C; next, control the block-static stop time during 2~2.5h and the temperature during 55~60 °C. Then, make it under the conditions of the vacuum for 0.5h and increase pressure of 1.3MPa for 1.5h, and keep the pressure at 1.3MPa for 8h; finally, release pressure and cooling for 2h.

According to GB/T11969-2008 *Test method for the performance of autoclaved aerated concrete*, the 100mm x 100mm x 100mm standard specimen was prepared and then put it into the autoclave. The DRM-□ concrete thermal conductivity detector (Xiangtan Xiang Yi Instrument Co., Ltd.) was used to test the coefficient of thermal conductivity of AAC. X-ray diffraction (D/MACX-RB Japan RIGAKU) and scanning electron microscope (JSM-5610LV Japanese electronics co, LTD.) were employed to analyse the composition and microstructure of the samples.

3. Results and discussion

3.1 Effect of water-binder ratio on the slurry performance

The water-binder ratio was an important technological parameter in the preparation and production of AAC. Water-binder ratio directly impacted the coordination of water slurry thickening velocity and gas velocity of co-ordination, suitable water-binder ratio would keep the volume of slurry stability in the process of casting and made gas fully generate in the process of gassing, slurry expansion properly, which could ensure uniform of pore structure inside the AAC.
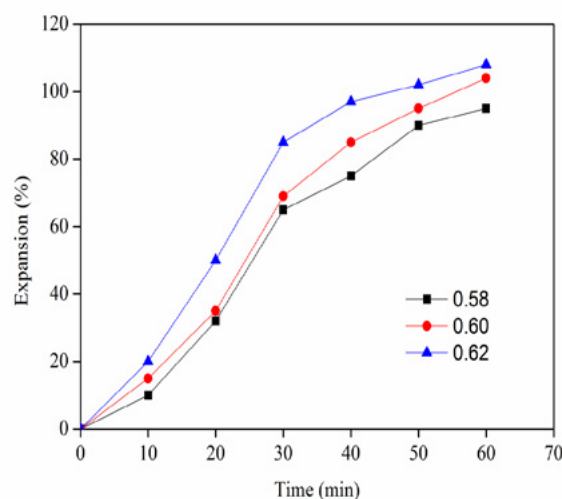

Figure 2. The relation curve of water-binder ratio with expansion height

Figure 2 was the result of the test of the water-binder ratio of 0.58, 0.60 and 0.62 respectively. The smaller the water materials ratio was, the greater the consistency of the slurry was, leading to the more difficulty

the gas phase became, and then, the smaller the swelling height was. When the water materials ratio was too large, the consistency of the slurry was low and the time of thickening would take longer. According to the Laplace equation:

$$p = p_0 + \frac{4\partial}{r}$$

(1)

Where: p—the pressure in the air bubble, Pa.

p_0—the atmospheric pressure, Pa.

∂—slurry consistency, Pa •cm.

r—bubble radius, cm.

It could be seen from the Equation (1) that the pressure of the stomata was related to the bubble radius and viscosity of the slurry. With water-binder ratio increasing, the viscosity of the slurry dropped, it was easy to cause the stomata to accumulate and produce the large stomata, and the gas reaction was intense. The excessive accumulation of large stomata and the unstable gas state could easily lead to the collapse mode. When the water-binder ratio was too low, increasing speed of slurry viscosity and the block hardening time was quick and short respectively. When the block was hardened and gas process was still going on, it could cause the block to crack. Both of these conditions would lead to the decrease of the strength of the block.

On the premise of ensuring the fluidity and thickening of the slurry and the consistency of the gas velocity, the improvement of the water content could significantly improve the airflow effect of the slurry. The water materials ratio would change the flow degree of the slurry, and the appropriate flow degree could ensure that the bubbles were uniform and avoided the deviation of bulk density in the slurry tank. The experimental results showed that when the water materials ratio was 0.60, the flow of the slurry was good, and the embryonic body was full of gas, the volume stability was fine, and there was no collapse mode phenomenon.

3.2   Influence of temperature on the properties of slurry

The progress of the aluminium powder gas was closely related to the temperature of the materials. The slurry was higher in temperature, the raw materials were more active, and the solubility in the solution was more, the reaction speed was faster and the reaction degree was higher. On the contrary, when the slurry temperature was low, reaction speed dropped, the whole process of aluminium gas was extended, and it was not only causing the AAC bulk density big, but also leading the phenomenon of "holding gas", which had a certain effect on the structure of pores.

But when the temperature of the slurry was too high, the early reaction speed would be too fast and the aluminium powder gas would violently react, which made it was easy to form irregular shape large pores and damaged to the porosity of pore wall around it, even produced crack when it was serious.

The temperature of different slurry had obvious influence on the process of slurry gas and thickening. The slurry temperature was affected by mixing water temperature and lime digestion temperature, while lime digestion temperature was restricted by raw materials, and it was usually controlled by changing the mixing water temperature to control the slurry temperature. As shown in Figure 3, when mixing water temperature was higher than 50°C, the amount of gas was large, but the slurry setting speed was quick and the fluidity loss was high, which had a certain influence on gas progress.

When the mixing water temperature was below 40°C, gas generation rate was slow and the inflation rate was low, which made its bulk density larger. Comprehensively considering the bulk density and compressive

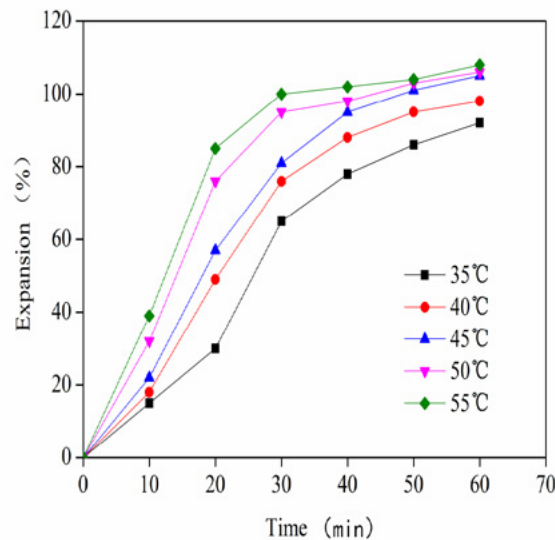strength, choosing the mixing water temperature of 45°C was more appropriate.

Figure 3. Mixing water temperatures and expansion height curve.

3.3 Influence of aluminium powder content on block performance

The aluminium powder was the gas agent which was most widely used. Its hair gas effect was good, and it was easy to control. The aluminium powder was made from the grinding particle produced by compressed air in a melting state. In order to prevent dust explosion and surface oxidation, the surface of aluminium powder usually had a layer of grease or a paste. Because of the slurry was highly alkaline, no degreasing was needed before using. But the aluminium powder particles were small and the surface was coated with grease, causing it was easy for particles reuniting.

So pre-distributed processing was required before using and then it could be mixed in the paste. In the slurry, the aluminium powder reacted with the $Ca(OH)_2$ formed by lime digestion or the cement hydration, produced the hydrogen and the reaction equation was:

$$Al + OH^- + H_2O \rightarrow AlO_2^- + \frac{3}{2}H_2 \uparrow \tag{2}$$

Figure 4 showed when the water materials ratio was 0.60, the curve of the aluminium powder content and the bulk density of the block. It could be seen from the Figure 4 that with the content of aluminium powder increasing, the bulk density of the block and the compressive strength of the block gradually reduced. Study [14] had shown that increasing the content of aluminium powder in a certain range had little influence on the pore diameter of AAC, but as the aluminium content continued to increase, a big pore percentage of AAC would increase correspondingly and the block compressive strength would decrease obviously.

Considering that this test was the preparation of the AAC at the B06 level, which was the product of the bulk density of $600 kg/m^3$, so it was more appropriate that the aluminium powder content was 0.12%.
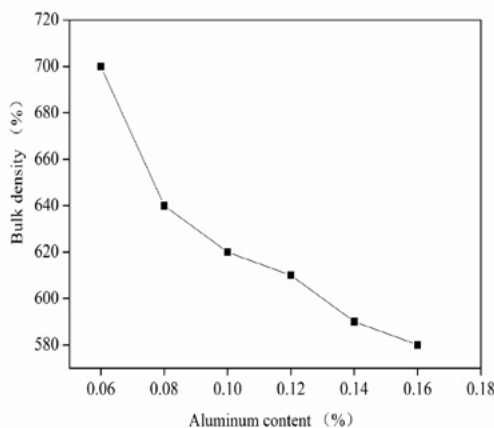
Figure 4. The relationship of aluminium powder content with masonry bulk density.

3.4   Effect of cement content on block performance

Cement in the AAC played a major role, which was to make the block had early compressive strength and easily to be cut. In the whole AAC reaction process, the cement only provided a small part of the calcium raw materials and made contribution to the strength due to the formation of hydrated calcium silicate gel. But in the AAC system, the main contribution of the strength was produced by the tobermorite crystals that were generated by the silica and calcium hydroxide in the autoclaved curing conditions. The later compressive strength of the block was not derived from the cement.

Table 4. Effect of cement content on AAC performance.

Number	Cement (wt%)	Sawing mud (wt%)	Lime + gypsum (wt%)	Aluminium powder (wt%)	Foam stabilizer (wt%)	Bulk density (kg/m³)	Compressive strength (MPa)
A1	6	70	24	0.12	0.01	598	3.31
A2	7	70	23	0.12	0.01	601	3.38
A3	8	70	22	0.12	0.01	604	3.44
A4	9	70	21	0.12	0.01	617	3.26
A5	10	70	20	0.12	0.01	615	3.35

*The mass ratio of lime to gypsum was 4: 1; and the water-binder ratio was 0.60.

   Table 4 was the impact of cement content on the bulk density and compressive strength of AAC. When the cement content increased, the compressive strength of AAC increased, when the cement content reached 8%, the strength reached the maximum. Then the compressive strength reduced with the increasing content of the cement. Besides making the body has early strength, cement mainly influenced on slurry thickening. The appropriate cement content could coordinate the slurry thickening speed and the gas making speed of aluminium powder to ensure a good stomatal structure, which was the key to improve the mechanical properties of products. In addition, the cement in the anti-carbonation and shrinkage performance were better than lime. However, the incorporation of excess cement would increase the cost of producing AAC, so the cement content of 8% was more appropriate.

3.5   Effect of siliceous and calcium raw materials contents on block performance

After determining appropriate water materials ratio, gas temperature, aluminium powder content and cement content, the test scheme of Table 5 was also designed in order to determine the best ratio of stone-

sawing mud, lime and gypsum, which made the performance of AAC better.

Stone-sawing mud and lime were the main siliceous materials and calcareous materials in AAC production process. The calcium hydroxide produced by lime and the SiO_2 in the stone-sawing mud were reacted under the conditions of autoclaved and generated the tobermorite and calcium silicate, which were the main source of the strength, while the gypsum was to inhibit the lime digestion and adjust the speed of the important role of slurry paste. The experimental results showed that when the mass ratio of lime to gypsum was about 4: 1, the mechanical properties of the block were better.

Table 5. Effect of stone-sawing mud, lime + gypsum on AAC performance.

Number	Cement (wt%)	Sawing mud (wt%)	Lime + gypsum (wt%)	Aluminium powder (wt%)	Foam stabilizer (wt%)	Bulk density (kg/m³)	Compressive strength (MPa)
B1	8	69	23	0.12	0.01	602	3.13
B2	8	70	22	0.12	0.01	604	3.44
B3	8	71	21	0.12	0.01	606	3.60
B4	8	72	20	0.12	0.01	612	3.51
B5	8	73	19	0.12	0.01	619	3.34

*The mass ratio of lime to gypsum was 4: 1; and the water-binder ratio was 0.60.

It could be seen from Table 7, with the stone-sawing mud content gradually increasing and lime + gypsum content correspondingly reducing, the prepared block bulk density and compressive strength gradually increased. When the content of sawing mud was 71%, the content of lime + gypsum was 21% and the mass ratio of lime to gypsum was about 4: 1 (sample B3) and the bulk density of block was 606 kg/m³, the compressive strength reached the maximum of 3.60MPa. When the content of sawing mud continued increasing and the lime + gypsum content decreased, although the bulk density increased, the compressive strength of the block showed a downward trend, which was indicated that the system of stone-sawing mud (siliceous material) was surplus, Lime gypsum (calcium material) content was insufficient and the number of hydrated products in the hydrothermal synthesis reaction was not as good as that of sample B3. On the other hand, the more or less content of lime + gypsum in system would affect the thickening rate of slurry and gas velocity, thus affecting the size and distribution of the pores in the block and ultimately the compressive strength of the block would be affected.

3.6 Hydration products and microscopic analysis

The XRD analysis (Figure 5) showed that the main product of AAC was the calcium silicate hydrate (C-S-H) which mainly consisted of tobermorite ($5CaO \cdot 6SiO_2 \cdot 5H_2O$)[15][16]. In addition, there was some quartz that partly participated in the reaction. The more the amount of tobermorite and C-S-H gel was produced, the higher the strength of AAC was. The quartz crystal in the sample was complete, had high crystallinity, played a skeleton role in the solid phase, and was also conducive to the strength of the structure.
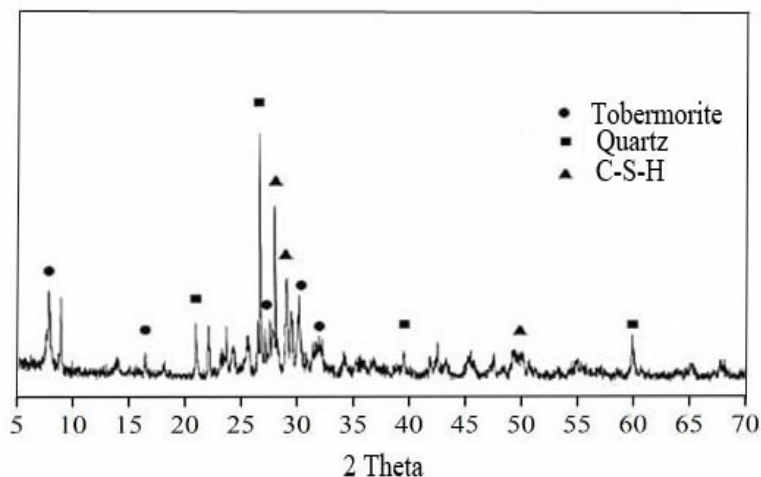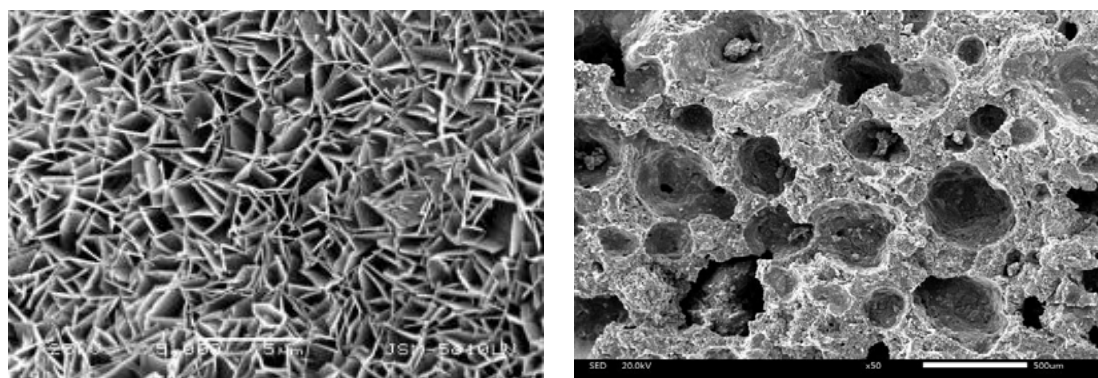
Figure 5. XRD analysis of AAC sample B3.

(a) X50   (b) X5000

Figure 6. SEM images of AAC sample B3.

The SEM images of the AAC sample B3 were shown in Figure 6. Besides to the macroscopic pores in the AAC, there were also many microspores at the pore wall (Figure 6a). The formation of pore had two main reasons: one was the water evaporation; the other was the chemical reaction. The macroscopic pores were uniformly distributed with a maximum size of around 10mm.In Figure 6 (b), there were also the tobermorite with a crystallized structure. The length of the blade was 2-3µm and the width around 1µm. The hydration products of the micro capillary in the AAC were the leaf shape tobermorite crystals with the double chain silicate structure and the tobermorite had good stability because they constituted net structure, which made AAC have good compressive strength.

3.7   The hydration reaction mechanism of AAC

At the initial reaction stage of AAC system, lime reacted with water in the slurry by digesting and forming calcium hydroxide to dissolve. The OH^- in calcium hydroxide provided enough alkalinity for the slurry, and the heat released from lime digestion improved the reaction speed. At the same time, the C_3S, C_3A and other minerals in the cement began to hydrate and formed hydrated calcium silicate, calcium hydroxide and calcium aluminate hydrate. Then, the system of liquid phase had certain alkalinity and SiO_2 began to dissolve in the liquid phase. The initial strength of the block was derived from the hydration products of C_3S, C_3A and other minerals in the cement[17] .

Under the conditions of alkali, environment, high temperature and high pressure for autoclaved curing, the system first produced a complete crystal of hydrogarnet ($C_3AS_nH_{6-2n}$) [18][19]. With the increase of the autoclave time, the solubility of Si^{4+} and Al^{3+} in the liquid phase got improved, which changed the alkaline environment of hydrogarnet and can make it broken down. Then, hydrated calcium silicate was generated [20][21][22]. Because the solubility of hydrated calcium silicate in the liquid phase is very low, when it reaches saturation will precipitate grain, the newly formed grain specific surface area is large, through the adsorption and water molecules connected to form a condensed state. During this period, more calcium-rich hydrated calcium silicate, such as C_2SH (A) and C_2SH_2, was produced in the system. With the increase of the concentration of SiO_2 in the liquid phase, the calcium-rich C_2SH (A), C_2SH_2 cannot be stable, and gradually converted to CSH (B) type hydrated calcium silicate and tobermorite [23] Tobermorite crystals grow into leaves and flake, and interlace each other, forming the network skeleton structure of AAC gradually, which is beneficial to improve its mechanical properties. The stone-sawing mud contained not only quartz but also a small amount of soda feldspar ($Na_2O•Al_2O_3•6SiO_2$) and potassium feldspar ($K_2O•Al_2O_3•6SiO_2$), which may provide active Al_2O_3 and SiO_2 for the reaction. Further studies are needed on how the soda feldspar and potassium feldspar are involved in the hydration reaction of the AAC.

4.   Conclusions

1.   1. Stone-sawing mud has high SiO_2 content, small size and high water content. When used for preparing AAC, it doesn't need to be dried or ground, which are the good disposal pathways.

2.   2. With an increase of the stone-sawing mud content and a decrease of the lime content, the bulk density of AAC increases gradually. The compressive strength of AAC firstly increases and then decreases and the maximum value 3.60 MPa can be obtained when the stone-sawing mud content is 71% and the lime content is 21%.

3.   3. The hydration products of the micro capillary in the AAC based on stone-sawing mud are the leaf shape tobermorite crystals with the double chain silicate structure and the tobermorite have good stability because they constitute net structure, which makes the AAC with improved mechanical properties.

5.   Reference

1.   Torres R, Fernandes HR, Olhero S, et al. Incorporation of wastes from granite rock cutting and polishing industries to produce roof tiles. J Eur Ceram Soc. 2009;29(1):23-30.

2.   Li XG, Liu ZL, Lv Y, et al. Utilization of municipal solid waste incineration bottom ash in autoclaved aerated concrete. Constr Build Mater. 2018;178:175-182.

3.   Wakili KG, Hugi E, Karvonen L, et al. Thermal behaviour of autoclaved aerated concrete exposed to fire. Cement Concrete Comp. 2015;62:52-58.

4.   Liu YQ, Leong BS, Hu ZT, et al. Autoclaved aerated concrete incorporating waste aluminum dust as foaming agent. Constr Build Mater. 2017;148:140-147.

5.   Verian KP, Ashraf W, Cao Y. Properties of recycled concrete aggregate and their influence in new concrete production. Resources Conservation Recycling. 2018;133:30-49.

6.   Uthaman S, Vishwakarma V, George RP, et al. Enhancement of strength and durability of fly ash concrete in seawater environments: Synergistic effect of nanoparticles. Constr Build Mater. 2018;187:448-459.

7.   Shen WG, Liu Y, Wang ZW, et al. Influence of manufactured sand's characteristics on its concrete

performance. Constr Build Mater. 2018;172:574-583.

8. Matsushita F, Aono Y, Shibata S. Carbonation degree of autoclaved aerated concrete. Cement Concrete Res. 2000;30(11):1741-1745.

9. Narayanan N, Ramamurthy K. Structure and properties of aerated concrete: a review. Cement Concrete Comp. 2000;22(5):321-329.

10. Alexanderson J. Relations between structure and mechanical properties of autoclaved aerated concrete. Cement Concrete Res. 1979;9(4):507-514.

11. Chen YL, Ko MS, Chang JE, et al. Recycling of desulfurization slag for the production of autoclaved aerated concrete. Constr Build Mater. 2018,158:132-140.

12. Huang XY, Ni W, Cui WH, et al. Preparation of autoclaved aerated concrete using copper tailings and blast furnace slag. Constr Build Mater. 2012, 27(1):1-5.

13. Chen YL, Chang JE, Lai YC, et al. A comprehensive study on the production of autoclaved aerated concrete: Effects of silica-lime-cement composition and autoclaving conditions. Constr Build Mater. 2017,153:622-629.

14. Font A, Borrachero MV, Soriano L, et al. Geopolymer eco-cellular concrete(GECC) based fluid catalytic cracking catalyst residue(FCC) with addition of recycled aluminium foil power. J Clean Prod. 2017,168:1120-1131.

15. Tada S.Material design of aerated concrete—an optimum performance design. Mater Struct. 1986;19(109): 21-26.

16. Isu N, Ishida H, Mitsuda T. Influence of quartz particle size on the chemical and mechanical properties of autoclaved aerated concrete (I) tobermorite formation. Cement Concrete Re. 1995;25(2):243-248.

17. Hui-wen W, Yong H, Gang L, et al. Study on the structure and properties of autoclaved aerated concrete produced with the stone-sawing mud. Constr Build Mater. 2018, 184:20-26.

18. Siauciunas R, Baltusnikas A. Influence of SiO_2 modification on hydrogarnets formation during hydrothermal synthesis[J]. Cement Concrete Research. 2003;33(11):1789-1793.

19. Klimesch DS, Ray A. Hydrogarnet formation during autoclaving at 180°C in unstirred matakaolin-lime-quartz slurries. Cement Concrete Res. 1998;28(8):1109-1117.

20. Klimesch DS, Ray A.DTA–TGA of unstirred autoclaved metakaolin–lime–quartz slurries. The formation of hydrogarnet. Thermochimica Acta. 1998;316(2):149-154.

21. Klimesch DS, Ray A. Effects of quartz particle size on hydrogarnet formation during autoclaving at 180 degrees C in the $CaO\text{-}Al_2O_3\text{-}SiO_2\text{-}H_2O$ system. Cement Concrete Res. 1998;28(9):1309-1316.

22. Wan H, Yong H, Gang L, et al. Study on the structure and properties of autoclaved aerated concrete produced with the stone-sawing mud[J]. Construction & Building Materials, 2018, 184:20-26.

23. Guo XL, Meng FJ, Shi HS. Microstructure and characterization of hydrothermal synthesis of Al-substituted tobermorite. Constr Build Mater. 2017;13

Mechanochemically activated clay as a sustainable cementitious binder

I. Tole, K. Habermehl-Cwirzen, A. Cwirzen

Building Materials, Department of Civil, Environmental and Natural Resources Engineering, Luleå University of Technology, Lulea, Sweden

Abstract

High-temperature requirements, emission of hazardous substances from cement kilns and the significant CO_2 footprint in the calcination step are factors requiring special attention in the cement industry. Local and commonly occurring clays can be a sustainable alternative for producing cementitious binders. Structural disorder in natural clay minerals can be induced through mechanochemical activation (MCA), by which the material develops an enhanced reactivity. The treatment of a Swedish natural clay through intensive grinding is carried out in order to assess its potential as a sustainable cementitious binder. Several grinding parameters influence a MCA product. The filling ratio of the jar, the rotation speed, the time of grinding, as well as wet and dry environment, are variated to optimize the MCA process. The MCA process does not require high temperatures or added chemicals and shorter processing times can avoid high-energy requirements during fine grinding. The structural changes of the clay were analysed by X-Ray Diffraction (XRD). Analysis of the particle size distribution of the raw and processed clay suggested a correlation with the grinding duration. An increased ratio of grinding media versus the amount of ground material, while longer grinding duration increased the overall efficiency of the MCA process. The strength activity index (SAI) indicated an enhanced pozzolanic activity for the mechanochemically processed clay. Compressive strength tests have shown a strong correlation between an enhanced amorphization rate and increased compressive strength values.

Keywords: alternative cementitious binders, mechanochemical activation, sustainable building materials, mechanochemistry, clay.

1.   Introduction

The building materials industry is facing several challenges for reducing the environmental impact coming from their production. The high amount of CO_2 emissions, the required high temperature, the volatile hazardous substances, the consumption of primary resources, etc., are some of the critical problems industries and researchers are tacking in order to increase the sustainability of building materials. Increasing the energy efficiency during clinker production, use of alternative fuels and alternative raw materials, and use of secondary cementitious materials (SCM) are some of the countermeasures to decrease the negative impact on the environment [1–3].

Different SCM, as blast furnace slag, silica fume, fly ash, calcined clays, etc., are largely used as partial replacement of cement. Use of calcined (highly kaolinitic) clays as a replacement of cement has shown very good pozzolanic reactivity, cost efficiency and good performance; moreover clay is a natural and widely available raw material [4]. Calcined highly kaolinitic clays are a dehydroxylated form of the 1:1 layer structure, called also metakaolinite [5]. Dehydroxylation of kaolin and other clay minerals can be achieved by mechanochemical activation (MCA) [6,7].

MCA is a process able to impose structural and chemical changes in the treated material through high-energy grinding, meanwhile avoiding the use of chemicals or high temperature requirements [8]. Amorphization of the clay minerals structure can be achieved in reasonable times with optimized process parameters. MCA can also amorphize and enhance the reactivity of such raw clay minerals as montmorillonite, illite and pyrophyllite [9–11].

The efficiency of MCA depends on several process parameters, as time of grinding, ball to processed material ratio, use of grinding aids, velocity, etc. Optimization of these parameters can give higher amorphization rates of the clay minerals structure in shorter time [12].

This study focused on the efficiency of the MCA in the amorphization of the structure and on the pozzolanic activity of a raw clay from Sweden. The process parameters as ball to powder ratio and time of grinding are varied in order to assess their influence on the processed material. Differently mechanochemically activated samples were investigated through indirect methods, as the so-called strength activity index (SAI), to evaluate their pozzolanic activity.

2.   Methodology

2.1   Materials

The raw clay used in this study was collected in the Sollentuna municipality in Stockholm County in east central Sweden. Atterberg limits were used in order to characterize the geotechnical properties of the raw material, classifying it as clay. The chemical composition of the raw material is shown in Table 1:

Table 1: Chemical composition of the raw clay used in the study.

Component	Content
	wt.%
SiO_2	52,6
Al_2O_3	15,1
Fe_2O_3	6,9
CaO	6,41
K_2O	3,78
MgO	2,51
Na_2O	1,68
TiO_2	0,696

Dry grinding was carried out using a planetary ball mill, type Retsch PM 100, with a stainless steel jar of 500 mL volume. Twelve stainless steel balls with the same diameter of 20 mm were used. Two different regimes of ball to powder (B/P) and time of grinding were applied. The speed was set to 500 rotation per minute (rpm). Sample D0 was prepared by hand grinding for 1 minute.

Table 2: Process parameters of mechanochemically treated clay.

Sample	Ball/Powder	Time of grinding
	wt.ratio (g/g)	min
D0	-	-
D35	3	5
D320	3	20
D255	25	5
D2520	25	20

2.2 Methods

2.2.1 X-Ray diffraction

Changes of the crystallinity due to the MCA process were determined by X-ray diffractometer, (type Empyrean from PANalytical, using Cu-Kα radiation with a wavelength of 1,54060 Å, generated at 45 kV and 40 mA. The step size was 0.0260 [°2θ] and the scan step size 87.4650 seconds. The temperature during the measurement was kept at 25 °C. The samples for the XRD analysis were prepared in a backload holder.

2.2.2 Particle size distribution

The particle size distribution was measured by Dynamic Light Scattering (DLS). A Malvern Zetasizer equipped with a back-scattering detector was used for testing the processed clay. The samples were prepared as a suspension in distilled water and three measurements per sample were made.

2.2.3 Strength Activity Index (SAI)

The ASTM C125 standard defines pozzolan as "a siliceous and aluminous material which, in itself, possesses little or no cementitious value but which will, in finely divided form in the presence of moisture, react chemically with calcium hydroxide at ordinary temperature to form compounds possessing cementitious properties" [13]. Assessment of pozzolanic activity can be done by different direct and indirect methods. The strength activity index (SAI) is an indirect method to evaluate the pozzolanic reactivity through comparative compressive strength tests [14]. Mortar beams were produced using cement as a binder and replacing 20% of the cement with the processed clay. The mortar mixes were prepared in a Hobart mixer with a mixing time of 5 min. The mix design of the mortar beams is shown in the table below:

Table 3: Mix design of the mortar beams prepared for the SAI test

Sample	Cement	Sand	Processed clay	Processed clay	Water
	g	g	Sample ID	g	ml
M0	450	1350	-	-	225
MD35	360	1350	D35	90	225
MD320	360	1350	D320	90	225
MD255	360	1350	D255	90	225
MD2520	360	1350	D2520	90	225

After demoulding at 24 hours, the beams were stored in a water bath. Compressive strength tests after 7 and 28 days were done on all the samples. The SAI result is a percentage of the strength value of the control mortar beam to the strength value of the mortar beam prepared with 20% of cement replacement:

$$SAI = A/B \times 100 \%$$
(1)

where A is the compressive strength value for the beam with 20% of cement replacement and B is the compressive strength value of the control mortar sample. To assess pozzolanic activity of the tested sample, ASTM C618 requires a SAI greater than 0.75 after 7 and 28 days for FA and natural pozzolans at a cement replacement of 20% [14].

3. Results and discussion

Minerals as kaolinite (Kln), illite (Il), montmorillonite (Mnt), muscovite (Ms), quartz (Qz) and calcite (Ca) were identified from the XRD analysis of the untreated samples. The MCA process has induced amorphization of the structure of the processed clay. Higher ball-to-powder ratio and longer time of grinding has caused substantial structural changes. XRD graphs in figure 1 indicated decreased intensities of the main peaks. Peaks related to clay minerals, as kaolinite or muscovite, were altered easier than quartz,

which peaks are almost not changed. This phenomenon can be associated to the different hardness that the two substances have [15]. Analysis of the FWHM of the kaolinite peak [001] were done by using Lorentz fitting in order to better evaluate the changes on the structural order, figure 2. Increased values of the FWHM indexes were determined for samples D35, D320 and D255, implying gradual degradation of the kaolinite lattice for longer time of grinding and higher ball-to-powder ratio. Only the sample D2520 has indicated values of FWHM higher than 0.4, suggesting an amorphized structure [16,17].
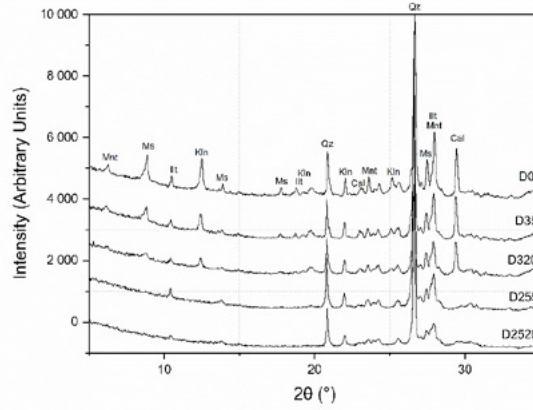

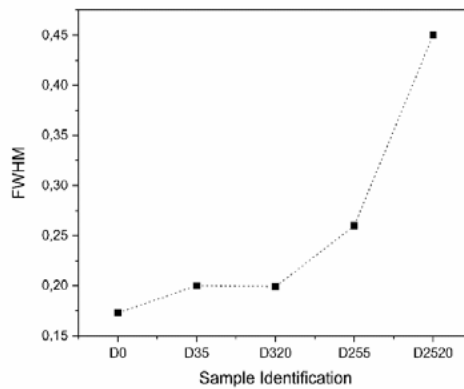Figure 1: XRD diffraction patterns for different B/P ratio and grinding time of a Swedish raw clay.

Figure 2: FWHM of the kaolinite peak [001] for the treated samples with different process parameters.

Particle size distribution has shown a direct correlation to the time of grinding and the ball-to-powder ratio values. Longer time of grinding and higher ball-to-powder ratio have led to an increased volume of smaller particles. The most amorphized sample, D2520, has also a higher volume of smaller particles as shown in figure 3.
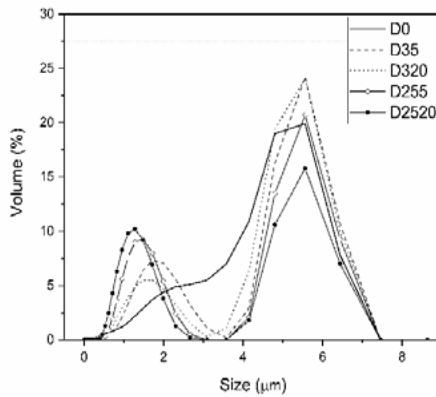
Figure 3: Particle size distribution of MCA clay with different process parameters.

Compressive strength tests results after 7 and 28 days are shown below in figure 4a) and 4b). The mechanical properties (after 7 days) of the mortar beams prepared with 20 % of replacement slightly decreased for the clay treated with lower ball-to-powder ratio (MD35, MD320) and with shorter time of grinding (MD35 and MD255). Sample MD2520 prepared with 20% of cement replaced by the processed clay, which has achieved higher amorphization of the structure through MCA, showed high compressive strength values after 7 days. After 28 days, the compressive strength of the samples prepared with 20% of cement replacement has reached higher values than the reference mortar sample prepared only with cement as a binder (M0). The replacement of cement by MCA clay indicated increased mechanical properties for all the analysed samples besides MD255. Sample MD255 has shown a slightly lower value of the compressive strength, while presenting a SAI index value (95%) higher than the minimum required (75%).
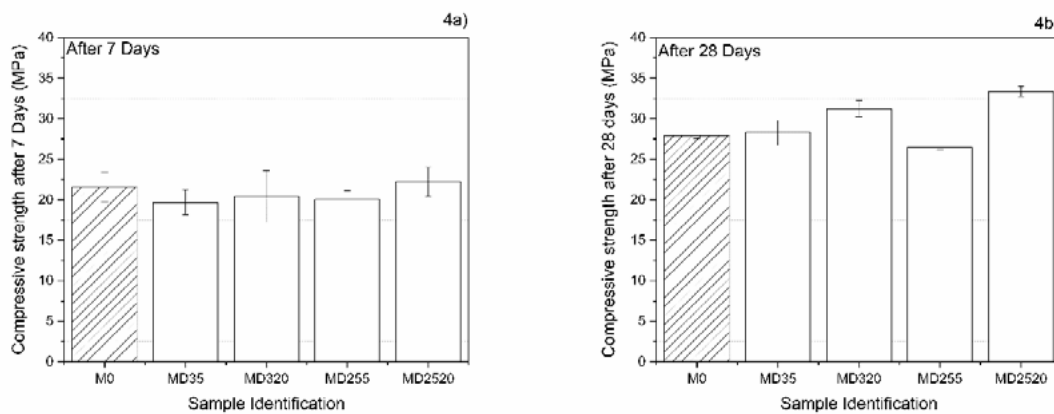

Figure 4: Compressive strength test results of reference mortar sample (M0) and mortar samples prepared with 20% of cement replaced by MCA clay, a) after 7 days, b) after 28 days

Calculation of the SAI index is done for the tested samples and the results are shown in figure 5. After 7 days the SAI indexes for all the samples prepared with 20% of cement replacement by the treated clay were higher than the required minimum of 75%. The maximum SAI index was registered for sample MD2520 with a value equal to 103%. Increased SAI index values were reported also for all the samples tested after 28 days. The minimum required value (75%) was exceeded for all samples. Sample MD2520 has reached a value of 120 % after 28 days, suggesting a direct relationship between the increased reactivity by MCA and the pozzolanic activity.
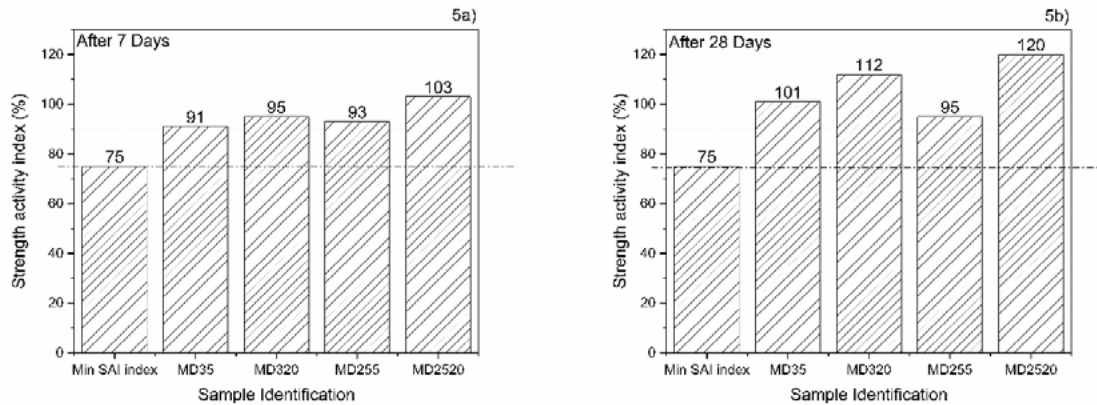
Figure 5: Strength activity index of mortar samples prepared with 20% of cement replaced by MCA clay, a) after 7 days, b) after 28 days

A more precise evaluation of the pozzolanic activity has to consider further direct tests on the studied samples. Frattini and Chapelle tests can give a clearer understanding of the increased pozzolanic activity of the ground clay. The filler effect, originated by the decreased particle size distribution, is another factor that can influence the mechanical properties of the material.

4. Conclusions

- MCA can be considered an environmentally friendly process able to increase the chemical reactivity of clay.

- Higher ball-to-powder ratios and longer time of grinding showed a better efficiency in the amorphization of the clay minerals structure.

- The particle size distribution is influenced by the process parameters of the mechanochemical activation. Higher amounts of smaller particles are achieved for longer time of grinding and for higher ball-to-powder ratios.

- MCA-treated clay showed good mechanochemical properties when used as a cement replacement. Compressive strength values measured after 7 and 28 days were increased for the mortar samples prepared with 20% of cement replacement by the MCA clay.

- SAI indexes, after 7 and 28 days, overpassed the minimum required value of 75%. Mortar prepared with the treated clay D2520 showed the best values of compressive strength and SAI indexes.

- Increased amorphization indicated an enhanced pozzolanic activity of the processed clay.

5. Acknowledgment

6. References

[1]   M.C. Bignozzi, Sustainable cements for green buildings construction, Procedia Eng. 21 (2011) 915–921.

[2]   H. Justnes, How to Make Concrete More Sustainable, J. Adv. Concr. Technol. 13 (2015) 147–154. doi:10.3151/jact.13.147.

[3]   M. Schneider, M. Romer, M. Tschudin, H. Bolio, Sustainable cement production—present and future, Cem. Concr. Res. 41 (2011) 642–650.

[4]   K. Scrivener, F. Martirena, S. Bishnoi, S. Maity, Calcined clay limestone cements (LC3), Cem. Concr. Res. 114 (2018) 49–56.

[5]   F. Bergaya, G. Lagaly, Handbook of clay science, Newnes, 2013.

[6]   R. Hamzaoui, F. Muslim, S. Guessasma, A. Bennabi, J. Guillin, Structural and thermal behavior of proclay kaolinite using high energy ball milling process, Powder Technol. 271 (2015) 228–237.

[7]   S. Ding, L. Zhang, X. Ren, B. Xu, H. Zhang, F. Ma, The Characteristics of Mechanical Grinding on Kaolinite Structure and Thermal Behavior, Energy Procedia. 16 (2012) 1237–1240. doi:https://doi.org/10.1016/j.egypro.2012.01.197.

[8]   P. Baláž, M. Achimovičová, M. Baláž, P. Billik, Z. Cherkezova-Zheleva, J.M. Criado, F. Delogu, E. Dutková, E. Gaffet, F.J. Gotor, Hallmarks of mechanochemistry: from nanoparticles to technology, Chem. Soc. Rev. 42 (2013) 7571–7637.

[9]   H. Yang, W. Yang, Y. Hu, C. Du, A. Tang, Effect of mechanochemical processing on illite particles, Part. Part. Syst. Charact. 22 (2005) 207–211.

[10]   J.L. Pérez-Rodríguez, L.M.S. Del Villar, P.J. Sánchez-Soto, Effects of dry grinding on pyrophyllite, Clay Miner. 23 (1988) 399–410.

[11]   M. Xia, Y. Jiang, L. Zhao, F. Li, B. Xue, M. Sun, D. Liu, X. Zhang, Wet grinding of montmorillonite and its effect on the properties of mesoporous montmorillonite, Colloids Surfaces A Physicochem. Eng. Asp. 356 (2010) 1–9. doi:10.1016/j.colsurfa.2009.12.014.

[12]   I. Tole, K. Habermehl-Cwirzen, M. Rajczakowska, A. Cwirzen, Activation of a raw clay by mechanochemical process-effects of various parameters on the process efficiency and cementitious properties, Materials (Basel). 11 (2018). doi:10.3390/ma11101860.

[13]   C. Astm, 125 Standard terminology relating to concrete and concrete aggregates, Annu. B. ASTM Stand. 4 (2003).

[14]   C. ASTM, Standard specification for coal fly ash and raw or calcined natural pozzolan for use in concrete, C618-12a. (2012).

[15]   É. Makó, R.L. Frost, J. Kristóf, E. Horváth, The effect of quartz content on the mechanochemical activation of kaolinite, J. Colloid Interface Sci. 244 (2001) 359–364. doi:10.1006/jcis.2001.7953.

[16]   A. Tironi, M.A. Trezza, A.N. Scian, E.F. Irassar, Potential use of Argentine kaolinitic clays as pozzolanic material, Appl. Clay Sci. 101 (2014) 468–476. doi:https://doi.org/10.1016/j.clay.2014.09.009.

[17]   B. Ilić, V. Radonjanin, M. Malešev, M. Zdujić, A. Mitrović, Effects of mechanical and thermal activation on pozzolanic activity of kaolin containing mica, Appl. Clay Sci. 123 (2016) 173–181. doi:10.1016/j.clay.2016.01.029

ICSBM 2019
ID 032

Phase and dimensional stability of volcanic ash-based phosphate geopolymers at elevated temperatures

J.N. Yankwa Djobo[1,2*], A. Elimbi[3] and D. Stephan[2]

[1]Local Materials Promotion Authority/MIPROMALO/MINRESI, 2396, Nkolbikok, Yaoundé-Cameroon

[2]Building Materials and Construction Chemistry, Technische Universität Berlin, Gustav-Meyer-Allee 25, 13355, Berlin, Germany

[3]Department of Inorganic Chemistry, Faculty of Science, University of Yaoundé I, 812, Yaoundé, Cameroon

Corresponding author: noeldjobo@gmail.com; noel.djobo@campus.tu-berlin.de

Abstract

Phosphate geopolymers are part of chemically bonded phosphate cements obtained from an aluminosilicate and phosphate solution. Their structure consisting of phosphate bonds make them suitable for use as refractory material. This study deals with the influence of phosphoric acid concentration (6, 8 and 10 mol/L) on the stability of volcanic ash-based phosphate geopolymers exposed to 100, 600 and 1000°C. The results reveal that the onset of crystallization is about 600ºC with the formation of aluminium phosphate (V) and tridymite, then crystallisation of iron (III) phosphate (V) and hematite at 1000°C. The degree of crystallisation of these phases increases with phosphoric acid concentration. The geopolymers obtained with 8 mol/L of phosphoric acid showed the best thermal stability at 1000°C in term compressive strength change. The maximum thermal linear shrinkage recorded was 3%. The major phases of all geopolymers remain stable up to 1000°C, after which melting of phases happens.

Keywords. Volcanic ash; phosphate geopolymers; thermal stability.

1. Introduction

Geopolymers are known as 3D network inorganic polymer obtained by chemical reaction of a solid precursor (aluminosilicate) and a hardener in a liquid state. The latter may be potassium or sodium silicate solution, or phosphoric acid [1]. The geopolymer gained its popularity because of the potential low CO_2 emission and energy efficiency during its manufacturing compared to conventional cement. Moreover, the superior thermal stability of geopolymer compared to Portland cement has also increased the interest toward that material for high-temperature applications. However, this characteristic is closely related to the type of aluminosilicate used as well as the synthesis conditions [2–4]. For example, an addition of calcium sources to Metakaolin (MK) improves the thermal resistance of geopolymers in term of compressive strength compared to solely MK-based geopolymers when exposed at 1000ºC [5]. It was reported a loss of 40% of initial strength after a cycle of heating-cooling of geopolymer from volcanic ash at 1000ºC [6]. When prepared in alkaline medium, the phases of volcanic ash-based geopolymers are not stable beyond 1000ºC as they start melting contrary to MK-based ones. It was also shown that volcanic ash based-geopolymers obtained with potassium silicate as alkaline solution develops superior stability at elevated temperatures

with thermal shrinkage less than 3% compared to the ones with sodium silicate [7]. In general, when exposed to elevated temperatures the physical properties of geopolymers obtained in alkaline solution are significantly deteriorated in the range of 750-900 °C [8,9]. The latter constitutes the highest temperature range of application of geopolymer obtained in alkaline medium in the field of heat resistance materials. This is due to cations present in the alkaline solution which lower the temperature of glass transition, hence induce sintering with decrease of the mechanical strength along with severe thermal shrinkage [4,7]. Up to now, few studies deal with the phase stability or physical properties of geopolymers obtained in an acidic medium after exposure at elevated temperatures.

The phases of MK-based geopolymers obtained with phosphoric acid were reported to be thermally stable, with linear shrinkage of 5.3% after exposure at 1450°C [10]. Also, phosphoric acid activation of synthetic Al_2O_3–$2SiO_2$ powders showed extremely high thermal stability of phases with no sign of melting up to 1550°C [11]. Recent work reported that the structural evolution of phases with temperature and their stability depend on the phosphate content of the matrix [12]. However, MK-based phosphate geopolymers have low thermal stability in term of compressive strength evolution. Bewa et al. reported a decrease of more than 75% of the compressive strength development only after exposure at 200°C [13]. While, Celerier et al. [14] showed the complete destruction and/or extensive cracks apparition with a significant decrease of the compressive strength of MK-based phosphate geopolymer after heating to 1000°C. These behaviours at elevated temperature were reported to depend on the Al/P ratio of the matrix, the reactivity of the MK used and its wettability. Moreover, the high-water content of the MK-based phosphate geopolymer was also responsible of the destruction of the binding phase because of the dehydroxylation that happens after heating. Since MK particles have a high specific surface area, thus high-water demand and high liquid to solid mass ratio are required for reaching good workability.

The investigation of geopolymers from volcanic ash and phosphoric acid has never been reported yet. Since the improved thermal stability of phases of MK-phosphate geopolymer was due to the high stability of the phosphate bond, the low thermal stability of phases of volcanic ash based geopolymer in alkaline solution could also be improved when synthesized in acidic medium. Moreover, volcanic ash has lower specific surface area compared to MK and generally low liquid to solid mass ratio is required for achieving good workability [15]. This work aims to investigate the influence of phosphoric acid concentration on thermal stability of volcanic ash-based phosphate geopolymers for high temperature application. These include the study of the transformation and transition of phases, the thermal shrinkage as well as porosity and compressive strength of geopolymers exposed to high temperatures. The thermal transformation and transition of phases were investigated by X-Ray diffractometry (XRD), Fourrier transformed infrared spectroscopy (FTIR), Thermogravimetry analysis coupled with Differential Scanning Calorimetry (TGA-DSC) and Dilatometry analysis. The porosity was determined using mercury intrusion porosimeter (MIP).

2.   Materials and methods

2.1   Materials

Volcanic ash (VA) was collected along "the Line of Cameroon" and ground in a ball mill to get a powder with particles size <200µm. The chemical analysis carried out by X-ray fluorescence is reported in Table 1. The particle size distribution carried out using laser particle size analyser (MASTERSIZER S, Malvern, UK) is depicted in Fig. 1. It shows a trimodal distribution with characteristic diameters as follows: d_{10}= 0.26 µm d_{50}= 3.7 µm and d_{90} = 57 µm. Orthophosphoric acid (H_3PO_4, 85wt.-%) was used to prepare the hardeners. The latter were obtained by diluting the as received orthophosphoric acid with water to get concentrations of phosphoric acid solution 6, 8 and 10 mol /L.

Table 1: Chemical composition of volcanic ash from Cameroon

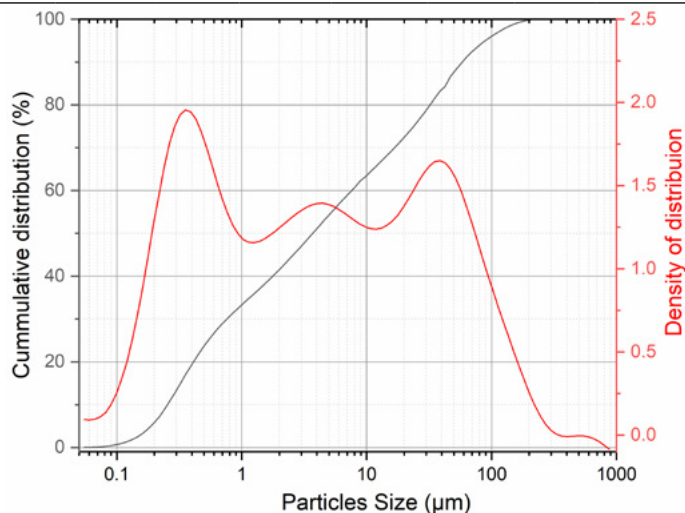| Oxides	SiO_2	Al_2O_3	Fe_2O_3	CaO	MgO	Na_2O	TiO_2	K_2O	MnO	P_2O_5	LOI	Total
Wt. -%	40.41	15.90	13.46	8.87	8.45	1.75	3.08	0.91	0.21	0.88	4.25	98.17

Fig. 1. Particles size distribution of milled volcanic ash

2.2   Experimental methods

The geopolymer pastes were prepared by mixing for 3 min volcanic ash and the hardeners according to liquid to solid mass ratios of 0.32, 0.36 and 0.4 respectively. These different ratios were chosen according to the workability of the pastes with each concentration of acid. The pastes obtained were poured in 40 mm cubic moulds, vibrated for 3 min and covered with a plastic foil to avoid cracks or pores due to rapid water evaporation. The specimens were kept at $27\pm3^{\circ}C$ for 24h before demolding, then stored in the same curing condition for 28d. Afterwards, the geopolymer specimens were heated to a temperature of 100, 600 and $1000^{\circ}C$ at a heating rate of $5^{\circ}C/min$ in a programmable electrical furnace and kept at this temperature for 4h.

The analysis of the mineralogical composition of the geopolymers before and after exposure to elevated temperatures was carried out using X-ray diffractometry (Bruker X-ray diffractometer (D8 Discovery, US)). The changes on the chemical bonds of unheated and heated geopolymers were investigated by FTIR spectroscopy (Nicolet 5700 spectrometer using KBr method). The porosity and pore size distribution of unheated geopolymers were investigated by mercury intrusion porosimeter (Auto pore IV 9500 scanning mercury porosimeter with pore size range between 0.005 and 360 µm).

The compressive strength of geopolymers before and after exposure to elevated temperatures was measured thanks to an Impact Test Equipment Limited. Thermal transformation and transition phases were monitored using Thermogravimetry analysis coupled with Differential Scanning Calorimetry (Linseis, Model STA PT1000). An optical dilatometer (ESS MISURA HSM ODHT Model 1600/80) was used to assess changes of length of specimens shaped 5 x 5 x 15 mm³.

3.   Results and discussion

3.1   Influence of phosphoric acid concentration on mineralogy at 27 and 1000°C

The phase compositions of raw volcanic ash and geopolymers before and after exposure to 1000°C are depicted in Figs 2 and 3 respectively. The main minerals identified in volcanic ash using X'Pert High Score Plus software are as follows: augite (PDF# 98-005-6926); albite high (PDF# 98-010-0499); jadeite-

diopside (PDF# 98-006-9709); forsterite, ferroan (PDF# 98-003-9795) and magnetite (PDF# 98-008-5807). In the unheated geopolymers, no new crystalline phases were identified (Fig. 2), but a significant decrease of peaks intensity of major minerals is visible. This behaviour is like what happens with volcanic ash-based geopolymers obtained in alkaline solution [16,17].

The intensities of the peaks of augite ($Al_{0.1}Ca_{0.83}Fe_{0.34}Mg_{0.77}Na_{0.02}O_6Si_{1.92}Ti_{0.02}$) at 29.80º (2.99Å), 35.53º(2.52Å) and 35.74º (2.51Å) respectively decrease by 38, 27 and 28% respectively after reaction of volcanic ash with 6 mol/L acid solution. Also, intensities of the main peaks of albite ($NaAlSi_3O_8$) at 2θ= 27.73º (3.21Å), 23.57º (3.77Å) and 21.87º (4.05Å) respectively are reduced by 26, 22 and 17% respectively. These data show that augite is more dissolved than albite.

This is likely due to the preferential dissolution of augite (Pyroxene group) in low pH (below 3-4) in comparison with albite (Feldspar group) [18,19]. However, the extent of dissolution of those minerals is not proportional to the acid concentration, though it remains low in volcanic ash. A tentative explanation to this behaviour might be the rapid dissolution of amorphous phase and fast setting as observed during mixing, which would have delayed the further dissolution of unreacted particles with time. Nevertheless, a deep investigation to understand the dissolution behaviour of volcanic ash in an acidic medium is requires and this will be carried out in our upcoming studies.
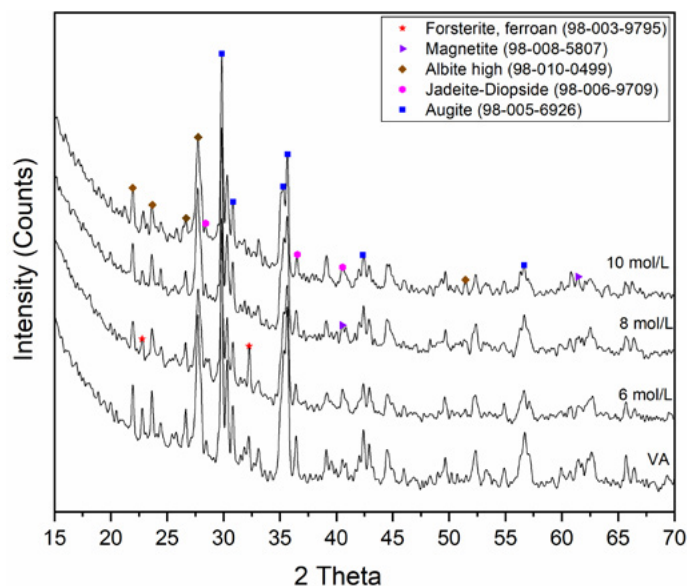

Fig. 2. X-ray patterns of volcanic ash and resulting geopolymers at 27 ºC

The X-ray patterns of heated geopolymers at 1000ºC (Fig. 3) show several changes in the phase compositions compared to unheated ones. The main diffraction peaks of minerals like Jadeite-Diopside (PDF# 98-006-9709); Forsterite, ferroan (PDF# 98-003-9795) and Magnetite (PDF# 98-008-5807) are no longer identifiable, which means that they were transformed into other phases. It can also be seen the significant decrease of intensities of peaks at 2θ=29.80º (2.99Å) and 27.74º (3.21Å) corresponding to the main peak of augite and albite respectively with acid concentration. This happens along with the change in the profile of the broad peak at 2θ=35.74 (2.51Å) on the X-ray pattern of volcanic ash which becomes narrow.

The extent of the decrease of the main peak intensity of these major minerals shows that in addition to acid concentration, the stability of augite is more sensitive to temperature than albite. The new crystalline phases are aluminium phosphate (V) (PDF# 98-028-0307), tridymite (PDF# 98-009-4090), hematite (PDF# 98-008-8418) and iron (III) phosphate (V) (PDF# 98-009-8063). Their main peaks are as follows: 2θ = 20.46º (4.33Å), 21.52º (4.12Å) and 23.15º (3.84Å) for aluminium phosphate (V); 2θ = 20.32º (4.36Å), 21.62º

(4.10Å) and 23.08º (3.85Å) for tridymite); $2\theta = 25.68º$ (3.46Å), 37.63º (2.38Å) and 20.33º (4.36Å) for iron(III) phosphate(V); $2\theta = 33.25º$ (2.69Å), 35.72º (2.51Å) and 54.23º (1.70Å) for hematite. Iron phosphate minerals have the similar structure like the SiO_2-based minerals [20]. It can be noticed an increase of these main peak intensities with the increase of phosphoric acid concentration.

The formation of aluminium phosphate(V) and silica-based minerals such as tridymite are common in phosphate geopolymers treated at 1000ºC [11,13,21–23]. The formation of these two minerals is due to the crystallization of amorphous $AlPO_4$-SiO_2 solid solution constituting the binding phase of the phosphoric acid-based geopolymer [23]. Thus, the increase of the amount of these minerals demonstrates the extent of dissolution of reactive phases that happens with the increase of phosphoric acid concentration. Moreover, the formation of hematite and iron phosphate is totally new in high-temperature heating of phosphate geopolymers. Their presence is a proof that in addition to $AlPO_4$-SiO_2 solid solution as binder in phosphate geopolymer there is also $FePO_4$ in the case of ferro-aluminosilicate materials like volcanic ash. Moreover, similarly to aluminium phosphate and trydimite, the presence hematite and iron phosphate come from the partly breakdown of the Fe-O-P bonds of the amorphous phase of the geopolymer binder.
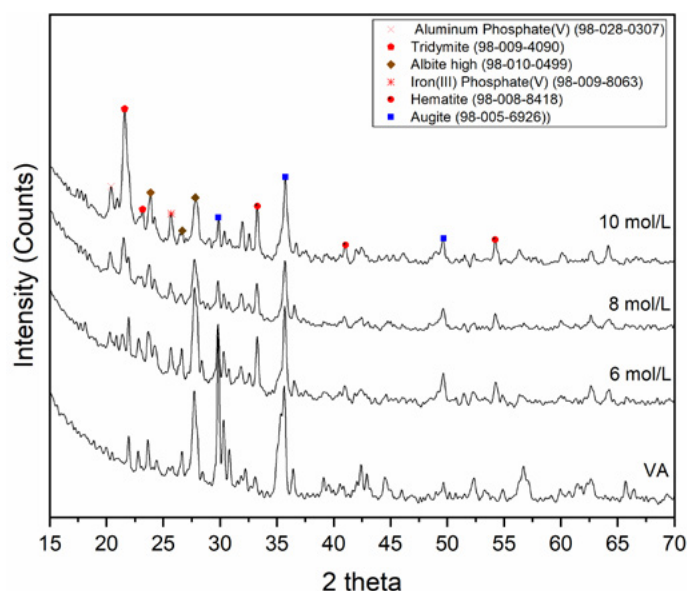

Fig. 3. X-ray patterns of geopolymer after heating at 1000ºC

Structural bond changes in geopolymer with varying phosphoric acid concentration before and after exposure to elevated temperatures are highlighted in Figs 4 and 5 respectively.

The vibration band appearing at 1650 and 3420 cm^{-1} in all IR spectra are respectively characteristic of bending and stretching vibrations of H-O-H and H-O bonds of water molecules. In Fig. 4, the band on VA at 1020 cm^{-1} is characteristic of stretching vibrations of Si-O bonds of silicate chain. With 6 mol/L of phosphoric acid used as a hardener, that band has shifted by about 52 cm^{-1} to a higher value after geopolymerization. It further shifted by 11cm^{-1} when the acid concentration rises respectively to 8 and 10 mol/L. Such increase of wavenumber is also noticeable on the band at 750 cm^{-1} of volcanic ash, which is characteristic of stretching vibration of Si-O bonds of the silicate network, that shifted to 792 cm^{-1} on geopolymer. This observation indicates that there is formation of new stronger bonds as a result of reaction occurring [17,24]. Such a phenomenon can be attributed to the formation of new bonds among tetrahedra $[AlO_4]^{5-}$, $[FeO_4]^{5-}$and $[PO_4]^{5-}$.

The changes observed in that main vibration band also ascertain that increasing the concentration of phosphoric acid improves the extent of dissolution of reactive phases as stated by XRD patterns. The

bands appearing at 630, 578 and 541cm⁻¹ are respectively related to the various vibrating modes of the Si-O bonds in the silicate chains of volcanic ash [25]. Fig. 5. shows the IR spectra of geopolymer with varying acid concentration after heating at1000°C.

After heating geopolymer, there is the significant decrease in the intensity of bands at 3420 and 1650 cm⁻¹ which are characteristic of vibration modes of water molecules. Compared to the IR spectra of geopolymer cured at 27°C (Fig 4.) it can also be observed a shift of the wavenumber of the main band characteristic of Si-O vibration (1072-1083cm⁻¹) to a higher value (1112 cm⁻¹) and the apparition of new bands at 1029 and 1064 cm⁻¹ respectively.
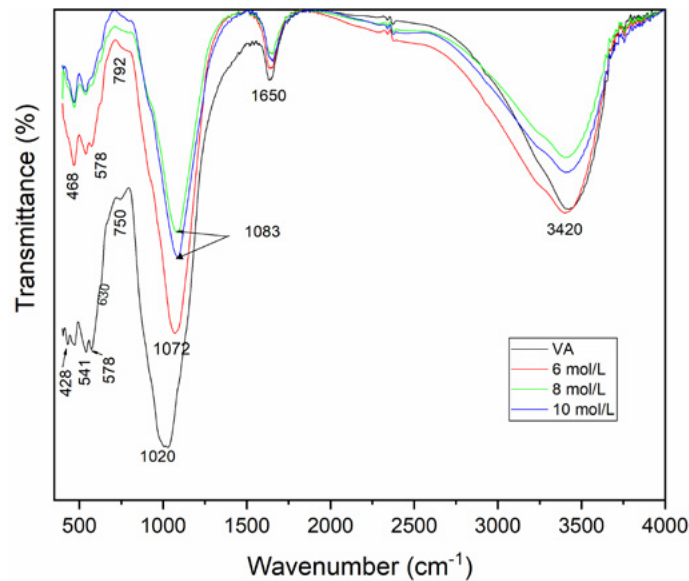
Fig. 4. IR spectra of volcanic ash and resulting geopolymers at 27 °C

Other changes are the disappearance of the vibration band at 541cm⁻¹ and the appearance of the band at 713cm⁻¹ after heating. Similar changes were observed in previous work [12,13]. In this study, these changes are attributed to the crystallization of tridymite and phosphate minerals as shown in XRD patterns of geopolymer after heating at 1000°C.

Fig. 5. IR spectra of geopolymer after heating at 1000°C

3.2 Influence of heating temperature on the mineralogy of phosphate geopolymer obtained with 10 mol/L acid concentration
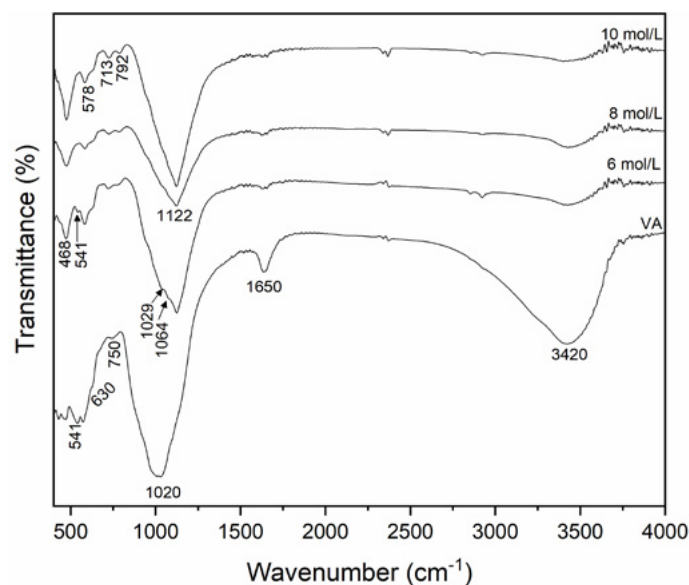
Fig 6 shows the X-ray patterns of volcanic ash-based geopolymers obtained with 10 mol/L of phosphoric acid after exposure to various temperatures. As it can be seen, the crystalline phases initially present in unheated geopolymers remain stable up to 600°C, where the onset of crystallisation is observed. The latter phenomenon is however characterised by the formation of new minerals, aluminium phosphate (V) (PDF# 98-028-0307) and tridymite (PDF# 98-009-4090).
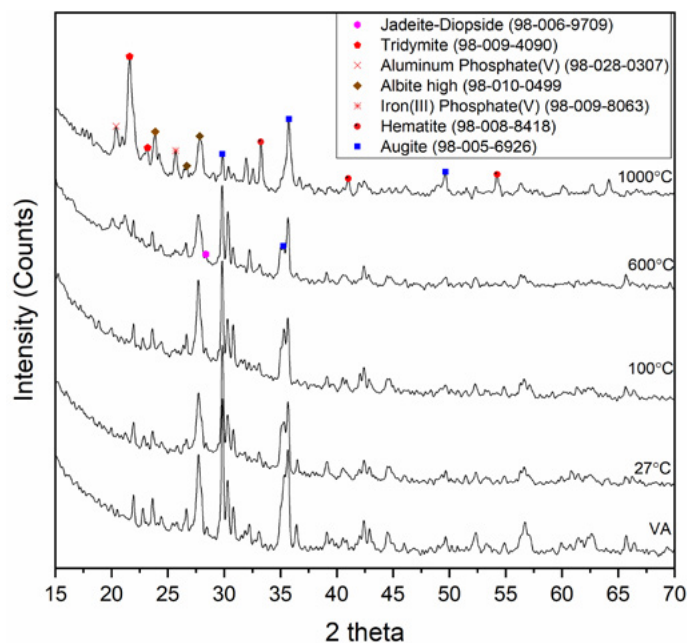

Fig. 6. X-ray patterns of geopolymer obtained with 10 mol/L acid concentration after heating at various temperatures

Although the initial minerals remain up to 600°C, their peak intensities somewhat diminish with increasing temperature. This is more prominent at 1000°C where other new minerals (hematite and iron (III) phosphate (V)) are formed along with the disappearance of some of the initial ones (jadeite-diopside; forsterite, ferroan and magnetite). There is also a significant increase of the peak intensities of aluminium phosphate (V) and tridymite at 1000°C.

It arises from these results that, the stability of minerals of the studied system are temperature sensitive and the onset of crystallization is at around 600 °C. The IR spectra of geopolymers obtained with 10 mol/L of phosphoric acid and heated at various temperatures are shown in (Fig. 7).

The effect of heating is highlighted by the main changes between 600 and 1000 °C. The latter include the shift of the main vibration band from 1093 to 1122 cm^{-1}, the disappearance of the bands at 541cm^{-1} and the appearance of the bands at 713, 1029 and 1064 cm^{-1}. These results confirm the fact that the onset of crystallisation of phosphate geopolymers is around 600 °C and are in accordance with the XRD data (Fig. 6).
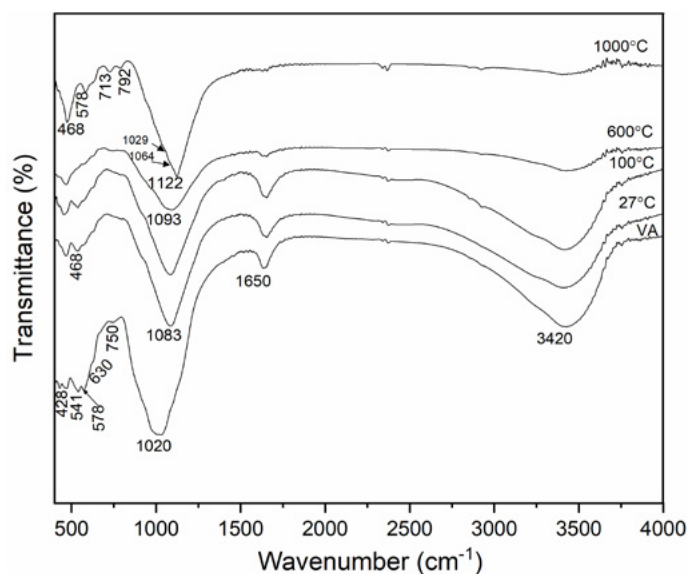
Fig. 7. IR spectra of geopolymer obtained with 10 mol/L acid concentration after heating at various temperatures.

3.3 Physical characteristics

3.3.1 Visual aspect

After maintaining geopolymers at various temperatures, changes in colour and the formation of cracks on the surfaces of some specimens were observed (Fig. 8). The specimens obtained with 6 mol/L of phosphoric acid show no sign of surface deterioration when exposed to 100°C, whilst other specimens show some cracks. The latter seem to be more prominent and larger on the specimen obtained with 10 mol/L of phosphoric acid than the one obtained with the concentration of 8 mol/L. The presence of these cracks can be due to the evaporation of free water present in the pores network or to the dehydroxylation of geopolymer binder. Thus, the extent of cracks demonstrates that the geopolymer obtained with 10 mol/L of phosphoric acid undergoes more damages at 100 °C compared to other specimens. At 600 °C, the geopolymer specimens obtained with 6 and 8 mol/L of phosphoric acid display minor microcracks and there are changes of initial colours from black to light and dark brown.

When heated to 1000°C all the specimens do not show any sign of external damage except the colour which is now light red and becomes dark with increasing phosphoric acid concentration. Based on a correlation between the change of colours and the mineral evolution with temperature, it can be concluded that the change of colour observed at 600 °C results from the crystallisation of aluminium phosphate(V) and tridymite, whereas those observed at 1000 °C corresponds to crystallisation of iron (III) phosphate and hematite.

3.3.2 Porosity

The total porosity and pore size distribution of unheated geopolymers are shown in Figs 9 and 10 respectively. Total porosity (Fig. 9) of geopolymers obtained with 6 or 8 mol/L of phosphoric acid are 22 and 21vol.-% respectively. The porosity significantly decreases to 10.7vol-% when the acid concentration rises to 10 mol/L, which means that the latter has fewer pores compared to the formers. However, it is clearly shown in Fig.10a that the specimen obtained with 10 mol/L of phosphoric acid exhibits larger pore diameters than those obtained with 6 and 8 mol/L respectively. The pore size ranges (Fig.10b) are 0.01-5µm, 0.01-1µm and 0.027-5 µm for specimens with 6, 8 and 10 mol/L of phosphoric acid respectively. Within these pore diameter ranges, the geopolymers obtained with 6 and 10 mol/L of phosphoric acid have

a unimodal pore diameter distribution with maxima at 0.09 and 0.55 μm respectively. Whereas specimens obtained with 8 mol/L of phosphoric acid show a bimodal distribution with maxima at 0.04 and 0.06 μm respectively. This difference in pore size distribution indicates the heterogeneity of the microstructure, which is related to geopolymerization [23,26]. The effect of pore size distribution on the thermal stability of geopolymers will be well discussed in the next section.
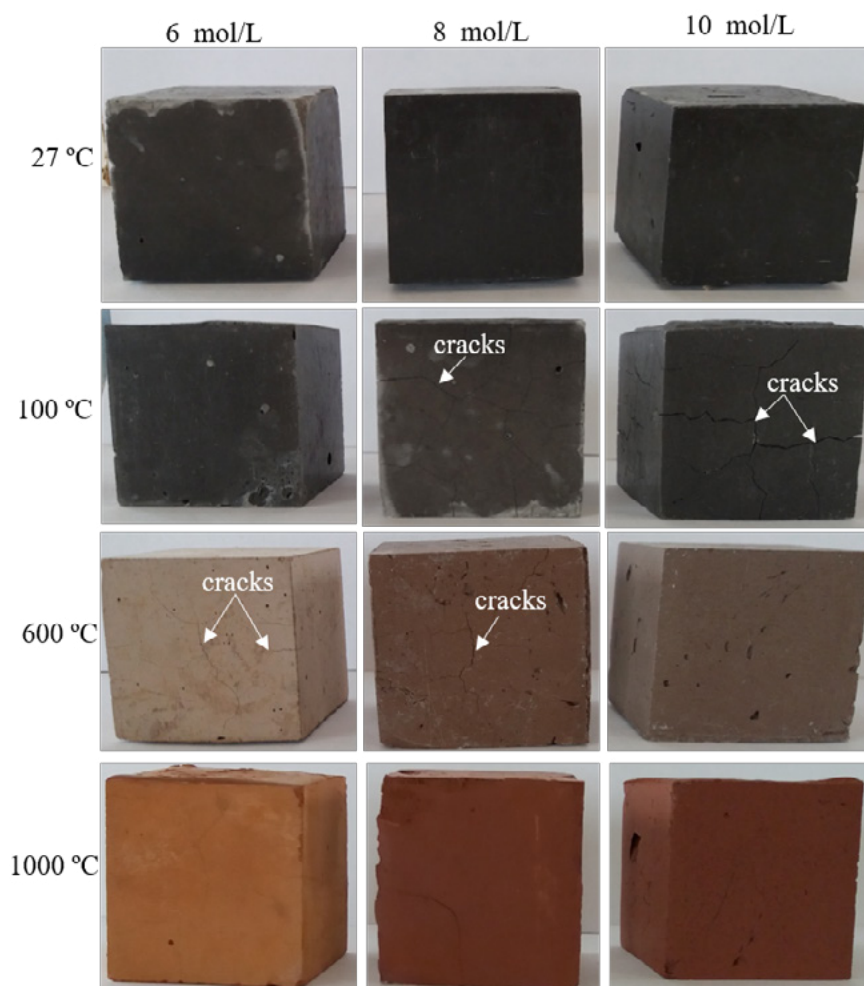
Fig. 8. Physical appearance of geopolymers before and after exposure to various temperatures

3.3.3 Compressive strength

Fig 11 depicts the 28d compressive strength evolution of geopolymer before and after heating at various temperatures for 4h. At room temperature, compressive strength increases with acid concentration. After heating at 100°C, the strength of geopolymer obtained with 6 mol/L of phosphoric acid increases by about 84% (49MPa) while that at the other temperatures decreases. For geopolymers obtained with 8 and 10 mol/L of phosphoric acid, the decrease of compressive strength is 14.7% (43MPa) and 17% (60MPa) respectively.

This trend correlates well with the observation made on (Fig 8) where major cracks were observed only on geopolymers obtained respectively with 8 and 10 mol/L of phosphoric acid. These observations allow to surmise that although high dissolution of reactive phase using hardener of 6 mol/L of phosphoric acid was observed in XRD patterns, the reaction of volcanic ash with 6 mol/L acid concentration remains low.
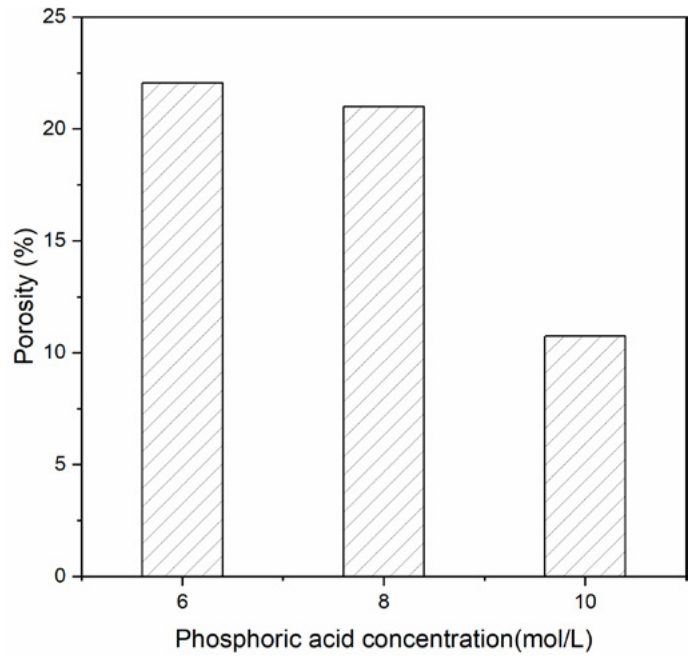
Fig. 9. Total porosity of geopolymers
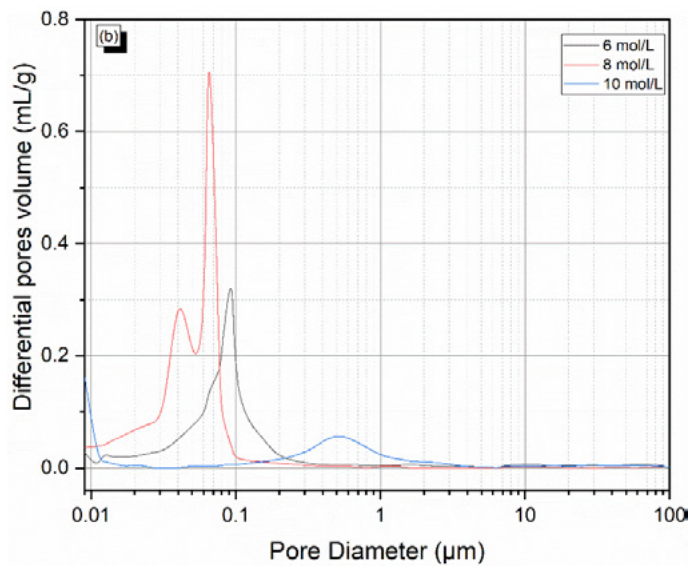
Fig. 10. Pores size distribution of geopolymers: (a) Cumulative pores volume, (b) Differential volume of intruded mercury.

Thus, when exposed at 100°C, the heat supplied rather improves the geopolymerization leading to a more condensed and stronger polymer chain. This seems to be the contrary for geopolymerization with 8 and 10 mol/L acid concentration. In these latter cases, the reactions that take place are faster and lead directly to the formation of strong geopolymer structures at room temperature. Thus, the heat supplied has rather triggered the dehydroxylation of the binding phase, leading to the formation of cracks, hence weakening of the structure.

The strength of geopolymer obtained with 10 mol/L of phosphoric acid continues to decrease till the temperature 1000°C (26.5MPa), whereas the strength of geopolymer obtained with 8 mol/L of phosphoric acid (56.5MPa) remains high compared to the one before heating. This difference of behaviour might be due to the pores size distribution of the geopolymers. In fact, the microstructure of the geopolymer obtained with 8 mol/L of phosphoric has high number of pores with various diameters, which allows

easy evaporation of water during the dehydroxylation stage of the binder with less impact on compressive strength.

Fig. 11. Compressive strength evolution of geopolymers with temperature

3.4 Phases and dimensional stability

3.4.1 Mass loss and phase stability
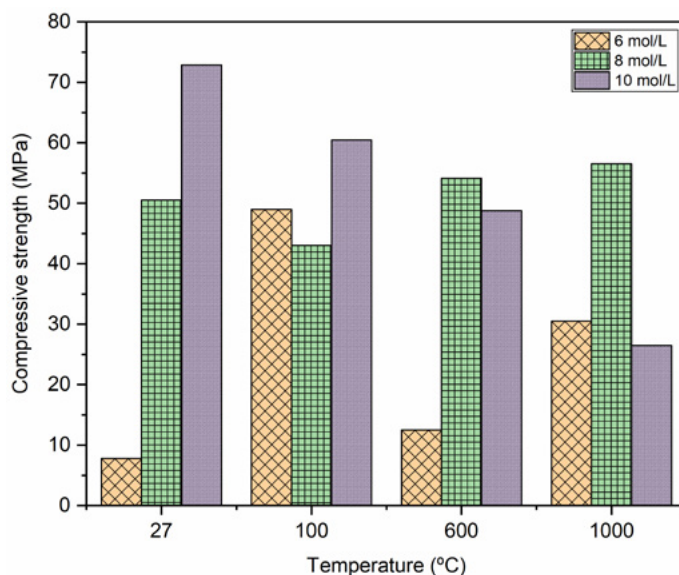
The monitoring of the mass change, the phases transformation and transition of the geopolymer with temperature were carried out by TGA-DSC (Fig 12). The TGA curves are characterized by a single mass loss of 13-14wt% which starts nearly at room temperature and ends at around 600°C. That mass loss is accompanied by an endothermic peak at 86°C. These changes correspond to the removal of free water contained in the pores network and the dehydroxylation of polymer chains of the geopolymer binder [26,27]. Between 600 and 1000 °C, there is not any significant mass change.

The DSC curves show respectively a succession of three small exothermic peaks at 634-657 °C, 690 and 820°C, and an endothermic peak at 805 °C. The first one (634-657 °C) corresponds to the crystallization of ferrous/ferric phosphate minerals from the amorphous phase. In the crystallization process of iron phosphate glasses, that first peak is generally followed by a second exothermic peak at 820 °C related to the crystallization of ferric phosphate minerals ($FePO_4$) [28,29]. The latter obviously confirms the crystallization of iron (III) phosphate identified only in the XRD patterns of geopolymer maintained at 1000°C.

The endothermic peak at 805 °C corresponds to the decomposition of remaining amorphous iron phosphate $FePO_4$ to crystallized Fe_2O_3 [28]. This confirms the crystallization of hematite observed in XRD patterns. Noteworthy that during the phase transition of iron phosphate there is sometime a competition between decomposition $FePO_4$ into Fe_2O_3 and the crystallization of new form of $FePO_4$ [30]. The temperature of the apparition of the first exothermic peak (634-657 °C) shifts to lower value with increasing phosphoric acid concentration. This is due to the increase of the content of Fe^{2+}/Fe^{3+} ions in the bulk composition [28]. The exothermic peak appearing at 690°C corresponds to the crystallization of aluminium phosphate and /or tridymite [23].
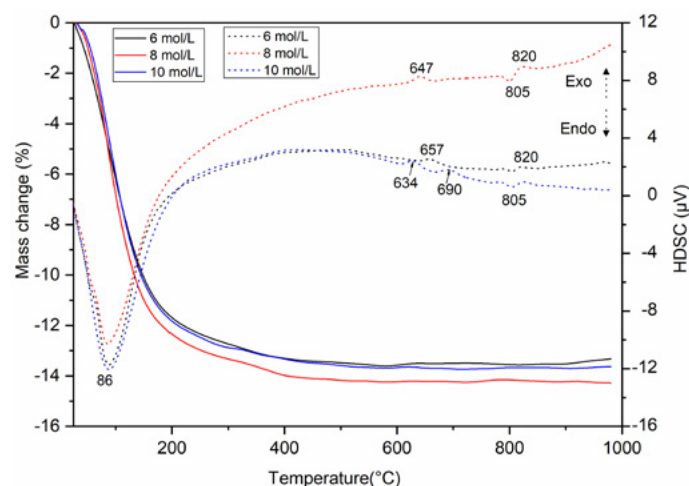
Fig. 12. TGA (solid lines) and DSC (dotted lines) curves of geopolymers with varying phosphoric acid concentrations

3.4.2 Dimensional stability

The dilatometry curves (Fig. 13a) show that up to 1000 °C, thermal linear shrinkage of geopolymers are 195, 2.9 and 3.1% respectively. These shrinkages are mainly observed in two temperature ranges (110-140 °C and 630-665 °C). It is worth pointing out that beyond 1000 °C the higher sintering of volcanic ash particles induces the beginning of melting of mineral phases [6,7]. This can explain the higher shrinkage beyond 1000°C. Hence, this shrinkage was not included in the total shrinkage calculation because the material melts and does not withstand.

The first shrinkage occurs between 25 to 600°C and reaches the maximum at 110-140 °C. This shrinkage is of about 1.6, 2.3 and 2.4% for geopolymer specimens obtained respectively with 6 8 and 10 mol/L of phosphoric acid. The increase of the first shrinkage with phosphoric acid concentration correlates with the extent of cracks as observed on the surface of specimens after exposure at 100 °C (Fig. 8). This shrinkage is linked to the mass loss recorded in TGA and which corresponds to evaporation of water.

The second shrinkage begins at around 600 °C and ends before 1000 °C, and is about 0.2, 0.6 and 0.7% for geopolymer specimens obtained respectively with 6, 8 and 10mol/L of phosphoric acid. This second shrinkage, which does not correspond to any mass loss, is due to the crystallization of ferrous / ferric phosphate minerals. The shift of the maximum temperature related to this second shrinkage (Fig. 13b) agrees with the similar phenomenon observed in the DSC curves (Fig.12), and which was ascribed to the increase of the amount of Fe^{2+}/ Fe^{3+} ions in the bulk composition.

The latter arising from the increased dissolution of the reactive phase of volcanic ash with the increase of phosphoric acid concentration. Most interesting in the differential curve of the percentage of expansion beyond 1000 °C is the delay of the temperature at which maximum shrinkage due to melting occurs (Fig. 13b). Such a behaviour means that the increase of dosage of phosphate bonds in the geopolymer binder prevent the early melting of phases.
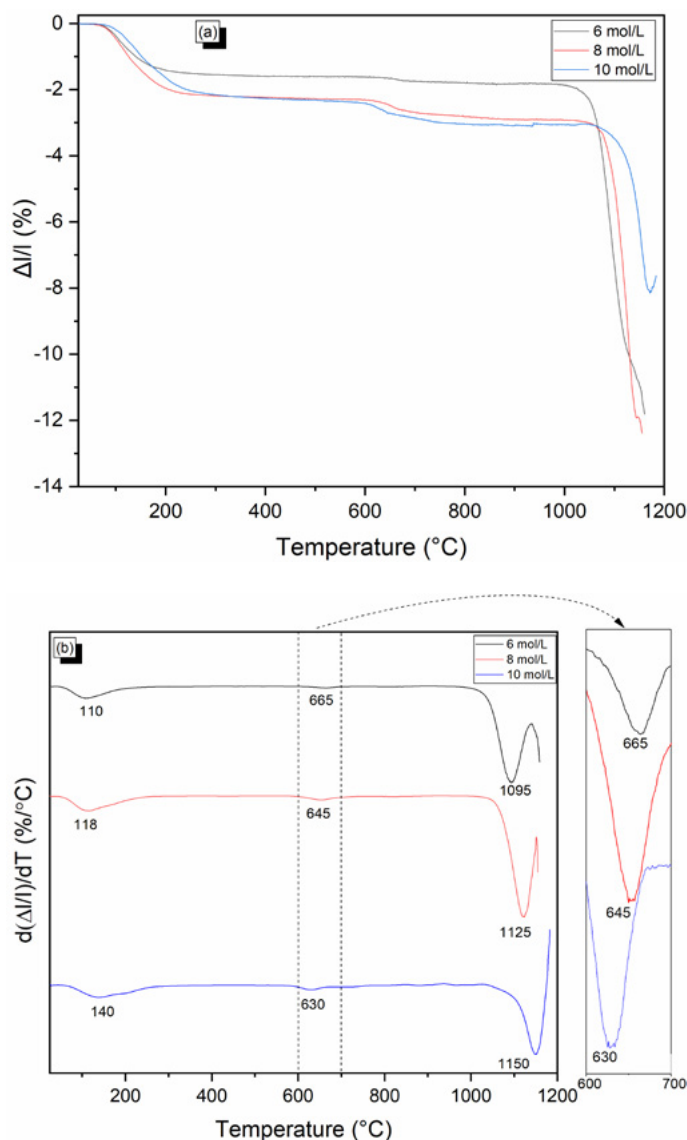
Fig. 13. Dimension change with temperature (a) % of expansion; (b) differential of the % of the expansion

4. Conclusion

The influence of phosphoric acid concentration on the thermal stability of volcanic ash-based phosphate geopolymers was reported. It appears that changes occurring in mineralogical phases are highly sensitive to temperature and phosphoric acid concentration. The major phases including geopolymer binder remain stable up to 1000 ºC and beyond the latter temperature, the melting of geopolymers becomes predominant. The geopolymer binder is based on ferro-silico-aluminophosphate ($AlPO_4$-SiO_2-$FePO_4$) chains. The total porosity of unheated geopolymers decreases from 22 to 10% with increasing phosphoric acid concentration. The heterogeneity of pore diameter distribution enhances the thermal stability of geopolymers in term of strength loss and thermal shrinkage.

The maximum strength loss was 63 % and the highest thermal shrinkage 3% after heating geopolymers up to 1000 °C. The geopolymers produced with phosphoric acid concentration of 8 mol/L demonstrated superior thermal stability. Thus, that phosphate geopolymer is suitable for high temperature application up to 1000 °C.

5. Acknowledgements

6. References

[1]   J. Davidovits, Geopolymer Chemistry and Applications, 4th ed, 2015.

[2]   M.M. Yadollahi, A. Benli, R. Demirboğa, Effects of elevated temperature on pumice based geopolymer composites, Plast. Rubber Compos. 44 (2015) 226–237. doi:10.1179/1743289815Y.0000000020.

[3]   H.K. Tchakouté, C.H. Rüscher, S. Kong, E. Kamseu, C. Leonelli, Thermal Behavior of Metakaolin-Based Geopolymer Cements Using Sodium Waterglass from Rice Husk Ash and Waste Glass as Alternative Activators, Waste and Biomass Valorization. (2016). doi:10.1007/s12649-016-9653-7.

[4]   A. Elimbi, H.K. Tchakoute, M. Kondoh, J.D. Manga, J. Dika Manga, Thermal behavior and characteristics of fired geopolymers produced from local Cameroonian metakaolin, Ceram. Int. 40 (2014) 4515–4520. doi:10.1016/j.ceramint.2013.08.126.

[5]   S.A. Bernal, E.D. Rodríguez, R. Mejía De Gutiérrez, M. Gordillo, J.L. Provis, Mechanical and thermal characterisation of geopolymers based on silicate-activated metakaolin/slag blends, J. Mater. Sci. 46 (2011) 5477–5486. doi:10.1007/s10853-011-5490-z.

[6]   P.N. Lemougna, K.J.D. MacKenzie, U.F.C. Melo, Synthesis and thermal properties of inorganic polymers (geopolymers) for structural and refractory applications from volcanic ash, Ceram. Int. 37 (2011) 3011–3018. doi:10.1016/j.ceramint.2011.05.002.

[7]   P.N. Lemougna, U.F. Chinje Melo, M.P. Delplancke, H. Rahier, Influence of the activating solution composition on the stability and thermo-mechanical properties of inorganic polymers (geopolymers) from volcanic ash, Constr. Build. Mater. 48 (2013) 278–286. doi:10.1016/j.conbuildmat.2013.06.089.

[8]   D.L.Y. Kong, J.G. Sanjayan, K. Sagoe-Crentsil, Comparative performance of geopolymers made with metakaolin and fly ash after exposure to elevated temperatures, Cem. Concr. Res. 37 (2007) 1583–1589. doi:10.1016/j.cemconres.2007.08.021.

[9]   D.L.Y. Kong, J.G. Sanjayan, Effect of elevated temperatures on geopolymer paste , mortar and concrete, Cem. Concr. Res. 40 (2010) 334–339. doi:10.1016/j.cemconres.2009.10.017.

[10]   L. Le-ping, C. Xue-min, Q. Shu-heng, Y. Jun-li, Z. Lin, Preparation of phosphoric acid-based porous geopolymers, Appl. Clay Sci. 50 (2010) 600–603. doi:10.1016/j.clay.2010.10.004.

[11]   L. Le-ping, C. Xue-min, H. Yan, L. Si-dong, G. Si-yu, The phase evolution of phosphoric acid-based geopolymers at elevated temperatures, Mater. Lett. 66 (2012) 10–12. doi:10.1016/j.matlet.2011.08.043.

[12]   M. Khabbouchi, K. Hosni, M. Mezni, C. Zanelli, M. Doggy, M. Dondi, E. Srasra, Interaction of metakaolin-phosphoric acid and their structural evolution at high temperature, Appl. Clay Sci. 146 (2017) 510–516. doi:10.1016/j.clay.2017.07.006.

[13]   C. Nobouassia Bewa, H.K. Tchakouté, D. Fotio, C.H. Rüscher, E. Kamseu, C. Leonelli, Water resistance and thermal behavior of metakaolin-phosphate-based geopolymer cements, J. Asian Ceram. Soc.

6 (2018) 271–283. doi:10.1080/21870764.2018.1507660.

[14]   H. Celerier, J. Jouin, N. Tessier-Doyen, S. Rossignol, Influence of various metakaolin raw materials on the water and fire resistance of geopolymers prepared in phosphoric acid, J. Non. Cryst. Solids. 500 (2018) 493–501. doi:10.1016/j.jnoncrysol.2018.09.005.

[15]   J.N.Y. Djobo, L.N. Tchadjié, H.K. Tchakoute, B.B.D. Kenne, A. Elimbi, D. Njopwouo, Synthesis of geopolymer composites from a mixture of volcanic scoria and metakaolin, J. Asian Ceram. Soc. 2 (2014) 387–398. doi:10.1016/j.jascer.2014.08.003.

[16]   P.N. Lemougna, U.F. Chinje Melo, M.P. Delplancke, H. Rahier, Influence of the chemical and mineralogical composition on the reactivity of volcanic ashes during alkali activation, Ceram. Int. 40 (2014) 811–820. doi:10.1016/j.ceramint.2013.06.072.

[17]   J.N.Y. Djobo, A. Elimbi, H.K. Tchakouté, S. Kumar, Reactivity of volcanic ash in alkaline medium, microstructural and strength characteristics of resulting geopolymers under different synthesis conditions, J. Mater. Sci. 51 (2016) 10301–10317. doi:10.1007/s10853-016-0257-1.

[18]   Y. Chen, S.L. Brantley, Temperature- and pH-dependence of albite dissolution rate at acid pH, Chem. Geol. 135 (1997) 275–290. doi:10.1016/S0009-2541(96)00126-X.

[19]   A.C. McAdam, M.Y. Zolotov, T.G. Sharp, L.A. Leshin, Preferential low-pH dissolution of pyroxene in plagioclase-pyroxene mixtures: Implications for martian surface materials, Icarus. 196 (2008) 90–96. doi:10.1016/j.icarus.2008.01.008.

[20]   P. Reale, B. Scrosati, C. Delacourt, C. Wurm, M. Morcrette, C. Masquelier, Synthesis and Thermal Behavior of Crystalline Hydrated Iron(III) Phosphates of Interest as Positive Electrodes in Li Batteries, Chem. Mater. 15 (2003) 5051–5058. doi:10.1021/cm031107z.

[21]   M. Irfan Khan, H.U. and Teoh. K. Min, Khairun Azizli, Suriati Sufian, M.I. Khan, T.K. Min, K. Azizli, S. Sufian, H. Ullah, Z. Man, Effective removal of methylene blue from water using phosphoric acid based geopolymers: Synthesis, characterizations and adsorption studies, RSC Adv. 5 (2015) 61410–61420. doi:10.1039/c5ra08255b.

[22]   C.M. Guo, K.T. Wang, M.Y. Liu, X.H. Li, X.M. Cui, Preparation and characterization of acid-based geopolymer using metakaolin and disused polishing liquid, Ceram. Int. 42 (2016) 9287–9291. doi:10.1016/j.ceramint.2016.02.073.

[23]   M. Lassinantti Gualtieri, M. Romagnoli, A.F. Gualtieri, Preparation of phosphoric acid-based geopolymer foams using limestone as pore forming agent - Thermal properties by in situ XRPD and Rietveld refinements, J. Eur. Ceram. Soc. 35 (2015) 3167–3178. doi:10.1016/j.jeurceramsoc.2015.04.030.

[24]   J.N.Y. Djobo, A. Elimbi, H.K. Tchakouté, S. Kumar, Mechanical activation of volcanic ash for geopolymer synthesis: effect on reaction kinetics, gel characteristics, physical and mechanical properties, RSC Adv. 6 (2016) 39106–39117. doi:10.1039/c6ra03667h.

[25]   I. Basile-Doelsch, R. Amundson, W.E.E. Stone, C.A. Masiello, J.Y. Bottero, F. Colin, F. Masin, D. Borschneck, J.D. Meunier, Mineralogical control of organic carbon dynamics in a volcanic ash soil on La Réunion, Eur. J. Soil Sci. 56 (2005) 689–703. doi:10.1111/j.1365-2389.2005.00703.x.

[26]   M. Lassinantti Gualtieri, M. Romagnoli, S. Pollastri, A.F. Gualtieri, Inorganic polymers from laterite using activation with phosphoric acid and alkaline sodium silicate solution: Mechanical and microstructural properties, Cem. Concr. Res. 67 (2015) 259–270. doi:10.1016/j.cemconres.2014.08.010.

[27]   Y.S. Wang, J.L. Provis, J.G. Dai, Role of soluble aluminum species in the activating solution for synthesis of silico-aluminophosphate geopolymers, Cem. Concr. Compos. 93 (2018) 186–195. doi:10.1016/j.cemconcomp.2018.07.011.

[28]   C.S. Ray, X. Fang, M. Karabulut, G.K. Marasinghe, D.E. Day, Effect of melting temperature and time on iron valence and crystallization of iron phosphate glasses, J. Non. Cryst. Solids. 249 (1999) 1–16. doi:10.1016/S0022-3093(99)00304-X.

[29]   C.J.R.G. Oliver, F.C. Lovey, A. Caneiro, D.O. Russo, D.S. Rodríguez, F. Soldera, J.E. Fiscina, J.M. Rincón, Crystallization of iron phosphate glasses containing up to 19 wt.% UO2.67, J. Non. Cryst. Solids. 356 (2010) 2986–2993. doi:10.1016/j.jnoncrysol.2010.06.034.

[30]   N. Aliouane, T. Badeche, Y. Gagou, E. Nigrelli, P. Saint-Gregoire, Synthesis and phase transitions of iron phosphate, Ferroelectrics. 241 (2000) 255–262. doi:10.1080/00150190008224999.

The Effect of NaOH Concentration on the Mechanical and Physical Properties of Alkali Activated Fly Ash-Based Artificial Lightweight Aggregate

P. Risdanareni [1,2], K. Schollbach [3,4], J. Wang [5], N. De Belie [1]

[1] Magnel Laboratory for Concrete Research, Ghent University, Tech Lane Ghent Science Park, Campus A, Technologiepark Zwijnaarde 60, B-9052 Ghent, Belgium.

[2] Department of Civil Engineering, Faculty of Engineering, State University of Malang, Semarang Street 5 Malang 65145, Indonesia

[3] Tata Steel, R&D, Microstructure & Surface Characterization (MSC), P.O. Box 10.000, 1970 CA Ijmuiden, the Netherlands

[4] Department of the Built Environment, Eindhoven University of Technology, 5612AP Eindhoven, The Netherlands

[5] Department of Civil Engineering, Xi'an Jiaotong University, Yanxiang road 99, 710029 Xi'an, China

Abstract

Aggregate is a non-renewable material that takes up a large portion of a concrete mixture. Replacing this material with artificial lightweight aggregate (LWA) that is generated from an industrial by-product such as fly ash, will significantly reduce the impact on the environment. Alkali-activation is a promising technique to generate LWA as it proofed to provide better properties to the LWA in comparison to the use of a Portland cement – fly ash binder. However, only limited studies can be found on applying this technique to produce LWA. Furthermore, the concentration of alkali activators such as NaOH, is an important parameter that needs to be investigated in order to produce LWA with excellent properties. Thus, in this research the NaOH concentration was varied (4 M, 6 M or 8 M) in order to obtain the optimum for producing LWA. Later on, the produced LWA with a diameter of 2-4 mm was used to replace the fine aggregates in the mortar. The mechanical and physical properties of the produced LWA were investigated, such as water absorption, density, particle size distribution, crushing resistance, and mineralogy and the compressive strength of the resulting mortar. The results showed that a maximum compressive strength of 64 N/mm^2 at 28 days could be achieved by mortar containing LWA 8M. Increasing the concentration of NaOH up to 8M had no significant effect on the water absorption value, particle distribution, density and crushing resistance of LWA. The result from Quantitative X-Ray Diffraction (QXRD) revealed that there is also no significant difference in the quantity of amorphous phase formed in the LWA with increasing NaOH concentration. This finding suggests that alkali-activated fly ash LWA can in the future be synthesized with a lower concentration of NaOH starting from 4M.

Keywords: lightweight aggregate, fly ash, alkali-activated, NaOH concentration

1.　　Introduction

The global consumption of construction aggregate exceeded 48.3 billion tons per year in 2015 and is expected to increase by 5.2% annually [1]. On the other hand, by 2010 the global production of fly ash around the world was around 780 million metric ton and is expected to increase with 1.6% annually [2]. Based on the same report, around 53% of this ash is already used as supplementary material in cement production. Furthermore, as around 70% of the concrete mixture is the aggregate, reducing natural aggregate consumption by replacing it with artificial aggregate generated from waste material such fly ash will be an effective way to reduce the amount of non-renewable material consumption as the concrete mixture.

Several efforts on employing fly ash as raw material to produce pelletized lightweight aggregate (LWA) with cement, glass powder or clay as a binder have already been conducted by researchers [3–5]. Researchers also reported that several aspects such as hardening method, curing method, and pelletizing procedure affected the properties of pelletized LWA [4, 6, 7]. However, almost all the reports are focused on optimizing the properties of LWA which used clay or cement as a binder [3-7]. Only limited studies can be found on using alkali activation of fly ash in producing LWA, although this technique proved to improve the mechanical and physical properties of pelletized aggregate [8-9].

Based on the literature study, the alkali activator solution plays an important role in geopolymerization as silica and alumina dissolvent [10]. The type of alkali solution [10], the concentration of alkali activator [11], [12], the ratio between binder and solution [13], and the curing regime [11] significantly affect the geopolymerization. Based on the literature, NaOH with the concentration range of 8-12 Molars gives optimal mechanical properties in concrete and mortar application [11, 12, 14]. In the literature, Geetha et al found that the lower concentration of NaOH needed to synthesize geopolymer LWA is 8 molar [9]. Increasing the molarity of NaOH proofed to reduce water absorption and increase the strength of LWA. However, a higher concentration of NaOH caused workability issues of fresh concrete that lead to a decrease in the mechanical properties of concrete [12, 15]. On the other hand, Gorhan et al. found different behaviour of geopolymer paste in mortar application. They found that the optimum NaOH concentration for fly ash based geopolymer is 6 molar [14]. In artificial aggregate application, the ratio between liquid/solid needed is not as high as in mortar or in concrete, a high concentration of NaOH will significantly decrease the workability of wet LWA. Hence, the effect of different concentrations of NaOH for alkali-activated LWA production is studied, as lower concentrations will also decrease the LWA production cost.

Summarizing, the aim of this study is to find a suitable NaOH concentration that gives a positive effect on the properties of alkali-activated fly ash LWA. In order to avoid the workability issue from the high concentration of NaOH, a low concentration of NaOH in the range of 4 to 8 molars was chosen in this study. The properties of LWA such as water absorption, specific density, particle size distribution, crushing value and its mineralogy were investigated. Furthermore, the LWA with the fraction of 2-4 mm was applied into mortar as a natural fine aggregate replacement to investigate its effect on the mechanical properties of the resulted mortar.

2.　　Methodology

2.1　　Materials

Fly ash (FA) from a thermal power plant in the Netherlands was used as a precursor to produce lightweight aggregate (LWA). The fly ash was sieved until passing the sieve of 125 micron. The chemical composition of FA is presented in Table 1. Based on the data in Table 1, it can be seen that the fly ash used in this research is rich in silica and alumina. Therefore, this material meets the requirement to become an alkali-

activated binder.

A liquid form of sodium silicate (Na_2SiO_3) which contains 26.3% silica, 7.9% sodium oxide, and 65.8% water and a powder form of sodium hydroxide (NaOH) with a purity of 97-98% was used as the alkali activator (AA). In order to obtain varied desired NaOH concentration, the NaOH was dissolved in the demineralized water until reaching the concentrations of 4, 6, and 8 Molar, respectively. Later on, sodium silicate and sodium hydroxide were mixed with a weight ratio of 1.5. Subsequently, the mixed alkali activator was left in room temperature conditions for at least 24 hours before use.

For mortar application, cement type I 52.5 N from Holcim was used as a binder while river sand with a fraction of 0/2 mm was used as the fine aggregate.

Table 1. Chemical Composition of fly ash

Compound	CaO	SiO$_2$	Al$_2$O$_3$	Fe$_2$O$_3$	K$_2$O	MgO	CuO	ZnO	SO$_3$	P$_2$O$_5$	TiO$_2$	LOI
% by Mass	3.790	57.400	26.167	5.987	1.877	1.433	0.015	0.023	0.982	0.881	1.127	0.319

2.2 Methods

2.2.1 Pelletizing Method

LWA was produced by agglomeration technique using a stainless steel pan granulator with a diameter of 500 mm and a depth of 95 mm. The pan granulator parameters that were chosen based on research by Baykal, *et al.* (2000), which are a speed of 60 rpm, a slope of 48° and pelletizing time of 20 minutes [7]. The weight ratio between fly ash and alkali activator of 0.25 was used based on previous research [8, 16, 17]. Firstly, fly ash was added into the pan, followed by adding alkali activator by means of spraying for about 10 minutes. During the pelletizing process, the powder form of fly ash turned into granules after being bonded with alkali activator liquid. Finally, due to gravity and the movement of the pan, the granules that had reached a stable form fell out from the pan. After that, wet granules were dried in curing room which have temperature of 28ºC and relative humidity 95 ±5 % for 24 hours. Dried LWA were sieved using sieve 2 mm in order to get LWA with particle size < 2 mm. Later on, the sieved LWA that have particle size < 2 mm were stored in sealed plastic bag in the curing room for 28 days before being used.
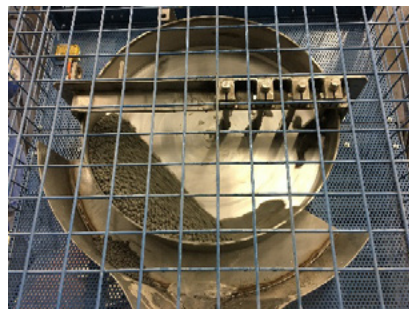
Fig 1. Pan granulator

2.2.2 Physical Properties Testing of LWA

• Mass Density and Water Absorption Test

Water absorption over 24 hours (WA$_{24}$) of all LWA was performed by following the guidelines of NBN EN 1097-6. The apparent particle density ρ_a (kg/m^3), the saturated surface dry (SSD) density ρ_{SSD} (kg/m^3) and the relative oven dried density ρ_{rd} (kg/m^3) were measured according to the same standard.

• Particle Size Distribution Test

Particle size distribution of all LWA was determined according to Belgian standard NBN EN 12620. The

standardized sieves column with the size of : 63, 45, 40, 31.5, 22.4, 20, 16, 14, 12.5, 10, 8, 6.3, 4, 2, 1, 0.5, 0.25, 0.125 and 0.063 mm were used. The data obtained from the cumulative percentage of material passing through each sieve were analyzed and plotted to a particle size distribution curve.

- Crushing Resistance Value

The strength of aggregates can be measured from its crushing resistance value. This test was performed by following Belgian standard NBN B11-205. Firstly, the dried aggregate sample was added into a metal cylinder mold with an inner diameter of 150 mm. After that, the no-friction plunger was put into the mold which was then loaded with 400 kN in 4 min and the load was maintained for 2 minutes before unloaded. Finally, the crushed aggregates were sieved with sieve number 2 mm in order to get data of aggregates that have a fraction < 2 mm. The crushing resistance value of aggregate was the mass ratio between the crushed aggregate that have a fraction <2 mm over the initial sample before loading.

- Mineralogy of LWA

X-ray diffraction (XRD) was used to determine the mineralogy of LWA while quantitative XRD (QXRD) was performed using Rietveld analysis. Firstly, around 10 wt% internal standard, in this case, ZnO was added into aggregate samples. Later on the mixed aggregate and ZnO were ground in a Mc Crone mill (Retsch) to a size of around 50 microns. The measurement was done with a D4 (Bruker) using a Co-Tube and equipped with a Lynx Eye detector. The settings were fixed divergence slits (0.5°), 0.04 rad Soller slits and a step size of 0.02.

2.2.3 Mortar Application

- Mortar Mix Design and Production

Mortar specimens were produced according to EN NBN 196 standard. The material needed for producing three mortar prisms with the size of 40x40x160 mm^3 is presented in Table 2. In this research, LWA with the fraction of 2/4 was used as a natural fine aggregate replacement in producing mortar. 16 % of the total volume of fine aggregate was replaced with LWA, while water to cement ratio of 0.5 was used. This aggregate replacement percentage was chosen as river sand has the same fraction composition.

As LWA has high water absorption, LWA were treated to achieve SSD condition before use in order to limit the water absorption during mixing. Hence, the mass of LWA in oven dried condition (OD) and entrained water needed to achieve SSD condition of LWA are presented in Table 2.

Table 2. Mix design of prisms mortar sample

Type	LWA OD 2/4 (g)	Entrained Water (g)	Sand 2/4 (g)	Sand (g)	Cement (g)	Water (g)
Reference	0	0	220	1130	450	225
FA 4M	120	34	0	1196	450	225
FA 6M	122	32	0	1196	450	225
FA 8M	125	29	0	1196	450	225

- Compressive Strength

The fresh mortar samples were cured in curing room which has temperature of 28°C and relative humidity (RH) of 95 ±5% for 24 hours before being demolded. The compressive strength of the mortar prisms was determined according to EN NBN 196 standard. This test was conducted after 7, 14 and 28 days of the samples that were cured in the curing room which has temperature of 28°C and RH of 95±5%. The value of this test was determined by averaging the value of 3 replicated samples.

3.   Results and discussion

3.1   Mass Density and Water Absorption

The mass, density and water absorption of all LWA are presented in Table 3. Based on Table 3, it can be seen that FA 8M has the highest apparent, oven dried and SSD density following by FA 6M and FA 4M. The apparent density of LWA was in the range of 2.2-2.3, oven dried density was in the range of 1.4 to 1.5 and SSD density of all specimens are 1.8. To be noted, artificial aggregate in the literature that uses cement as a binder has an apparent density in the range of 2.0-2.3, and 1.6-1.7 for sintered fly ash based geopolymer LWA [8, 17].

The relationship between apparent density and is oven dried density indicated the porosity of the material. The open porosity of all samples is in the range of 33-34 %; this result is similar with the research by Baykal *et al.* which reports open porosity in the range of 31-34 % for cold bonded fly ash LWA [7].

The water absorption of all samples is in the range of 22-23 %. This result is similar to previous literature that uses cement as a binder which has a water absorption in the range of 18.3-46.8 % [7, 18, 19]. However, the water absorption value obtained from this research is still quite high compared to geopolymer bottom ash LWA that has water absorption in the range of 10-12% [9]. This is due to a different size of LWA that have been tested, Geeta *et al.* only used aggregate with the size of 10-12.5 mm for water absorption tests [9]. The size of the aggregates is directly proportional to its strength and density [19]. In addition, LWA with a denser structure normally contains less pores which leads to lower water absorption [16].

Based on the results of the density and water absorption test of LWA, it can be concluded that increasing NaOH concentration proved to slightly reduce the water absorption and the open porosity of LWA and increase its density. The alkali solution acts as silica and alumina dissolvent of fly ash in geopolymer reaction, thus with a higher amount of OH⁻ in the highly concentrated NaOH, the more stable geopolymer formed [10].

Table 3. Mass Density and Water Absorption

Test	FA 4M	FA 6M	FA 8M
Apparent particle density ϱ_a (kg/m³)	2.2 ±0.05	2.2±0.01	2.3±0.01
Oven Dried Density ϱ_{rd} (kg/m³)	1.4±0.04	1.5±0.01	1.5±0.01
SSD particle density ϱ_{ssd} (kg/m³)	1.8±0.01	1.8±0.01	1.8±0.07
(ϱa-ϱrd)/ϱa x 100%	34.7 ±2.1	34.1±0.7	33.4±0.2
Water absorption (%)	23.9±1.8	23.2±1.1	22.1±0.3

3.2   Particle Size Distribution

Based on particle size distribution data that are displayed in Figure 2, FA 6M has more fine particles compared to the others. The FA 6M sample has approximately 9% pellets that have a diameter less than 2 mm, while FA 8M has 6% and FA 4M has 2%. For all samples, there is only less than 5% of pellets that have a particle size bigger than 10 mm. These big pellets usually have irregular shape due to not being perfectly compacted or sticking to each other during the pelletizing process. This result is quite similar with previous research by Tang *et al.* which has approximately 7% of pellets with a diameter less than 2 mm and 5% pellets with a diameter bigger than 10 mm for cold bonded bottom ash aggregate [16].

There is only a slight difference between the curve of FA 6M and 8M samples. However, according to NBN EN 12620 about the definition of minimum and maximum aggregate size, FA 8M and FA 4M meet the requirements of an aggregate 2/10, while FA 6M is classified as aggregate 2/8. Moreover, it can also

be noted that all of the LWA have less big particles compare to natural aggregate with the fraction of 2/8.

From the result above, it can be concluded that NaOH concentration has a slight effect on the pellets size according to the similarity of the particle size distribution of all LWA. This result has a good agreement with previous research by Shivaprasad *et al.* who found that the formation of geopolymer pellets depends more on liquid content rather than the Na_2O content [8].
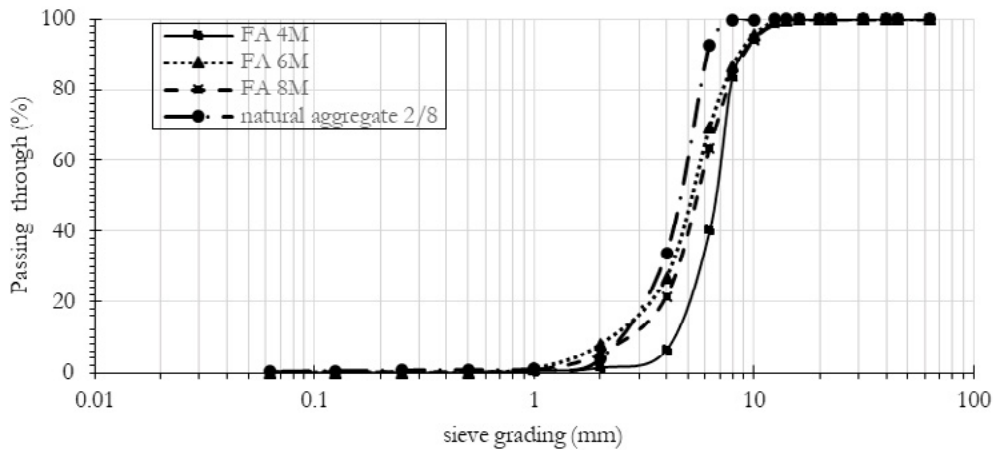
Fig.2 Particle size distribution of LWA

3.3 Crushing Resistance Value

Based on the result presented in Table 4, it can be concluded that increasing the molarity of NaOH up to 6 Molars brought a positive impact to aggregate strength. However, there is only a less than 5% difference in crushing resistance value among all samples. This result is entirely unexpected, as a higher concentration of NaOH was expected to give a higher crushing value. This slight difference was presumably due to a difference in the particle size of LWA. Furthermore, as some of the LWA were compacted after being tested, it is quite difficult to determine its crushed part.

Based on the literature, it can be noted that the crushing strength of LWA increases with the increase of particle size [19]. However, LWA in this research has quite a small fraction compared to LWA in the literature which mostly has a fraction of 4/16. Hence, it is quite difficult to find a suitable method to determine its crushing value [3, 4].

Compared to bottom ash and limestone aggregate, the crushing resistance value of this LWA is almost equal to limestone aggregate which has a particle size of 2/6 and a crushing strength of 63.8% [20]. Due to the different standard method that has been used to determine the strength of aggregates, it is quite difficult to compare the result obtained in this research with another LWA in the literature.

Table 4. Crushing Resistance (CR) value of LWA

Type	CR Value (%)
FA 4M	61.4 ±0.2
FA 6M	62.8 ±0.7
FA 8M	60.0 ±0.9

3.4 Mineralogy of LWA

Based on Quantitative X-Ray Diffraction (QXRD) analysis results displayed in Figure 4, the main phases in LWA are Amorphous (82-83%), Quartz (3.6-4%), Mullite (6.2-6.9%), Magnesioferrite (2.1-2.2%), Gaylussite (1-2.2%), and Hematite (1-1.2%). It can also be seen in Figure 4, that geopolymerization proved

to significantly dissolve Quartz and Mullite in fly ash into Amorphous gel. This phenomenon is indicated by the decreasing quantity of Quartz and Mullite and increasing quantity of amorphous phase in the resulting LWAs sample. However, the Rietveld method that has been used in this study cannot determine which part of the amorphous content is the alumino-silicate (N-A-S-H) gel or the unreacted glassy fly ash.

There is no significant difference in the quantities of amorphous and crystalline phases among all of the LWA samples. This result is not in accordance with the initial expectation that increasing the concentration of NaOH in the mixture will lead to increase the amorphous phase in LWA as there will be more OH⁻ to dissolve Quartz and Mullite in fly ash into alumina-silica gel [10]. However, a similar result was also obtained in the literature which investigated the microstructural properties of dry mixed geopolymer with low alkali activator concentration that obtained similar total amount of non-crystalline phase [21].

Based on previous research on QXRD of alkali activated low calcium fly ash, increasing the amount of amorphous product will lead to increase the strength of the geopolymer paste [22]. However, in this study, there is no trend occurring between the NaOH concentration and the strength of LWA, and there is no significant difference in amount of amorphous among all the samples. Therefore, it is quite difficult to draw conclusions in describing the correlation between the amorphous phase and the strength of LWA in this study.

As higher concentrations of NaOH probably only change the composition of the N-A-S-H gel, tests with lower concentration of NaOH (2M or less) will allow to obtain the best NaOH concentration to activate fly ash-based LWA.
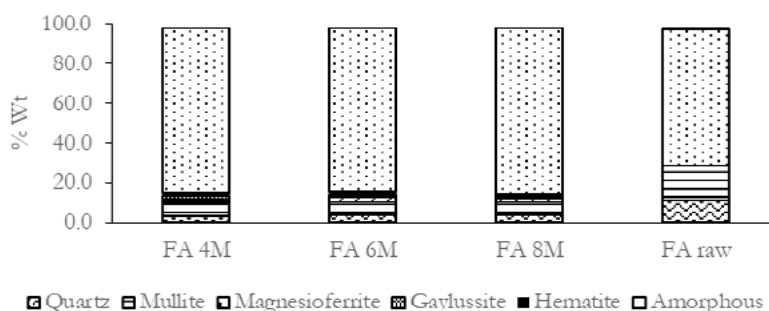
Fig. 4 QXRD analysis of LWA

3.5 Mortar Application

3.5.1 Compressive Strength

Based on mortar compressive strength data displayed in Figure 5, FA 8M provided the highest compressive strength at an age of 28 days followed by FA 6M and FA 4M. Until the age of 14 days, the FA 8M sample did not show high compressive strength.

Replacing 16% by volume of fine natural aggregate with fly ash LWA caused a reduction in compressive strength of the resulting mortar. The sample containing FA 8M LWA had the lowest compressive strength reduction. It has less than 5% reduction of strength with 16% replacement ratio. Compared to cold bonded and geopolymer LWA in the literature, this aggregate gives better mechanical properties. For example, cold bonded bottom ash aggregates have a reduction in the strength of 25% with a 50% replacement ratio [16]. Compared to geopolymer sintered aggregate with a NaOH concentration of 10 molars which caused a 16% strength reduction with 50% replacement rate, this LWA still had acceptable strength reduction [23].
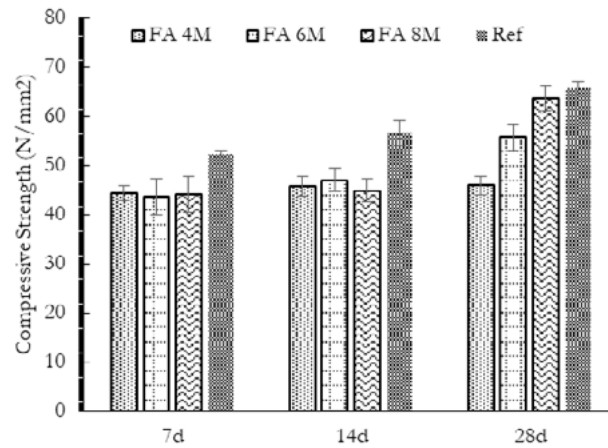
Fig. 5. Compressive Strength of mortar

4.   Conclusions

This paper presents the effect of NaOH concentration on mechanical and physical properties of fly ash-based alkali activated LWA. From the results obtained in this study, the following conclusions can be drawn :

1. The mass density of LWA increased along with the increasing NaOH concentration while increasing NaOH concentration proved to slightly reduce the water absorption of LWA.

2. The concentration of NaOH has a slight effect on the particle size distribution of LWA.

3. There is some unexpected trend occurring in crushing resistance strength, FA 6M has a higher CR value than FA 8M. The difficulties to determine the real crushed part of LWA after CR test might cause this irregular trend.

4. Based on QXRD analysis, increasing the NaOH concentration have no significant effect on the quantity of the Amorphous phase formed.

5. The maximum compressive strength of 64 N/mm^2 and the strength reduction less than 5% could be achieved by mortar containing LWA 8M.

5.   Acknowledgment

6.   Reference

[1]   Freedonia, "World Construction Aggregates - Industry Study with Forecasts for 2015 & 2020," *Free. Gr.*, p. 6, 2012.

[2]   C. Heidrich, H. Feuerborn, and A. Weir, "Coal Combustion Products : a global perspective," *World Coal Ash Conf.*, p. 17, 2013.

[3]   M. Gesoğlu, T. Özturan, and E. Güneyisi, "Effects of fly ash properties on characteristics of cold-bonded fly ash lightweight aggregates," *Constr. Build. Mater.*, vol. 21, no. 9, pp. 1869–1878, 2007.

[4]   E. Güneyisi, M. Gesoğlu, Ö. Pürsünlü, and K. Mermerdaş, "Durability aspect of concretes composed of cold bonded and sintered fly ash lightweight aggregates," *Compos. Part B Eng.*, vol. 53, pp. 258–266, 2013.

[5]   I. Kourti and C. R. Cheeseman, "Properties and microstructure of lightweight aggregate produced from lignite coal fly ash and recycled glass," *Resour. Conserv. Recycl.*, vol. 54, no. 11, pp. 769–775, 2010.

[6]   R. Manikandan and K. Ramamurthy, "Effect of curing method on characteristics of cold bonded fly ash aggregates," *Cem. Concr. Compos.*, vol. 30, no. 9, pp. 848–853, 2008.

[7]   A. Gu, "Utilization of fly ash by pelletization process ; theory , application areas and research results," vol. 30, pp. 59–77, 2000.

[8]   K. N. Shivaprasad and B. B. Das, "Determination of optimized geopolymerization factors on the properties of pelletized fly ash aggregates," *Constr. Build. Mater.*, vol. 163, pp. 428–437, 2018.

[9]   S. Geetha and K. Ramamurthy, "Properties of geopolymerised low-calcium bottom ash aggregate cured at ambient temperature," *Cem. Concr. Compos.*, vol. 43, pp. 20–30, 2013.

[10]   H. Xu and J. S. J. Van Deventer, "The geopolymerisation of alumino-silicate minerals.," 2000.

[11]   D. Hardjito, "Studies on Fly Ash-Based Geopolymer Concrete," *Curtin Univ. Technol.*, no. November, p. 94, 2005.

[12]   R. M. Hamidi, Z. Man, and K. A. Azizli, "Concentration of NaOH and the Effect on the Properties of Fly Ash Based Geopolymer," *Procedia Eng.*, vol. 148, pp. 189–193, 2016.

[13]   C. Y. Heah *et al.*, "Study on solids-to-liquid and alkaline activator ratios on kaolin-based geopolymers," *Constr. Build. Mater.*, vol. 35, pp. 912–922, 2012.

[14]   G. Görhan and G. Kürklü, "The influence of the NaOH solution on the properties of the fly ash-based geopolymer mortar cured at different temperatures," *Compos. Part B Eng.*, vol. 58, pp. 371–377, 2014.

[15]   P. Risdanareni, J. J. Ekaputri, and Triwulan, *The influence of alkali activator concentration to mechanical properties of geopolymer concrete with trass as a filler*, vol. 803. 2015.

[16]   P. Tang, M. V. A. Florea, and H. J. H. Brouwers, "Employing cold bonded pelletization to produce lightweight aggregates from incineration fine bottom ash," *J. Clean. Prod.*, vol. 165, pp. 1371–1384, 2017.

[17]   N. U. Kockal and T. Ozturan, "Characteristics of lightweight fly ash aggregates produced with different binders and heat treatments," *Cem. Concr. Compos.*, vol. 33, no. 1, pp. 61–67, 2011.

[18]   P. Gomathi and A. Sivakumar, "Accelerated curing effects on the mechanical performance of cold bonded and sintered fly ash aggregate concrete," *Constr. Build. Mater.*, vol. 77, pp. 276–287, 2015.

[19]   M. Gesoğlu, E. Güneyisi, R. Alzeebaree, and K. Mermerdaş, "Effect of silica fume and steel fiber on the mechanical properties of the concretes produced with cold bonded fly ash aggregates," *Constr. Build. Mater.*, vol. 40, pp. 982–990, 2013.

[20]   P. Van den Heede *et al.*, "Sustainable high quality recycling of aggregates from waste-to-energy, treated in awet bottom ash processing installation, for use in concrete products," *Materials (Basel).*, vol. 9, no. 1, pp. 1–24, 2016.

[21]   Z. Chen, J. S. Li, B. J. Zhan, U. Sharma, and C. S. Poon, "Compressive strength and microstructural properties of dry-mixed geopolymer pastes synthesized from GGBS and sewage sludge ash," *Constr. Build. Mater.*, vol. 182, pp. 597–607, 2018.

[22]   G. V. P. Bhagath Singh and K. V. L. Subramaniam, "Quantitative XRD study of amorphous phase in alkali activated low calcium siliceous fly ash," *Constr. Build. Mater.*, vol. 124, pp. 139–147, 2016.

[23]   P. Risdanareni, J. Jaya Ekaputri, I. Maulidiyawati, and P. Puspitasari, "Mechanical properties of concrete composed of sintered fly ash lightweight aggregate," in *MATEC Web of Conferences*, 2018, vol. 195.

Performance evaluation of functional alkali activated lightweight composites produced with an eco-silica source based activator

X. Gao [1], Q.L. Yu[2]

[1] School of Civil Engineering and Architecture, Wuhan University of Technology, Wuhan 430070, China

[2] Department of the Built Environment, Eindhoven University of Technology, P.O. Box 513, 5600 MB, Eindhoven, The Netherlands

Abstract

Alkali activated slag-fly ash lightweight composites with moderate densities between around 1200 and 1500 kg/m^3 are prepared and characterized in this study. An eco-olivine nano-silica is applied to prepare sustainable silicate based activators to replace commercial sodium silicates. Na_2O contents of 2.0, 3.5 and 5.0 wt.% are investigated in order to reach a suitable balance between performance, costs and application. The results show the positive effect of density and Na_2O content on strength, while strength increment between Na_2O dosage of 3.5% and 5.0% are limited. The reduction of Na_2O content shows a dramatic delay of the reaction process up to around 3 d. The thermal conductivity and acoustical absorption properties of the lightweight products are characterized. A calculation on the carbon footprint shows an evident advantage of using alkali activated materials to replace Portland cement, also the utilization of olivine nano-silica further reduces the carbon emission of the activator by around 25%.

Keywords: alkali activation; eco-nano-silica; thermal properties; acoustic absorption; carbon emission.

1.   Introduction

Lightweight concrete has been widely applied as both structural and non-structural components in a wide range of weights and strengths for various applications, due to its properties such as low density, good thermal insulation and fire resistance. In addition, Portland cement is commonly used as binding material for lightweight concrete, but its production is responsible for around 7% of the global carbon emissions and high energy costs. In order to reduce the negative environmental impacts, the development of sustainable alternatives such as alkali activated materials has been investigated because of the excellent mechanical properties, durability and thermal resistance together with low energy and carbon costs. Some efforts have also been spent on applying alkali activated materials in producing lightweight products; including for instance the study of design methodologies of ultra-lightweight geopolymers by applying the particle packing approach, the effect of key factors such as suitable ratios between binder, activator and aggregates [1]; the development of lightweight geopolymers with foaming agent especially for thermal insulating properties [2]; investigating the relations between density, mechanical properties and thermal conductivity of geopolymers with medium to low densities [3-5]; the utilization of different alkali binders and unconventional aggregates [6-8].

In alkali activated materials, the activator plays an important role on the activation process by providing necessary alkalinities for the decomposition of raw materials and formation of reaction products. The

commonly used activators are alkali hydroxides, silicates, carbonates, sulfates, aluminates or oxides; and it is widely accepted that silicate based ones usually result in ideal mechanical properties and relatively low porosity [9]. The silicate based activator exhibits advantages by providing the alkaline environment continuously and moderately, also the additionally provided silicates from the activator will participate into the reaction products and lead to a refined microstructure, and sufficient content of M_2O promotes the activation efficiency while exceeding dosage show limited further contribution. However, the primary drawback of silicate based activators is its negative environmental impact. The commercial process of sodium silicate production includes the melting of sodium carbonate and quartz sand around 1400 to 1500 °C with carbon release of above 400 kg/ton [10]. In order to achieve a more eco-friendly binder system, a green olivine nano-silica is applied as alternative silica source to prepare activator solutions in this study. The olivine nano-silica is produced by dissolving olivine stone in acid under temperatures lower than 95 °C, and this process shows advantages in carbon emission, energy consumption and total costs [11]. Therefore an alkali activated product with further reduced overall environmental impacts can be expected.

The objective of this study is to evaluate an eco-silicate source based alkali activator in designing lightweight composites, using blended alkali activated binder. The lightweight composites are designed with the aim to have moderate densities together with excellent mechanical, thermal and acoustic properties. The effect of activator dosages, addition of lightweight aggregates on early age reaction is investigated by using isothermal calorimeter. The mechanical properties, thermal conductivity and sound absorption properties are evaluated and the effect of the alkali content on these properties is investigated.

2. Methodology

2.1 Materials

The powder raw materials used in this work are blast furnace slag and Class F fly ash, their major chemical compositions are shown in Table 1. Commercial lightweight aggregates produced from natural expanded silicate with three particle sizes are applied: 0.5-1 mm, 1-2 mm and 2-4 mm, with particle densities of 600, 550 and 500 kg/m³, respectively. CEN standard sand is also used as fine aggregate. Analytical sodium hydroxide and laboratory prepared olivine nano-silica (19.04% SiO_2 and 80.96% H_2O by mass) were used to produce alkali activators. The olivine nano-silica was produced by dissolving olivine in acid at low temperatures, followed by a washing and filtering process [12,13]. Desired activator parameters were obtained by mixing calculated dosage of sodium hydroxide, olivine nano-silica and distilled water.

Table 1 Mix proportions of alkali-activated slag-fly ash composites (kg/m³)

Sample	Precursors			Activator			Sand	Lightweight aggregates		
	Slag	Fly ash	Nano-s	NaOH	H_2O	0-2	2-4	1-2	0.5-1
D15-5.0	384	96	170.8	30.9	77.7	370	200	150	30
D15-3.5	384	96	119.6	21.7	119.1	380	200	150	30
D15-2.0	384	96	68.3	12.4	170.7	390	200	150	30
D12-5.0	384	96	170.8	30.9	77.7	0	240	180	30
D12-3.5	384	96	119.6	21.7	119.1	10	240	180	30
D12-2.0	384	96	68.3	12.4	170.7	20	240	180	30
D14-3.5	384	96	119.6	21.7	119.1	260	230	140	30
D13-3.5	384	96	119.6	21.7	119.1	135	245	150	30

2.2   Sample preparation and testing methods

Three levels of equivalent Na_2O content were used in this study: 2.0%, 3.5% and 5.0% (by mass of the binder). A fixed activator modulus of 1.4 and a slag/fly ash mass ratio of 8/2 were used based on the previous experiences. Mixtures are designed to have oven dry densities between 1200 and 1500 kg/m^3 according to EN 206-1. The detailed mix proportions are presented in Table 2, for instance, sample with the label of D15-5.0 means it was designed to have a density level of 1500 kg/m^3 and a Na_2O content of 5.0%. Specimens were prepared and poured into molds of 40 x 40 x 160 mm^3, then covered with a plastic film to prevent the moisture loss. All specimens were demolded after 24h of curing and cured at room temperature and a relative humidity of 95% until testing age.

The compressive strength was determined according to EN 196-1. Samples were tested at the ages of 7 and 28 d, respectively. The early age hydration heat release was investigated by an isothermal calorimeter with TAM Air, Thermometric. Measurements were carried out for 72 h under a constant temperature of 20 °C. The thermal conductivity (k) and the mass heat capacity (c) were measured by using a heat transfer analyser (ISOMET 2104). The acoustic absorption coefficient was measured according to EN 10534-2.

3.   Results and discussion

3.1   Compressive strength

The 7 and 28 d compressive strength of samples with different density levels and a Na_2O content of 3.5% are shown in Figure 1. The relations between the oven dry density and strength are briefly depicted. It can be seen that as the density decreases, there is an obvious reduction in strength at both 7 and 28 d. The highest 28 d strength reaches 30.7 MPa in mixtures with a density of 1471 kg/m^3, and it gradually reduces to 20.6 MPa in samples with a density of 1163 kg/m^3. Considering the fact that those mixtures are having the same binder content, the reduced compressive strength is mainly attributed to the replacement of normal sand by lightweight aggregates, and a less overall capacity of the aggregates against compressive loading is resulted. The 7 d strengths share a similar tendency with the 28 d's. The 7 d compressive strengths shown in Figure 1 are all above 88% of the 28 d strength. This is because of the nature of the alkali activated binder system and the ceiling effect of the lightweight aggregates, which presents a relatively fast reaction process and exhibits large percent of the strength at early ages [14].

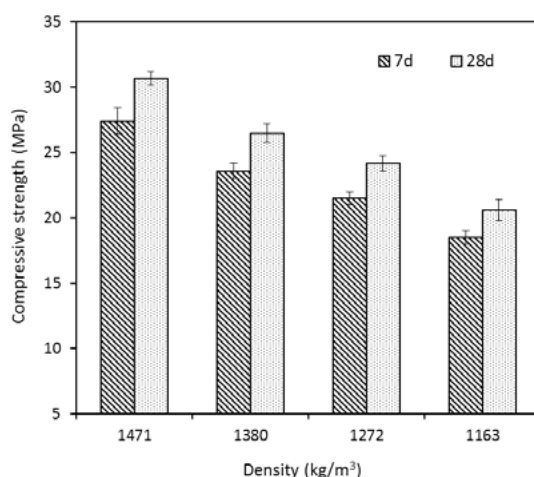Fig. 1 Compressive strength of lightweight composites with different densities

Figure 2 depicts the effect of the equivalent Na_2O content on 28 d compressive strength of mixtures with two density levels: 1500 and 1200 kg/m^3, represented with sample label of D-15 and D-12 in the figure. As can be seen in Figure 2 that there is an obvious increment of strength when increasing the Na_2O content

from 2.0% to 3.5%, and the increase of strength exhibits a limited scale when further increasing the Na_2O content to 5.0%.

This phenomenon reveals that both Na_2O content and density show an important influence on strength. On the one hand, increasing the alkalinity (Na_2O %) will promote the activation of the binder that consequently leads to a higher strength from the aspect of the binder matrix; while on the other hand, the usage of lightweight aggregate limits the strength development by the relatively low crushing strength of the aggregate.
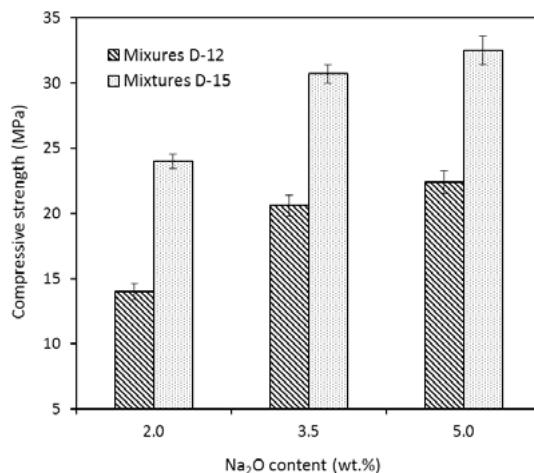
Fig. 2 Compressive strength of lightweight composites with different Na_2O contents

3.2 Reaction kinetics

The isothermal calorimeter test was performed on mixtures with the Na_2O content of 2.0%, 3.5% and 5.0%, respectively, and lightweight aggregates were added with an aggregate/binder ratio of 0.8, in order to evaluate their effect on the early age reaction. Figure 3 illustrates the normalized heat flows of samples with and without lightweight aggregates during the first 6 d; and shows that the mixtures with a Na_2O content of 5% exhibit a main reaction peak at around 16 h, with a peak intensity of 1.35 mW/g. The induction stage shows an induction period between around 6 and 10 h, followed by an evident increase of heat flow representing the intensive chemical reaction.

When reducing the Na_2O content to 3.5%, a significantly retarded reaction process can be observed. The induction period appears at around 9 to 22 h, the beginning of this stage is 3 h later than the one in sample with a Na_2O content of 5%, also the duration of this stage is more than 3 times longer. The location of the main reaction peak is also delayed to 37 h, which is 21 h later than the 5% Na_2O mixtures. Besides, the peak intensity is reduced to 0.63 mW/g and the deceleration period exhibits a more moderate reduction of heat release. A further lowered Na_2O dosage of 2.0% results in a dramatic delay of the reaction process.

Fig. 3 Normalized heat releases of AA slag-fly ash lightweight composites

3.3 Thermal conductivity
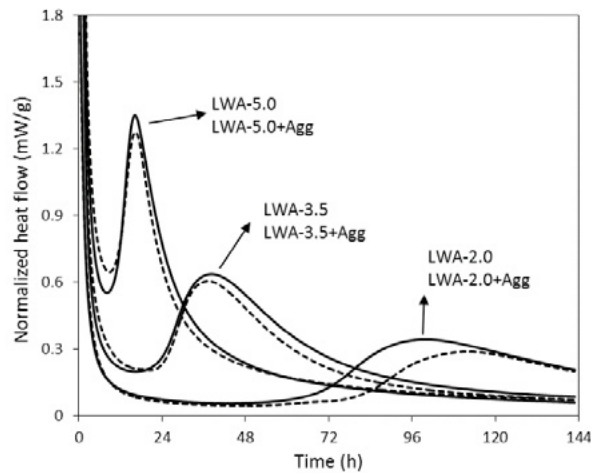
In terms of the building materials, a low thermal conductivity contributes to an enhanced indoor thermal comfort, saving the energy cost and preventing the fire caused collapses; while lightweight concrete products based on alkali activated materials are capable of achieving those requirements with a further lowered environmental impact. Figure 4 shows the thermal conductivity of samples with a Na_2O content of 3.5% and different density levels used in this study, and a comparison with the available literature.
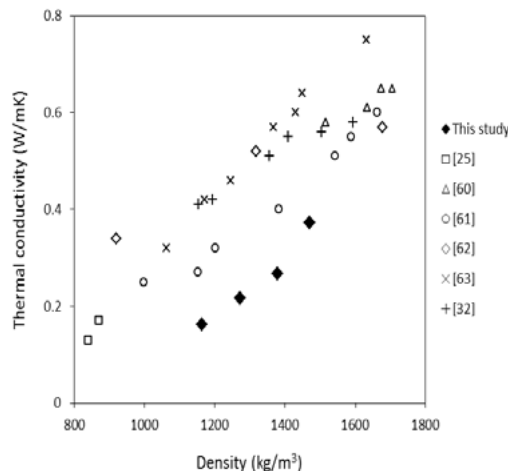
Fig. 4 Thermal conductivity of lightweight composites with different densities

A reduction of thermal conductivity with the decrease of the density can be observed in general. This is because that besides the density, the differences in matrix composition, type of binder and aggregates also show an influence on the property of thermal insulation [15-16]. The thermal conductivity reduces to 0.29 W/(m·k) in samples with a density level of 1400 kg/m³, with a reduction rate of 21.6%. The reduction of density from around 1500 to 1400 kg/m³ results in a decreased standard sand dosage of 31.6% by mass, indicating its negative influence on thermal insulation. Further reduction of the density to around 1300 and 1200 kg/m³ leads to further reduced thermal conductivities of 0.22 and 0.16 W/(m·k), respectively. It should be noticed that the thermal conductivity of 0.2 W/(m·k) can be classified to the T2 level of thermal insulation products based on the standard of EN 998-1. It can be seen from Figure 4 that the thermal conductivity values from this study are lower than that from the literature, which may indicate the advantage of using the alternative binder system together with the lightweight aggregate in this case.

3.4 Acoustical absorption

Owing to the massive addition of the porous lightweight aggregates, the resulting alkali activated lightweight concrete is expected to exhibit good sound absorption behaviours. Figure 5 exhibits the sound absorption coefficient as a function of frequency, four mixtures with a Na_2O content of 3.5% with different density levels were tested. For instance, the mixture with label of D-15 refers to the sample with a density around 1500 kg/m³. Generally speaking, the absorption coefficient is significantly increased with the decrease of density, in another word with the increase of lightweight aggregate content within the matrix; and all mixtures mainly show absorption of sound with medium frequencies between around 300 to 1700 Hz. Specifically, mixtures with a density of round 1500 kg/m³ present a peak absorption coefficient of 0.2, between 800 and 1000 Hz. The peak absorption coefficient increases to around 0.35 and 0.52 in samples with a density about 1400 and 1300 kg/m³ respectively, while the main absorption frequency range remains similar. A further reduction of density to around 1200 kg/m³ results in an increased absorption coefficient to above 0.7, with shifted main absorption frequency to higher values. In terms of the low frequency and high frequency ranges, this lightweight product shows limited sound absorption effect. It should be mentioned that the medium frequency usually refers to the sound from humans and daily life.
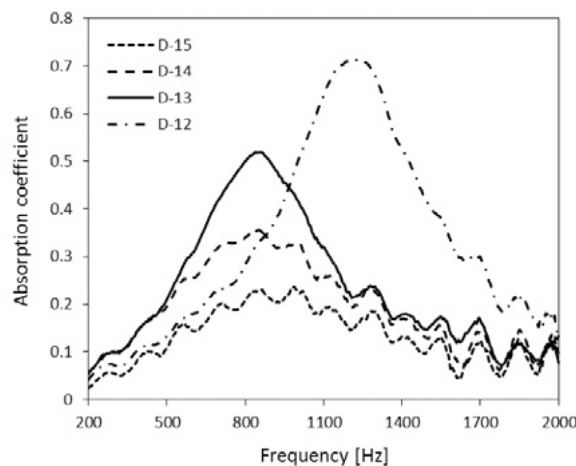
Fig. 5 Acoustic absorption of lightweight composites with different densities

3.5 Advantages in carbon footprint

Applying alkali activated materials shows an advantage in carbon emission towards Portland cement. While within the alkali binder systems, the Na_2O content is directly linked to the environmental issues. Moreover, the replacement of olivine nano-silica to commercial waterglass will further reduce the overall carbon emission. A calculation on the CO_2 footprint of the mixtures used in this study is shown in Table 2. The carbon footprint is usually calculated as the total CO_2 emissions in unit volume of concrete. The carbon footprint used in this calculation is 1.915 tCO_2/t for NaOH, 1.514 tCO_2/t for commercial waterglass, 0.82 tCO_2/t for Portland cement, 0.143 tCO_2/t for slag and 0.027 tCO_2/t for fly ash. Concerning the olivine nano-silica, a CO_2 footprint of 0.461 tCO_2/t is taken from the LCA analysis in VTT (EU F7th project, ProMine internal report), based on an average European industrial case scenario. The values shown above are based on the effective solids contents excluding water. It can be observed that the carbon emission of Portland cement is few times higher than alkali activated materials; the contribution of CO_2 is all from the cement clinkers. In terms of the alkali activated materials, the carbon emission from the binder accounts for around 37% to 69% of the overall emissions. When reducing the Na_2O contents from 5.0% to 2.0%, the carbon emission from the commercial sodium silicate based activator can be reduced by 60%, such a big reduction of carbon footprint may bring attentions on using suitable Na_2O dosages and reaching a balance between performances and environmental impact. Moreover, when olivine nano-silica is applied as

commercial waterglass replacement, the carbon emission in terms of activator can be further reduced by around 25%. In overall, those reduced carbon emissions from Na_2O content and alternative silica source provide great potentials for the future mix design and applications.

Table 2 Calculation on the carbon footprint (kg/m^3)

Sample	Precursors	Activator (exclude H_2O)			CO_2 emissions from activator	CO_2 emissions from binder	Total CO_2 emissions
		Olivine-nano-s	Water glass	NaOH			
D15-5.0-NS		32.5	0	30.9	74.2		131.7
D15-5.0-WG		0	42.3	18.3	99.1		156.6
D15-3.5-NS	384 Slag + 96 Fly ash	22.7	0	21.7	52.0	57.5	109.5
D15-3.5-WG		0	29.6	12.8	69.3		126.8
D15-2.0-NS		13.0	0	12.4	29.7		87.2
D15-2.0-WG		0	16.9	7.3	39.6		97.1
Ref-OPC	480 OPC	0	0	0	0	393.6	393.6

4. Conclusions

This paper evaluates the mechanical properties, thermal property, acoustical absorption of eco-friendly alkali activated slag-fly ash lightweight composites (LWC) with different density classes. The effect of Na_2O contents and the utilization of alternative silica source on early age reaction and carbon footprints on the designed LWC are assessed. Mixtures with 28 d compressive strength up to 32.5 MPa and densities between 1200 and 1500 kg/m^3 are resulted, and a direct correlation between strength and density is observed. The reduction of Na_2O content from 5% to 2% significantly prolongs the reaction process, but shows negligible effect on the silicate structure. Compared to the commercial waterglass, the utilization of olivine nano-silica reduces the carbon footprint from activator by around 25%. The lightweight concretes exhibit very low thermal conductivity between 0.16 and 0.37 W/(m·k), as well as good sound absorption coefficient up to 0.7 for medium frequencies. The application of alkali activated binders and applying this activator to lightweight concrete suggests an additional approach of preparing construction and building materials with multi-functional properties and greatly reduced environmental impacts.

5. Acknowledgment

6. Reference

1 Huiskes D, Keulen A, Yu Q, Brouwers H (2016) Design and performance evaluation of ultra-lightweight geopolymer concrete. Mater Des 89:516-526. doi: 10.1016/j.matdes.2015.09.167

2. Vaou V, Panias D (2010) Thermal insulating foamy geopolymers from perlite. Miner Eng 23(14):1146-1151. doi: 10.1016/j.mineng.2010.07.015

3 Posi P, Teerachanwit C, Tanutong C, Limkamoltip S, Lertnimoolchai S, Sata V, Chindaprasirt P (2013) Lightweight geopolymer concrete containing aggregate from recycle lightweight block. Mater Des (1980-2015) 52:580-586. doi: 10.1016/j.matdes.2013.06.001

4 Yang K-H, Lee K-H, Song J-K, Gong M-H (2014) Properties and sustainability of alkali-activated slag foamed concrete. J Clean Prod 68:226-233. doi: 10.1016/j.jclepro.2013.12.068

5 Aguilar RA, Díaz OB, García JE (2010) Lightweight concretes of activated metakaolin-fly ash binders, with blast furnace slag aggregates. Constr Build Mater 24(7):1166-1175. doi: 10.1016/j.conbuildmat.2009.12.024

6 Ibrahim WMW, Hussin K, Abdullah M, Kadir AA, Deraman LM, Sandu AV (2017) Influence of Foaming Agent/Water Ratio and Foam/Geopolymer Paste Ratio to the Properties of Fly Ash-based Lightweight Geopolymer for Brick Application. Rev Chim 68(9):1978-1982.

7 Al Bakri Abdullah MM, Yahya Z, Tahir M, Faheem M, Hussin K, Binhussain M, Sandhu AV (2015) Fly ash based lightweight geopolymer concrete using foaming agent technology Rev Chim 66(7):1001-3.

8 Al Bakri AMM, Kamarudin H, Nizar IK, Sandu AV, Binhussain M, Zarina Y, Rafiza AR (2013) Design, processing and characterization of fly ash-based geopolymers for lightweight concrete application. Rev Chim 64(4):382-387.

9 Brough A, Atkinson A (2002) Sodium silicate-based, alkali-activated slag mortars: Part I. Strength, hydration and microstructure. Cem Concr Res 32(6):865-879. doi: 10.1016/S0008-8846(02)00717-2

10 European Commission (2007) Reference document on best available techniques for the manufacture of large volume inorganic chemicals – solids and others industry.

11 Lazaro A, Brouwers H, Quercia G, Geus J (2012) The properties of amorphous nano-silica synthesized by the dissolution of olivine. Chem Eng J 211:112-121. doi: 10.1016/j.cej.2012.09.042

12 Lazaro A, Quercia G, Brouwers H, Geus J (2013) Synthesis of a green nano-silica material using beneficiated waste dunites and its application in concrete. World J Nano Sci Eng 3(3):41-51. doi: 10.4236/wjnse.2013.33006

13 Jonckbloedt RCL (1997) The dissolution of olivine in acid, a cost effective process for the elimination of waste acids. PhD Thesis, Utrecht University.

14 Gao X, Yu Q, Brouwers H (2015) Reaction kinetics, gel character and strength of ambient temperature cured alkali activated slag–fly ash blends. Constr Build Mater 80:105-115. doi: 10.1016/j.conbuildmat.2015.01.065

15 De Korte A, Brouwers H (2010) Calculation of thermal conductivity of gypsum plasterboards at ambient and elevated temperature. Fire Mater 34(2):55-75. doi: 10.1002/fam.1009

16 Zehner P, Schlunder EU (1970) Thermal conductivity of granular materials at moderate temperatures. Chem Ing Tech 42:933-41.

Effect of expansive agent on shrinkage and Long-term Performance of SCC

G. Ling [1,2], Z. Shui [2], T. Sun [2,*], X. Gao [3], X. Li [1,2,] G. Wang [2]

[1]School of Materials Science and Engineering, Wuhan University of Technology, Wuhan 430070, China;

[2]State Key Laboratory of Silicate Materials for Architectures, Wuhan University of Technology, Wuhan 430070, China;

[3]School of Civil Engineering and Architecture, Wuhan University of Technology, Wuhan 430070, China;

*Correspondence: sunt@whut.edu.cn

Abstract

In this study, the effects of incorporating different expansive agent on the workability, mechanical properties and auto shrinkage behavior of self-compacting concretes (SCCs) have been investigated. UHA, MgO and Liquid expansive agent are added at 15%, 5% and 1% by cement weight. Academy of Construction Sciences (1986) and GL2000 model are utilized to calculate the shrinkage model of SCC with different expansive agent. Results show that at the compressive strength of SCCs at early ages is lower than those of the reference concrete, although while in the long term their strength increases as a result of pozzolanic reactivity by supplementary cementitious materials. Adding different expansive agents to mixtures impart a significant change in the measured autogenous shrinkage. Moreover, comparing the results calculated from the model and obtained from experiment, it is found that they were very similar. That is, the calculation model has fine accuracy and can predict the long-term performance of SCC.

Keywords: Self-compacting concrete, expansive agent, workability, autogenous shrinkage, long-term performance.

1. Introduction

Self-compacting concrete is characterized by excellent workability, which can be spread to a long distance without any vibration in complicated formwork, congested structure, and the areas which are hard to reach. The main benefit by using SCC in building structures is shortening the construction period, and it is widely applied in many construction industries due to its excellent workability. In order to obtain good performance, the amount of cementitious materials and water reducers in SCC is usually higher, which will have influence on the volume stability of SCC [1,2]. This is not to be neglected, especially for mass concrete engineering. Improving the volume stability of self-compacting concrete is becoming a subject of great concern [3-5].

Supplementary cementitious materials (SCMs) such as fly ash (FA), blast furnace slag (BFS) and silica fume (SF) are widely used in the preparation of SCC [6-8]. As proper amount of SCMs can improve the fluidity and stability of SCC, meanwhile, they can reduce the shrinkage of SCC and improve the volume stability. However, this effect of SCMs on shrinkage is limited [9]. A lot of research has been done to obtain more efficient methods to improve the volume stability of SCC [10,11]. The methods for mitigating shrinkage include adding mineral additives [12-14], chemical admixtures [15-20], fibers [21, 22], and by the control

of curing conditions such as internal curing [23]. The expanding agent were used for over four decades to minimize the effects of drying shrinkage. In that case, CaO-based expansive agent was utilized [24]. Compensation of the thermal shrinkage with delayed expansion of slow hydrating MgO is an effective and economic method for preventing the thermal cracking of concrete. The reason for the volume expansive is that the generation of ettringite (AFt), which was a hard rod-like crystal, processing the high certain strength. This method bring out good results by improving joint space and limit curing, but its practical application still requires special precautions. To overcome the limitations resulting from the use of individual products, and to minimize shrinkage, the effect of expansive agents has been tested. However, less research has been carried out on the combined use of different expansive agents on the shrinkage in SCC.

In this study, the effect of three different expansive agents (UHA, MgO and Liquid expansive agent) on the performance and shrinkage of SCC were investigated. Then, according to the Academy of Construction Sciences (1986) and GL2000 model, the shrinkage calculation model of SCCs with different expansive agents is calculated, and the long-term performance has been predicted.

2. Methodology

2.1 Materials

In the study, Fly ash (FA), blast furnace slag (BFS) and metakaolin (MK) were used as the replacement of cement, with up to 45% by weight of cement replaced. The type of Portland cement II•R was used in this study. FA and BFS utilized in this research as cementitious material obtained from power plant and steel mills, respectively. Metakaolin was obtained from Maoming Kaolinite Technology Co Ltd, which was produced by calcination of kaolin at 750 °C. The chemical compositions of the cementitious materials s are presented in Table 1.

Natural river sand with maximum size of 4.75 mm was utilized as fine aggregates. The values of specific gravity and water absorption are 2.66 and 0.55%, respectively. The limestone gravel with maximum size of 16 mm and with a specific gravity of 2670 kg/m^3 was also used as coarse aggregates. Commercially available polycarboxylicether type superplasticizer (SP) possesses specific gravity of 1.07 is used in this research. Three different expansive agents are used in the paper, they are UHA, MgO and liquid expansive agent, the recommended dosage are 10-15%, 4-8% and 0-1%, respectively.

Table 1: Chemical composition of raw materials.

	SiO_2	Al_2O_3	CaO	MgO	Fe_2O_3	K_2O	Na_2O	TiO_2	SO_3	LOI
	%	%	%	%	%	%	%	%	%	%
PII• R	18.93	4.67	62.49	0.77	3.98	0.72	0.13	0.27	4.43	3.26
FA	50.01	32.12	1.5	0.83	3.91	0.94	0.77	1.5	1.09	3.74
BFS	31.78	16.44	34.12	10.57	0.47	0.29	0.67	1.35	3.4	0.35
MK	57.37	38.63	0.03	0.07	0.77	0.49	0.39	0.4	0.15	1.04

2.2 Mixture proportions and specimen preparation

The water-to-binder (cement + FA+BFS+MK) mass ratio (w/b) of SCC was 0.33, and the replacement ratio of the supplementary cementitious materials was up to 45% by weight of the cement, as presented in Table 2 . All mixes were performed in accordance with ASTM C192 [24] in a power-driven revolving pan mixer. Cubes of 100×100×100 mm and 100×100×515mm were cast in steel moulds and compacted on a

vibrating table. The cube specimens were removed from moulds after casting for 24h, and then allowed to cure under standard conditions (20±2 °C and relative humidity of 98%), for compressive strength test were carried out, respectively. The rectangular specimens of 100×100×515mm were test autogenous strains development.

Table 2: Mixture proportion of SCC (kg/m³).

| NO. | W/B | SP | water | sands | gravels | cement | FA | GGBFS | MK | Expansive Agents | | |
										UHA	MgO	Liquid
		%	kg/m³	kg/m³	kg/m³	kg/m³	kg/m³	kg/m³	kg/m³	kg/m³	kg/m³	kg/m³
E_0	0.33	5.0	165	859	761	275	165	40	20	0	0	0
E_U	0.33	5.5	165	859	761	275	132	7	20	75	0	0
E_M	0.33	4.5	165	859	761	275	153	28	20	0	25	0
E_L	0.33	5.0	165	859	761	275	165	40	20	0	0	5
E_{UM}	0.33	5.5	165	859	761	275	136	11	20	50	15	0
E_{ML}	0.33	4.5	165	859	761	275	158	33	20	0	15	3

2.3 Tests

The compressive strength was measured with hydraulic universal testing machine. Each proportion was measured as a set of 3 samples. Samples were tested for compressive strength after 3 days, 7 days and 28 days. Autogenous shrinkage measurement was conducted using non-contact sensors. This measurement technique accounted for the benefits of using the eddy-current displacement sensor (ECDS) for measuring autogenous shrinkage.

3. Results and discussion

3.1 Workability and mechanical properties of SCC

The slump flow and V-flow time tests have been carried out to evaluate the workability of SCCs which contain different amount of expansive agents, and the results are shown in Table 3. The slump flow of E_U and E_0 are approximate, but it should be noticed that the SP dosage of E_U is higher than E_0. This is because that a mass of fibers in UHA expansive agent will increase the viscosity and reduce the fluidity of SCC. Meanwhile, the homogeneity of SCC is improved, resulting in decrease of V-flow time for E_U. Compare E_M, E_L and E_0, it can be seen that mixing MgO and liquid expansive agent will increase the workability of SCC, and the influence of MgO expansive agent is more pronounced.

It is necessary to reduce the SP dosage when adding 5% MgO expansive agent to maintain the stability of SCC. Because the amount of UHA expansive agent is larger, the influence of UHA expansive agent on concrete performance is dominant. When composite using of UHA and MgO expansive agent (E_{UM}), the workability is similar to E_U, as the addition of UHA expansive agent is more, and its influence is dominant. Likewise, the workability of E_{ML} is similar to E_M. In general, the workability of each SCC mixture can meet the requirements of self-compacting.

Table 3: Workability and mechanical properties of SCC

NO.	Slump flow	V-flow time	3d Compressive strength	28d Compressive strength
	mm	s	MPa	MPa
E_0	660	13	37.12	65.97
E_U	660	7.3	30.04	61.81
E_M	650	8.3	33.75	72.07
E_L	680	12	31.32	63.82
E_{UM}	665	9	30.20	65.48
E_{ML}	670	9	33.23	67.70

The compressive strength at 3 days and 28 days of SCCs which contain different expansive additive are evaluated and shown in Table 3. As shown in Table 3, the compressive strength of all SCC mixtures (E_U, E_M, E_L, E_{UM}, E_{ML}) are lower than the controlled E_0 at 3 days, but the compressive strengths of each mixtures at 28 days are similar to non-expansive mixtures (E_0). It is evident that, the strength of SCCs at 3 d decrease when adding 15% UHA (E_U) and 1% liquid expansive agent (E_L), and this reduction of the compressive strength was equal to from approximately 19.1% and 9.1% compared to E_0, respectively. Nevertheless, the compressive strength loss is 6.3% and 3.2% for E_U and E_L at 28 d, respectively. This may be due to the fact that UHA expansive agent contains a large amount of FA and has low pozzolanic activity, while liquid expansive agent will inhibit the hydration process of cement, which will lead to a decrease of strength of SCC at early age, but with the extension of curing time, these adverse effects are gradually weakened. The compressive strength of SCC increased by 9.2% when add 5% MgO expansive agent (E_M) at 28 d. This is because that the addition of MgO can improve the alkalinity of cement paste, promote the pozzolanic reaction of mineral admixtures, and thus improve the strength of concrete in the later curing age [25]. The compressive strength of SCC at 28 d does not change obviously when mixing 10% UHA and 3% MgO expansive agents (E_{UM}), and it increases slightly by adding 3% MgO and 0.6% liquid expansive agents.

3.2 Volume stability of SCC

Autogenous shrinkage of each SCC samples are continuously measured as a function of time up to 60 days and the results are shown in Fig. 1. By observing the autogenous shrinkage curve of each group of SCC samples, the autogenous shrinkage of concrete develops rapidly in 24 h after forming. Due to the hydration reaction of cement, the content of free water in concrete decreases fleetly during the first 24 h, and the volume of concrete changes obviously. The autogenous shrinkage rate of E_0 reached 150×10^{-6} at 1 d, and it is 211×10^{-6} at 7 d, increased 61×10^{-6} during 1 d to 7 d. The shrinkage rate of E_U was only 50×10^{-6} at 1 d and 66×10^{-6} at 7 d, it is equal to from approximately 33.3% and 31.3% of E_0. It can be assumed that the expansion effect of UHA is striking both during setting and later hydration. The shrinkage curve of E_M group is basically the same as E_U at first 24 h, and the shrinkage rate reaches 140×10^{-6}. But after that, the concrete begins to expand, and the shrinkage rate is only 59×10^{-6} at 7 d. During this process, the expansion amount is 81×10^{-6}. Therefore, it can be seen that the expansion effect of MgO expansive agent is mainly in the course of concrete curing. This is due to the formation of $Mg(OH)_2$ crystal by hydrolysis of MgO during concrete curing process, resulting in the volume expansion of SCC. During the condensation process of SCC that contains liquid expansive agents (E_L), the phenomenon of micro-expansion (expansion rate 50×10^{-6}) appeared in the early stages, with that rapid contraction occurred. The shrinkage rate is 230×10^{-6} at 1 d, 53.3% higher than E_0 at 1 d. and then the volume change slowed down. The shrinkage rate was 167×10^{-6} at 7 d, slightly lower than that of E_0.
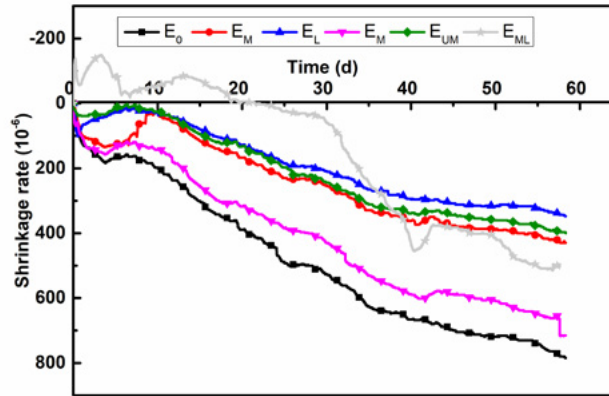
Fig. 1 The autogenous shrinkage curves of SCC with expansive agents at 60 days.

The shrinkage rate of concrete E_{UM} is 280×10^{-6} at 1 d, the total shrinkage rate 86.7% higher than E_0. Subsequently, the shrinkage of E_{UM} slows down significantly and the expansion occurs. The shrinkage rate of E_{UM} was 149×10^{-6} at 7 d, 29.4% lower than that E_0. The expansion is 91×10^{-6} during this process. It shows that the mixture of UHA and MgO expansive agent increases the shrinkage of concrete during the setting process, but has expansion effect in the curing process. The shrinkage rate of E_{ML} is - 100×10^{-6} at 1 d, and -110 $\times10^{-6}$ at 7 d. That is, the combined use of MgO and liquid expansive agent has a significant effect on reducing the shrinkage during condensation.

By analyzing the shrinkage curves of different SCC in 60 d, it can be seen that different expansive agents can reduce the shrinkage of SCC compared with SCC without expansive agents (E_0). The shrinkage rate of E_U, E_M, E_L, E_{UM} and E_{ML} at 60 d are 776×10^{-6}, 427×10^{-6}, 343×10^{-6}, 715×10^{-6} and 503×10^{-6}. UHA expansive agent can reduce the shrinkage of concrete in the early stage, then it has obvious expansive effect in 5-10 days, after that, there was a sustained reduction in shrinkage. MgO expansive agent has remarkable effect on reducing shrinkage. This effect initiates at first 12 h, and with the prolongation of curing time, it still has obvious effect. The shrinkage of SCC at 60 d is only inhibited for 8.7% by adding liquid expansive agent (E_L), the effect of reducing shrinkage is not obvious.

The effect of composite use of UHA and MgO expansive agent (E_{UM}) is between the two, and the shrinkage cruve of E_{UM} at early age is similar to that of E_M, which indicates that MgO expansive agent plays a very important role in the early stage. However, due to the reduction of MgO, the expansion effect is weakened. MgO and liquid composite expansive agent are the most special group. From the Fig. 1, evident expansion could be found in the early stage, but the expansion effect is not adequate to resist shrinkage deformation after 15 d, as a result the component begin to retraction. Then, the shrinkage increased rapidly after 30 days, and outdid the other groups gradually.

3.3   Prediction of long-term performance of SCCs

The calculation methods for concrete shrinkage and creep mainly contains Academy of Construction Sciences (1986) model [26], CEB-FIP series model [27, 28], BS series model [29], GZ series model [31] and GL2000 model [32], and so on. The factors considered in these models are different, and the calculation accuracy is also different. The concrete self-shrinkage model selected in this modeling is the GL2000 model of the Academy of Construction Sciences (1986) and GL2000 model were employed in the course of this calculation. The basic equation for shrinkage development with time of concrete is as formula (1).

$$\varepsilon_s(t,t_c)_0= \left(\frac{t-t_c}{t-t_c+0.15(V/S)^2} \right)^{0.5} \times 10^{-3} \tag{1}$$

Where, t_c means the time when concrete begins to dry; t means the test time; $\mathring{a}_s(t,t)$ means the concrete

shrinkage strain at age t□ V means the volume of specimens; S means the superficial area of specimens.

The influence function of environmental relative humidity on concrete shrinkage as formula (2).

$$f_s(RH) = 1.18 - 1.39 RH^4 \tag{2}$$

Where, $f_s(RH)$ means the influencing function of environmental relative humidity on Shrinkage of concrete; RH means the environmental relative humidity.

As for the effect of concrete compressive strength on shrinkage, according to GL2000 model, the function is as formula (3):

$$f_s(f_{cu,k}) = \left(\frac{30}{f_{cu,k}}\right)^{0.5} \tag{3}$$

Where, $f_s(f_{cu,k})$ means the influencing function of compressive strength grade on Shrinkage of concrete; $f_{cu,k}$ means the compressive strength grade of concrete.

In summary, the suggested formula for calculating concrete shrinkage is as formula (4):

$$\varepsilon_s(t,t_c) = \varepsilon_s(t,t_c)_0 \cdot f_s(RH) \cdot f_s(f_{cu,k}) \cdot f_s(T_{cement}) \tag{4}$$

Where, $\varepsilon_s(t,t_c)$ means the concrete shrinkage strain at age t; $f_s(T_{cement})$ means influencing function of cement type on Shrinkage of concrete.

In the calculation, the starting drying time of concrete is 1d, the environment relative humidity is 55%, the compressive strength grade of concrete is C50, and the influence coefficient of cement is 0.7. The formula for calculating shrinkage of concrete is as formula (5):

$$\varepsilon_s(t) = 567 \times \left(\frac{t-1}{t+177}\right)^{0.5} \times 10^{-6} \tag{5}$$

The addition of expansive agent will affect the shrinkage of concrete, and the influence varies with the types and dosage of expansive agent. According to the experimental results of autogenous shrinkage, it can be seen that different expansive agents have different effects on the shrinkage of self-compacting concrete at the initial stage during concrete hardening, but in general, the trend of shrinkage curve for each SCC mixture is similarity. The difference is that after adding different expansive agents, the shrinkage of each SCC specimens varies in the first 10 days, and the final shrinkage value is also different. The equation for

calculating the shrinkage of concrete considering the influence of expansive agent is as formula (6):

$$\varepsilon_{sn}(t) = f_{sh}(n) \times 567 \times \left(\frac{t-1}{t+1777}\right)^{0.5} \times 10^{-6} \tag{6}$$

Since the volume stability of different SCC mixtures in the first 10 days are not regular, and its value has little influence on the long-term stability of SCC, the autogenous shrinkage test data after 10 days are choosed as the basis for analyzing the influence of expansive agents on autogenous shrinkage of SCC.

Comparing the autogenous shrinkage of SCC contains expansive agent to the controled SCC (without expansive agent). It is found that there is an obvious correlation between the proportion of their shrinkage value and time. On this basis, the fitting process and results of each group are obtained as shown in Fig. 2.

2a)   2b)
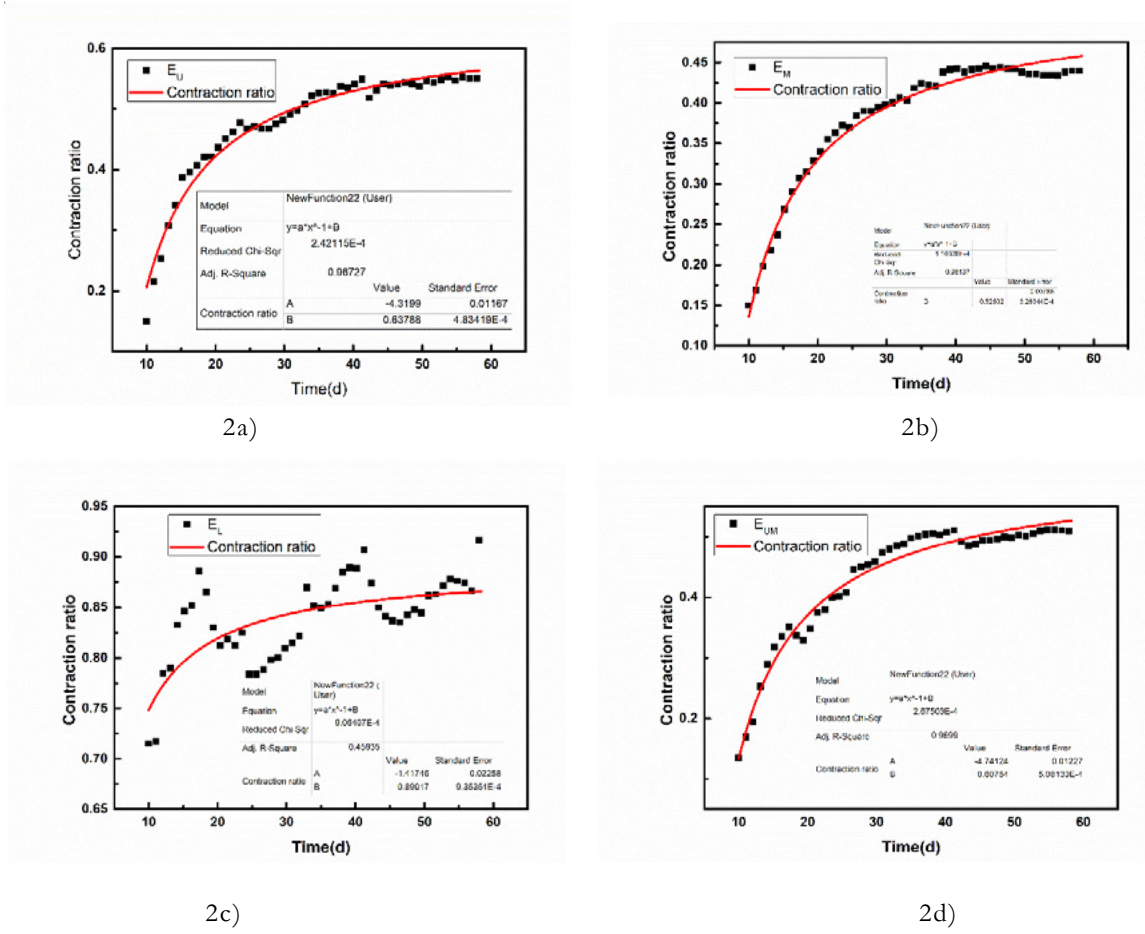

2c)   2d)

Fig. 2: Fitting of influencing parameters of different expansion agents.
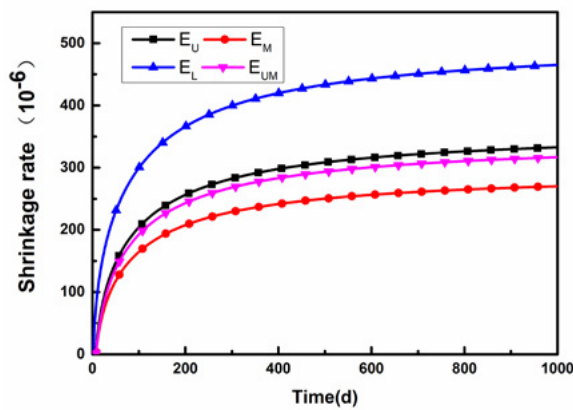
Fig. 3: Shrinkage curves of SCC contains expansion agents.

According to the data fitting process, the equation for calculating the shrinkage-time relationship of each

$$\varepsilon_{EU}(t) = (-\frac{4.320}{t} + 0.64) \times 567 \times (\frac{t \cdot 1}{t + 172})^{0.5} \times 10^{-6}$$

$$\varepsilon_{EM}(t) = (-\frac{3.894}{t} + 0.53) \times 567 \times (\frac{t \cdot 1}{t + 172})^{0.5} \times 10^{-6}$$

$$\varepsilon_{EL}(t) = (-\frac{1.417}{t} + 0.89) \times 567 \times (\frac{t \cdot 1}{t + 172})^{0.5} \times 10^{-6}$$

$$\varepsilon_{EUM}(t) = (-\frac{4.741}{t} + 0.61) \times 567 \times (\frac{t \cdot 1}{t + 172})^{0.5} \times 10^{-6}$$

(7)

(8)

(9)

(10)

The shrinkage curves of each group of specimens obtained from the formula with time are shown in Fig. 3. It can be seen that the shrinkage displacement curves are very close to the autogenous shrinkage test results. It shows that this prediction model has fine accuracy and has certain guiding significance for the prediction of long-term volume stability of concrete in practical engineering.

4.   Conclusions

1.   Utilizing UHA expansive agents has negatively effect on the workability of the fresh SCC, while MgO expansive agents has contrary effects. These effects can be compensated by adjusting the dosage of water reducing agent. Therefore, it can be concluded that the inclusion of the expansive additives in the studied dosages does not limit the workability properties of SCC.

2.   Generally, the inclusion expansive in SCC induced a slight decrease of the compressive strength. This strength loss was more pronounced at an early-age than on the long-term.

3.   In terms of autogenous shrinkage, the use of the different expansive agents can reduce the shrinkage of SCC compared with SCC without expansive agents, the effect of reducing shrinkage varies with expansive agents. In particular, the contemporaneous use of UHA and MgO proved to be very effective, and it caused strong initial expansion of SCC, which gradually decreased, but still remained positive after 60 days.

4.   The shrinkage mode of SCCs with different expansive agents is obtained by utilizing Academy of Construction Sciences (1986) and GL2000 model, and the long-term performance has been predicted.

5.   Acknowledgment

6.   References

[1] G. DS, 2005, The European guidelines for self-compacting concrete specification production and ues. Norfolk: The Self-Compacting Concrete European Project Group.

[2] Rozière E, Granger S, 2007, Influence of paste volume on shrinkage cracking and fracture properties of self-compacting concrete, Cem Concr Compos, 29(8), 626-636, 10.1016/j.cemconcomp.2007.03.010.

[3] M.S. Meddah AT-H, 2009, Durability performance and engineering properties of shale and volcanic ashes concretes, ACI Mater J, 106(4), 241-250, 10.1016/j.conbuildmat.2015.01.020

[4] Behfarnia K, Farshadfar O, 2013, The effects of pozzolanic binders and polypropylene fibers on durability of SCC to magnesium sulfate attack, Constr Build Mater, 38, 64-71, 10.1016/j.conbuildmat.2012.

08.035

[5] Corinaldesi V, 2012, Combined effect of expansive, shrinkage reducing and hydrophobic admixtures for durable self-compacting concrete, Constr Build Mater, 36, 758-764, 10.1016/j.conbuildmat.2012.04.129.

[6] Craeye B, De Schutter G, Desmet B, Vantomme J, 2010, Effect of mineral filler type on autogenous shrinkage of self-compacting concrete, Cem Concr Res, 40(6), 908-913, 10.1016/j.cemconres.2010.01.014.

[7] José Oliveira M, Ribeiro AB, Branco FG, 2014, Combined effect of expansive and shrinkage reducing admixtures to control autogenous shrinkage in self-compacting concrete, Constr Build Mater, 52, 267-75, 10.1016/j.conbuildmat.2013.11.033.

[8] Le HT, Müller M, Siewert K, Ludwig H-M, 2015, The mix design for self-compacting high performance concrete containing various mineral admixtures, Mater Design, 72, 51-62, 10.1016/j.matdes.2015.01.006.

[9] Maltese C, Pistolesi C, Lolli A, Bravo A, Cerulli T, Salvioni D, 2005, Combined effect of expansive and shrinkage reducing admixtures to obtain stable and durable mortars, Cem Con Res, 35(12), 2244-2251, 10.1016/j.cemconres.2004.11.021.

[10] Chatterji S, 1995, Mechanism of expansion of concrete due to the presence of dead-burnt CaO and MgO, Cem Concr Res, 25(1), 51-56, 10.1016/0008-8846(94)00111-B.

[11] Collepardi M, Borsoi A, Collepardi S, Ogoumah Olagot JJ, Troli R, 2005, Effects of shrinkage reducing admixture in shrinkage compensating concrete under non-wet curing conditions, Cem Concr Compos, 27(6), 704-708, 10.1016/j.cemconcomp.2004.09.020.

[12] Collepardi M, Troli R, Bressan M, Liberatore F, Sforza G, 2008, Crack-free concrete for outside industrial floors in the absence of wet curing and contraction joints, Cem Concr Compos, 30(10), 887-891,

10.1016/j.cemconcomp.2008.07.002.

[13] Meddah MS, Suzuki M, Sato R, 2011, Influence of a combination of expansive and shrinkage-reducing admixture on autogenous deformation and self-stress of silica fume high-performance concrete, Constr Build Mater, 25(1), 239-250, 10.1016/j.conbuildmat.2010.06.033.

[14] Z. Cao JX, 2003, Construction Technology of Dam with MgO Concrete. Beijing: China Electric Power Press.

[15] Chen C LC, 2006, Study and application of MgO concrete, Concrete, 199(5), 45-53.

[16] Polat R DR, Khushefati W H, 2015, Effects of nano and micro size of CaO and MgO, nano-clay and expanded perlite aggregate on the autogenous shrinkage of mortar, Constr Build Mater, 81, 268-275, 10.1016/j.conbuildmat.2015.02.032.

[17] Güneyisi E GM, 2008, Properties of self-compacting mortars with binary and ternary cementitious blends of fly ash and metakaolin, Mater Struct,41(9), 1519-1531, 10.1617/s11527-007-9345-7.

[18] Güneyisi E GM, Özbay E, 2009, Evaluating and forecasting the initial and final setting times of self-compacting concretes containing mineral admixtures by neural network, Mater Struct, 42(4), 469-484. 10.1617/s11527-008-9395-5.

[19] Laskar AI, Talukdar S, 2008, Rheological behavior of high performance concrete with mineral admixtures and their blending, Constr Build Mater, 22(12), 2345-2354, 10.1016/j.conbuildmat.2007.10.004.

[20] Ponikiewski T, Go³aszewski J, 2014, The influence of high-calcium fly ash on the properties of fresh and hardened self-compacting concrete and high performance self-compacting concrete, J Cleaner Prod, 72, 212-221, 10.1016/j.jclepro.2014.02.058.

[21] Vejmelková E, Keppert M, Grzeszczyk S, Skaliñski B, Èerný R, 2011, Properties of self-compacting concrete mixtures containing metakaolin and blast furnace slag., Constr Build Mater, 25(3), 1325-1331, 10.1016/j.conbuildmat.2010.09.012.

[22] Zhao H, Sun W, Wu X, Gao B, 2015, The properties of the self-compacting concrete with fly ash and ground granulated blast furnace slag mineral admixtures, J Cleaner Prod, 95, 66-74, 10.1016/j.jclepro.2015.

02.050.

[23] **Güneyisi E, Gesoðlu M, Özbay E**, 2010, Strength and drying shrinkage properties of self-compacting concretes incorporating multi-system blended mineral admixtures, Constr Build Mater, 24(10), 1878-1887, 10.1016/j.conbuildmat.2010.04.015.

[24] ASTM. Standard Practice for Making and Curing Concrete Test Specimens in the Laboratory. USA1997.

[25] D Shen MD, L Mo, 2012, Effect of restraint degree on the expansion and tensile splitting strength of concrete containing MgO-based expansive agent, Concrete, 10, 14-17.

[26] CEB-FIP, 1978, Model Code for Concrete Structures.

[27] ACI Committee 209, 1982, Prediction of Creep, Shrinkage and Temperature Effects in Concrete Structures [S].

[28] ACI Committee 209, 1992, Prediction of creep, shrinkage and temperature effects in concrete structures[S], Manual of concrete practice, Part 1, American Concrete Institute, 209R 1-92.

[29] BS 5400: Part4:1984. Code of Practice for Design of Concrete Bridges[S]. British standard Institute.

[30] Z. P., Bazant, S. Baweja, 1995, Creep and shrinkage Prediction Model for Analysis and Design of Concrete Structures-Model B3, RILEM Recommendation, Mater Struct, 28, 357-365, 10.1007/BF02473152.

[31] N. J. Gadrner, J. W. Zhao,1993, Creep and shrinkage Revisited, ACI Mater J, 90, 236-246, 10.1007/978-1-4612-5424-9.

[32] N. J. Gardner and M.J, Lockman, 2001, Design provisions for Drying shrinkage and Creep of Normal-Strength Concrete, ACI Mater J,98(2), 159-167.

Converter slag - ladle slag - gypsum ternary binder – effect of CaO slaking

E. D. Adesanya[1], K. M. Ohenoja[1], P. K. Kinnunen[1], M. H. Illikainen[1]

Fibre and Particle Engineering Research Unit, University of Oulu, Finland[1]:

Abstract

The present study reports on the utilization of steel slags as non-cement binders. Converter slag (also known as basic oxygen furnace slag, BOFS) and ladle slag (also known as ladle furnace slag or falling slag, LS), both generated as a by-product during steelmaking processes, were used. LS is highly calcareous and aluminous containing mayenite and calico-olivine as main phases. LS can react with water to produce cement-like hydration products, but optimal water/binder ratio is critical in order to prevent hydration product conversion and strength loss. Another option is to add an optimum amount of gypsum to produce ettringite and AH3 with good mechanical properties. CN slag utilization in concreting is affected by the volume instability caused by its high free lime content. Here, the free lime content is slaked through hydraulic weathering to form calcium hydroxide. The resulting slurry is then used as co-cementitious binder with ladle slag and gypsum in a ternary mix. This method was found to be successful and experimental results showed that free lime content in converter slag can be reduced ensuring volume stability through designed weathering. The new cementitious binder properties were structurally analysed through compressive strength, length change, and ultrasonic pulse velocity (UPV). The hydration products and hydration kinetics were determined through thermogravimetry analysis (TGA/DTA) and isothermal calorimetry.

Keywords: Steel slag, Free lime, Ettringite, Slaking, Portlandite.

* Standard cement chemistry notations were used, hence CaO represents C, Al_2O_3 as A and H_2O as H

1.   Introduction

Steel slags are by-products from steelmaking process and in 2016 about 18.4 million tonnes of these slags were produced in Europe alone [1]. Only 4.4% of these produced slags are used in cement and concrete applications while approximately 23% are either landfilled or stored. These slags include Electric-arc furnace, ladle slag (LS, also known as refining slag) and basic-oxygen furnace (BOF) slag also known as converter slag (CN). Increasing global demand for cement, as well as governmental legislation and costs related to landfilling have prompted studies into utilising of these slags in cement and concrete as a sustainable alternative to OPC.

In contrast to the glassy granulated blast furnace slag (GGBFS) in which the calcium and magnesium oxides reacts to form non-expansive products and is widely used to supplement Portland cement, predominantly crystalline steel slags are composed of free lime (f-CaO) and free MgO (f-MgO). During hydration, these oxides form hydroxides which increases the volume of the matrix causing volumetric expansion and strength reduction in the mortar. This anomaly and steel slags (EAF and BOF) less cementitious activity has limited the use of steel slags as a cementitious binder. The volume instability of these slags have been previously reported [2,3], and mostly in cements and concretes they have been used as aggregates.

Various methods have been proffered to overcome the barriers of steel slags utilization in cements or as

a cementitious binder. Muhmood et al. [4] remelted and water quenched CN slag, and they reported an increase in the hydraulicity of the slag and also reduction in the f-CaO content. Jiao et al. [5] also remelted CN slag and reported significant reduction in f-CaO amount by adding 20% of silicon oxide (SiO_2) during remelting. Also, f-CaO and f-MgO in steel slags have been eliminated through accelerated carbonation to form carbonates [6–10]. Liang et al. [6] reported increase hydration activity and ettringite promotion when steel slag was carbonated before hydrating with Portland cement. Likewise after accelerated carbonation, Pang et al. [10] reported that the f-CaO content of BOF slag aggregate reduced from 7% to under 1%. Other previously studied methods to control f-CaO and f-MgO in steel slags include by natural weathering [3,11,12] and also through attrition scrubbing and chelation [13].

Here we aim to utilize steel slags in a synergistic-ternary mix of converter slag, ladle slag (LS) and gypsum and to determine the effect of slaking of f-CaO in CN on the hydrated properties of the ternary mix. Hydration kinetics through isothermal calorimetry, thermogravimetry analysis (DTA/TGA), compressive strength, volume shrinkage and expansion were determined.

2. Methodology

2.1 Materials

Ladle slag and converter slag used were supplied by SSAB Europe Oy (Raahe, Finland). Both slags were taken from the cooling pit where they have exposed to varying natural weather conditions. Both slags were sieved and the fractions below 2 mm then milled for 2 h. Gypsum used was purchased from VWR Finland (product no. 22451.360). Standard CEN Sand was used as aggregate in the mortars. The chemical compositions of the binders were analysed by X-ray fluorescence (XRF) (PANalytical Omnian Axiosmax) in oxides and presented in Table 1.

Table 1. Chemical compositions of the binders used in the study (%wt.).

Oxide	CaO	SiO_2	Al_2O_3	MgO	SO_3	Fe_2O_3	Others	f-CaO
LS	45.7	9.5	29.8	6.2	0.4	0.8	7.6	0.0
G	41.4	1.0	0.1	0.5	53.8	0.1	3.1	-
CN	49.7	12.6	1.6	2.0	0.3	24.8	8	7.0

The slags were milled using a laboratory sized 10L tumbling ball mill (Germatec) containing 200 steel balls with a diameter of 30mm. The f-CaO content in both slags was determined using the methodology described in SFS-EN 451-1:2004 [14]. The method quantifies dissolved amount of CaO in a specified mixture of butanoic acid, 3-oxo-ethyl ester, and butan-2-ol during 3h boiling time [15].

2.2 Preparation of samples

The samples were prepared according to the mix composition in Table 2. The converter slag was prepared a day before to slake the free lime prior to mixing with other binders. Equivalent amount of water and converter slag were mixed using a shear mixer for 4 mins and covered at ambient temperature for 24 h. After 24 h, Ladle slag-gypsum (LSG) blend was then added to the slaked converter slag (SCN) and mix using a Kenwood mixer. As a reference sample, non-slaked converter slag (CN) was also mixed with LSG. The resulting mortar mix was then jolted on a vibratory table and then cast in 50 x 50mm cubical molds for strength test and ultrasonic pulse velocity analysis, and 40 x 40 x 160mm molds for shrinkage and expansion measurements. Paste sample was prepared the same way without sand aggregates, for use in characterization analysis.

Table 2. Mix composition of the mortars used in the experiment.

Sample name	LS (g)	Gypsum (g)	CN (g)	Sand (g)	w/b
SCN-LSG	157.5	67.5	225	1000	0.5
CN-LSG	157.5	67.5	225	1000	0.5

2.3   Measurements

Compressive strength of the mortars at 7, 28 and 56 days was done using Zwick testing equipment with a load cell of 100kN and force speed of 2.4kN/s. The drying shrinkage and expansion were calculated using Eq. (1).

$$LC(\%) = \frac{L_i - L_x}{G} \tag{1}$$

where Li is the difference between the comparator reading and the reference bar after 24 h, Lx is the length at each curing age (1, 3, 7, 14, 21, 28 and 56 days) of the mortar and G is the nominal length.

Ultrasonic pulse velocity was undertaken using a Matest ultrasonic pulse equipment (Matest, Italy) to check the quality of the mortars during curing period.

Thermogravimetric analysis (TGA) was carried out using a Netzsch STA 409PC/PG instrument. Approximately 25mg of milled paste samples was heated from 40 to 1000°C at a heating rate of 10°C/min in an aluminium crucible under a nitrogen protective atmosphere with a gas flow of 20mL/min. From the TGA data, quantification of calcium hydroxide (CH) was done according to Eq. (2)[16].

$$CH\,(\%) = \left(A\frac{74}{18} * B\frac{74}{44} \right) \tag{2}$$

where A and B are the area under DTA curve corresponding to the total mass lost due to the de-hydroxylation of CH and de-carbonation reaction respectively. The ratio 74/18 and 74/44 is the ratio of the molar mass of CH and H_2O and ratio of CH and CO_2.

Calorimetry was undertaken on the paste samples using a TAM Air isothermal calorimeter. The paste samples were mixed ex-situ and approximately 8g of the paste was inserted into the ampoule and into the calorimeter. The measurement was performed for 5 days at 20°C. Dry binder mass was used to normalize the heat flow.

3.   Results and discussion

3.1   Effect of slaking on hydration kinetics of the ternary binder

The calorimetry curves for the both binders are shown in Fig.1. The first peak corresponds to the heat released through initial dissolution and wetting of the solid particles in the binder [17,18]. Then an induction period which is influenced by the pre-treatment of CN slag in the binder. For SCN-LSG, the induction period was shorter with a difference of approximately 10 hrs to CN-LSG. This may be attributed to the possible reaction of the earlier formed calcium hydroxide (CH) with gypsum to form ettringite. Similar observation have been previously reported elsewhere [19]. The second significant peak is consistent with ettringite formations [20], the intensity of this peak was lower for CN-LSG compared with SCN-LSG. In cement systems, ettringite formation is limited by the formation of calcium hydroxide [21]. This favours ettringite formation in already slaked CN slag. Total heat released after 5 days of hydration was about 189 J/g and 174 J/g for SCN-LSG and CN-LSG respectively.
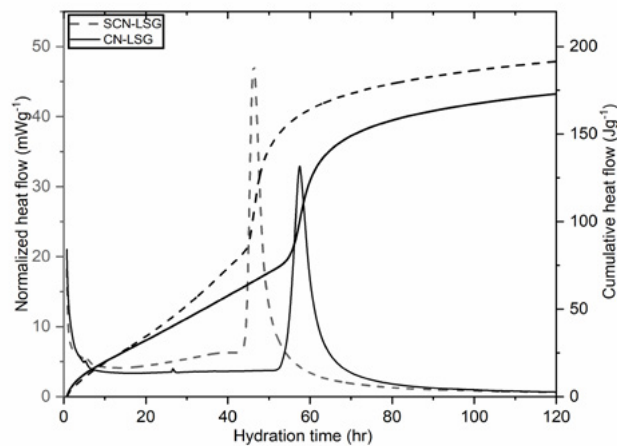
Figure 1: Heat flow and cumulative heat flow curves for SCN-LSG and CN-LSG during hydration.

3.2 Influence of slaking on $Ca(OH)_2$ amount

The results from TGA/DTA (Fig.2) shows that slaking of converter slag influenced the amount of $Ca(OH)_2$ produced during hydration. Four endothermic curves exist in the figure, the first endothermic curve between 50-250°C is attributed to the decomposition of ettringite [22]. The loss of water in gibbsite $(Al(OH)_3)$ is indicated by the second curve between 200-300°C [23]. The third curve (390-470°C) is attributed to dehydration of $Ca(OH)_2$/Portlandite (also see Eq. 4), and the endotherm between 650-770°C indicates carbonated phases most likely calcite [23]. **Though the analysis was done in a nitrogen environment, carbonation of the sample during preparation is possible and its reaction path is shown in Eq. (5).** The endotherm intensity of Portlandite curve of SCN-LSG is more than CN-LSG, which suggest that more f-CaO have been reacted during slaking. Calculated amount of 19% and 13% of CH were obtained for SCN-LSG and CN-LSG. Also, f-CaO amount determined according to SFS-EN 451-1:2004 [14], shows that the f-CaO content of the ternary mix paste was 0.23% and 0.61% for SCN-LSG and CN-LSG respectively after 28 days.
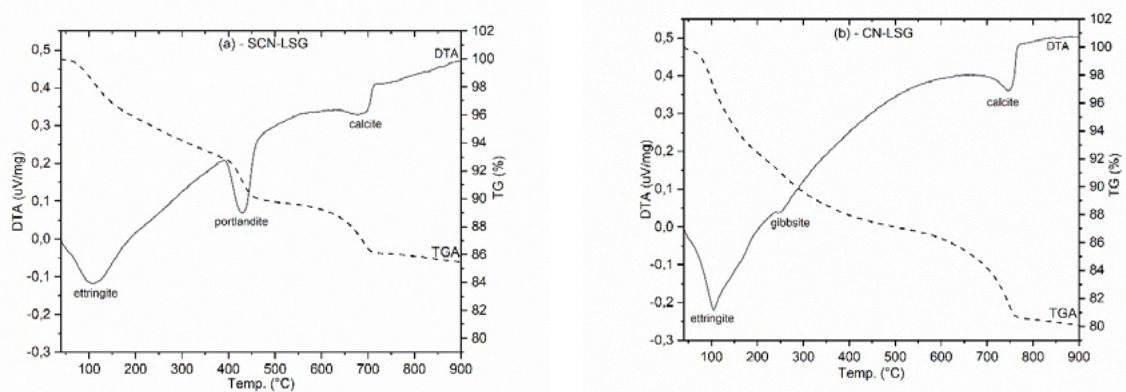
Figure 2: DTA/TGA curves of the ternary binders at 56 days (a) SCN-LSG and (b) CN-LSG.

The higher amount of Portlandite with slaked mortars is accrued to a faster reactivity of free lime during slaking than in un-slaked mortar. The fact that CaO reacts quickly during hydration can suggest that the large fraction of the f-CaO in steel slags will hydrate in a few days if it is exposed to water [24]. And also through fine grinding of the slag before slaking.

$$Ca(OH)_2 \xrightarrow{390-470°C} CaO + H_2O \qquad (4)$$

In ambient temperature (during slaking), the reaction in Eq. (4) proceeds to the left.

$$Ca(OH)_2 + CO_2 \longrightarrow CaCO_3 + H_2O \qquad (5)$$
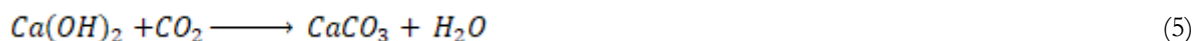
3.3   Volumetric shrinkage and expansion

The volumetric stability of both mortars was analysed through drying shrinkage and linear expansion test (Fig.3) and compared with mortars containing just ladle slag and gypsum (LSG) (see previous study [20]). The SCN-LSG and CN-LSG mortars shrunk for the first three days, with the former experiencing a higher shrinkage value. However, from 7 days both samples exhibited expansion with SCN-LSG showing a greater expansion value than CN-LSG. The increased expansion in this sample shows the existence of unstable phases in the binder and may be attributed to higher ettringite formation in the hardened mortar than in CN-LSG. In CN-LSG, the formation of ettringite is limited by portlandite formation.
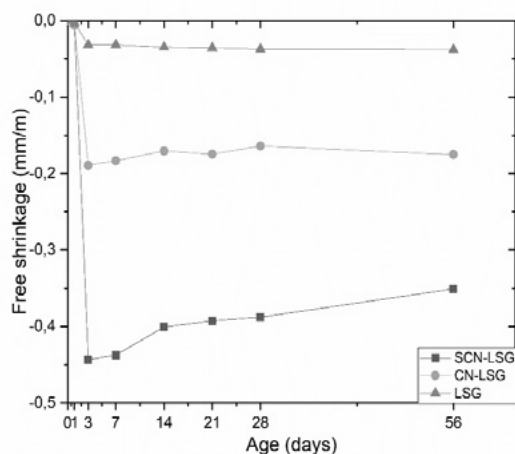

Figure 3: Length change of the mortars in comparison with a reference sample with no converter slag.

3.4   Ultrasonic pulse velocity of mortars

The mortars quality analysed through UPV in Fig. 4, shows SCN-LSG having a better microstructure than CN-LSG. The higher the rate of UPV the fewer the internal pores and cracks in the mortar anticipated. Overall, the mortars UPV continue to increase up to 56 days of analysis. The results here is consistent with the expected stability and quality of slaked slags forming calcium hydroxide before ternary mix than un-slaked slag in the ternary mix.

3.5   Compressive strength of mortars

The graph of the strength test obtained for the mortars containing slaked and un-slaked converter slag is shown in Fig. 5. Up to 28 days of curing, both mortar samples experienced similar strength, however after 56 days of curing CN-LSG experienced reduction in strength while SCN-LSG showed no strength gain after 28 days. The strength loss experienced with CN-LSG is attributed to the volume instability leading to cracks from the expansive reaction of f-CaO to CH. In addition, in Fig.6 is shown the physical appearance of both mortars, visible cracks can be seen with mortars with un-slaked converter slags after 7 days of the binder's hydration. The unchanged strength of SCN-LSG can be attributed to the dilution effect of CN slags.
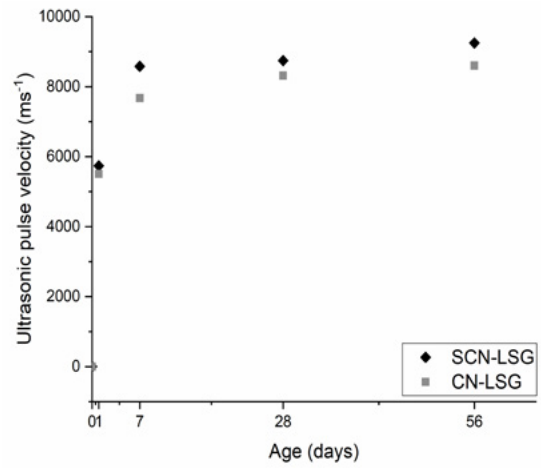
Figure 4: Ultrasonic pulse velocity for mortar samples.
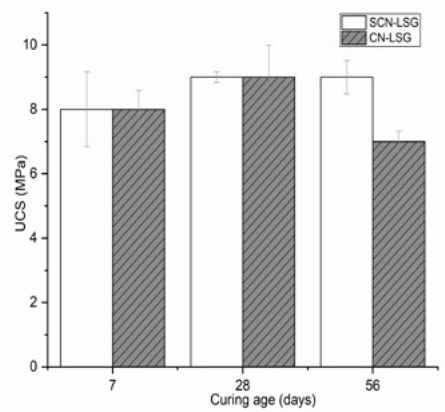
Figure 5: Compressive strength of the mortars at 7, 28 and 56 days after hydration.

Figure 6: Physical outlook appearance of both mortars after 56 days; Left: CN-LSG (NW) and Right: SCN-LSG (W).

The dilution effect occurs due to low-hydraulicity of CN slags in the ternary binder, which as a result may slow down the reaction kinetics of the co-binders. To further enhance the physical properties and applications of the ternary mortar mix, it is suggested a reduction to 30% of converter slag content in the mix.

4.   Conclusions

The experimental findings in this study proffers a sustainable and economical method to free lime content reduction in steel slag and will contribute to utilization or reuse of steel slags in concrete materials By slaking free lime in converter slag before mixing with other cementitious co-binders, the free lime content of the hardened binder was found to reduced from 7% to 0.23% after 28 days due to enhanced formation of portlandite verified through DTA/TGA. The calculated amount of portlandite from TGA at 56 days was 29% for slaked slag mortars and 13% for un-slaked slag mortars. After 56 days, 9 MPa compressive strength was achieved for the ternary mix mortars. However, the strength can be increased by reducing (30%) the amount of slaked converter content in the ternary mix.

5.   Acknowledgment

6.   References

[1]   Euroslag, Statistics 2016, Euroslag. (n.d.). https://www.euroslag.com/products/statistics/statistics-2016/ (accessed April 5, 2019).

[2]   Lizarazo-Marriaga Juan, Claisse Peter, Ganjian Eshmaiel, Effect of Steel Slag and Portland Cement in the Rate of Hydration and Strength of Blast Furnace Slag Pastes, Journal of Materials in Civil Engineering. 23 (2011) 153–160. doi:10.1061/(ASCE)MT.1943-5533.0000149.

[3]   N. Palankar, A.U. Ravi Shankar, B.M. Mithun, Durability studies on eco-friendly concrete mixes incorporating steel slag as coarse aggregates, Journal of Cleaner Production. 129 (2016) 437–448. doi:10.1016/j.jclepro.2016.04.033.

[4]   L. Muhmood, S. Vitta, D. Venkateswaran, Cementitious and pozzolanic behavior of electric arc furnace steel slags, Cement and Concrete Research. 39 (2009) 102–109. doi:10.1016/j.cemconres.2008.11.002.

[5]   J. Ma, Y. Zhang, T. Hu, S. Sun, Utilization of converter steel slag by remelting and reducing treatment, IOP Conf. Ser.: Mater. Sci. Eng. 382 (2018) 022088. doi:10.1088/1757-899X/382/2/022088.

[6]   X.-J. Liang, Z.-M. Ye, J. Chang, Study on hydration characteristics of carbonated steel slag and slag as Portland cement admixtures, Gongneng Cailiao/Journal of Functional Materials. 43 (2012) 1540–1544.

[7]   Monkman Sean, Shao Yixin, Shi Caijun, Carbonated Ladle Slag Fines for Carbon Uptake and Sand Substitute, Journal of Materials in Civil Engineering. 21 (2009) 657–665. doi:10.1061/(ASCE)0899-1561(2009)21:11(657).

[8]   S. Eloneva, E.-M. Puheloinen, J. Kanerva, A. Ekroos, R. Zevenhoven, C.-J. Fogelholm, Co-utilisation of CO2 and steelmaking slags for production of pure CaCO3 – legislative issues, Journal of Cleaner Production. 18 (2010) 1833–1839. doi:10.1016/j.jclepro.2010.07.026.

[9]   S. Eloneva, A. Said, C.-J. Fogelholm, R. Zevenhoven, Preliminary assessment of a method utilizing carbon dioxide and steelmaking slags to produce precipitated calcium carbonate, Applied Energy. 90 (2012) 329–334. doi:10.1016/j.apenergy.2011.05.045.

[10]   B. Pang, Z. Zhou, H. Xu, Utilization of carbonated and granulated steel slag aggregate in concrete, Construction and Building Materials. 84 (2015) 454–467. doi:10.1016/j.conbuildmat.2015.03.008.

[11]   G. Adegoloye, A.-L. Beaucour, S. Ortola, A. Noumowe, Mineralogical composition of EAF slag and stabilised AOD slag aggregates and dimensional stability of slag aggregate concretes, Construction and Building Materials. 115 (2016) 171–178. doi:10.1016/j.conbuildmat.2016.04.036.

[12]   C. Pellegrino, P. Cavagnis, F. Faleschini, K. Brunelli, Properties of concretes with Black/Oxidizing Electric Arc Furnace slag aggregate, Cement and Concrete Composites. 37 (2013) 232–240. doi:10.1016/j.cemconcomp.2012.09.001.

[13]   Y.-C. Ding, T.-W. Cheng, P.-C. Liu, W.-H. Lee, Study on the treatment of BOF slag to replace fine aggregate in concrete, Construction and Building Materials. 146 (2017) 644–651. doi:10.1016/j.conbuildmat.2017.04.164.

[14]   SFS-EN 451-1, Method of testing fly ash- Part 1: determination of free calcium oxide, 2004.

[15]   K. Ohenoja, P. Tanskanen, V. Wigren, P. Kinnunen, M. Körkkö, O. Peltosaari, J. Österbacka, M. Illikainen, Self-hardening of fly ashes from a bubbling fluidized bed combustion of peat, forest industry residuals, and wastes, Fuel. (2016). doi:10.1016/j.fuel.2015.10.093.

[16]   N. Shafiq, M.F. Nuruddin, Degree of hydration of OPC and OPC/Fly ash paste samples conditioned at different relative humidity, International Journal of Sustainable Construction Engineering and Technology. 1 (2011) 47–56.

[17]   E. Adesanya, K. Ohenoja, T. Luukkonen, P. Kinnunen, M. Illikainen, One-part geopolymer cement from slag and pretreated paper sludge, Journal of Cleaner Production. 185 (2018) 168–175.

[18]   C. Shi, R.L. Day, A calorimetric study of early hydration of alkali-slag cements, Cement and Concrete Research. 25 (1995) 1333–1346. doi:10.1016/0008-8846(95)00126-W.

[19]   M. Palou, E. Kuzielová, M. Žemlička, R. Novotný, J. Másilko, The effect of metakaolin upon the formation of ettringite in metakaolin–lime–gypsum ternary systems, J Therm Anal Calorim. 133 (2018) 77–86. doi:10.1007/s10973-017-6885-0.

[20]   H. Nguyen, E. Adesanya, K. Ohenoja, L. Kriskova, Y. Pontikes, P. Kinnunen, M. Illikainen, Byproduct-based ettringite binder – A synergy between ladle slag and gypsum, Construction and Building Materials. 197 (2019) 143–151. doi:10.1016/j.conbuildmat.2018.11.165.

[21]   B.A. Clark, P.W. Brown, Formation of Ettringite from Monosubstituted Calcium Sulfoaluminate Hydrate and Gypsum, Journal of the American Ceramic Society. 82 (1999) 2900–2905. doi:10.1111/j.1151-2916.1999.tb02174.x.

[22]   M. Fridrichová, K. Dvořák, D. Gazdič, J. Mokrá, K. Kulísek, Thermodynamic Stability of Ettringite Formed by Hydration of Ye'elimite Clinker, Advances in Materials Science and Engineering. (2016). doi:10.1155/2016/9280131.

[23]   N.C. Collier, TRANSITION AND DECOMPOSITION TEMPERATURES OF CEMENT PHASES - A COLLECTION OF THERMAL ANALYSIS DATA, Ceramics - Silikaty. (2016) 1–10. doi:10.13168/cs.2016.0050.

[24]   I.Z. Yildirim, M. Prezzi, Chemical, Mineralogical, and Morphological Properties of Steel Slag, Advances in Civil Engineering. 2011 (2011) e463638. doi:10.1155/2011/463638.

CSA as A Revisited Vernacular Technique for Earth Stabilization

B. Cicek [1], N. Pires Martins[2], C.Brumaud[2] G. Habert[2]

[1] Chair of Design and Structural Systems, Bauhaus-University Weimar, Weimar Germany,

[2] Chair of Sustainable Construction, ETH-Zürich, Zürich, Switzerland

Abstract

The Calcium Sulfoaluminate (CSA) is presently receiving a lot of interest in the building sector. It is being used to produce CSA-Cements, which generates less CO_2 than Ordinary Portland Cement (OPC), but still requires the production of clinker at high temperature. For the moment, its application is mainly limited to China. On the other hand, the considerable interest in modern earth-based building materials has led to the increase of new types of products such as precast earth, prefabricated earth panels and boards on the market. Their major drawbacks are the low water stability and moderate strength leading to cement stabilization, which as a consequence reduce their environmental advantage. This paper deals with the rediscovery of a vernacular technique of producing CSA for a new stabilized earth-mixture. The first laboratory analyses on this mix-design have proven a high water-resistance. Furthermore, the results show a remarkable increase in compressive strength. Finally, the characterization of the stabilization effect has been performed through X-ray powder diffraction patterns (XRD) and clearly identify the production of ettringite using very low CO_2 intensive raw materials. These results open a new avenue for earth stabilization and secure the implementation of this material in the conventional construction industry.

Keywords: Calcium Sulfoaluminate (CSA), stabilized earth, XRD, earth-based building materials

1.   Introduction

Calcination is the release of CO_2 from carbonates during pyroprocessing of the raw mix. Calcination CO_2 is directly linked with the clinker production, used for the production of Portland cement. In addition, calcination of cement kiln dust is a relevant source of CO_2 in countries where such dust is discarded [1]. In fact, the kiln temperature required for the manufacture of CSA clinker is ~1250°C, which is 200°C lower than the temperature used for Portland cement clinker [2]. CSA cement, which is more expensive than a Portland cement (PC) can reduce only less than 14% of production temperature. Therefore, the production of cement types in general contributes significantly to global CO_2 emission. While we often talk about the environmental problems caused by very energy-intensive sectors, earthen architecture needs to be as stronger as it has been in the past. At present, there are a few countries, where environmentally friendly architecture is getting more and more popular. This popularity is due to a recently growing construction sector, which offers contemporary earthen products and completion methods to the planners and costumers [3]. However in contemporary earthen architecture, cement is being commonly used to stabilize the earth material. An environmental friendly strategy to substitute cement with other additives is needed. For this purpose, a variety of alternative materials with lower environmental impacts can be used. Their use is based on the importance of minimizing CO_2 emissions, as well as increasing interest

in the production of cementitious materials that develop good mechanical properties and good stability in corrosive environments[4]. This paper deals with an alternative solution, consisting in combining trass, gypsum and lime to replace the use of cement in a vernacular way.

1.1 CSA and Stabilization

CSA-cement forms predominantly ettringite (anhydrous calcium Sulfoaluminate), belite (dicalcium silicate) and gypsum (gypsum calcium sulphate). These reaction products are responsible for the stable strength of CSA concrete. In this study, it was aimed to produce similar water insoluble reaction products with the help of proposed additives to develop an earth-mix with a higher and durable strength. To overcome the common drawbacks of earth construction materials, utilizing the stabilization effect is a significant application. However, it was only in 1920 that a scientific approach could be developed [5]. Soil stabilization is known as the process that enables the control of dimensional changes that clays suffer when they come into contact with water [6]. While mechanical stabilization allows controlling the binder and water repellents, the chemical stabilization allows the dost control, water erosion-control and micro and macro structural stability [7]. Since ancient times, small proportions of lime [6], pozzolan and gypsum were used in combination with earth. Murthy *et al.* [7] classified the stabilizing agents as traditional and non-traditional. According to this classification gypsum, lime and pozzolans are traditional agents. Trass is rich in acid reactive components such as SiO_2 and Al_2O_3, it shows a very high pozzolanicity in a highly alkaline environment. Lime alone has several effects on stabilization. It provides an environment with a high pH, which accelerates the pozzolanic reactivity. It extends the rapid hardening of gypsum and makes it possible to gain about extra 20 min of working time [17][18]. Also, lime reacts with the clay minerals of the soil, or with any other fine, pozzolanic components such as hydrous silica, to form a tough water-insoluble gel of calcium silicate, which cements the soil particles [19]. The interaction between clay particles and lime is, however, a long-term process. Diamond *et al.* [20] reports this stage as an accumulation of soil-lime reaction products, causing a slow development of strength. The addition of gypsum supplies mainly sulphate to the mixture which forms, together with the trass minerals, the ettringite.

Since the beginning of modern research on stabilization, several studies have tried to explain the effects of gypsum, lime and pozzolan stabilization. In 2007, Vroomen [8] researched the properties of cast gypsum-stabilized earth. According to this study, a great advantage of gypsum over cement is that it can be produced locally by small-scale enterprises and it demands a low amount of energy in production as it can be calcined at approx. 125°C instead of 1100°C. In 2011, Lopez *et al.* [9] studied the chemical reaction between soil, fly ash (15%), gypsum (10%), lime (2%). They stated, when fly ash and lime are mixed with water, there is no chemical reaction in the initial phase. However, with increasing curing time a pozzolanic reaction begins between the fly ash and the gypsum. In 2012, Pekmezci *et al.* [10] published a paper showing the performance of earth structure by using lime (2,5-5%) and gypsum (8-10%) addition. In this study, however, the fly ash, which is a by-product and classified as an artificial pozzolan, is being substituted with a natural pozzolan called trass. This is due to several drawbacks: its production is seasonally limited and its usage encourages the sectors producing by-products of burning processes and therefore, contributes to environmental impacts. Jackson *et al.* [11]reports, with the current decline in coal-fired energy, fly ash is now becoming technically and/or economically unfeasible for use in concrete. Furthermore, artificial pozzolans result from chemical and/or structural modifications of original material, which may have weak pozzolanic characteristics, or not. On the contrary, natural pozzolans do not require any treatment before their use [9].

2. Materials and procedures

2.1 Materials

The earth used for the preparation of stabilized earth specimens consists of 30% commercially available

mineral earth material for plastering (Stroba Naturbaustoffe Ag, Switzerland) and of 70% standard sand CEN EN 196-1. The X-ray powder diffraction technique revealed, thanks to Rietveld methods [32,33], that the main mineralogical components are muscovite/illite (24.8wt%), quartz (21.3wt%), kaolinite (21.3wt%) and smectite (16.6wt%). The complete mineralogical composition is given in Table 1.

Table 1: chemical composition of terrasol used for sample preparation

	Anastase	Calcite	Chlorite	Goethite	Kaolinite	Microcline	Muscovite/ Illite	Plagioclase-Albite	Pyrite	Quartz	Rutile	smectite
(%)	0.3	<0.2	1.1	9.1	21.3	2.3	24.8	1.2	0.4	21.3	1.6	16.6

Three different additives (trass, gypsum and lime) were used in combination to stabilize the earth material. The trass (Tubag, Germany) was used as pozzolanic additive. It is also known as "rheinischer Trass". Its chemical composition, obtained through X-ray fluorescence spectrometry (XRF), is given in Table 2. Trass is a natural pozzolanic material, which can be found in various regions of the earth. The mineral composition of trass is mainly volcanic glass, zeolitized to a different extent (clinoptilolite), and secondary components from cyrstaloclasts of magnetite, zircron, apatite, biotite, quarz, sanidine, plagioclase [12]. XRD pattern of the trass is given in Figure 1. Commercially available hemihydrate gypsum ($CaSO_4 \cdot 1/2H_2O$) was used. Moreover, a hydrated lime ($Ca(OH)_2$) was used as an additive.

Table 2: Chemical composition of the trass studied by X-ray fluorescence analysis. Values are given in mass % [13].

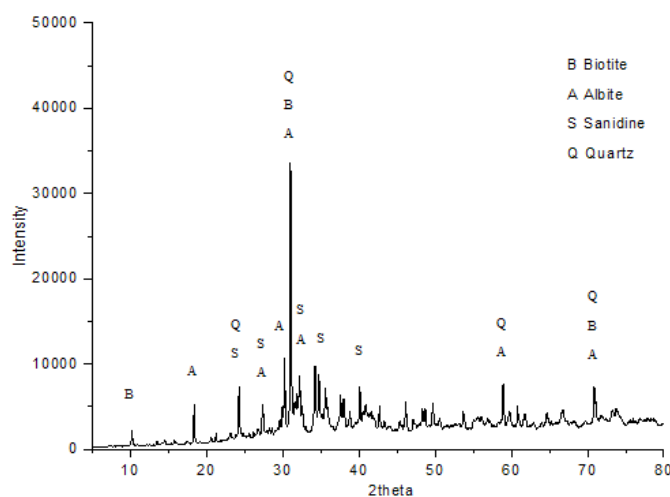| Component,(%)	SiO_2	Al_2O_3	TiO_2	Fe_2O_3	MgO	Mn_2O_3	P_2O_5	CaO	SO_3	K2O	Na_2O
	56.90	18.50	1.10	6.30	2.20	0.2	0.2	5.20	0.20	5.70	3.50

Figure 1: X-ray diffraction spectrum of the trass used in this study.

2.2 Sample preparation:

Three different stabilized earth samples were produced by using different proportion of trass, gypsum, and lime as additives to determine their efficiency on water resistance and on the strength of earth materials.

The mass of lime was kept constant at 2.5 wt% in all series: only the proportion of trass and gypsum was varied form one sample to the other. For all samples, the water to binder ratio was determined as 0.4 allowing to obtain a pourable material. The mix samples were poured into standard steel moulds (4cm x 4cm x 16cm). The mixture proportions and labelling of the stabilized earth samples are given in Table 3. After the addition of water, the mixing and the casting of specimens were no longer than 10 minutes. The mixing of the material was done manually. Samples were stored at 23°C and 50% relative humidity.

Moreover, to identify the pozzolanic reaction products, XRD analyses were performed on mix-designs mentioned in Table 3. The samples for the XRD analyses were prepared without earth. Therefore, the chemical interaction between additives and clay was not investigated in this study. XRD samples were cured for 7 days at 23°C and 50% relative humidity.

Table 3: The labelling and mixture proportions of the specimens

Labelling	PE	T10G8	T14G4	T16G2
Description	Plain earth with 30% terrasol and 70% standard sand	Earth with 10wt% trass, 8wt% of gypsum and 2.5wt% of lime	Earth with 14wt% trass, 4wt% of gypsum and 2.5wt% of lime	Earth with 16wt% trass, 2wt% of gypsum and 2.5wt% of lime

2.3 Procedures

The pozzolanic activity can be determined by physical, chemical or mechanical means. In this research, together with the water insertion test, the compressive strength (mechanical method) and XRD analysis (physical method) have been conducted to determine the pozzolanicity of the proposed mix-design. To determine the water resistance of stabilized and non-stabilized earth specimens, water insertion test was done. The water insertion was carried out according to the standard DIN 18945. The specimens were cured at 23°C and 50% relative humidity for 14 days. The loss of material was determined by filtering the residue in the dip tank. 7 and 28-day compressive strength tests were carried out on prismatic specimens with the dimensions of 40 x 40 x 160 mm. Mineralogy of the samples is determined on randomly oriented powder specimens with X-ray diffraction analysis [14]. X-ray diffraction measurements were made using a Bragg-Brentano X-ray diffractometer (D8 Advance, Bruker AXS, Germany) using CoKα radiation. The qualitative phase analysis was carried out with the software package DIFFRACplus (Bruker AXS) [15].

3. Results and discussions

3.1 Water Contact Tests

One of the main decaying factors in earth constructions is the presence of water. Once plain earth gets contact with water, it swells, and the dissolution and erosion are inevitable. To overcome this weakness, stabilization of earth can be a significant application. The loss of mass of the stabilized earth specimens and plain earth after the water insertion test is plotted in Figure 2. According to the water insertion test described in DIN 18945, the loss of mass has to be less than 5% of the total mass to be considered as acceptable. After 10 min. of water insertion, the loss of mass of the plain earth samples was determined as 38.406% of the total mass. However, as can be seen in Figure 2, all stabilized earth samples have shown similar behaviour and the loss of mass of all stabilized series is between 0.02-0.03 percent of total mass, which is significantly lower than the limit value. Moreover, no cracks were observed due to swelling: the proposed combination of additives significantly improved the water stability of the earth specimens. However, it can be observed that the change in trass/gypsum ratio does not influence the water resistance of the stabilized earth specimens.
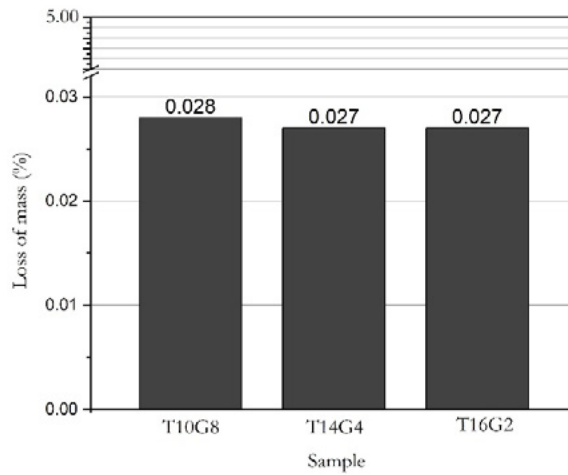
Figure 2: Loss of mass of stabilized earth samples after water insertion test.

3.2 Compressive strength

The 7 and 28-days results of compressive strength tests of stabilized earth specimens are shown in Figure 3. As can be seen in Figure 3, the maximum compressive strength is obtained for T16G2 samples containing 16wt% of trass and 2wt% of gypsum. While T10G8 containing the highest amount of gypsum does not show an increase in compressive strength from 7 to 28 days, the samples prepared with a higher amount of trass progressively gain strength from 7 to 28 days. Samples containing 14 and 16wt% of trass show a similar parallel behaviour of strength improvement from 7 to 28 days. Using higher content of trass allows improving the compressive strength of stabilized earth materials. These results show that the compressive strength of the earth material can be significantly improved with the proposed mix design of additives.
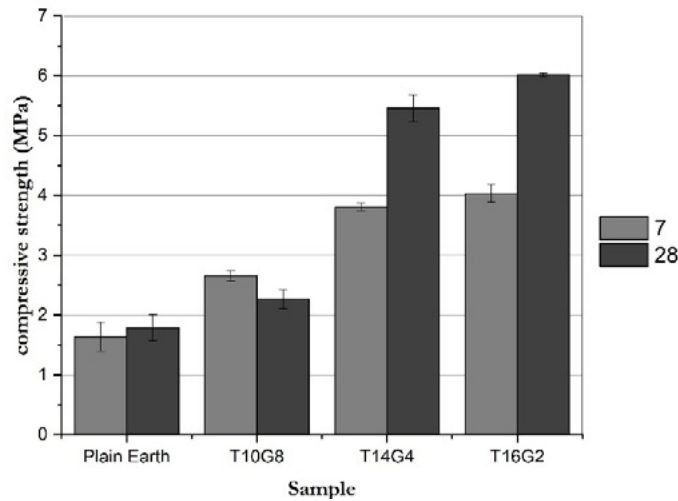
Figure 3: Compressive strength of the studied specimens.

3.3 XRD Analyses

The mechanism of stabilization is based on pozzolanic activity, which causes a durability effect in an environmentally friendly way. To better understand this mechanism and to identify the products of pozzolanic reactions, the mineralogical composition of the mix-designs were analysed with the help of X-ray diffraction (XRD). The XRD results of 7day cured mix-designs are given in Figure 4. As can be seen in the XRD pattern, the sample with 10 wt% of trass and 8 wt% of gypsum (T10G8) displays high amounts of gypsum. As expected, the intensity of gypsum peaks is being reduced by increasing the amount of trass. Very weak peaks of ettringite can be observed in T10G8. However, it can be noted that, with the

increasing amount of trass in samples, the intensity of the ettringite peak is getting higher. The reason for this behaviour is assumed to be the pozzolanic effect of trass. The chemical additives react with particles of trass to produce hydration products such as ettringite ($Ca_6A_{12}(SO_4)_3(OH)_{12} \cdot 26H_2O$). A part of Aluminium is being consumed by the formation of ettringite. However, we found in all samples a notable amount of analcime ($NaAlSi_2O_6 \cdot H_2O$), which also consumes a part of aluminium in trass. On the other hand, a great amount of calcite and muscovite was observed in all series.
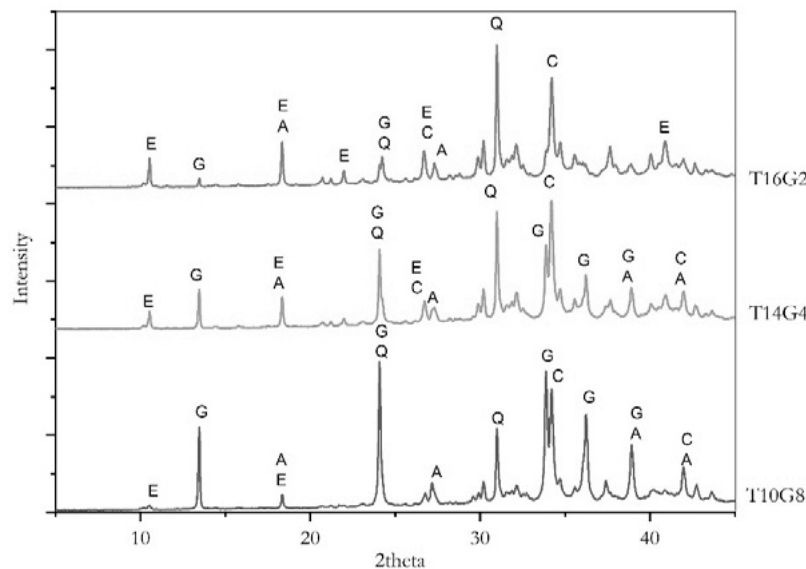
Figure 4: XRD pattern of the studied mixes of additives (without earth). (E; Ettringite, G; Gypsum, A; Analcime, Q;Quartz, C;Calcite)

4.   Conclusions

This paper focuses on the stabilization effect of trass (pozzolan) + gypsum ($CaSO_4$ ½H_2O) + lime ($Ca(OH)_2$) system on the mechanical and physical properties of the unfired earth, as a vernacular solution to replace the use of cement in earth stabilization. The results drawn from this study can be summarized as follow:

1. The water-resistance and the compressive strength of the plain earth were improved by the presence of trass, gypsum and lime.

2. Ettringite, which is typical hydration product of Portland cement, could be produced with the proposed mix design.

3. With the increasing amount of trass, the precipitation of ettringite was increased. This provokes the progressively improvement of compressive strength of the stabilized earth.

4. Although samples containing the highest amount of gypsum showed in early age higher stability than plain earth samples, the strength improvement of these stabilized earth samples was mainly limited with the setting of gypsum alone.

5.   Acknowledgment

6. References

[1]   Vanderborght, B.; Brodmann, U. Development, W. B. C. for S., 2001, *The Cement CO2 Protocol: CO2 Emissions Monitoring and Reporting Protocol for the Cement Industry.*

[2]   Chaunsali, P., and Mondal, P., 2015, "Influence of Calcium Sulfoaluminate (CSA) Cement Content on Expansion and Hydration Behavior of Various Ordinary Portland Cement-CSA Blends," J. Am. Ceram. Soc., **98**(8), pp. 2617–2624.

[3]   Cicek, B., 2016, "A Methodolgy for an Active and Sustainable Earthen Construction Sector," *SBE16 Istanbul. Smart Metropoles, Integrated Solutions for Sustainable and Smart Building & Cities*, E. Erkal, A., Acuner, ed., Istanbul.

[4]   Gallardo H., M., Almanza R., J. M., Cortés H., D. A., and Escobedo B., J. C., 2016, "Mechanical and Chemical Behavior of Calcium Sulfoaluminate Cements Obtained from Industrial Waste," J. Latin-American Assoc. Qual. Control. Pathol. Recover. Constr., **6**(1), pp. 15–27.

[5]   Houben, H., Guillaud, H., 1994, *Earth Construction – A Comprehensive Guide*, Intermediate Technology publications, London.

[6]   Mileto, C. Vegas, F., García Soriano, L., Cristini, V., ed., 2015, "Earthen Architecture: Past, Present and Future," *International Conference On Vernacular Heritage, Sustainability And Earthen Architecture*, CRC Press/Balkema, valencia, Spain, pp. 176–178.

[7]   Murthy, G., Kavya, S., Krishna, V., and Ganesh, B., 2016, "Chemical Stabilization of Sub-Grade Soil With Gypsum and Nacl," **9**(5), pp. 569–581.

[8]   Vroomen, R., 2007, "Gypsum Stabilised Earth," Eindhoven University of Technology, The Netherlands.

[9]   Marín López, C., Reyes Araiza, J. L., Manzano-Ramírez, A., Piñón, J. P., Hernández Landaverde, M. A., De Jesús, J., Bueno, P., and Marroquín De Jesús, Á., 2011, "Effect of Fly Ash and Hemihydrate Gypsum on the Properties of Unfired Compressed Clay Bricks," Int. J. Phys. Sci., **6**(17), pp. 5766–5773.

[10]   Pekmezci, B. Y., Kafesçioğlu, R., and Agahzadeh, E., 2012, "Improved Performance of Earth Structures by Lime and Gypsum Addition," Metu J. Fac. Archit., **29**(2), pp. 205–221.

[11]   Jackson, M. D., Oleson, J. P., Moon, J., Zhang, Y., Chen, H., and Gudmundsson, M. T., 2018, "Extreme Durability in Ancient Roman Concretes," Am. Ceram. Soc. Bull., **97**(5), pp. 22–28.

[12]   Yoleva, A., Djambazov, S., and Chernev, G., 2011, "Influence of the Pozzolanic Additives Trass and Zeolite on Cement Properties," J. Univ. Chem. Technol. Metall., **46**(3), pp. 261–266.

[13]   "Ein Werk Der Natur. TubagTrass" [Online]. Available: http://www.joostdevree.nl/bouwkunde2/jpgt/tras_1_tubag_trassbroschuere_24s_sept2010_www_tubag_de.pdf. [Accessed: 10-Apr-2019].

[14]   Bish, D.L., Plötze, M., 2011, "X-Ray Powder Diffraction with Emphasis on Qualitative and Quantitative Analysis in Industrial Mineralogy. In Advances in the Characterization of Industrial Mineral," G.E. Christidis, ed., EMU and Mineralogical Society, London, pp. 35–76.

[15]   Döbelin, N., Kleeberg, R., 2015, "Profex: A Graphical User Interface for the Rietveld Refinement Program BGMN," J. Appl. Crystallogr., **48**, pp. 1573–1580.

[16]   Gava, G. P., and Prudêncio, L. R., 2007, "Pozzolanic Activity Tests as a Measure of Pozzolans'

Performance. Part 1," Mag. Concr. Res., **59**(10), pp. 729–734.

[17]   Isik, B., and Tulbentci, T., 2008, "Sustainable Housing in Island Conditions Using Alker-Gypsum-Stabilized Earth: A Case Study from Northern Cyprus," Build. Environ., **43**(9), pp. 1426–1432.

[18]   Kafesciogli, R., Toydemir, N., Özüekren, B., Gürdal, E., *Yapi Malzemesi Olarak Kerpicin Alci Ile Stabilizasyonu*, Istanbul.

[19]   Ingles, O.G., Metcalf, J. B., 1972, *Soil Stabilization. Principles and Practice*, Butterworths Pty. Limited, Sydney, Melbourne, Brisbane.

[20]   Diamond, S., and Kinter, E. B., 1965, "Mechanisms of Soil-Lime Stabilization," Highw. Res. Rec., **92**, pp. 83–202.

Assessment of mine tailings as precursors for alkali-activated materials for on-site applications

R. Obenaus-Emler[1], M. Falah[2], M. Illikainen[2]

[1]Montanuniversität Leoben, Leoben, Austria

[2]University of Oulu, Oulu, Finland

Abstract

Year after year the mining industry generates 5-7 billion metric tons of tailings worldwide. They are mostly disposed rather than valorised. The substantial amounts of tailings has led to growing concerns about their ecological and environmental impacts such as occupation of large areas of land, generation of windblown dust, and contamination of surface and underground water. Over the past years the mining industry has been subjected to increase environmental principles. As the consequence, besides waste rock and water management, tailings management becomes a progressively important factor for ecologic and economic reasons. Mine tailings from flotation processes are normally disposed in impoundments on the surface. This may cause environmental and safety problems including serious water pollution arising from contamination of surface water, groundwater, and soils due to the leaching of heavy metals, process reagents, and Sulphur compounds. Recently the process of alkali-activation and geopolymerisation has been explored as a potential method for tailings consolidation and heavy metal fixation. The tailings of many existing mining operations contain the aluminosilicate minerals needed for alkali-activation at least to some extent. From a sustainability point of view it makes sense to use alkali-activated products from tailings directly on the mine site as e.g. (1) backfill material applied to fill open cavities from the (underground) mining operation and (2) cover materials for surface deposits of tailings in order to store them ecologically safe and sealed off from the environment. Mine tailings from different mining operations around the world have been investigated regarding their potential use as precursors for alkali-activated materials. An assessment of the release of gel forming elements into alkaline solutions was performed by leaching experiments under various conditions (time, concentration of the solvent, and temperature). Compared to traditional alkali-activated precursor materials the release of aluminium and silicon is in general low for the mine tailings investigated. However, results indicate a favourable ratio of Si/Al for the formation of gels similar to other alkali-activated products. Additionally, the leached calcium can contribute to the strength of the resulting products by forming C-S-H gels when a considerable amount of Si is present in the pore solution either from the activator or dissolved from the material itself. The results of the leaching tests were used to facilitate the mix design for alkali-activated products. In order to increase the mechanical strength of the final product different approaches were considered: (1) addition of reactive materials (e.g. blast furnace slag), (2) increasing the reactivity of the tailings by grinding, and (3) increasing the reactivity by curing at elevated temperature. Depending on the tailings type, the mix design, and the curing conditions the final material shows a compressive strength in excess of 30 MPa even for curing at low temperatures. The investigated mine tailings can potentially be used for various applications on the mine site. With regard to specific target applications a further evaluation of long term properties of the resulting products (e.g. freeze-thaw resistance) has to be performed. Furthermore, results indicate that products with even higher

strength can be manufactured by further reducing the particle size of the tailings or by the addition of other reactive materials.

Keywords: Alkali-activated binders, mine tailings, alternative raw materials, environmental impact.

1.   Introduction

Whenever a mine is developed, in general huge amounts of host rock have to be mined additionally and subsequently stored. The amount of (mostly valueless) waste rock varies much, depending on the ore body and whether the ore is mined from an open-pit or an underground mine. Due to intergrowth of minerals, even the mined ore itself contains valueless material. Furthermore, some ore might be left behind in the mine due to the chosen mining method, low grades, or other economic reasons. The dilution of the ore with waste rock can be substantial resulting in increased mineral processing costs and amount of tailings but no economic revenue. [1]

One of the major environmental issues of the mining industry is the waste streams that can reach over 90 % of the total mass for many ore types. When using a flotation process in mineral processing this waste stream (i.e. tailings), is a mixture of different minerals, process chemicals, and water in the form of a thick slurry. The tailings are mostly deposited in tailings storage facilities (TSFs) at the surface or sometimes used as paste backfill to fill underground cavities. Since the storage of tailings normally plays a minor role in the mining industry, little effort has been made regarding the valorisation of the tailings up to now.

Recently, more attention is paid to the deposition of tailings in TSFs at the surface by general public and especially legal authorities. Various problems are related to the storage of tailings at the surface [2]:

1.   When tailings contain sulphide minerals, such as pyrite (FeS_2) or pyrrhotite ($Fe_{1-x}S$), oxidation in the presence of oxygen and water (either from rainfall, surface water streams or from mineral processing) results in the formation of sulphuric acid. If not being captured this may lead to severe ecological problems and the so called acidic mine drainage (AMD).

2.   The huge amounts of tailings results in very large deposits on the surface, which the authorities do not permit any more or a suitable large space cannot be found or is strongly opposed by the communities close to the mine.

3.   When dams are used for the deposit a dam failure can result in an ecological disaster.

As a consequence the disposal of mine tailings is a major environmental liability becoming increasingly important for current and future mining operations especially on ore bodies with low grades. In order to prevent the problems related to tailings storage, new approaches are needed and might even become critical for future mining operations. [1,2]

There are different ways and means to reduce the potential environmental hazards related to the storage of mine tailings and waste rock: (1) Isolation of waste materials from the nearby environment by capping, (2) chemical stabilization of especially mine tailings by adding chemicals or cementitious materials to immobilize heavy metals, and (3) a combination of these two methods. For the simultaneous use of isolation and stabilization techniques, the tailings surface can be treated by binders such as organic polymers, water glass or Ordinary Portland cement (OPC) to improve the resistance of the surface to erosion and reduce water infiltration, isolating the underlying tailings from the surrounding environment [3-5]. Although OPC has its benefits in the stabilization of certain mine tailings, it has several drawbacks such as low acid resistance, high cost as well as high energy consumption and CO_2 emissions related to the production of OPC.

Using the concept of alkali-activation, alumosilicate raw materials can be turned into valuable cementitious-

like materials. Depending on their composition, the resulting alkali-activated materials or geopolymers have comparable properties to OPC, but may also show additional advantages such as rapid development of mechanical strength, high acid resistance, immobilization of toxic and hazardous materials, and a considerable reduction in greenhouse gas emissions [6-9]. Simplified, geopolymers can be formed by the reaction of aluminosilicate raw materials with highly alkaline solutions by leaching of Al and Si from the solid precursors with subsequent formation of a gel with a molar ratio of M:Al:Si roughly equal to 1:1:4, where M represents an alkali earth metal [6,10]. Initially metakaolin and fly ash were used as the main raw materials for geopolymers and have become model compounds for the comparison with other precursor materials. In recent years a number of other raw material sources (e.g. various other types of fly ash, natural minerals, metallurgical waste materials as well as their mixtures) have been studied to synthesize geopolymers [11].

The tailings of many existing mining operations contain the aluminosilicates needed for alkali activation at least to some extent and therefore offer an interesting alternative source material for alkali activated materials and geopolymers [11]. Even though natural rock can be thought of as a rather non-reactive material, the fine particle size distribution of the tailings might be advantageous right away or allowing for additional processes steps for substantially increasing the reactivity.

In a nutshell, this study addresses the valorisation of mine tailings as precursors to alkali-activated materials to be used for applications primarily at the mine site. The dissolution of relevant species is assessed by leaching in alkaline conditions and compared to other precursor materials. Furthermore, the compressive strength of alkali activated mixtures was determined in order to verify the suitability for the intended applications. The resulting alkali-activated materials can be used directly at the mine site as (1) a back fill material to fill underground cavities or (2) a covering layer for surface deposits of tailings. Depending on their properties the resulting materials could also be used for other applications (e.g. construction industry). The best-case scenario leads to a mining activity without any needs to deposit tailings on the surface or a minimized amount of tailings deposited on the surface using a covering layer for safely storing the tailings shielded from environmental conditions. Hence, in the near future mining operations can be more ecologically friendly and probably even more economically feasible compared to traditional mining operations.

2.   Methodology

In order to assess the reactivity of solid precursor materials the leaching of relevant species in alkaline solutions was studied at a constant solid to liquid ratio with varying conditions for time, temperature und solvent concentration.

The results of the leaching experiments were taken into account for the mix design of alkali-activated materials and can also help to understand the possible reaction mechanisms during hardening. Enhancing the reactivity of the solid materials was investigated in order to increase the mechanical strength of the final products by the following approaches: (1) addition of other reactive materials, (2) increasing the specific surface area of the tailings, and (3) curing the products at elevated temperature. However, the main focus was put on using the tailings as delivered without further pre-treatment steps (like e.g. grinding or calcination) and thereby making it possible to apply solutions directly at the mine site without additional high investment into large infrastructures.

2.1   Materials

In this study the tailings from the following mining operations were investigated:

1. MT 1 – tailings from a copper/nickel mine (Northern Europe, low content of sulphides)

2. MT 2 – tailings from a copper/zinc mine (Southern Europe, high content of sulphides)

3. MT 3 – tailings from a platinum mine (Africa)

4. MT 4 – tailings from an iron ore mine (South America)

All tailings samples were supplied wet (mostly as slurries) and dried at 110 °C prior to any laboratory experiments. In order to prevent oxidation of samples containing a high amount of sulphides, only small portions were dried shortly before use.

Additionally to the tailings samples metakaolin (MK) and granulated blast furnace slag (GBFS) were used as solid additives. MK was delivered as a dry powder. GBFS was delivered moist with a particle size distribution smaller than 4 mm. The GBFS was dried at 110°C and comminuted using a ball mill to a final specific surface area of approximately 3300 cm²/g.

The chemical composition of solid materials was determined by XRF on fused beads of the original sample after determination of the loss on ignition (LOI). The qualitative mineralogical composition was determined by XRD on loose powder bed samples. Different particle size fractions of the samples were obtained by dry classification. The particle size distribution of the samples was determined by laser diffraction (dry dispersion).

Furthermore, a chemical grade concentrated sodium hydroxide solution (NaOH) and a sodium silicate solution (waterglass, Na_2SiO_3) were used. The concentrated NaOH solution was diluted to the desired concentration using deionized water. The waterglass solution used has a solids content of approximately 35,3 m% with a mass ratio Na_2O to SiO_2 of 3:10.

2.2 Leaching experiments

Leaching of solid precursor materials in alkaline conditions was performed using a similar procedure as described in literature (e.g. Xu and van Deventer [12,13]) using a solids to liquid ratio of 2 g per 100 ml of solvent. The standard conditions for the leaching experiments are a duration of 24 hours at a temperature of 40°C using a 5M NaOH solution, but additional parameter studies for relevant parameters have been performed for some materials. In order to prevent contamination of the leachates with Si from glass containers, plastic equipment was used for storage and during the experiments. The leaching was done by the following procedure:

1. Preheating of the solid precursor material in a sealable plastic container.

2. Addition of preheated solvent.

3. Mixing of solids and solvent using a bottle roller with 60 rpm for the desired reaction time.

4. Filtration of solids and leachate.

5. Dilution of the leachate 1:50 with deionized water.

6. Acidification to a pH between 2 and 3 using 4M HCl to prevent precipitation prior to analysis.

7. Determination of the concentration of leached species by ICP-MS.

The elemental concentrations of the leachates were corrected by the concentrations in the blank solvents treated by the same procedure.

In order to investigate the leaching residue after the experiment the filtration residue was washed with deionized water in order to eliminate excess NaOH of the leaching experiment. The residue was dried at 110°C and further investigated. However, the change of mass of the dried solid residue compared to the initial sample was below the detection limit for the chosen experimental setup (< 0,5 m%).

MT 3 was chosen for further leaching experiments with additional variation of the temperature. The experiments were carried out with 1M, 5M, and 10M NaOH solution for leaching durations of 24 and 72 hours.

2.3   Mix design and testing

The crucial property of resulting alkali-activated materials for this investigation was the uniaxial compressive strength. It was tested using small cylindrical samples with a diameter of 40 mm and a height of 30 mm.

With regard to a possible installation of the alkali-activated mixes by pumping the consistency is crucial for the mix design. In order to ensure a desired viscosity of the mix the liquid to solids ratio was kept constant for a given solid raw material. Since there is a high variation in the density of the activator solution depending on its composition (concentration) a certain volume of liquid activator solution was used for a given mass of solids. For the activator solution mix the NaOH solution and the waterglass solution were premixed and the volume adjusted to the desired amount by addition of deionized water. The activator solution was then mixed with the solids by hand in a small beaker with a rod until a homogeneous mix was obtained. The mix was poured into silicone moulds and compacted by vibration. The samples were then covered with a silicone mat and stored in locked boxes until testing at the chosen curing temperature. The compressive strength was determined by recording the maximum force using a universal testing machine.

For MT 1 an activator screening with mixtures of NaOH and waterglass solutions was performed initially with a constant amount of 27.5 ml of activator solution for 100 g of solid mine tailings. The samples were cured for 7 days at a temperature of 60°C prior to determination of the compressive strength. The results showed, that the highest strength was achieved when using waterglass solutions as an activator with only little to no further addition of NaOH. Therefore, further experiments were carried out using only waterglass solutions with concentrations between 10 to 30 m% of solid waterglass and testing after curing for 7, 14 and 28 days. Since the results were quite promising, further experiments were performed with the same recipes and curing at 40°C and room temperature (RT). The other mine tailings were studied less extensive.

In addition to the determination of the strength of the final products, selected samples with high strength have been further investigated by XRD and SEM.

3.   Results and discussion

3.1   Material characterisation

Table 1 shows the characteristic parameters of the particle size distribution of the mine tailings as delivered. The fineness is governed by the specific ore characteristics and related to the intergrowth of the valuable minerals with the matrix minerals. In general the tailings show a high fineness which is favourable for alkali-activation. Table 2 summarizes of the chemical composition of the solid precursor materials. The metakaolin (MK) used in this study is a technical grade stochiometric metakaolin with at least 95 m% of $Al_2Si_2O_5$ and a x_{50} of 1.5 μm. Table 3 gives an overview of the mineralogical composition (in alphabetical order) of the mine tailings samples. Due to the granulation process the GBFS has solidified in a glassy state and does not show any peaks in the XRD pattern.

Table 1: Characteristic parameters of the particle size distribution of mine tailings.

	MT 1	MT 2	MT 3	MT 4
	Cu/Ni tails	Cu/Zn tails	Pt tails	Fe tails
x_{90} [μm]	54	25	90	9.0
x_{50} [μm]	7.5	4.6	10	2.4
x_{10} [μm]	0.9	1.0	1.6	0.8

Table 2: Chemical composition of the solid precursor materials determined by XRF.

		MT 1	MT 2	MT 3	MT 4	GBFS
		Cu/Ni tails	Cu/Zn tails	Pt tails	Fe tails	
Main components [g/100g]	Na_2O	0.30	0.32	1.48	0.03	0.69
	MgO	22.55	1.90	16.98	0.40	9.79
	Al_2O_3	2.06	8.04	9.79	5.73	10.50
	SiO_2	46.59	31.06	54.02	11.74	39.50
	P_2O_5	0.02	0.06	0.02	0.29	
	SO_3	1.24	0.24	0.16	0.09	1.37
	K_2O	0.10	0.67	0.41	0.99	1.62
	CaO	13.42	0.94	6.80	0.82	32.20
	TiO_2	0.26	0.21	0.18	0.22	0.63
	Cr_2O_3	0.31	<0.01	0.36	0.01	0.59
	MnO	0.15	0.10	0.20	0.08	1.65
	Fe_2O_3	11.92	35.50	9.34	77.30	
	LOI	2.35	18.37	1.82	2.92	
	$\sum$	101.27	97.41	101.56	100.62	98.54

Table 3: Mineralogical composition of the mine tailings determined by XRD.

	MT 1	MT 2	MT 3	MT 4
	Cu/Ni tails	Cu/Zn tails	Pt tails	Fe tails
Albite			X	
Antigorite	X		X	
Calcite	X		X	
Chlorite	X	X	X	
Diopside	X			
Enstatite			X	
Hematite			X	X
Lizardite	X			
Magnesiohornblende	X		X	
Muscovite	X	X	X	X
Pyrite		X	X	X
Quartz		X	X	
Siderite		X	X	X
Talc			X	

3.2 Leaching of solid precursor materials in alkaline solution

The sample of MT 1 has been chosen to study the influence of leaching time in more detail for 5M and 10M NaOH. The results of the leaching experiments at 40°C with test durations of 4, 8, 24 and 72 hours are summarized in Figures 1 and 2.
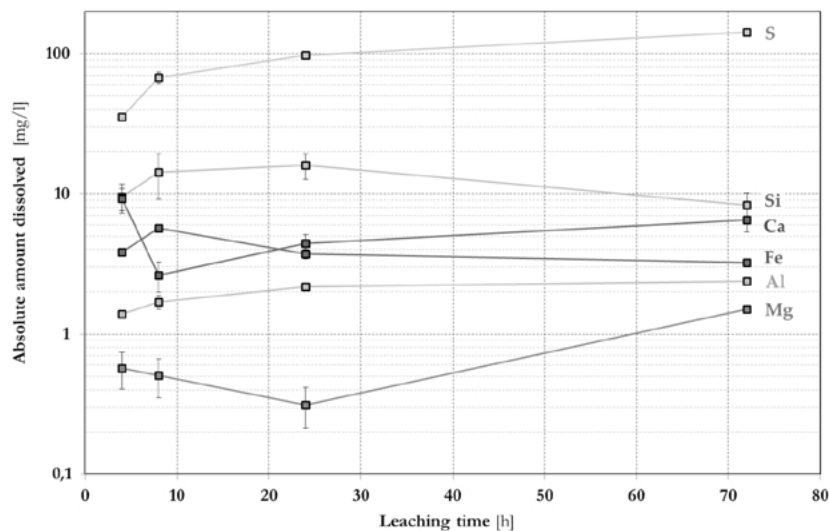
Figure 1: Results of the leaching experiments for MT 1 with 5M NaOH at 40°C.
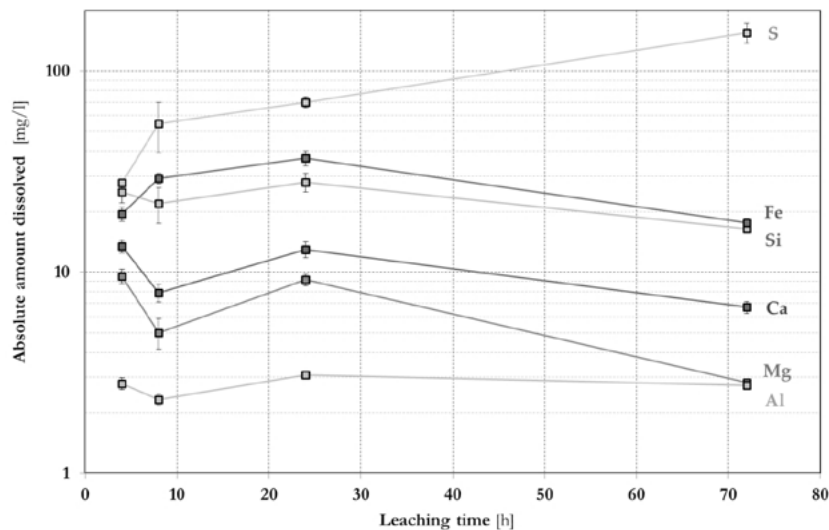

Figure 2: Results of the leaching experiments for MT 1 with 10M NaOH at 40°C.

The results show that the amount of dissolved species is increased for a higher concentrated NaOH solution (except for S and intermediate test durations). The maximum amount of dissolved species can be found after leaching durations of 24 hours especially for the experiments with 10M NaOH. This might be caused by subsequent formation of precipitates or gels from the solution reducing the amount of most of the species except Sulphur.

For leaching in 10M NaOH approximately 1.4 m% of the initial Al and 0.6 m% of the initial Si have been dissolved which adds up roughly to the detection limit for the mass balance. However, subsequent analysis of the leaching residue by XRF, XRD and SEM did not reveal weather precipitates have been formed or from which mineral phases the individual species have been dissolved.

For MT 3 the absolute amount of dissolved Si and Al in dependence of leaching duration and temperature are summarized in figures 3 and 4. Similar trends as for MT 1 can be observed from the leaching experiments of MT 3 although the maximum concentration of dissolved species is not reached after a leaching duration of 24 hours. The amount of dissolution is directly proportional to the concentration of the solvent but its dependence is not as strong as the influence of the leaching temperature. Increasing the temperature from 40°C to 80°C increases the amount of dissolved species roughly by a factor of 2. The results show that using a 1M NaOH solution at a temperature of 80°C the absolute amount of dissolved species is still

higher than using a 10M NaOH solution at 40°C even for shorter leaching duration. This means that a short thermal treatment at a higher temperature might be favourable for alkali activated materials in contrast to curing at moderate temperatures for a longer time.
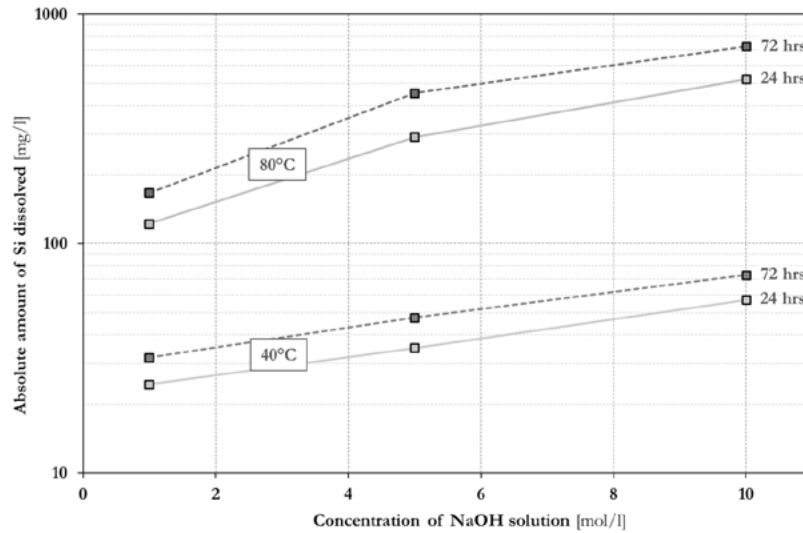
Figure 3: Absolute amount of dissolved Si from MT 3 for different leachate concentrations at various temperatures.
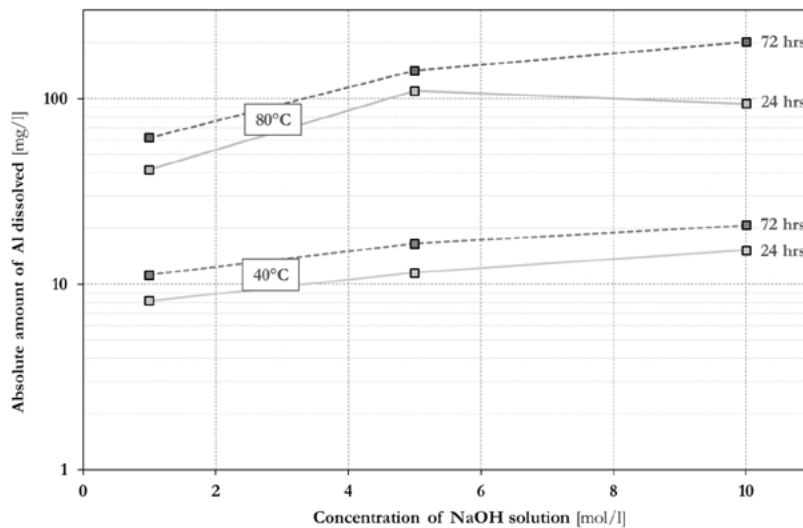
Figure 4: Absolute amount of dissolved Al from MT 3 for different leachate concentrations at various temperatures.

The experiments with MT 1 and MT 3 suggested to perform further tests with other materials with 5M and 10M NaOH solution for a test duration of 24 hours. A temperature of 40°C was chosen due to more simple and safe handling. The results are summarized in table 4. The mine tailings show little reactivity in alkaline solutions compared to granulated blast furnace slag and metakaolin.

For the mine tailings the amount of dissolved species corresponds to below 5 m% of the initial amount in the tailings sample whereas for GBFS roughly 60 m% and for MK roughly 80 m% are dissolved after a leaching duration of 24 hours.

Table 4: Summary of the absolute amount of species dissolved from MTs, GBFS, and MK in NaOH solutions at a temperature of 40°C and a leaching duration of 24 hours with a solids to liquid ratio of 2 g per 100 ml of solvent.

		MT 1	MT 2	MT 3	MT 4	GBFS	MK
		Cu/Ni tails	Cu/Zn tails	Pt tails	Fe tails		
5M NaOH	**Ca**	4.4		7.4	28.0		
	Mg	0.3		0.5	1.8		
	Al	2.2	8.0	11.6	32.0		1977
	Si	16.0	14.0	35.2	80.2		2911
	Fe	3.7			1.3		
	S	97.2			9.5		
10M NaOH	**Ca**	13.0		4.1	23.3	21.8	
	Mg	9.2		0.6	3.6	2.3	
	Al	3.1	14.5	15.3	70.2	603	2122
	Si	28.0	58.0	57.0	134	2450	3148
	Fe	37.0			2.5	1.9	
	S	70.0			13.2	880	

(Absolute amount dissolved [mg/l])

3.3 Mechanical properties of alkali-activated mixtures

The results of mixtures with MT 1 and waterglass are summarized in figure 5. In general a lower curing temperature resulted in lower strength especially for short curing times. The strength of MT 1 activated with waterglass solutions and cured for 28 days at RT ranges from 3.8 MPa up to 14.2 MPa depending on the concentration of solid waterglass in the activator solution. The early strength after curing for 7 days at room temperature was around 1 MPa only. In order to increase the early strength of the alkali-activated products two options have been tested:

1. Grinding of the original tailings with x_{50} of 7.5 μm to a product with x_{50} of roughly 6 μm increased the strength after curing at room temperature to 7.5 MPa for an activator solution with 15 m% of solid waterglass in the activator solution.

2. Replacing 10 m% of the original tailings with ground granulated blast furnace slag increased the strength in a similar way as (1).

The investigations with the other mine tailings have not been carried out as extensive as for MT 1. Hence, the results are not shown as detailed as for MT 1, but summarized in table 5. For MT 2, MT 3, and MT 4 mixtures of waterglass and NaOH have been used as activator solution using a similar screening process as for MT 1. Similarly, the amount of liquid activator has been adjusted in order to result in a mix with desired viscosity. In general a higher strength can be reached with a higher concentration of activator components in the solution. MT 2, MT 3, and MT 4 show lower strength compared to MT 1.

For MT 4 the addition of metakaolin was successfully tested to increase the strength of the final product. A strength up to around 30 MPa was achieved for curing at 60°C for 28 days. Due to the fine particle size of metakaolin the amount of liquid activator solution had to be adjusted.

Unfortunately XRD and SEM could not clearly identify the source related to the high strength of these materials. In contrast to geopolymers or alkali-activated materials the degree of reaction is rather low so that the microstructure of the alkali-activated materials from the mine tailings was found to be rather unchanged.
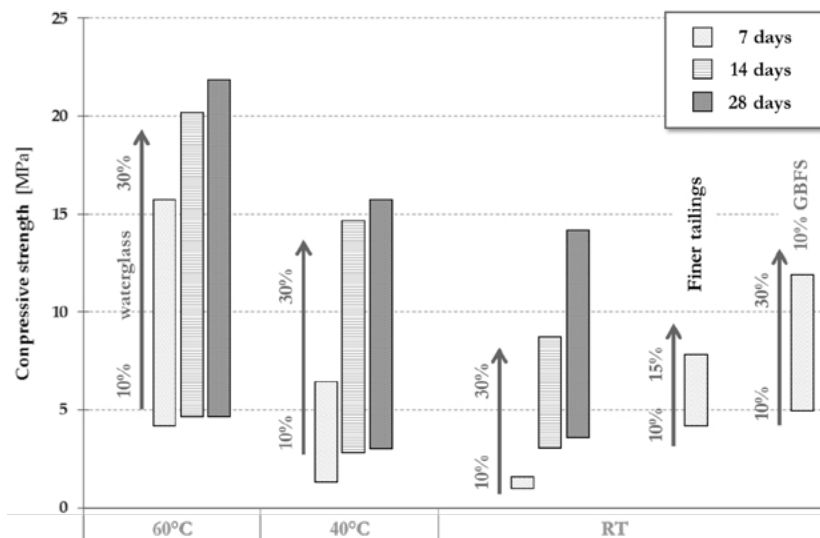
Figure 5: Compressive strength after 7, 14, and 28 days of samples made from MT 1 with waterglass solutions as an activator and curing at different temperatures. The lower end of the bars corresponds to recipes with the lowest concentration of waterglass in the activator solution (10 m%) and the upper end to the highest concentration tested in a given series. 'Fine tailings' corresponds to the same sample but ground to a x_{50} of roughly 6 µm. '10% GBFS' corresponds to a mixture where 10 m% of the mine tailings was replaced by granulated blast furnace slag.

Table 5: Overview of the strength of alkali-activated products from the mine tailing.

Additives		Activator		Curing		σ_c
		Amount	Composition	**T** [°C]	**t** [days]	[MPa]
MT 1		27.5 ml / 100 g	waterglass	60	7	~ 5 to 15
					14	~ 5 to 20
					28	~ 5 to 22
		27.5 ml / 100 g	waterglass	40	7	~ 1,5 to 6.5
					14	~ 3 to 15
					28	~ 3 to 16
		27.5 ml / 100 g	waterglass	RT	7	~ 1.0 to 1.5
					14	~ 3 to 8
					28	~ 3.5 to 14
	Fine tails to reach x_{50} ~6 µm	27.5 ml / 100 g	waterglass	RT	7	~ 4 to 7,5
	GBFS (10 m%)	27.5 ml / 100 g	waterglass	RT	7	~ 5 to 12
MT 2		38.75 ml / 100 g	NaOH and waterglass	60	7	~ 1.0 to 3.5
MT 3		33.75 ml / 100 g	NaOH and waterglass	60	14	~ 1.5 to 5
		33.75 ml / 100 g	NaOH and waterglass	RT	14	~ 1.0 to 2
					28	~ 1.5 to 4
MT 4		37.5 ml / 100 g	NaOH and waterglass	60	7	~ 1.0 to 1.5
					14	~ 1.5 to 2
					28	~ 2 to 3
	Metakaolin (10 m%)	40 ml / 100 g	NaOH and waterglass	60	7	~ 1.5 to 3
					14	~ 3.5 to 6
					28	~ 5 to 30

4.   Conclusions

The results of the leeching experiments showed, that in general the dissolution of significant species from

the mine tailings is little compared to reactive products like granulated blast furnace slag or metakaolin. However, alkali-activation can lead to final products with considerable strength depending on the curing conditions. Furthermore, finer ground tailings or reactive materials have a positive effect on the strength of the final products.

One possible on-site application of alkali-activated materials is mine backfill. Depending on the mining method and whether a primary or secondary stope is being filled, the ultimate strength of installed backfill ranges from 0.2 to 5 MPa. Secondary stopes, or areas where tailings are being placed for safe disposal only require sufficient strength to resist liquefaction, whereas primary stopes may need strength to stand vertical up to 50m high. Cut and fill operations – where quick access is crucial – often require rapid strength development (i.e. more than 2 MPa in approximately the first seven days after installation).

The results for alkali-activated products from the mine tailings indicate that an application as mine backfill seems possible. However, further material properties of the final products (e.g. water resistance) have to be determined additionally. Additionally, the setting behaviour of the backfill can be of importance, especially for long pumping distances.

For the covering layers of surface deposits of tailings a parameter set of physical and chemical properties can only be defined knowing the environmental conditions on the site of installation. Geochemical modelling can assess if such an application is possible with a specific alkali-activated product taking relevant physical and chemical properties into account.

Unfortunately a further assessment of high strength products did not reveal the source of the strength. The following reaction mechanisms are theoretically possible for the given chemical system when adding NaOH and waterglass as an activator:

1. **Waterglass bond**: Formation of a gel due to a reaction with polyvalent cations or due to a reaction with CO_2 leading to silification of dissolved Si according to: $Na_2O \cdot nSiO_2 \cdot xH_2O + CO_2 \rightarrow nSiO_2 \cdot xH_2O + Na_2CO_3$

2. **Formation of a C-S-H gel**: Formation of a gel due to the reaction of dissolved Ca from tailings with dissolved Si from the addition of waterglass and/or leached from the tailings.

3. **Formation of a N,C-A-S-H gel**: Formation of a gel as for the alkali-activation of granulated blast furnace slags or fly ash.

4. **Formation of a geopolymer gel**.

The first three reaction mechanisms seem likely depending on the concentration of relevant species in the pore solution of the mix. However, the formation of a geopolymer gel seems rather unlikely when using mine tailings only as the solid precursor material.

5. Outlook and further procedure

The results currently available don't allow for a direct link between the specific chemical and mineralogical composition of the tailings and their leaching behaviour or performance in alkali-activated materials. However, the data from the leaching experiments can be used for geochemical modelling to link dissolution to certain mineral phases. For that purpose a more detailed mineralogical assessment of the raw material as well as the leaching residues needs to be done by e.g. QEMSCAN. Additionally, modelling can help to assess the formation of gel phases taking place while hardening of the alkali-activated products.

6. Acknowledgment

7. References

[1]   Obenaus-Emler, R.; Illikainen, M.; Falah, M.; Kinnunen, P.; Heiskanen, K. (2019): Geopolymers from mining tailings for more sustainable raw material supply. MATEC Web of Conferences 274:05001, RICON17. doi: 10.1051/matecconf/201927405001.

[2]   Kossoff, D.; Dubbin, W.E.; Alfredsson, M.; Edwards, S.J.; Macklin, M.G.; Hudson-Edwards, K.A. (2014): Mine tailings dams: Characteristics, failure, environmental impacts and remediation. Applied Geochemistry 51, pp 229-245.

[3]   IAEA, The long term stabilization of uranium mill tailings (2004). doi:10.1016/j.jenvrad.2004.01.030.

[4]   Lange L.C.; Hills, C.D.; Poole, A.B. (1996): Preliminary Investigation into the Effects of Carbonation on Cement-Solidified Hazardous Wastes. Environmental Science and Technology 30, pp 25-30. doi:10.1021/es940702m.

[5]   Ahmari, S.; Zhang, L. (2013): Durability and leaching behavior of mine tailings-based geopolymer bricks. Construction and Building Materials 44, pp 743-750.

        doi: 10.1016/J.CONBUILDMAT.2013.03.075.

[6]   Zhang, L.; Ahmari, S.; Zhang, J. (2011): Synthesis and characterization of fly ash modified mine tailings-based geopolymers. Construction and Building Materials 25, pp 3773-3781.

        doi: 10.1016/J.CONBUILDMAT.2011.04.005.

[7]   Barnhisel, R.I.; Darmody, R.G.; Daniels, W.L.; Skousen, J.G.; Sexstone, A.; Ziemkiewicz, P.F. (2000): Acid Mine Drainage Control and Treatment. Reclamation of drastically disturbed lands, pp. 131-168. doi: 10.2134/agronmonogr41.c6.

[8]   Majidi, B. (2009): Geopolymer technology, from fundamentals to advanced applications: a review. Materials Technology 24, pp 79-87. doi: 10.1179/175355509X449355.

[9]   Drechsler, M.; Graham, A. (2007): Geopolymers – An Innovative Materials Technology Bringing Resource Sustainability to Construction and Mining Industries. Common Ground Proceedings 10th Australia new Zealand Conference on Geomechanics Brisbane. doi: 10.13140/2.1.1880.5762.

[10]   Van Deventer, J.S.J.; Provis, J.L.; Duxson, P.; Lukey, G.C. (2007): Reaction mechanisms in the geopolymeric conversion of inorganic waste to useful products. Journal of Hazardous Materials 139, pp 506-513. doi: 10.1016/J.JHAZMAT.2006.02.044.

[11]   Rao, F.; Liu, Q.: Geopolymerization and Its Potential Application in Mine Tailings Consolidation: A Review (2015). Mineral Processing and Extractive Metallurgy Review 36, pp 399-409.

        doi: 10.1080/08827508.2015.1055625

[12]   Xu, H.; van Deventer, J.S.J: The geopolymerisation of natural alumino-silicate minerals (1999). Geopolymer '99 Proceedings, pp 43-63.

[13]   Xu, H.; van Deventer, J.S.J: The geopolymerisation of natural alumino-silicate minerals (2000). International Journal of Mineral Processing 59, pp 247-266. doi: 10.1016/S0301-7516(99)00074-5.

ICSBM 2019
ID xxx

Experimental development of alternative lightweight concretes

D. Zwicky

Professor, Dr. sc. techn., dipl. Bauing. ETH, Institute of Construction and Environmental Technologies iTEC, School of Engineering and Architecture Fribourg HEIA-FR, University of Applied Sciences and Arts Western Switzerland HES-SO, daia.zwicky@hefr.ch

Abstract - It is difficult to compete with normalweight concrete: it is pourable, usually self-compacting, hardening reasonably fast, cheap and locally available in large quantities. Its excellent fire protection and good acoustic insulation for airborne sound are further advantages in construction. But, regular concrete is very heavy, being disadvantageous for transportation and hoisting and results in the fact that a concrete structure predominantly supports its self-weight. Also, concrete qualities applied in building construction usually provide a far too high strength, as geometry is often dictated by constructability (minimum dimensions for concreting). Concrete further provides poor thermal insulation and unpleasant user experience (it "feels" cold), and is rather challenging to recycle. Last but not least, concrete manufacture is largely based on non-renewable resources and has a high environmental impact. Thus, alternative lightweight concretes should be further developed. Starting from earlier developments on "wood-based concrete" (or wood-cement compounds WCCs), essentially consisting of Portland cement (PC) and other mineral binders and of up to 60% of untreated sawdust, this study aimed at improving their mechanical properties by integrating an aggregate skeleton from organic aggregates (fruit pits, crushed nut shells) and lightweight aggregates from largely available or renewable resources (expanded clay and glass). 15 different recipes for "WooCon" (from wood-concrete) were designed and evaluated, in a first phase, for possible self-compaction as a basic fresh-state requirement for their targeted application in prefabrication. In a second phase, basic mechanical properties of 5 retained WooCon recipes were evaluated, by testing elastic modulus, compressive strength, and their development over 28 days as a further important prefabrication requirement. These results were also used to modify predictive expressions for correlating compressive strength and elastic modulus. In a third phase, estimates of economic and ecological performances were established, in order to assess the competitiveness of the newly developed WooCon recipes. The fourth evaluation phase of long-term properties (shrinkage and creep) of the 3 most promising WooCon recipes is currently ongoing. The study results show that adding an aggregate skeleton to WCCs, i.e. converting them into WooCon, can notably improve workability properties, up to self-compaction. Compressive strength can be doubled and elastic modulus can be tripled. Strength development can be predicted by generally accepted expressions and can even reach very rapid early hardening. Elastic modulus can be correlated quite accurately to compressive strength. In all evaluated mechanical properties, a marked influence of the applied percentage of organic aggregates could be observed. Economic impacts of WooCon majorly reside in costs for organic aggregates and cement, and result in unit prices up to 2.5 times higher than regular lightweight concrete (LC); however, if contextualised for mechanical elements, WooCon can perform better than regular LC. Lime filler and cement are the major contributors to ecological impact (global warming potential, GWP) but the overall result shows 75-80% reductions in comparison to regular LC.

Keywords: Alternative lightweight concrete, Lab tests, Fresh-state properties, Mechanical properties, Analytical predictions.

1.   Introduction

This study aims at further developing wood-cement compounds (WCCs) as an alternative to regular lightweight concrete (LC), starting from the encouraging results from earlier developments. These WCCs essentially consist of Portland cement (PC) and other mineral binders and of up to 60% of untreated sawdust [1][2], one of the cheapest and most largely available renewable resource, usually having a maximum granular size of 2 mm with 95% smaller than 1 mm [1] (i.e. these WCCs are rather wood-based mortars).

They can be produced in standard manufacture processes, are pourable and (possibly) self-compacting [2], and material costs are approx. 30-35% lower than regular LC [3]. They show very low self-weight: 1'100--1'300 kg/m³ when saturated while oven-dry densities are between 450 kg/m³ and 870 kg/m³ [4]; at ambient humidity, material densities are around 650 kg/m³ to 1'100 kg/m³. They also provide excellent fire protection (min. 23'/cm [5]), have a thermal conductivity comparable to regular LC but show significantly higher thermal storage capacity [6], and considerably contribute to acoustic insulation [7]. End-of-life re-valorisation can be done by combustion, providing calorific values of 25-50% of wood chips but also 55-70% ash contents [8]. However, these ashes proved further effective as lightweight aggregates or can even be recalcinated, with reactivity ratios of up to 70% of virgin PC [9].

But, the main weaknesses of these structurally-targeted WCCs are slow strength development [2], very low stiffness (1-3 GPa) and compressive strength (2-5 MPa) and, above all, very high shrinkage (3-7‰ after 1 year) and creep coefficients (5.5-8.5 after 1 year) [1]. Adding sand to WCC and replacing an important part of PC by lime filler improves workability, strength and its development, stiffness, and shrinkage behaviour [10] but it also increases density and does not really subscribe to an ecological development (sand resources). Furthermore, application of these WCCs in structural slabs still results in some ecological challenges [11].

To further develop these WCCs, without being too far at the account of their advantageous performances, new recipe improvements were investigated [3]. Above all, the integration of an aggregate skeleton, made of organic components (e.g. fruit pits, nut shells) and lightweight aggregates from expanded clay and glass (i.e. largely available or renewable resources), targeting their transformation into real wood-based concretes, named "WooCon". Their manufacture procedures should keep to usual concrete processes, construction performances should be similar (i.e. pourable, self-compacting, reasonably fast hardening), and they should provide adequate mechanical performances. If material costs are somewhat higher, this can possibly be compensated through lower self-weight, appropriate fire protection, improved thermal properties, enhanced end-of-life re-valorisation (rather than down-cycling), and lower ecological impact.

2.   Methodology

The study [3], forming the basis for this paper, was structured in several phases:

1. Preliminary survey research for locally available (lightweight) aggregates for possible application, considering availability, particle density, and particle size distribution PSD

2. Recipe design, with WCCs as a basis, and preliminary estimations of density and unit prize

3. Lab tests for evaluation of self-compaction properties and further workability performances, to identify the 5 most promising WooCon recipes

4. Lab tests for short-term stiffness, compressive strength and strength development, to identify the 3 most promising recipes for long-term testing

5. Estimative calculation and comparison of economic and ecological performances to regular LC

6. Launch of lab tests for long-term properties, i.e. shrinkage and creep, for the 3 retained WooCon recipes

The last phase is currently still ongoing, and is not further commented here. In phase 5, estimations are based on purchase prizes for the lab test quantities, not necessarily valid on an industrial upscaling. As the further development of WooCon may also involve spin-off activities, some degree of confidentiality is applied hereafter. Specific components and their overall percentages are given but detailed compositions incl. individual PSD as well as mixing process details are kept confidential.

2.1   Recipe design

For a good aggregate skeleton, PSD of different aggregate size classes should be combined appropriately. To do so, the development of recipes was based on the PSD limits proposed in [12], see Figure 1. Bearing further in mind the target of self-compaction, a limitation to aggregate sizes of 16 mm and a water/cement ratio (w/c) between 0.4 and 0.55 is considered [13]. In the first project phase, a limitation to 1'000 km of transportation, exclusion of edible sources, and available PSDs of aggregates were considered, resulting in the choice of the following basic ingredients as aggregate candidates (besides saw dust and lime filler):

•   Mineral aggregates: lightweight expanded clay aggregates (LECA), expanded glass aggregates (e.g. "Misapor", "Poraver"), sand, and gravel (besides lime filler and cement)

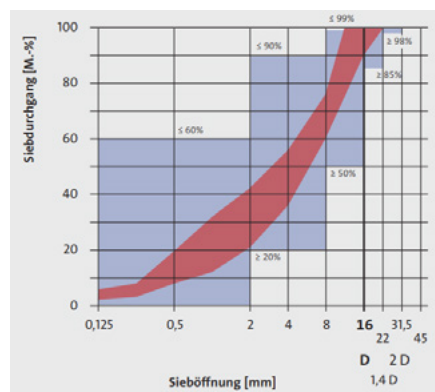•   Organic aggregates: crushed walnut shell, grape seeds, and cherry pits (besides sawdust)

Figure 1: PSD limits for concrete aggregates [12].

2.2   Fresh-state properties

The first selection phase targeted at evaluating self-compaction and manufacturing performances. The latter considers mixing time, workability, necessary quantity of added water, and possible segregation effects while the former looks at slump flow classes, Table 1. For self-compacting concrete, SF2 is usually targeted in practice while the other two classes are only required or admitted, respectively, in special cases.

Table 1: Slump Flow (SF) requirements for self-compacting concrete [14].

Slump Flow class	Flow diameter
	mm
SF1	550-650
SF2	660-750
SF3	760-850

These different criteria are considered in a weighted multi-criterion ranking.

2.3   Mechanical properties

Density, elastic modulus and compressive strength were determined on cylinder specimens, with 150 mm diameter and 300 mm height, at 3, 7 and 28 days. Compressive strength was determined in an automatized test bench. For stiffness at 3 days, manual jack management was applied due to the expected low values, based on earlier experience. As results were considerably higher, the automatized test bench could also be used at 7 and 28 days. Test specimens were stripped 1 day after concreting and stocked in a climate chamber.

Strength development as a function of hardening time is assessed by [15]:

$$f_{cm}(t) = \beta_{cc}(t) \cdot f_{cm} = f_{cm} \cdot e^{s\left(1-\sqrt{28/t}\right)} \tag{1}$$

where f_{cm} = average cylinder compressive strength, t = age in days, and s = strength development exponent. Specific exponents are derived from experimental results, and can be compared to values between 0.25 and 0.20 for normal and rapid cement hardening, respectively, in regular concrete. For lightweight concrete, high strength aggregates should provide $s = 0.05$ while $s = 0.25$ for low strength aggregates [15].

Correlations between average elastic modulus E_{cm} and f_{cm} are based on the expression from [16] for regular LC. It considers impacts of aggregate type and concrete density ρ

$$E_{cm} = k_E \cdot f_{cm}^{1/3} \cdot \eta_{lE} = k_E \cdot f_{cm}^{1/3} \cdot \left(\frac{\rho}{2200}\right)^2 \tag{2}$$

where k_E = aggregate type coefficient, and η_l = correction factor for LC stiffness. Experimental results are used to calibrate specific k_E values and are compared to standard values, varying between 8'000 and 12'000 for river bed gravel aggregates, between 8'000 and 10'000 for crushed lime aggregates, and between 6'000 and 8'000 for micaceous rock aggregates, respectively. Deviations from these values are possible, particularly for self-compacting concrete [16]. As this formulation contains 3 unknowns (aggregate factor, strength exponent, and density exponent) but only 2 independent test results are available, i.e. f_{cm} and ρ, more specific expressions cannot be calibrated from the test results.

2.4   Economic and ecological performances

Economic performances of the retained WooCon recipes were established, on the basis of lab test purchase prices (Table 2) to determine unit prices per m^3. Organic aggregate prices are high because they are not sold (yet) in industrialised quantities.

Table 2: Approximate cost and GWP indicators of basic materials [3].

Component	Purchase price	GWP
	CHF/m^3	kg CO_2 eq./m^3
PC 52.5R	1'770	0.129
Lime filler	330	0.155
Sawdust	25	0.011
Superplasticiser	8'300	0.030
Sand / gravel	60	0.014
Expanded clay	420	0.417
Expanded glass	400	0.207
Crushed walnut	3'800	0.001
Grape seeds	4'500	0.001
Cherry pits	3'300	0.001
LC 12/13	500	0.417
WCC with sand [2],[10]	230	0.114

These cost estimations are further compared to a regular LC 12/13 [16] w.r.t. unit prices but also in a (simplified) construction context, considering material densities and strengths. Analogous evaluations are done for estimative ecological performance, for global warming potential (GWP) per m³ and in contextualized construction situations. Table 2 shows the admitted impact per WooCon component, partly based on [17]. Organic aggregates are principally waste and water is considered free.

3.   Results and discussion

3.1   Recipe design

In all recipes, cement content was 300 kg/m³, with lime filler at 250 kg/m³, and sawdust at 60 kg/m³ , with a constant ratio $w/c = 0.5$. As a function of the aggregate types incl. their individual PSD, the necessary proportions were determined with Figure 1.

Table 3 shows an overview of the WooCon recipes (respecting confidential information, see section 2), expected densities and unit prices. Mix designs with artificial mineral lightweight aggregates (expanded clay and glass) are interesting w.r.t. to unit price but generally result in greater density. Mix designs with organic aggregates result in lighter concrete mixes but also in considerably increased unit cost.

Table 3: General composition of WooCon aggregates and percentage of organic aggregates.

Recipe	LECA	MISAPOR	Sand/ gravel	Walnut shell	Grape seeds	Cherry pits	Organic aggregates	Density kg/m³	Cost CHF/m³
1	20%	68%	12%	–	–	–		890	350
2	45%	43%	12%	–	–	–		900	350
3	20%	25%	55%	–	–	–	0%	1'160	310
4	45%	–	55%	–	–	–		1'170	310
5	–	68%	32%	–	–	–		1'000	330
6	X	X	X	–	–	X	25%	910	540
7	X	X	–	X	–	X	37%	840	660
8-9	X	X	–	X	–	–	12%	820-830	470
10-11	X	X	–	–	X	–		820-830	490
12	–	X	–	X	X	X	57%	860	870
13	–	X	–	–	X	X		850	890
14	X	X	–	–	X	X	37%	840	680
15	–	X	X	–	X	X	45%	920	750
16	X	X	–	–	X	–	32%	840	700
17	–	X	–	–	X	–		830	700

3.2   Fresh-state properties

Mix designs 16 and 17 were not further considered due to their closeness to other recipes but at higher cost. The remaining 15 WooCon recipes were tested according to the multi-criteria approach, Table 4.

Purely mineral-based WooCon recipes perform relatively poor at the fresh state. This is partially due to long mixing time but, above all, due to the quantities of added water necessary to reach a satisfactory workability. This can essentially be explained by the very porous aggregates with very high water absorption. These voids must be filled before additional water is available for creation of the cement paste. Only recipe 3 attained the usually required slump flow class SF2.

Most recipes with organic aggregates perform considerably better at the fresh state; none reaches SF2 but all figure in class SF1. Recipes 11 and 15 showed the highest slump flows, close to the lower limit of SF2;

however, they also showed unacceptable segregation effects. Comparing to Table 3 shows no correlation between organic aggregate content and slump flow, nor to manufacture performance, in general.

Based on Table 4, recipes 6, 10, 12, 13 and 14 were retained for short-term hardened state testing. The necessary water to improve workability and slump flow can be explained by different reasons: mixer and handling equipment are moistened, binding some of the initial water; but, more important are the mix components: lime filler, sawdust, and porous aggregates absorb a lot of water and need to be saturated before water is available for the cement paste. Stripping of test specimens showed that the additional water leaches ("sweating" and evaporation). Nevertheless, w/c ratios are different from the target value, and result in 0.66, 0.69, 0.67, 0.64, and 0.74 for recipes 6, 10, 12, 13, and 14, respectively.

Table 4: Multi-criteria evaluation of fresh-state properties.

Criterion	SF diameter	Mixing time	Workability	Added water	Segregation	Slump Flow	Total
Weight	mm	1	1	2	2	1	15
Maximum points		2	2	3	1	3	
1	600	0	0	0	1	2	4
2	480	0	0	0	1	0	2
3	665	2	2	0	1	3	9
4	565	1	1	0	1	1	5
5	625	1	1	0	0	2	4
6	570	2	2	2	1	1	11
7	590	2	2	2	0	1	9
8	565	1	1	2	1	1	9
9	465	1	1	1	1	0	6
10	595	2	2	3	1	1	13
11	630	1	1	2	0	2	8
12	585	2	2	3	1	1	13
13	560	2	2	3	1	1	13
14	535	2	2	2	1	0	10
15	625	2	1	2	0	2	9

3.3 Mechanical properties

3.3.1 Density

Experimental density showed considerable difference to expected values (Table 3). Table 5 shows average values and coefficients of variation (COV). The latter confirm homogeneous mixing. As the experimental densities are approx. 1.8-1.9 higher than expected, further investigations were performed, besides the leaching identifies at stripping. Test samples prepared by wet-grinding, leading to sample saturation of the containing considerable amounts of porous and water-absorbing components (sawdust, expanded clay and expanded glass aggregates). Oven-drying at 120°C during 24h revealed approx. 25% humidity content.

A further reason was suspected in the possibility that material masses can partially occupy the same volume, i.e. the components settle when mixed, adding to the porosity. Rough experimental verification showed that dry-mixed components loose approx. 30 Vol.-% when wetted. Combining different components in groups of two showed that water is absorbed up to 90% by porous components, and that PC and lime filler are absorbed up to 30% in sawdust or expanded glass volumes. These effects needs to be considered when material densities and fabrication volumes are predicted.

Table 5: Experimental densities and comparison to expected values.

Recipe	Expected density	Experimental densities					
		At 3 days		At 7 days		At 28 days	
	kg/m³	kg/m³	COV	kg/m³	COV	kg/m³	COV
6	910	1630	2%	1610	1%	1660	1%
10	830	1590	3%	1570	2%	1580	1%
12	860	1570	1%	1560	1%	1600	2%
13	850	1580	1%	1560	1%	1600	1%
14	840	1540	1%	1510	1%	1550	1%

3.3.2 Strength and development

Table 6 shows average values and COV of compressive strength at the different test days, also recalling the percentages of organic material in the aggregate skeleton.

Table 6: Compressive strength at different ages.

Recipe	Organic aggregates	Compressive strength							
		At 3 days			At 7 days			At 28 days	
		MPa	COV	s	MPa	COV	s	MPa	COV
6	25%	13.6	4.4%	0.138	14.9	0.9%	0.189	18.0	1.8%
10	12%	15.6	7.1%	0.093	17.2	3.9%	0.093	18.9	0.5%
12	57%	8.3	7.5%	0.243	11.2	3.6%	0.198	13.6	4.0%
13	57%	8.0	2.8%	0.233	10.6	3.7%	0.197	12.9	2.5%
14	37%	10.7	4.8%	0.128	11.8	3.5%	0.163	14.0	3.8%

Figure 2 (a) shows the correlation between content of organic aggregates in the skeleton and the reference strength at 28 days. A reduction trend in compressive strength as a function of organic aggregate content is visible, but only from a approx. 20% or $\eta_{fc} = (30/f_{ck})^{1/3} \leq 1$. In analogy to [16] where a reduction coefficient for high-strength concrete of is prescribed for determining design values, a correction factor $\eta_{fc,org}$ for organic aggregates is proposed, referring to a regular, purely mineral-based LC with $f_{cm,0}$ = 18.8 MPa (i.e. value of recipe 10), shown as dashed line in Figure 2 (a):

$$\eta_{fc,org} = \left(\frac{0.2}{\rho_{org}}\right)^{1/3} \leq 1 \tag{3}$$

where ρ_{org} = percentage of organic aggregates in the skeleton.

The experimental results were also used to determine strength development exponents s, Eq. (1), Table 6. Such values cannot be determined for 28 days test results, see Eq. (1). Values are close to or below the value for PC 52.5R (s = 0.20), Figure 2 (b), except for 3 days test results of recipes 12 and 13. Overall, the WooCon recipes show a normal or rapid strength development for organic aggregates content up to approx. 40%. The higher is the organic content, the slower is the strength development. Referring to lightweight concrete, the strength development generally seems to be below or closer to low strength aggregates (s = 0.25) than to high strength aggregates (s = 0.05), except for recipe 10. This recipe has the lowest organic aggregate content, and it confirms that the mineral lightweight aggregates can be considered high strength.

Figure 2 (b) shows a clear influence of the percentage of organic aggregates: the higher it is, the slower is the strength development (recipe 6 is somewhat above this trend). Thus, organic aggregates seem to be low strength in the understanding of [15]. Except for recipes 12 and 13 with the highest organic aggregate contents, the strength development at 3 days is faster than at 7 days.
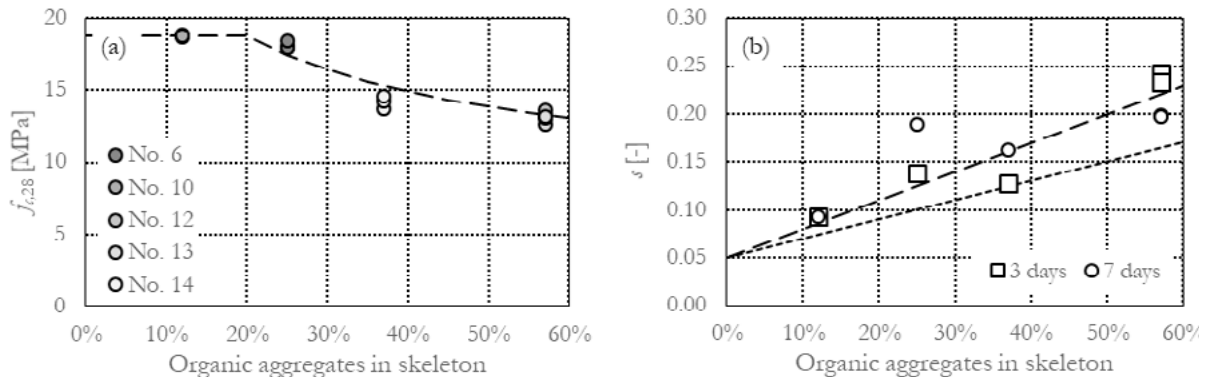
Figure 2: Correlation between organic aggregate content and (a) compressive strength at 28 days, and (b) strength development over 3 and 7 days.

The dotted line in Figure 2 (b) also shows a simple interpolation for high and low strength aggregate values from [15], admitting fast development (s = 0.05) for 100% mineral lightweight aggregates and normal development (s = 0.25) for 100% organic aggregates; as all experimental values are above this line (and thus, the mixes harden slower than predicted by this interpolation), there seems to be a limit of organic matter of approx. 70% where the upper limit of [15] is reached. Based on the few available results, a formulation for strength development of WooCon mixes s_{org} is proposed, shown as dashed line in Figure 2 (b):

$$s_{org} = 0.05 + 0.30 \cdot \rho_{org} \qquad (4)$$

3.3.3 Correlation of elastic modulus and strength

Table 7 shows average values and COV at the different test days, also recalling the percentages of organic material in the aggregate skeleton. The values are given with two significant digits in view of practical relevance. Figure 3 (a) shows the correlation of experimental compressive strength and elastic modulus: not surprisingly, stiffness increases with increasing compressive strength which, in turn, depends on the organic content (Figure 2 (a)).

Table 7: Elastic modulus at different ages.

No.	Organic aggregates	Elastic modulus											
		At 3 days				At 7 days				At 28 days			
		MPa	COV	$\eta_{/E}$	k_E	MPa	COV	$\eta_{/E}$	k_E	MPa	COV	$\eta_{/E}$	k_E
6	25%	6900	9%	0.55	5'300	7700	2%	0.54	5'800	9000	1%	0.57	6'100
10	12%	7700	6%	0.52	5'900	7700	6%	0.51	5'900	8500	1%	0.52	6'200
12	57%	4500	7%	0.51	4'400	5400	6%	0.50	4'800	6100	3%	0.53	4'800
13	57%	4600	3%	0.52	4'500	5400	3%	0.50	5'000	6500	4%	0.53	5'200
14	37%	5300	18%	0.49	4'900	5600	5%	0.47	5'200	6200	5%	0.50	5'200

Eq. (2) is used to determine individual k_E values, considering $\eta_{/E}$ from Table 7. For mineral aggregates only, k_E seems to be in the recommended order for micaceous rock aggregates (albeit, rather at the lower limit of k_E = 6'000), which seems principally plausible for the relatively soft lightweight mineral aggregates. Thus, the use of $\eta_{/E}$ alone is not sufficient for predicting the stiffness of LC containing organic aggregates and thus, the directives of [16] cannot be transposed to WooCon like that. There also seems to be a limit of approx. 20% of organic aggregate content below which no significant effect of using organic aggregates can be observed, as it is also the case for the compressive strength (Figure 2 (a)).
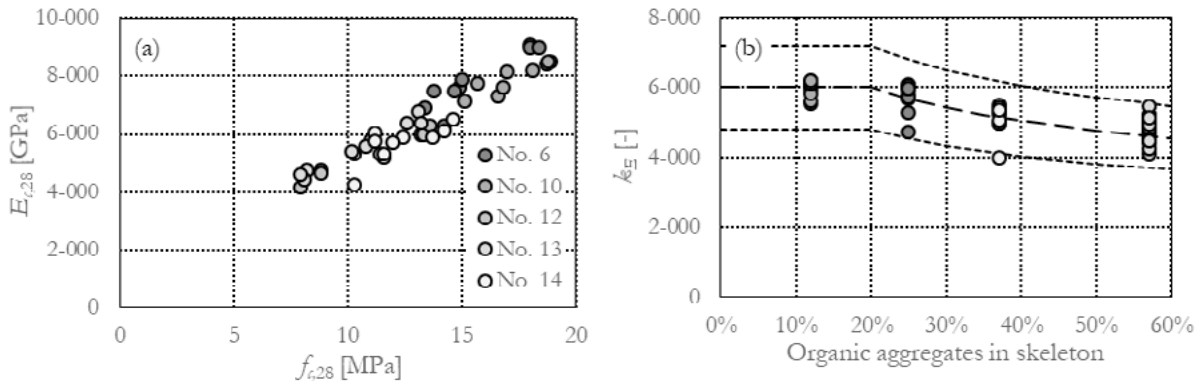
Figure 3: Correlation between (a) compressive strength and elastic modulus, and (b) organic aggregate content and average aggregate type coefficient [16].

Admitting that the expression for η_{IE} and the exponent to f_{cm} in Eq. (2) remain unchanged, an additional correction factor $\eta_{E,org}$ for consideration of organic aggregates is proposed (based on the few available results), referring to a basic (and conservative) value of $k_{E,0}$ = 6'000 for purely mineral-based LC (i.e. 0% organic aggregates), shown as dashed line in Figure 3 (b) together with a variation bandwidth of ±20%:

$$\eta_{E,org} = \left(\frac{0.20}{\rho_{org}}\right)^{0.25} \leq 1$$

(5)

Figure 3 (b) shows that, with this correction, there is a reasonable correlation to experimental results.

3.4 Economic and ecological performances

3.4.1 Economic performance

With the input from Table 2, the economic performance is determined per WooCon recipe and compared to a standard LC 12/13, having approximately the same average compressive strength, and to an earlier WCC containing sand [2],[10]. The elastic modulus of the LC is estimated from Eq. (2), admitting k_E = 6'000 and ρ = 1'600 kg/m³ (ca. average of WooCon recipes) while for the WooCon recipes and the earlier WCC the reported values are applied.

A first comparison addressed the cost per m³. Further comparisons, neglecting stability problems, relate to the cost of 1 m² of wall with 3 m height supporting 300 kN/m on top, failing in compression at the bottom and with self-weight being considered, and to the same wall limiting its shortening to 3 mm. These two cases require a certain thickness which, in turn, results in a cost per m². All results are normalized to the performance of the regular LC, with Figure 4 showing the results.
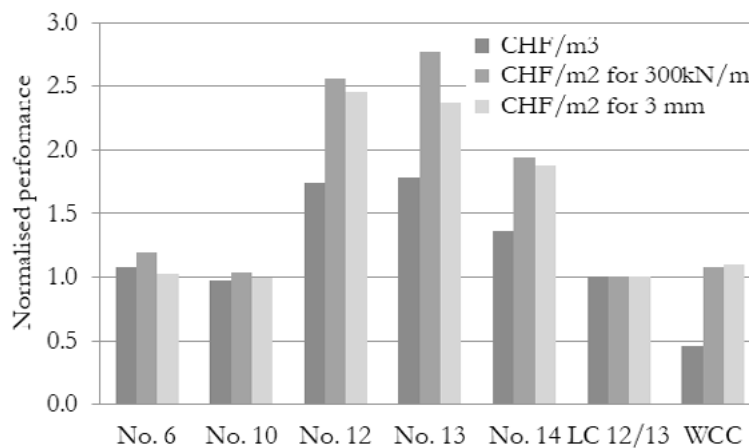

Figure 4: Comparison of economic performances.

Recipes 6 and 10 have cost per m³ comparable to a regular LC while recipes 12 and 13, with the highest contents of expensive organic aggregates, are up to approx. 75% more expensive. Recipe 14 costs approx. 35% more than a regular LC. All current recipes show considerably higher unit cost than the earlier WCC; this is not really a surprise, as further and more expensive components are added in the current mixes. 25-40% of cost are associated to the cement and lime filler, and 30-65% come from the organic aggregates.

In terms of cost per m² for strength of the evaluated wall, recipes 6 and 10 show an economic performance increase smaller than 20%. Recipes 12 and 13 cost up to 180% more. Recipe 14 almost reaches the double cost of a regular LC. Earlier WCC shows a comparable cost to the latter. Considering required stiffness in cost evaluation, recipes 6 and 10 perform as a regular LC while recipes 12 and 13 cost up to 150% more. Recipe 14 requires almost 90% of additional cost. Earlier WCC requires some 10% of additional cost in comparison to regular LC.

3.4.2 Ecological performance

Figure 5 shows comparative ecological performances, referring to the cases of economic performance.
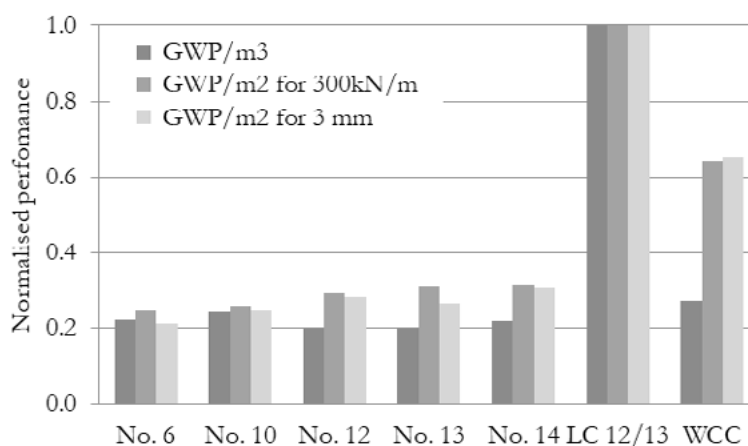

Figure 5: Comparison of ecological performances.

This comparison shows the greatest impact of using organic aggregates, resulting in a GWP reduction of approx. 80% in comparison to regular LC. All WooCon recipes also perform better than earlier WCC, with reductions of 20-30%. Considering GWP for strength of the evaluated wall, reductions of 70-75% are possible with WooCon in comparison to regular LC. Compared to earlier WCC, reductions of 50-60% are found. Considering stiffness requirements of the evaluated wall, GWP is reduced by 70-80% using WooCon instead of regular LC while reductions of 50-70% are found compared to earlier WCC.

3.4.3 Combined impacts

To compare ecological impact to economic consequences, reference is made to the cases of wall strength and wall stiffness, Figure 6. Recipes 6 and 10, with a moderate content of organic aggregates up to 25% are the most viable option. Comparing earlier WCC to regular LC, it becomes evident that this development was the good way to go, as cost remain approximately comparable but ecological impact is considerably reduced. However, their poor mechanical performance did require improvement, as explored here.

Adding an aggregate skeleton definitely did improve strength and stiffness, and can be achieved by very moderate cost increase if a wise selection of aggregate types is done. As replacing mineral lightweight aggregates with organic aggregates comes at increased price but also decreased mechanical performance, overall resulting in increased ecological impact, a compromise must be found. From the data collected in this study, it can be concluded that a maximum of approx. 25% of organic aggregate content should

be respected if material cost increases shall be limited to 20%. Going beyond this replacement ratio of mineral-based lightweight aggregates results in over-proportional cost increased for a small gain in ecological performance. The most important impact, however, would probably be achieved if organic aggregates would be available in industrial volumes.
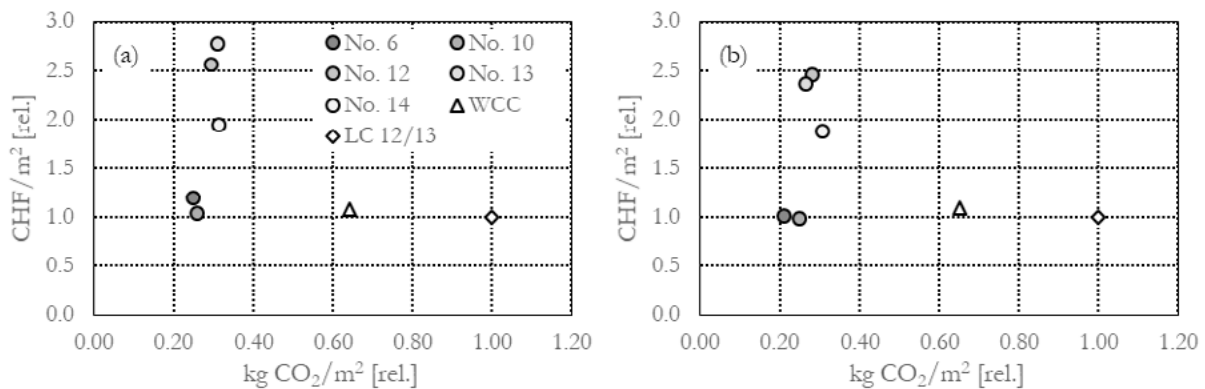

Figure 6: Comparison of ecological performances and economic consequences for (a) wall strength and (b) wall stiffness.

3.5   Outlook

Long-term properties evaluation, i.e. shrinkage and creep tests, is currently ongoing for recipes 6, 10, and 12, started at the beginning of February 2019 and extending over 1 year. Having three test benches available, two of the five recipes had to be discarded. Recipe 13 has been eliminated as it contained a fewer number of organic aggregates while recipe 14 was not further considered due to the poor slump flow performance.

Further advances of WooCon recipes target the replacement of lime filler and cement with more advanced cement types (e.g. CEM V or VI) as well as the development and the identification of new types of lightweight aggregates to be applied – obviously, with a limited ecological impact and at reduced cost.

4.   Conclusions

The results of this study allow to draw the following conclusions:

- Integrating an aggregate skeleton in wood-cement compounds (WCC), transforming them into "real" lightweight wood-based concrete (WooCon) increases workability and allows attaining, for certain compositions, minimum slump flows required for self-compacting concrete. Mixes with organic aggregates generally perform better at fresh state than mixes with purely mineral-based aggregates.

- Density and production quantity predictions of hardened WooCon are challenging, due to the partial fusion of components into the same volumes (water into expanded aggregates, cement and lime filler into sawdust and expanded glass aggregates) and due to the water-absorbing behaviour (up to 25% of humidity in saturated samples). Overall, these effects may result in volume loss factors up to 1.9.

- Stiffness and strength of WooCon are considerably higher than those of WCC. Stiffness can go up to values comparable to timber while strength attains values comparable to regular low-strength lightweight concrete (LC), being principally suitable for structural applications. Both, stiffness and strength, depend on the content of organic matter in the aggregate skeleton, starting to decrease (in comparison to mineral-based LC) from approx. 20% organic content. Preliminary expressions for reduction factors as a function of organic aggregate content are proposed in the paper.

- Strength development of WooCon is comparable to regular LC and is principally acceptable for industrial fabrication. It also depends on the organic aggregates content: the more organic aggregates, the slower the strength development. A preliminary prediction expression is also given in the paper.

- Elastic modulus and compressive strength can be correlated according to code expressions. Predicting elastic modulus as a function of compressive strength also requires introducing a reduction coefficient for organic aggregate content higher than 20%, for which an expression is given in the paper.

- The economic performance of WooCon can be comparable to regular LC if organic aggregate content is limited to approx. 25%. Higher organic aggregate contents lead to more than proportional reductions of stiffness and strength, requiring larger material volumes. This conclusion strongly depends on the future development of potential availability of organic aggregates on industrial scale.

- The ecological performance of WooCon, compared to regular LC, is improved by up to 80%. An optimum organic aggregate content, for the input hypotheses, again seems to be at approx. 25%.

- Economic and ecological performance evaluations should always be contextualised, e.g. for same load-bearing capacity or stiffness of a structural element; comparing unit impacts alone may be misleading.

5. Acknowledgment

6. References

1. Zwicky D. (2015). "Mechanical Properties of Wood-Cement Compounds". In: Proceedings of the 10th Conference on *Advanced Building Skins*, Berne, Switzerland, pp. 126-135.

2. Macchi N. & Zwicky D. (2016). "Pourable Wood-Cement Compounds – Properties, Potential and Challenges of a New Structural Material". In: Cruz P.J.S. (ed.), Structures and Architecture: Beyond their Limits, Proceedings of the 3rd *International Conference on Structures and Architecture* (ICSA), Guimarães, Portugal, Leiden: CRC Press/Balkema, pp. 145-152.

3. Meszes A.A. (2019). *Optimisation des recettes des bétons allégés par le bois*. Semester project report, Master course, Univ. of Applied Sciences and Arts of Western Switzerland HES-SO, School of Engineering and Architecture Fribourg HEIA-FR, Switzerland.

4. Ropp J. (2014). *Combustion and behaviour of a wood-cement composite (WCC) at high temperature*. Internal report AGP 38761, Systèmes Industriels de Bioénergies SIB, Institut de Génie Thermique IGT, Haute Ecole d'Ingénierie et de Gestion du Canton de Vaud HEIG-VD.

5. Ropp J. (2015). *Combustion of a timber-WCC slab*. Supplement to internal report AGP 38761, SIB, IGT, HEIG-VD, Switzerland.

6. Zwicky D. & Macchi N. (2016). "Wall Elements made of Timber and Wood-Cement Compounds – Building-Physical Properties and Structural Performance". In: Cruz P.J.S. (ed.), Structures and Architecture: Beyond their Limits, Proceedings of the 3rd *International Conference on Structures and Architecture* (ICSA), Guimarães, Portugal, Leiden: CRC Press/Balkema, pp. 75-83.

7. Maeder M. & Zwicky D. (2016). "Multi-functional Features of Pourable Wood-Cement Compounds – Mechanical, Building-physical, Economic and Ecological Performance"; In: Eberhardsteiner J., Winter W., Fadai A. and Pöll M. (eds.), Proceedings of the *World Conference on Timber Engineering* (WCTE), Vienna, Austria, paper ID 1059.

8. Zwicky D. (2015). "Combustibility of Wood-Cement Compounds". In: Proceedings of the 10th Conference on *Advanced Building Skins*, Berne, Switzerland, pp. 164-172.

9. Ruch H. (2017). *Options de recyclage/réutilisation des bétons allégés par le bois*. Semester project report, Bachelor course, HEIA-FR, Switzerland.

10. Macchi N. (2015). *Development of self-compacting wood-concrete compounds*. Semester project report, Master course, HES-SO, HEIA-FR, Switzerland.

11. Maeder M. and Zwicky D. (2016). "Ecological Performance of Timber / Wood-Cement Compound Composite Slabs"; In: Habert G. and Schlueter A. (eds.), Expanding Boundaries: Systems Thinking in the Built Environment, Proceedings of the *Sustainable Built Environment (SBE) regional conference*, Zurich, Switzerland, Zurich: vdf, pp. 702-706, DOI 10.3218/3774-6_113.

12. EN 12620 (2002). *Aggregates for concrete.*

13. Holcim (2015). *Guide pratique du béton – Concevoir et mettre en œuvre des bétons durables.* Holcim Edition, Switzerland, 6th edition.

14. EN 206-1 (2013). *Concrete – specification, performance, production and conformity.*

15. Model Code (2010). *Model Code: Final draft, Vol. 1.* Lausanne: fib, bulletin no. 65.

16. SIA 262 (2013). *Construction en béton.* Zurich: Swiss Societey of Engineers and Architectes SIA.

17. KBOB (2016). *Ökobilanzdaten im Baubereich*, edition 2009/1, revision 2016.

Fire resistance of aerated alkali-activated cements

J. Rodriguez-Sanchez [1,2], M. Fedorciuc-Onisa [2], H. Kinoshita [1], J.L. Provis [1], S. MacLachlan [2]

[1] Department of Material Science and Engineering, University of Sheffield, Sheffield S1 3JD, United Kingdom**,**

[2] Lucideon Limited, Stoke-on-Trent ST4 7LQ, United Kingdom.

Abstract

The present study investigates the effects of long-time exposure to moderate and high temperatures on the strength, mass, volume, and chemical composition of aerated alkali-activated cements. Pure metakaolin, pure ground granulated blast furnace slag and their blends with different weight ratios are studied to understand the roles of each solid precursor against fire attack. Different design compositions are also prepared with varied porosity to investigate the relationship between mechanical strength and porosity after fire exposure. Preliminary results show that the strength of foamed metakaolin-based specimens drops progressively when exposed at temperatures up to 750 °C, beyond which it starts to rise due to densification of the gels to form glass and ceramics. The results also suggest that all chemically and physically bound water within the samples is vaporized after 4 h exposure to 750 °C, while the volume shrinkage increases continuously from 11.8 % at 500 °C to 52.4 % at 1000 °C. The collapse of the pore structure and the loss of free water might be the main reasons for the large shrinkage rates and the strength loss of this composition type. The information obtained regarding the effects of composition and pore structures will allow a higher degree of control over the fire resistance properties of sustainable alkali-based concretes.

Keywords: Sustainability; Alkali-activated concrete; Porous concrete; Fire resistance.

1.   Introduction

Its mechanical properties, abundance of raw materials, and relatively low-cost production have made Portland cement (PC)-based concrete the most commonly used construction material worldwide. However, when PC-based concrete is exposed to high temperatures, such as in a fire, physical and chemical transformations take place, resulting in deterioration of its mechanical properties. This deterioration varies according to the concrete mix proportions, constituents, and porous structure, and can be determined by complex physicochemical transformations occurring during heating [1].

The hydration of the silicate constituents of PC yields two main hydration products. Calcium-silicate-hydrate (C-S-H) is the most abundant whilst calcium hydroxide ($Ca(OH)_2$), also known as portlandite, is the secondary phase and plays an important role in the chemical and microstructural composition of the cement paste and its behaviour against fire [2]. Its relatively low thermal decomposition temperature of about 400 °C determines the breakdown of PC pastes. Even if PC-based structures or construction materials are able to withstand a fire above that temperature, a complete evaluation of their remaining mechanical properties will still be necessary after cooling since the thermal decomposition of $Ca(OH)_2$ is commonly followed by the expansive rehydration of lime (CaO) which can induce further damage in the long term, potentially with fatal consequences [3].

Another key parameter in determining fire resistance is the porosity of the concrete structure. During fire attack, gel water and pore solution are vaporized both out of the sample and towards the unheated face of the concrete body which is being attacked due to the lower pressures of these regions. However, if the permeability of the pore structure is not high enough, the steam can cause a moisture clog. As a result, the very dry zone which spans from the clog to the external surface of the concrete body will experience a continuous pressure build-up which may lead to its explosive spalling [4]. This phenomenon is common for PC-based concretes and especially for high strength PC concretes since they typically have a relatively small average pore size and low degree of pore connectivity, and both of these increase the risk of spalling [5,6].

Unlike PC, alkali-activated cements not only exhibit a much better behaviour against fire but also show excellent final mechanical properties, good chemical stability, and low attributed CO_2 emissions [7,8]. They are derived from the reaction of solid aluminosilicates sourced from metallurgical slags, coal fly ash and/or calcined clays, with an alkaline solution (typically hydroxide or silicate-based) that induces the formation of strong, insoluble binding phases including calcium-aluminium-silicate-hydrate, C-A-S-H, and/or sodium/ potassium-aluminium-silicate-(hydrate), N/K-A-S-(H), gels [9], but not portlandite unless Portland cement or lime is added within the mixture design. The relatively high decomposition temperatures of these binding phases (which can be as high as 1000-1200 °C for N/K-A-S-(H) [10]), together with a larger average porosity and lack of chemical and mechanical structural damage caused by their dehydration, make alkali-activated concretes one of the most attractive substitutes for PC in applications which require outstanding fire resistance properties [7]. However, despite a large number of studies dealing with the fire resistance of alkali-activated cements [7,9–13], the effect of the alkali-activated cement composition and its pore structure on their fire resistance properties has not yet been studied systematically across the full range of compositions of potential commercial interest.

The present study investigates the effects of relatively long-time exposure (4 h) to moderate and high temperatures (500 – 1000 °C) on the strength (flexural and compressive), mass, chemical composition and shrinkage of alkali-activated cement samples with varying composition and porosity. The results will help in understanding the relationship between mechanical strength and porosity after fire exposure, which will allow a higher degree of control over the fire resistance properties of sustainable alkali-based concretes for multiple applications.

2. Methodology

2.1 Materials

2.1.1 Raw materials

The aluminosilicate sources used in this work are metakaolin (MK) Metafort, (Sibelco Ltd, Belgium), and ground granulated blast furnace slag (GGBS) from Hanson UK. Pure sodium hydroxide (NaOH) pellets and K120 potassium silicate solution (density 1.60 g/cm³) were supplied by Tennants Distribution Ltd. (Manchester, UK) to prepare the activator solutions. The foaming agent is supplied by Sika (Baar, Switzerland).

2.1.2 Specimen preparation

NaOH pellets were dissolved in water and subsequently mixed with K120 solutions using a mechanical mixer. Pure MK, pure GGBS or combinations of these powders were then added to the mixer batch and mixed with the activator solutions. The amounts of activator solution, GGBS and MK powders were adjusted to achieve target molar ratios of Na:K:Al:Si:H_2O, and activator/binder ratio. By the end of the mixing stage of the binder, foam was prepared and immediately mixed with the binder slurry at several binder/foam ratios (wt.). The foamed slurries were subsequently poured into three-gang moulds with 40

x 40 x 160 mm dimensions, and covered with polyethylene film. The specimens were then cured and subsequently demoulded afterwards for their characterization.

2.2   Methods

2.2.1   Pore structure

The pore structure of the specimens is assessed by mercury intrusion porosimetry (MIP). A geometrical model based on the Washburn equation, as shown in (1), is applied to determine the pore diameter.

$$D = -4\,\gamma\,\cos\theta\,/\,P, \tag{1}$$

where D (m) is the calculated pore diameter, γ (N/m) is the surface tension, θ (°) is the contact angle between mercury and the pore wall, and P (Pa) is the applied pressure. The surface tension (γ) and contact angle (θ) selected in this study are 0.485 N/m and 140°, respectively [14]. The applied pressure (P) ranges from 0.007 to 207 MPa.

2.2.2   Fire resistance

Foamed geopolymer specimens with different compositions and binder/foam ratios were fired at 500 °C, 750 °C, and 1000 °C for 4 h. Then, the specimens were naturally cooled down inside the kiln before determining the volume changes, mass losses, chemical composition changes and strength changes. Volume changes were measured using a calliper, mass losses using a precision balance, and chemical changes by scanning the samples under X-ray fluorescence (XRF). Flexural strength changes were measured according to the EN 196-1 [15] standard three-point bending test on 40 x 40 x 160 mm prisms using an ELE international compressive stage, whereas compressive strength was measured by the EN 196-1 standard compression test on 40 x 40 x 40 mm cubes using the same instrument. At least three replicates for each mix design were tested, and all experiments are performed using the same batches of raw materials, activators and water.

3.   Preliminary results

An important aspect of the selection of construction materials for residential and commercial applications is the ability to retain structural integrity during and after fire exposure. Figure 1 shows the effect of fire attack on the compressive and the flexural strength of pure MK samples with a final density, ρ, of 600 kg/m³.
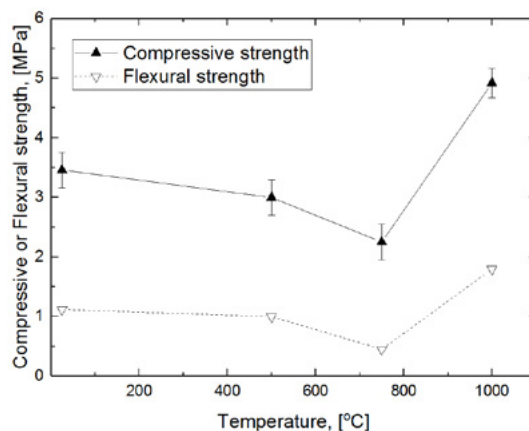

Figure 1: Compressive and flexural strength of MK-based samples (ρ = 600 kg/m³) after fire attack tests.

The compressive strength decreases from 3.46±0.27 MPa at room temperature to 2.25±0.34 MPa at 750

°C. Then, it rises up to 4.92±0.22 after exposure to 1000 °C. A similar trend is observed for the flexural strength, but with lower values.

The mechanisms governing the strength variation are typically different for each kind of alkali-activated material. The strength of MK-based geopolymer binders usually tends to decrease gradually up to 800 °C, while it increases on exposure to 1000 °C [16], and the results in Figure 1 agree well with this trend. Duxson et al. [17] suggested that the transformation of reaction products from amorphous to crystalline (including anhydrous members of the zeolite family) at high temperatures can explain such behaviour. Amorphous aluminosilicate gels tends to lose free water below 200–300 °C with negligible change in the structural framework. After heating above this range, gels release chemically bound T–OH (T being either Si or Al) groups and condense to form T–O–T linkages, along with relocation of alkali cations, resulting in increased overall connectivity. The densified gels start to crystallise at a certain onset temperature, which is influenced greatly by the composition, in particular by the Si/Al ratio and alkali cation type [18]. For instance, Na-aluminosilicate geopolymer gel with Si/Al = 1.15 forms nepheline upon heating to 650 °C, and at 800 °C with Si/Al = 2.15 [17]. On the other hand, K-aluminosilicate geopolymer gels form tetragonal leucite at 1000 °C when starting from an initial composition of $KAlSi_2O_6 \cdot 4.78D_2O \cdot 0.72H_2O$ [13] or 1050 °C with a composition of $KAlSi_2O_6 \cdot 5.5H_2O$ [19].

The preliminary results included here are from samples which contain both Na and K cations and are characterized by Si/Al = 2.0. The chemical composition analysis is in progress to enable full description of the transformations taking place.

Figure 2 shows the relative change of volume and mass of MK-based samples (ρ = 600 kg/m³) after fire attack tests. In agreement with previous comments, it can be observed that the relative mass of the samples experiences very little changes when exposed to moderate temperatures (<5.0 % loss at 500 °C). It then drops considerably between 500 °C and 750 °C (up to ≈15.0 %) and then does not drop any further, even after exposure to 1000 °C (16.7 %), suggesting that all chemically and physically bound water within the samples has been vaporized. On the other hand, the relative volume of the specimens is less stable and it drops dramatically from 11.8 % at 500 °C to over a 52.0 % after firing at 1000 °C. The highest shrinkage increment appears between 750 °C and 1100 °C, and is probably related to a combined effect of gel sintering [20] and pore collapse.
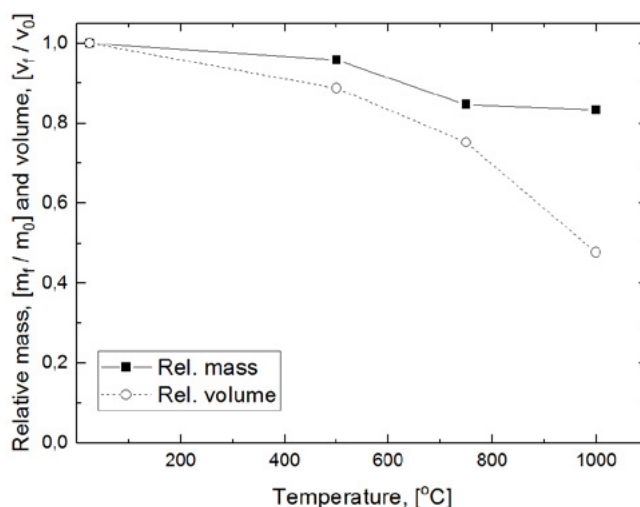

Figure 2: Relative changes of mass and volume of MK-based samples (ρ = 600 kg/m³) after fire attack tests.

Combining findings from strength and thermal shrinkage, our results agree well with previous studies [21] which have proposed that: (1) the large shrinkage along with the loss of free water are the main reason for the loss of strength below 800 °C; (2) the shrinkage due to the release of chemically bound –OH and gel densification at high temperature does not affect the strength to a major extent, and (3) the densification of the gels to form glass and ceramics above an onset temperature is the main reason for the post-cooling strength increase. Nevertheless, further studies and specially the characterization of the chemical changes will provide more information to explain the behaviour of the samples tested here.

4.   Outlook

The present study is a work in progress. Further effort will complete the experimental programme and analyse and interpret the results.

To date, all tested samples had the same binder/foam ratio. The fire-resistance characteristics are expected to be better for those samples with a lower value, since a larger proportion of foam should yield more porous specimens and thus withstand heat transfer better. On the other hand, a larger porosity level will presumably result in poorer mechanical properties but the effect of fire attack still needs to be evaluated. Moreover, the role of the composition will be evaluated from the characterization of pure GGBS and MK/GGBS blends with different weight ratios. Based on previous results [11], samples with a higher initial amount of MK will be expected to exhibit better fire resistance properties since they will lead to the formation of N/K-A-S-(H) gels rather than C-A-S-H ones, which typically exhibit a lower thermal decomposition temperature. Furthermore, Duxson et al. [12] proposed that the resistance to dehydration shrinkage of alkali-activated MK samples is proportional to the Young's modulus of the samples. Binders with a higher Young's modulus should be able to withstand greater capillary strain forces developed during dehydration, and as such the onset temperature of the initial shrinkage will be higher. This future work will test these hypotheses and characterise the effect of the pore network structure and the Young's moduli.

5.   Acknowledgment

6.   References

[1]   G.A. Khoury, Effect of fire on concrete and concrete structures, Progr Struct Eng Mater. 2 (2000) 429–447.

[2]   S. Diamond, Calcium hydroxide in cement paste and concrete—microstructural appraisal. Materials science of concrete special volume: calcium hydroxide in concrete, Am. Ceram. Soc. (2001) 37–58.

[3]   G.A. Khoury, Compressive strength of concrete at high temperatures: a reassessment, Mag. Concr. Res. 44 (1992) 291–309. doi:10.1680/macr.1992.44.161.291.

[4]   M.Zeiml, D.Leithner, R.Lackner, H.A.Mang, How do polypropylene fibers improve the spalling behavior of in-situ concrete?, Cem.Concr.Research. 36 (2006) 929–942.

[5]   A. Behnood, M. Ghandehari, Comparison of compressive and splitting tensile strength of high-strength concrete with and without polypropylene fibers heated to high temperatures, Fire Saf. J. 44 (2009) 1015–1022. doi:10.1016/j.firesaf.2009.07.001.

[6]   K.D. Hertz, Concrete strength for fire safety design, Mag. Concr. Res. 57 (2005) 445–453. doi:10.1680/macr.2005.57.8.445.

[7]   F. Pacheco-Torgal, Z. Abdollahnejad, A.F. Camões, M. Jamshidi, Y. Ding, Durability of alkali-activated binders: A clear advantage over Portland cement or an unproven issue?, Constr. Build. Mater. 30 (2012) 400–405. doi:10.1016/j.conbuildmat.2011.12.017.

[8]   J.L. Provis, J.S.J. van Deventer, Alkali Activated Materials, Springer, 2014.

[9]   J.L. Provis, S.A. Bernal, Geopolymers and Related Alkali-Activated Materials, Annu. Rev. Mater. Res. 44 (2014) 299–327. doi:10.1146/annurev-matsci-070813-113515.

[10]   J.L. Provis, C.Z. Yong, P. Duxson, J.S.J. van Deventer, Correlating mechanical and thermal properties of sodium silicate-fly ash geopolymers, Colloids Surfaces A Physicochem. Eng. Asp. 336 (2009) 57–63. doi:10.1016/j.colsurfa.2008.11.019.

[11]   T.W. Cheng, J.P. Chiu, Fire-resistant geopolymer produce by granulated blast furnace slag, Miner. Eng. 16 (2003) 205–210. doi:10.1016/S0892-6875(03)00008-6.

[12]   P. Duxson, G.C. Lukey, J.S.J. Van Deventer, Physical evolution of Na-geopolymer derived from metakaolin up to 1000 °c, J. Mater. Sci. 42 (2007) 3044–3054. doi:10.1007/s10853-006-0535-4.

[13]   C.E. White, J.L. Provis, T. Proffen, J.S.J. Van Deventerz, The effects of temperature on the local structure of metakaolin-based geopolymer binder: A neutron pair distribution function investigation, J. Am. Ceram. Soc. 93 (2010) 3486–3492. doi:10.1111/j.1551-2916.2010.03906.x.

[14]   Y.S. Wang, J.L. Provis, J.G. Dai, Role of soluble aluminum species in the activating solution for synthesis of silico-aluminophosphate geopolymers, Cem. Concr. Compos. 93 (2018) 186–195. doi:10.1016/j.cemconcomp.2018.07.011.

[15]   BSI, BS EN 196-1:2016 Methods of testing cement. Determination of strength, (2016).

[16]   S.A. Bernal, E.D. Rodríguez, R. Mejía De Gutiérrez, M. Gordillo, J.L. Provis, Mechanical and thermal characterisation of geopolymers based on silicate-activated metakaolin/slag blends, J. Mater. Sci. 46 (2011) 5477–5486. doi:10.1007/s10853-011-5490-z.

[17]   P. Duxson, G.C. Lukey, J.S.J. Van Deventer, Evolution of gel structure during thermal processing of Na-geopolymer gels, Langmuir. 22 (2006) 8750–8757. doi:10.1021/la0604026.

[18]   D.L.Y. Kong, J.G. Sanjayan, K. Sagoe-Crentsil, Factors affecting the performance of metakaolin geopolymers exposed to elevated temperatures, J. Mater. Sci. 43 (2008) 824–831. doi:10.1007/s10853-007-2205-6.

[19]   P. Sarin, J.L. Provis, J.L. Bell, R.P. Haggerty, P.J. Chupas, J.S.J. van Deventer, P.E. Driemeyer, W.M. Kriven, Atomic Structure of a Cesium Aluminosilicate Geopolymer: A Pair Distribution Function Study, Chem. Mater. 20 (2008) 4768–4776. doi:10.1021/cm703369s.

[20]   P. Hlaváček, V. Šmilauer, F. Škvára, L. Kopecký, R. Šulc, Inorganic foams made from alkali-activated fly ash: Mechanical, chemical and physical properties, J. Eur. Ceram. Soc. 35 (2015) 703–709. doi:10.1016/j.jeurceramsoc.2014.08.024.

[21]   Z. Zhang, J.L. Provis, A. Reid, H. Wang, Geopolymer foam concrete: An emerging material for sustainable construction, Constr. Build. Mater. 56 (2014) 113–127. doi:10.1016/j.conbuildmat.2014.01.081.

Durability parameters of self-compacting concrete with binary and ternary combinations of Portland cement, limestone filler and metakaolin

L. R. M. Miranda[1], V. M. S. Capuzzo[2]

[1]Magnel Laboratory for Concrete Research – Ghent University.

[2]Postgraduate Program in Structure and Civil Construction – University of Brasilia.

Abstract

The use of fine mineral additions in self-compacting concrete (SCC) is unavoidable to improve its self-sustaining characteristics and reduce consumption of Portland cement. The cement industry has been studying supplementary cementitious materials (SCM) that can fulfil world production demand, but it is important that this replacement is done rationally, ensuring that SCC performance is maintained for the setting conditions as well as the mechanical properties and durability. Corrosion of reinforcement is one of the main causes of concrete structures deterioration in urban environments rich in CO_2 been the carbonation of concrete one of the main mechanisms that lead to this corrosion. Carbonation is a phenomenon that occurs naturally in concrete structures, requiring the presence of a certain concentration of carbon dioxide and a certain moisture content in the atmosphere. Under natural exposure conditions (0.03 to 1% CO_2), the advance of the carbonation front takes several years to present analysable results. Therefore, many researches are developed using an accelerated test system. In this context, the aim of this work was to analyse the performance against accelerated carbonation of SCC with a 20% substitution of Portland cement by limestone filler and metakaolin, both isolated and in combination. The accelerated carbonation test followed the recommendations of ISO 1920-12: 2015. In addition, mechanical properties were measured and the mercury intrusion porosimetry (MIP) test was performed. The results of the mix containing only metakaolin were the best for all properties evaluated, indicating that the structure of its paste is the densest and most rigid of all concretes or that the use of metakaolin promoted an increase in the resistance of the paste transition zone with the aggregates. On the other hand, the mix with 20% of limestone filler had the worse mechanical performance and lower durability against carbonation. The filler effect was not able to compensate the Portland cement removal, probably due to the high w/c ratio adopted. The mix with the ternary combination, in general, presented a performance superior to the limestone one and inferior to metakaolin one, in all properties analysed.

Keywords: Carbonation, self-compacting concrete, supplementary cementitious materials.

1. Introduction

The use of fine mineral additions in SCC is inevitable to improve its self-compacting properties and reduce material consumption, especially Portland cement. This reduction decreases the heat of hydration generated by the high consumption of cement, besides bringing economic advantages. Several benefits can be seen in the use of mineral additions, and this use is already carried out in the production process or incorporated later as replacement or addition to the mass of cement used, so that the cement industry has been studying

supplementary cementitious materials that can fulfil world demand of production [1]. The use of mineral additions as a substitute for Portland cement is now a common practice in the construction industry, but it is important that this substitution be made in a rational way, ensuring that the performance of the SCC is maintained, both for the settings conditions and for mechanical properties and durability, resulting in the optimal design of a concrete with lower clinker amount. It is, therefore, necessary that the intrinsic requirements of any new system be evaluated [2].

This practice also comes with an environmental approach, as the construction sector is nowadays responsible for 40% energy consumption, 40% solid waste generation, 38% greenhouse gas emissions and 12% water depletion. One of the main environmental impacts of concrete itself comes from CO_2 emissions during Portland cement production, which accounts for more than 5% of the global anthropogenic release of CO_2. It is visible that reducing the clinker content of Portland cement will help to reduce the environmental impact of concrete [3-4]. Carbonation is one of the main causes of deterioration of concrete structures in urban environments rich in CO_2, being one of the principal mechanisms responsible for steel corrosion. The concentration gradient between the concrete and the environment leads to the diffusion of carbon dioxide, which reacts with the hydrated compounds of the cement, resulting in a reduction of the alkalinity of the system. Carbonation is a phenomenon that occurs naturally in concrete structures and it is directly related to the ease that carbon dioxide has to diffuse inside the concrete, the environmental conditions and the permeability properties of the concrete [5-7]. Works on carbonation in SCC fortify the vast incorporation of mineral additions and residues in the production of SCC, like [8] tungsten Mine Tailings, [9] waste glass powder, [10] municipal solid waste incineration (MSWI), [11] copper slag and [12] spent garnet.

Under natural exposure conditions (0.03 to 1% CO_2), the advance of the carbonation front takes several years to present analysable results. Therefore, many researches are developed using an accelerated test system, which submits the concrete to high levels of CO_2 and allows a rigid control of all exposure conditions, providing a rapid response of the behaviour of the material to carbonation. Due to no worldwide regulation analysis methods regarding accelerated carbonation test system, comparison of the results of researches conducted in several countries is difficult because of the great variability on test parameters. However, with the enactment of ISO 1920-12: 2015, which may be very relevant to future studies on accelerated carbonation, it is expected an improvement in this comparison possibility and a more solid database on the subject [7; 13-14].

In this context, the aim of this work was to analyse the performance under accelerated carbonation of self-compacting concretes with 20% replacement of Portland cement by limestone and metakaolin, isolated and combined, in order to verify the combined action of the additions. The fresh state parameters of the concretes were evaluated according to the definitions of Brazilian standard [16]. In addition, the mechanical properties were measured and the mercury intrusion porosimetry test was carried out to verify how the pore refinement influences the ingress of the deleterious agent.

2. Methodology

2.1 Materials

The following materials were used in the experimental program:

• Portland cement composite with filler (Brazilian CP II F - 40), with a minimum compressive strength of 40 MPa at 28 days;

• Limestone filler and metakaolin as mineral additions;

• Composition of two types of sands, a natural of quartz origin and a crushed of limestone origin, as small

aggregate;

• Two granulometric bands of large aggregate of limestone origin, one with a maximum characteristic size of 12,5 mm and the other with 19 mm;

• Third generation superplasticizer, with modified polycarboxylic ether chemistry.

The chemical composition of the fine materials used was obtained by the X-ray fluorescence spectrometry (EDX). From Table 1 is possible to notice the predominance of calcium oxide (75,2%) in the cement, since it is a composite cement with up to 10% of limestone, that is a high content of clinker and rich in calcium carbonate. The metakaolin, which is obtained from the calcination of kaolinite clays, is basically composed of silica (SiO_2) and alumina (Al_2O_3) in the amorphous phase. The limestone filler has 83.10% CaO by mass and the presence of SiO_2 (6.63%) in quartz and kaolinite is also observed.

Table 1: Chemical composition of the fine materials

Chemical compost	% by weight		
	Metakaolin	Limestone filler	Cement CP II F - 40
SiO_2	50,54	6.63	9.29
CaO	0.00	83.10	75.20
Al_2O_3	42.28	2.12	2.46
Fe_2O_3	3.23	2.16	4.41
TiO_2	1.63	0.26	0.53
K_2O	1.07	0.94	1.87
MgO	1.02	3.61	2.69
SO_3	0.09	0.23	2.76
SrO	0.00	0.96	0.47

2.2 Methods

2.2.1 Mix design

The experimental program carried out for the production and analysis of SCC was conceived considering a reference concrete (REF), with no substitution content and three scenarios of Portland cement substitution: 20% replacement of Portland cement by metakaolin (M20), 20% replacement of Portland cement by limestone (F20) and 20% Portland cement replacement by a composition of 15% metakaolin and 5% limestone (M15F5). The ternary mixture was performed because the synergy of the combination between calcined clays and limestone have presented favourable results as an alternative to clinker, as in the case of LC3 cement.

The SCC dosage was performed using the granular skeleton composition concept by the unit weight test. The granular skeleton of all mixtures was composed of 33.6% of gravel 19 mm, 14.4% of gravel 12.5 mm, 32% of crushed sand and 20% of natural sand. The limits determined by the ACI 237 R-07 of fixed binder consumption at 475 kg/m³ and fixed water/binder ratio (w/b) of 0.55 were used as criteria. The value of 0.55 was chosen because it comprises the aggressiveness class III of Brazilian standard NBR 6118 [26], one of the most vulnerable material scenarios. It was also determined that the slump-flow final value should be within the range of SF2 class (between 660 and 750 mm) delimited by Brazilian standard NBR 15823-1 [16] and the necessary adjustments were made by adding superplasticizer.

REF was the first concrete produced and from the determination of its unitary proportion the other mixtures were performed with the aforementioned Portland cement substitutions. This proportion was 1: 0: 0: 0.64: 1.03: 0.46: 1.08: 0.55 and is in the format Portland cement: limestone filler: metakaolin: natural sand: crushed sand: gravel 12.5 : gravel 19: w/b. The bulk consumption of the mixtures is shown in Table 2.

Table 2: Bulk consumption of the materials

	Mixture consumption (kg/m³)								
	Cement	Limestone filler	Metakaolin	Natural sand	Crushed sand	Gravel 12,5	Gravel 19	Water	Superplasticizer
REF	475,00	0.00	0.00	306.11	489.77	220.40	514.26	261.25	1.66
F20	379.83	94.96	0.00	303.26	485.21	218.35	509.47	261.14	2.14
M20	380.00	0.00	95.00	299.98	479.96	215.98	503.96	261.25	7.12
M15F5	379.75	23.73	71.20	301.83	482.92	217.32	507.07	261.08	4.03

2.2.2 Fresh and hardened state test

In order to evaluate the SCC behaviour in the fresh state, slump-flow, t_{500} , V-funnel , L-box and visual stability index tests were performed according to self-compacting criteria established by Brazilian standard [16].

For the mechanical properties evaluation cylindrical specimens of 100 x 200 mm were cast, with top regularization by grinding. Each result presented consists of the average value obtained from three specimens. Axial compression strength test was performed according to [18] at the ages of 7, 14 and 28 days. The specimens stayed curing in a humid chamber until the determined ages. At 28 days, tensile strength by diametrical compression and static elastic modulus tests were also performed, following the recommendations of [19] and [20], respectively.

The accelerated carbonation test was performed in compliance with the recommendations of [15]. This standard sets the carbonation chamber conditions, with a temperature of 22 ± 2 ° C and relative humidity of 55 ± 5%, but for hot climates, such as Brazil, the values change, passing to a temperature of 27 ± 2 ° C and relative humidity of 65 ± 5%. CO_2 concentration shall be 3,0 ± 0,5% by volume for any climatic condition. Prismatic specimens of 400 x 100 x 100 mm were used. Before the test begins, the prismatic specimens were sealed with paraffin, leaving only two faces exposed to the test conditions for a direction in the CO_2. diffusion flow. They were then placed in the accelerated carbonation chamber for 70 days and carbonation front depth measurements were performed at 56, 63 and 70 days of exposure using a phenolphthalein pH indicator solution and a digital calliper with a resolution of 0, 01 mm.

Mercury intrusion porosimetry was performed in pastes, in samples of approximately 1 cm³. The equipment used was AutoPore IV 9500 V1.05 from Micromeritics Instrument Corporation. During the test, mercury was intruded into the samples continuously at a 130° contact angle and a mercury surface tension of 4.85 x 10^{-1} N/m with a pressure increase of 0.0007 to 414 MPa were considered.

3.   Results and discussion

3.1   Fresh state

As a research premise the mixtures were fixed with variation only of the Portland cement substitution by SCM. In order to reach the defined slump-flow range, adjustments were made in the superplasticizer content. A higher superplasticizer content was required for the mixtures containing metakaolin, due to its high specific surface area influences the water demand and increases viscosity. The same was found by [21], who produced SCC with Portland cement substitutions by metakaolin at replacement levels of 5, 10, 15 and 20% and found that higher the content, higher the superplasticizer consumption. No evident exudation or segregation was observed in any of the concretes. According to the results shown in Table 3, it can be affirmed that they are all in agreement with [16] fluidity, passing ability and cohesion requirements.

Table 3: Results of fresh state characteristics

	REF	F20	M20	M15F5
t_{500} **(s)**	1.47	1.25	2.15	1.86
SLUMP-FLOW (mm)	683	685	675	690
V-FUNNEL (s)	2.95	2.69	3.16	2.26
L-BOX	0.82	0.9	0.9	0.87
SPECIFIC GRAVITY (kg/m³)	2350	2310	2320	2300
SUPERPLASTICIZER (%)	0.35	0.45	1.1	0.85

3.2 Mechanical properties

According to the compressive strength, the concretes presented resistance gains with the advancing age and the mixtures containing metakaolin achieved higher performance than the reference concrete. The improvement in the resistance with metakaolin use in comparison to limestone filler is evident in the binary combinations, once M20 has achieved a resistance 50.9% higher than the REF and the F20 had a loss of 15.4%. Only F20 caused a decrease in compressive strength. The high reactivity mineral additions have a high surface area, responsible for potentiating lime fixation by pozzolanic activity, which promotes an increase in the compressive strength of the hydrated matrix [22]. In this context, it is expected that the mixes with metakaolin will increase resistance even with less clinker in the composition. The M15F5 increased by 29.4%.

Table 4 - Mechanical properties of self-compacting concretes at 28 days

	REF	F20	M20	M15F5
COMPRESSIVE STRENGTH (MPa)	41.0	34.7	61.8	53.0
TENSILE STRENGTH (MPa)	4.1	3.3	4.7	3.9
ELASTIC MODULUS (GPa)	31.9	29.7	36.5	33.7

This increase of resistance with the increase of the Portland cement substitution content by metakaolin was also obtained by [23], which produced SCC with substitutions of 7, 11, 14 and 20% metakaolin. [24], produced SCC with 10 and 20% replacement of Portland cement by metakaolin and 10, 20 and 30% substitution for blast furnace and fly ash granulated slag, and the mixtures with 20% metakaolin presented higher resistance. It is known that the use of inert materials in the concrete causes the filler effect, which promotes refinement of the pore system, since the fineness of particles serves as a nucleation point for the formation of hydrates. Because of this, it is common for concretes to increase strength, but the high water/binder ratio adopted for the mixtures in this work probably had greater influence.

In the tensile strength, the tendency of the concrete behaviour was similar to that observed in the compressive strength, but with lower percentages of gain or loss of resistance. M15F5 was the mixture with the highest behaviour change, since it presented a compressive strength gain of 29.4% in relation to the REF, and a decrease of 4.5% in tensile strength. The values found for elastic modulus in SCC, in general, are lower than those commonly observed in conventional concretes. According to [25], this is due to SCC higher paste content. Since the deformability of the paste is higher than that of the aggregates, a decrease in stiffness of the entire system occurs. In the mixtures containing metakaolin there was an increase in the elastic modulus values. M15F5 promoted a 5.7% increase in modulus of elasticity. On the other hand, the M20, as in the other properties, presented the highest result, with its elastic modulus being 14.5% higher than the reference concrete.

3.3 Accelerated carbonation

All values presented are the average of at least 6 readings taken along the surfaces of the specimens exposed to the CO_2 diffusion flow. There was an increase in the measured value with the advance of the time of SCC exposure to the accelerated carbonation environment, more accentuated in the limestone mixtures.

It can be seen (Figure 1) that at 56 days, the mixtures with limestone filler showed a carbonation depth lower than the REF, but with the advancement of the exposure time the value became higher. M15F5 presented values slightly higher than REF and M20 lower values, for all measurement times. It is noted that the carbonation values of M15F5 and M20 have a stabilizing tendency, while F20 showed a clear growth in time.

F20 had a bigger measured depth, with a value 24% higher than the REF at the end of the test. The increase caused by M15F5 was 4%, while the M20 promoted a decrease of 55%.

The limestone filler reacts more rapidly in the system with metakaolin than in the binary mixture of filler and Portland cement. These results point to synergistic effects on the combined substitution of additions. However, calcium hydroxide consumption may mean that high-level substitution mixtures may carbonate more quickly [1]. According to [3] the use of a larger amount of lime (>20%) requires reduction of the water/cement ratio to produce concrete with similar durability performance, which is not the case of the mixtures in this work.

In the limestone filler mixtures the advance of the carbonation front occurred in a uniform way, with the identification of a linear carbonation front. In the ones with metakaolin the advance of the carbonation front was very small, due to the improvement of paste quality. In the ternary mixture (M15F5) a weakening in the paste/aggregate transition zone was observed, which facilitated diffusion of the carbon dioxide. This tendency led to points with high carbonation depths and others with practically no advanced front, so that the average generated a slightly higher result than the REF, although visually its carbonated surface was smaller.
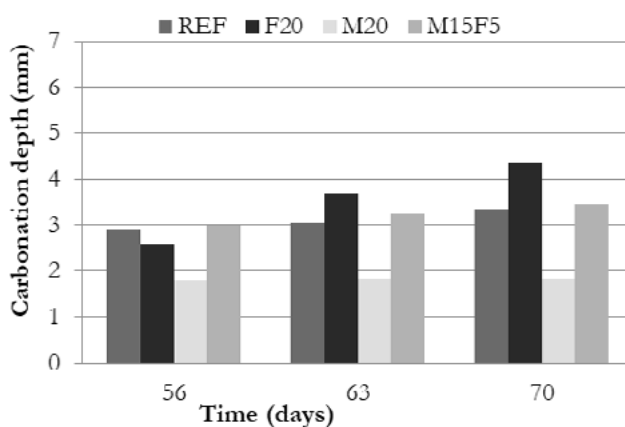

Figure 1: SCC carbonation depths

Using the equation that proposes that the carbonation depth is proportional to the square root of exposure time ($x = K . \sqrt{t}$), the carbonation coefficients (K) of each mixture were determined using the depth readings of the specimens after 70 days of exposure. With this coefficient it is possible to estimate the time required to reach any desired carbonation depth value for the CO_2 concentration used in the accelerated test (3.0 $\pm$ 0.5%). The nominal cover recommended by [26], for concrete exposed to environmental aggression class III, is 40 mm. Thus, extrapolations were made to determine how much time it would take to carbonation front of each concrete in this study to reach that value.
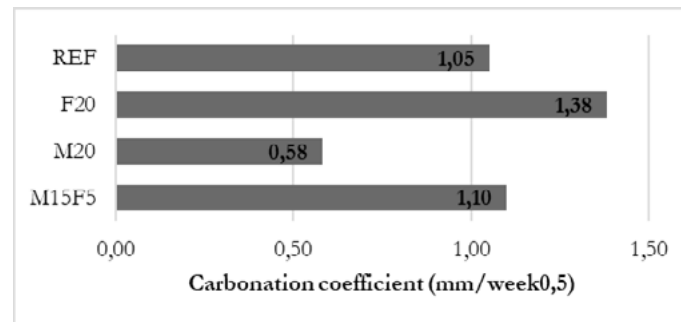
Figure 2: Specimens carbonation coefficient

In the REF, F20, M20 and M15F5 would be required approximately 27.83, 16.11, 91.22 and 25.36 years, respectively, for a carbonation depth of 40 mm.

It is known, however, that CO_2 concentration of the environment is around 0.04%, a value 75 times lower than the concentration used in the determination of the aforementioned carbonation coefficients. Thus, without considering other interactions of the structures with the environment and the deteriorations to which they can be subjected in situations of use, carbonation would take longer to reach the structures reinforced with the studied SCC mixtures than usual structures life expectancy. It can be seen that SCC is a good alternative for extending life of concrete structures, especially if carbonation is considered the main aggressive factor, even in mixtures with 20% less Portland cement in its composition.

3.4   Mercury intrusion porosimetry

The carbonation resistance of concrete is also influenced by its pore structure. The diffusivity of fluids/ions in the concrete is a function of the porosity and characteristics of the structure of the pore network (geometry, distribution, interconnectivity and tortuosity). The higher the porosity of the system, the greater the space available for the diffusion of carbon dioxide, therefore, the lower the resistance to carbonation of the system [27]. It is observed that the maximum value of intruded volume in the pores occurred in the mesopore range (0.002 to 0.05 µm), indicating a refined porous structure in the concretes. It is also possible to observe pores with dimensions above 50 µm which, according to [28], are spherical and correspond to the air voids incorporated. REF is the mixture with the lower amount of these macropores while F20 has the largest amount.
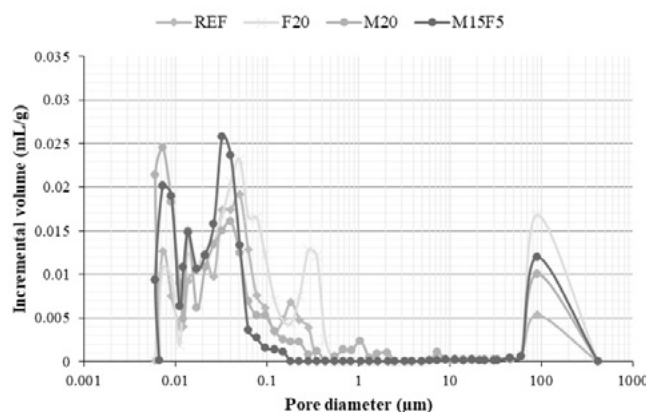

Figure 3: Relation between incremental volume and pore diameter in MIP test

In the region close to the diameter of 0.05 µm, the use of metakaolin caused an increase in pore volume, with the amount of M20 being higher, followed by M15F5, that is, a refinement characterized by an increase in volume of smaller pores. It is also noted that F20 showed a significant peak in the capillary pore range, in

addition to the greater amount of mesopores and greater amount of accumulated volume, which indicates higher susceptibility of this mixture to the entry of deleterious agents.

M20 presented largest volume of pores of small diameter. The amount of these pores increases with the formation of hydrates, which shows the pozzolanic action. In both mixtures containing metakaolin, a porous structure composed of a larger volume of mesopores is also observed, the action of the isolated addition (M20) being more pronounced than in combination with the limestone filler (M15F5). [29] studied the absorption characteristics of the concrete with the increased substitution of metakaolin and confirmed a reduction in the water absorption in the system due to the decrease of concrete porosity.

Both M20 and M15F5 showed the highest values of total pore area, probably due to the porosity refinement due to the formation of a higher amount of C-S-H by the pozzolanic action. F20 had the highest volume of intruded mercury. Regarding permeability, F20 once again had the highest observed value. In relation to tortuosity, M15F5 had the highest value among the mixtures, which in general presented close values.

4.   Conclusions

• Through the analysis of the fresh state results it can be affirmed that the concretes complying the fluidity, passing ability and cohesion requirements defined by [16];

• As the granular skeleton was the same for all SCC, the variation in values is attributed to the stiffness of the pastes. Since M20 results were the best for all mechanical properties evaluated, it is understood that the structure of their paste is the densest and most rigid of all concretes or that the use of metakaolin increased the resistance of the transition zone between paste and aggregates;

• M15F5, in general, presented a performance superior to the mixture with limestone and inferior to the one with metakaolin, in all properties analysed;

• The mix with 20% of limestone filler (F20) had the worse mechanical performance and lower durability against carbonation. The filler effect was not able to compensate the Portland cement removal, probably due to the high w/c ratio adopted;

• At the same time as the pozzolanic reaction consumes the calcium hydroxide, and thus decreases the amount of the hydration product responsible for guaranteeing the alkalinity of the cementitious matrix, the formation of secondary C-S-H promotes a decrease in the pore diameter of the hydrated paste. Thus, even with the lowest amount of CH, the mix with metakaolin presented a better resistance to the advance of the carbonation front compared to the reference one, which shows that the pore refinement was effective in preventing the diffusion of CO_2, even in a less alkaline environment.

5.   Acknowledgement

6.   References

[1] M. Antoni, J. Rossen, F. Martirena, K. Scrivener, Cement substitution by a combination of metakaolin and limestone. Cem. Concr. Res. 42 (2012) 1579-1589, http://dx.doi.org/10.1016/j.cemconres.2012.09.006

[2] Y. Dhandapani, T. Sakthivel, M. Santhanam, R. Gettu, R. G. Pillai, Mechanical properties and durability performance of concretes with Limestone Calcined Clay Cement (LC3). Cem. Concr. Res. 107 (2018) 136-151, https://doi.org/10.1016/j.cemconres.2018.02.005.

[3] S.Palm, T. Proske, M. Rezvani, S. Hainer, C. Müller, C. Graubner, Cements with a high limestone content – Mechanical properties, durability and ecological characteristics of the concrete. Constr. Build. Mater. 119 (2016) 308-318, https://doi.org/10.1016/j.conbuildmat.2016.05.009.

[4] G. De Schutter, K. Lesage, V. Mechtcherine, V. N. Nerella, G. Habert, I. Agusti-Juan, Vision of 3D printing with concrete — Technical, economic and environmental potentials. Cem. Concr. Res. 112 (2018) 25–36, https://doi.org/10.1016/j.cemconres.2018.06.001.

[5] V. G. Papadakis, C. G. Vayenas, M. N. Fardis, Fundamental Modeling and Experimental Investigation of Concrete Carbonation. ACI Mat. Jour. 88 (1991) 363-373.

[6] V. Shah, S. Bishnoi, Carbonation resistance of cements containing supplementary cementitious materials and its relation to various parameters of concrete. Constr. Build. Mater. 178 (2018) 219-232, https://doi.org/10.1016/j.conbuildmat.2018.05.162.

[7] H. F. W TAYLOR, Cement Chemistry.(1997). 2 ed. Londres. Thomas Telford.

[8] Y. J. Kim, Y. J. Kim, Y. W. Choi, An Experimental Research on Self-consolidating Concrete using Tungsten Mine Tailings. KSCE Journal of Civil Engineering 20(4) (2016) 1404-1410, https://doi.org/10.1007/s12205-015-0196-4.

[9] M Matos, T. Ramos, S. Nunes, J. Sousa-Coutinho, Durability Enhancement of SCC With Waste Glass Powder. Materials Research 19 (2015) 67-74, http://dx.doi.org/10.1590/1980-5373-MR-2015-0288.

[10] M. Carsana, M. Gastaldi, F. Lollini, E. Redaelli, L. Bertolini, Improving durability of reinforced concrete structures by recycling wet ground MSWI bottom ash. Materials and Corrosion 67 (6) (2016) 573-582. https://doi.org/10.1002/maco.201608881.

[11] R. Sharma, R. A. Khan, Durability assessment of self-compacting concrete incorporating copper slag as fine aggregates. Constr. Build. Mater. 155 (2017) 617-629, https://doi.org/10.1016/j.conbuildmat.2017.08.074.

[12] H. L MUTTASHAR, M. A. M. ARIFFIN, M. N. HUSSEIN, M. W. HUSSIN, S. B. ISHAQ, Self-compacting geopolymer concrete with spend garnet as sand replacement. Jour. Build. Eng. 15 (2018) 85-94, https://doi.org/10.1016/j.jobe.2017.10.007.

[13] RICHARDSON, M. G. (1998). Carbonation of reinforced concrete: Its causes and management. New York: CITIS Ltd, Publishers

[14] C. Pauletti, E. Possan, D. C. C. Dal Molin, Carbonatação acelerada: estado da arte das pesquisas no Brasil. Ambiente Construído 7 (2007) 7-20,

[15] International Standard. ISO 1920-12:2015 – Testing of concrete – Part 12: Determination of the carbonation resistance of concrete – Accelerated carbonation method. Geneva, Switzerland.

[16] Brazilian Association of Technical Standards. NBR 15823-1. Self-compacting concrete Classification, control and fresh state acceptance. ABNT, Rio de Janeiro, Brazil, 2017

[17] American Concrete Institute. ACI 237R-07: Self-Consolidating Concrete. 2007.

[18] Brazilian Association of Technical Standards. NBR 5739. Concrete – compressive strength of cylindrical samples. ABNT, Rio de Janeiro, Brazil; 2007

[19] Brazilian Association of Technical Standards . NBR 7222. Concrete and mortar – Determination of

tensile strength by diametrical compression of cylindrical specimens. ABNT, Rio de Janeiro, Brazil; 2011

[20] Brazilian Association of Technical Standards . NBR 8522. Concrete – Determination of static elastic modulus to compression. ABNT, Rio de Janeiro, Brazil; 2008

[21] K. A. Melo, A. M. P. Carneiro, Effect of metakaolin's finesses and content in self-consolidating concrete. Constr. Build. Mater. 24 (2010) 1529-1535, https://doi.org/10.1016/j.conbuildmat.2010.02.002.

[22] J. HOPPE FILHO, A. GOBBI, E. PEREIRA, V. A. QUARCIONI, M. H. F. MEDEIROS, Pozzolanic activity of mineral additions to Portland cement (Part I): Pozzolanic activity index with lime (PAI), X-ray diffraction (XRD), thermogravimetry (TG/DTG) and modified Chapelle. Revista Matéria 22 (2017) http://dx.doi.org/10.1590/s1517-707620170003.0206.

[23] I.P. Sfikas, E.G. Badogiannis, K.G. Trezos, Rheology and mechanical characteristics of self-compacting concrete mixtures containing metakaolin. Constr. Build. Mater. 64 (2014) 121-129, https://doi.org/10.1016/j.conbuildmat.2014.04.048.

[24] S. Dadsetan, J. Bai, Mechanical and microstructural properties of self-compacting concrete blended with metakaolin, ground granulated blast furnace slag and fly ash. Constr. Build. Mater. 146 (2017) 658-667, https://doi.org/10.1016/j.conbuildmat.2017.04.158.

[25] European Federation For Specialist Construction Chemical And Concrete Systems – EFNARC. Specification and Guidelines for Self-Compacting Concrete. Specification, Production and Use. EFNARC, United Kingdom, 2005. 63p.

[26] Brazilian Association of Technical Standards . NBR 6118. Concrete Structural Projects – Procedure. ABNT, Rio de Janeiro, Brazil; 2017

[27] B. B. Das, B. Kondraivendhan, Implication of pore size distribution parameters on compressive strength, permeability and hydraulic diffusivity of concrete. Constr. Build. Mater. 28 (2012) 382-386, https://doi.org/10.1016/j.conbuildmat.2011.08.055.

[28] MEHTA. P.K.; MONTEIRO, P.J.M. Concreto: Microestrutura, propriedades e materiais. 3ª ed. São Paulo: Ed. IBRACON, 2014.

[29] J. M. Khatib, R. M. Clay, Absorption characteristics of metakaolin concrete. Cem. Concr. Res. 34 (2003) 19-29, https://doi.org/10.1016/S0008-8846(03)00188-1.

Eco-synthesis of zeolite from coal fly ash

K.M. Klima, Q.L. Yu, H.J.H. Brouwers

Department of Built Environment, Eindhoven University of Technology, Eindhoven 5600 MB

Abstract

In this work, pure zeolite Na-P1 is successfully synthesized from Coal Combustion Fly Ash via the fusion process. The obtained phase can be applied as a reactive filler in geopolymer composite and can be assessed in terms of temperature stability. First, a known amount of Coal Combustion Fly Ash was subjected to calcination in a muffle furnace at 800°C in order to eliminate the unburnt carbon. After that, the sample was subjected to a hydrochloric acid treatment (4.5M) in a reflux condenser. It is intended to reduce the iron contained in the ash, but also to reduce other impurities like potassium, calcium or magnesium. Owing to the acid treatment it is possible to increase the efficiency of zeolite conversion.

This step allows synthesizing highly pure zeolite P1. The solid mixture of treated fly ash and NaOH with a mass ratio 1:1.25 undergoes the reaction, as a result of which the silicates and aluminates of sodium are obtained at 550oC in 1.5 hours in the muffle furnace. Further hydrothermal activation through grinding and mixing with deionized water in a mass ratio of 1:10 for 3 hours at room temperature was applied. The sample was kept in a drying oven at 85oC within 90 hours in a sealed container made of polypropylene. The identification of zeolite P was carried out using powder X-ray diffraction, scanning electron microscope and Fourier transform infrared spectroscopy. These methods allowed to identify the crystalline phase and confirm the effectiveness of the synthesis procedure.

The thermal properties and stability aspects of zeolite Na-P1 were determined by thermogravimetric-differential scanning calorimetry (TG-DSC). The study provides a protocol for synthesizing pure zeolite P1 from fly ash, in addition, it allows for the accomplishment of the first step toward fire resistant geopolymer synthesis by using coal combustion fly ash. Preliminary results show that the applied method of the synthesis successfully allows obtaining a pure product. The characterization of the material confirmed the presence of zeolite Na-P1 as well as the first test of thermal analysis was carried out. The heat resistance of synthetic zeolite P1 is up to 790oC, however, its performance in geopolymer matrix has to be investigated.

Keywords: Zeolite, fire-resistance, filler, geopolymer.

Influence of Particle Size Distribution and MSWI Bottom Ash Aggregate Replacement in Zero-Slump Concrete

P.M.F. van de Wouw, M.V.A. Florea, H.J.H. Brouwers

Department of the Built Environment, Eindhoven University of Technology, P.O. Box 513, 5600 MB Eindhoven, the Netherlands.

Abstract

In Europe, approximately 18 million tonnes of bottom ash (BA) is being produced annually through the incineration of municipal solid waste (MSWI). Currently, this is either stockpiled, limitedly applied as road base material, or, in the Netherlands, for some specifically treated BA fractions the application as aggregate in concrete is becoming more accepted. With the application of BA in concrete, stockpiling, the extraction of virgin materials, and the CO_2 production footprint can be reduced. Earth-moist or zero-slump concrete (ZSC) mass products are ideal for the incorporation of MSWI BA due to their absence of reinforcement, higher porosity, and primarily non-structural applications.

This study focusses on investigating how the mix design of ZSC is influenced by coarse and fine aggregate replacement with BA over a distribution modulus range. To this aim, a spherical central composite design approach is used to acquire a broad understanding on the interaction and influence of the 3 independent variables (sand replacement, gravel replacement, and distribution modulus (q)) on ZSC mix design.

It is found that for BA containing ZSC, pre-saturation of the BA reduces the required mixing water. Additionally, both the additions of fine and coarse pre-saturated BA increase the total amount of water in the system while an equal workability is maintained. In turn, this water can potentially contribute to internal curing at a later stage. Due to the porosity of the BA, the overall density of the concrete is found to decrease with an increase in both fine and coarse aggregate replacement. Furthermore, an increased q-value with an equal cement content and workability results in a lower powder content with a higher binder concentration in the powders, and therefore a lower water-binder ratio. Finally, for the particle packing optimisation with porous materials, the use of the envelope volume (including porosity and voids) of particles is proposed.

Keywords: Zero-Slump Concrete, MSWI Bottom Ash, Mix Design, Aggregate Replacement, Distribution Modulus.

1.   Introduction

Through the incineration of municipal solid waste (MSWI) in a waste-to-energy plant, electric power and hot water are produced. Annually, this results in approximately 18 million tonnes of bottom ash (BA) being produced in Europe (1.7 million tonnes in the Netherlands) [1,2]. Currently, this is either stockpiled, limitedly applied as road base material, or, in the Netherlands, for some specifically treated BA fractions the application as aggregate in concrete is becoming more accepted [3].

Concrete, with a worldwide production of approximately 33 billion tonnes annually, accounts for the use of 27 billion tonnes of aggregates per year [4]. Hence, both the consumption of raw materials and the

lowering of the environmental impact of concrete have attracted attention in recent years [5,6]. To this end, the application of industrial by-products such as MSWI BA have been extensively studied as potential aggregate replacement for the production of concrete [7–13]. With the application of BA in concrete, stockpiling, the extraction of virgin materials, and the CO_2 production footprint can be reduced [14–17].

Concrete mass products such as paving blocks, kerbstones, masonry blocks, roofing tiles, sewage pipes, and concrete slabs, are produced with zero-slump concrete (ZSC), otherwise known as earth-moist concrete or no-slump concrete. Contrary to concrete with a plastic consistency, after filling and intense vibratory compaction under compression, the unhardened product is directly extractable and successively transferrable to a curing location with controlled conditions [18]. Most ZSC does not contain reinforcement which could be harmed by chlorides present in BA. In comparison with a regular vibrated concrete, alkali-silica reaction (ASR) is found to be less of a problem in ZSC due to a higher porosity and larger pores, enabling a bigger volume of ASR gel, resulting in less expansion and a lower amount of cracks [19]. Furthermore, since ZSC is scarcely used in a structural application, it is a safe application in the unforeseen circumstance that a deficiency should occur.

The packing of continuously graded particles was studied by Andreasen and Andersen (A&A) [20] who based their work on that of Fuller & Thomsen [21], resulting in a semi-empirical equation for the cumulative volume fraction *F(D)*. Funk & Dinger [22] further developed this work, introducing the modified version of the A&A equation:

$$F(D) = \frac{D^q - D_{min}^q}{D_{max}^q - D_{min}^q} \tag{1}$$

where

D = particle size;

D_{min} = minimum particle size;

D_{max} = maximum particle size;

q = distribution modulus.

Making use of the modified A&A equation, Brouwers and Radix [23] proposed a particle-packing based mix design method for self-consolidating concrete (SCC). This methodology is flexible regarding materials and applications by altering the physical constraints (real-world limits), logical constraints (boundary conditions reflecting requirements for the designed concrete), and policy constraints (boundary conditions set by standards and legislation). Therefore, it has been applied in applications such as: SCC [24–26], ultra-high performance concrete [27–29], ultra-lightweight concrete [30–32], and ZSC [33–36].

This study focusses on investigating how the mix design of ZSC is influenced by coarse and fine aggregate replacement by BA over a distribution modulus range.

2. Methodology

2.1 Materials

A mixture used for the carrier layer of ZSC products is used as a starting point. This mixture consists of five components: cement, fine and coarse aggregates, water, and a plasticising admixture. A blended Portland cement (CEM III/A 42.5N) was selected as binder because it works well in full scale production and has been proven to be beneficial for the implementation of BA [37,38]. To enable the optimisation of the particle size distribution (PSD) while maintaining an equal binder (cement) content (v/v %) throughout the different mixtures, a commercially available quartz powder is included in the mix design as inert virgin

filler. A quartz sand (125 μm-4.0 mm) extracted in the Netherlands is used in the original mix design and applied as fine virgin aggregate. To enable a continuous grading of particles in accordance with the modified A&A equation, a virgin quartz micro sand is used to fill the gap between the PSD of the cement and the fine aggregates. The coarse virgin aggregates consist of a broken limestone (1.0-11.2 mm) from Belgium. A lignosulfonate-based plasticising admixture is used to assist in the compaction of the ZSC mixtures. The plasticiser dosage is fixed at a plasticiser/binder ratio of 0.1% and, as the cement dosage is fixed, is therefore constant throughout all mixtures (v/v %).

The BA used in this study for the replacement of natural aggregates was obtained from a municipal solid waste-to-energy plant in the Netherlands. The investigated 63 μm-16 mm granulate fraction is the result of extensive prior treatment in the form of weathering, size reduction, dry and wet separation of organics, magnetic and para-magnetic extraction of metals, and washing. It has been sampled according to EN 932-1 [39]. Prior to further analysis, the material was dried at 105 °C to an oven-dry state where a constant mass was reached [40]. By doing so, the moisture content was determined (10.67%, ±1.01%). After drying, a correct particle size distribution (PSD) can be obtained in accordance with EN 933-1 and EN 933-2 [41,42] (with additional sieve sizes: 22.4 mm, 11.2 mm, 5.6 mm, 2.8 mm, 1.4 mm, 710 μm, 355 μm, 180 μm, and 91 μm), and the effect of agglomeration during the sieve analysis is minimised. In order to investigate the influence of both fine and coarse aggregate replacement, the 63 μm-16 mm oven-dried BA is sieved into respectively a <2 mm and an >2 mm fraction which correlates best with the size fractions of the virgin aggregates replaced. By sieving a second set of BA samples at 2 mm prior to oven drying, the intrinsic moisture content of both the fine and coarse BA fraction generated was determined, being 13.70% (±0.03%) and 7.79% (±0.19%), respectively. Based on this, an overall pre-saturation level of 10.0% was chosen for the 63 μm-16 mm BA, resulting in a 12.5% and 7.1% pre-saturation for respectively the fine and the coarse BA fraction in order to minimise the loss of mechanical resistance, workability and durability. The corresponding pre-saturation water was added to the oven-dried BA fractions and left to equilibrate in an air tight container for a minimum of 1 week while being turned over daily.
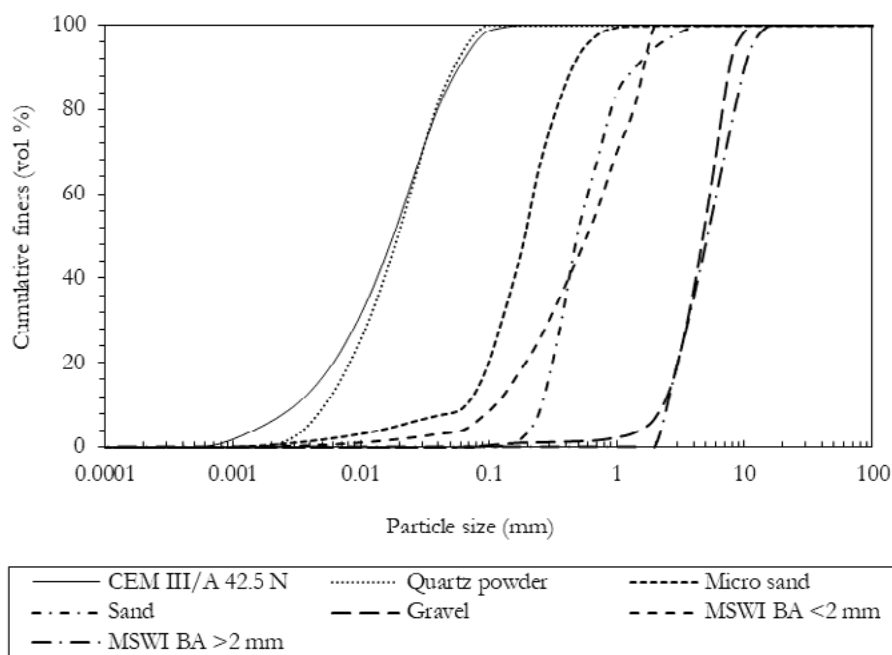

Figure 1 PSDs of all granular materials applied

With the addition of the quartz powder and micro sand to the standard mix design, a reference mix is created which allows an equal binder content, a continuous grading, and a compensation for differences

between the PSD of the virgin aggregates and the BA. Hence, including the pre-saturated coarse and fine BA fraction, a total of seven granular materials are used. Their PSDs are given in Figure 1.

2.2 Methods

2.2.1 Experiment design

This study employs a spherical central composite design approach [43] to acquire a broad understanding on the interaction and influence of the 3 independent variables (sand replacement, gravel replacement, and distribution modulus (q)) on ZSC mix design. Consequently, just 18 mix designs are needed out of a potential 125 (5^3) for 3 independent variables distributed over 5 levels in the ranges of 0-100% sand replacement, 0-100% gravel replacement, and a distribution modulus of 0.25-0.40 as suggested by Hüsken [34] (Figure 2), (Table 1), strongly reducing the necessary number of tests to quantify the above-mentioned correlations. To determine the reproducibility of the results, the design of centre point (15-18) is reproduced in quadruplicate.
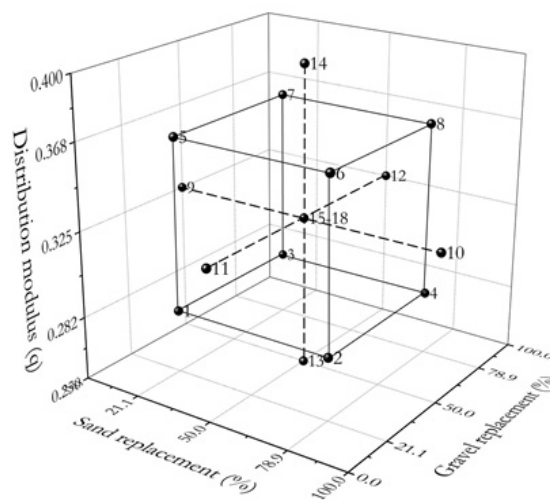

Figure 2 Geometric presentation of the inscribed central composite design for the 3 natural variables: (1) sand replacement (0-100%), (2) gravel replacement (0-100%), and (3) distribution modulus (q: 0.25-0.40).

Table 1 Mixture variable values

	Mix	Sand repl. (vol.-%)	Gravel repl. (vol.-%)	q
Factorial (cube points)	1	21.1	21.1	0.28
	2	78.9	21.1	0.28
	3	21.1	78.9	0.28
	4	78.9	78.9	0.28
	5	21.1	21.1	0.37
	6	78.9	21.1	0.37
	7	21.1	78.9	0.37
	8	78.9	78.9	0.37
Axial (star points)	9	0	50	0.33
	10	100	50	0.33
	11	50	0	0.33
	12	50	100	0.33
	13	50	50	0.25
	14	50	50	0.40
Centre (point)	15	50	50	0.33
	16	50	50	0.33
	17	50	50	0.33
	18	50	50	0.33

2.2.2 Mixture development methodology

The abovementioned 18 mix designs are defined by the values given in Table 1, the PSDs given in Figure 1, and the densities of the materials. Additional constraints are: BA <2 mm replaces both sand and micro sand, BA >2 mm replaces gravel, and the binder content is fixed (vol.-%). With the Brouwers and Radix'

mix design method [23], the ratios of all solid ingredients are calculated to compose the optimal particle gradation given by the modified A&A equation (Eq. 1). This is achieved by approaching unity for R^2 between composed mix PSD and the target PSD [44].

The algorithm in Brouwers and Radix' method [23] uses a volume-based expression of the particles based on the materials individual specific density (ρ^{spe}) as this is more suitable than using the retained mass of the sieve analysis when composing a mix with materials of different densities. However, in contrast to commonly used aggregates, BA contains a considerable porosity. ρ^{spe} solely takes into account the skeletal volume (solid material and closed pores) of the material, resulting in a larger effective volume at an equal ρ^{spe} for particles with an open porosity. Hence, ρ^{spe} is not applicable for porous materials. When the pores of the BA are assumed to be non-permeable to any of the present solid particles, the envelope volume (V_E) of particles, including porosity and voids, is most applicable.

Generally, the bulk density of both the original and the replacement material are used to exchange materials by volume. However, since the ZSC samples are compacted in the Intensive Compaction Tester (ICT, see 2.2.3), the compacted bulk density or ICT density (ρ^{ICT}) of the aggregates is determined under equal conditions. In this way, the PSD of the BA is adjusted to represent the PSD of replaced aggregates as closely as possible to achieve an equal void fraction (φ). Correlating the obtained ρ^{ICT} s together with the ρ^{spe} of the considered virgin aggregate fraction, an average ρ^E is approximated for the equivalent BA fraction.

2.2.3 Sample preparation and testing

The solids for 3 specimens were dry mixed with a planetary mixer (Hobart, model A-200-FM) in a 10 litre bowl at 107 rpm for 1 minute prior to an additional 3 minutes after the addition of water and plasticizer. Sequentially, the mixing bowl was covered to prevent dehydration prior to further processing.

A gyratory ICT (Invelop Oy, model ICT-100R) is used for the compaction of the ZSC samples (Figure 3c.). The working principle of the ICT (Figure 3a.) relies on the application of a constant pressure (F_{ict}) on a sample placed in a cylindrical mould. The mould rotates at a maximum of 120 rpm for up to 512 work cycles (n) at a gyratory angle (α_{ict}) whereby the sample height (H_{ict}) is continuously measured. As a result of the gyratory inclination a shear movement develops, aiding the compaction (Figure 3b.). The settings applied, recommended by Hüsken [34] for ZSC samples produced with the ICT, are given in Table 2.
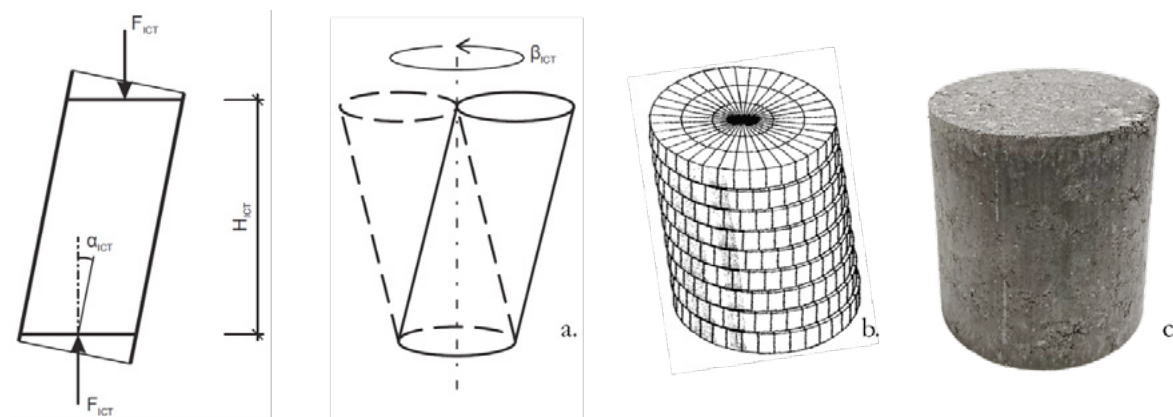

Figure 3 Intensive Compaction Tester: a. Working principle [34,45], b. Shear body of sample [46], c. ICT produced BA containing ZSC cylinder

Table 2 Gyratory Intensive Compaction Tester settings

Parameter	Symbol	Units	Available range	Selected
Compaction pressure	F_{ict}	kPa	<330	250
Gyratory angle	α_{ict}	mrad	<50	40
Cycle number	n	–	2–512	150
Velocity		rpm	30-120	60
Sample height	H_{ict}	mm	100-110	±105
Mould diameter	□	mm	100	100

The applied pressure can potentially affect the integrity of the particles due to crushing or grinding [47]. However, since the forces applied are (at least) comparable with ZSC production in practice, its occurrence is an acknowledged side effect of the process.

Multiple test samples of each mix were prepared with the ICT to determine the optimal moist state to achieve sufficient compaction (based on packing fraction), yet show no sign of excess water (the so-called "slurry point") [35]. The 15 resulting recipes were used to create 6 concrete samples per mix for further analysis.

3. Results and discussion

As can be seen in Figure 4, the achieved R^2 is close to unity for all resulting values; however, sand replacement (R_s), gravel replacement (R_g), and distribution modulus (q) have a different influence. The R^2 value for R_s is rather stable with a slight increase at 50% replacement. This can be explained by the fact that the ratio between sand and micro sand is not fixed, resulting in less constraints to optimise the mixture. R_g shows a near unity value for 0% followed by a distinctly lower value at 20%, gradually increasing over the higher replacement levels. With a maximum particle size (D_{max}) of ±16.0 mm, the BA gravel is coarser than the replaced limestone gravel with a D_{max} of ±11.2 mm. In turn, at low replacement levels, with an equivalently low content of the largest size fraction, the adjustment of D_{max} from 11.2 mm to 16.0 mm cannot be compensated, resulting in a decreased R^2. With an increase in q, R^2 decreases. This is caused by the reduced slope in the target curve for the smaller size fractions together with an increased slope for the larger size fractions, in turn resulting in a higher deviation.

The water content of the mixes is determined by the required workability and it depends on the 3 independent variables investigated (Figure 5). The total water content in the mix (W_t) is composed of the pre-saturation water in the BA (W_s) together with the water (including plasticiser) added during the mixing (W_m). For an increase in q, it can be seen that W_s remains rather stable, while W_t is reduced under the influence of W_m, which is related to a lower powder content (Figure 6). For an increase in q value, the binder content of the fines increases correspondingly, resulting in a lower W_t/B (Figure 7) which is in line with the findings of Hüsken [36].
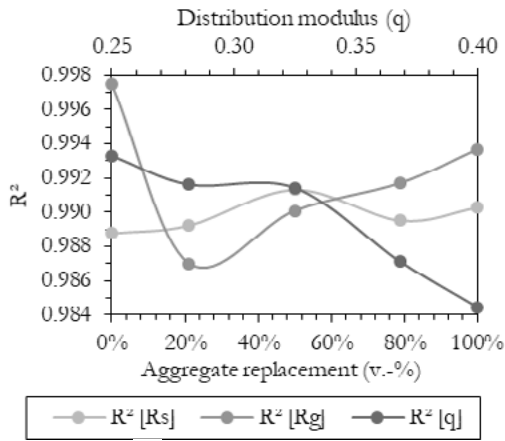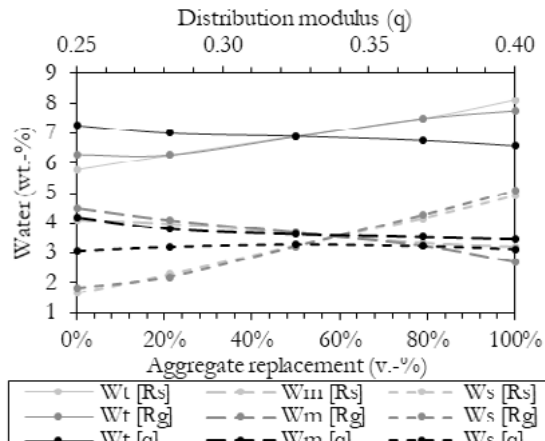
Figure 4 R_s, R_g, and q vs. R^2

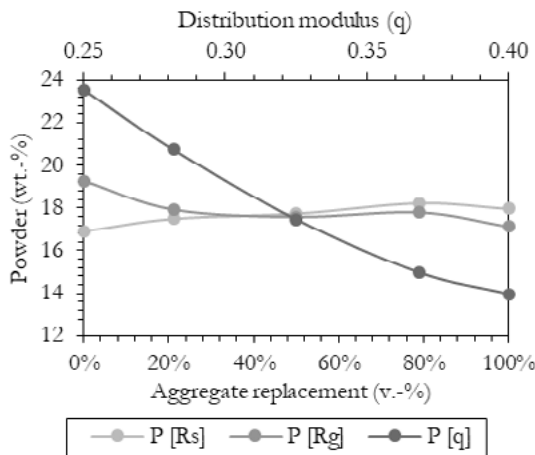Figure 5 R_s, R_g, and q vs. W_t, W_m, and W_s

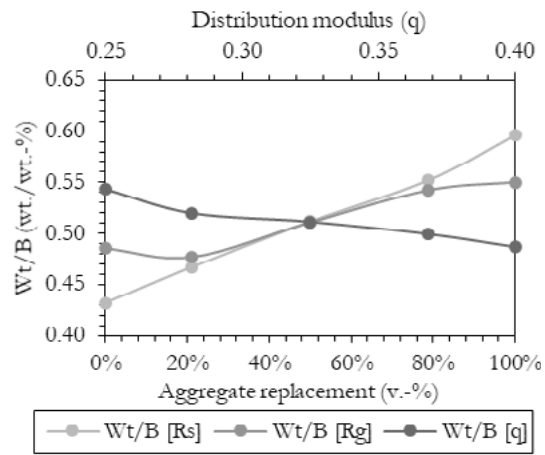Figure 6 R_s, R_g, and q vs. powder content

Figure 7 R_s, R_g, and q vs. W_t/B

As expected, Figure 6 shows a nearly constant powder content for R_s and R_g, and the small deviations can be linked to the deviations in material PSDs. In both W_t and W_s, an increase can be seen for R_s and R_g. W_m, however, decreases with an increase in replacement. This indicates that, during the mixing, per percent of fine and coarse BA replacement, sufficient water is released by the BA to reduce 0.23% and 0.39% of mixing water, respectively. Additionally, as the workability remains equal, it can be concluded that with the addition of both fine and coarse pre-saturated BA, the amount of water in the system is increased without a water increase in the paste (Figure 7). At a later stage, this additional water can contribute to hydration by supporting internal curing as suggested by Keulen et al. [38].

Based on the materials properties and the mix proportions, the theoretical maximum density of the mix can be calculated (Figure 8). For this purpose, ideal particle packing without any air content is assumed. For both R_s and R_g, as expected, the density decreases with increased replacement. The deviation from the trend at 0% replacement for R_g can be linked to the larger D_{max} of the BA >2 mm, inherently shifting the gradation curve and correlating properties.
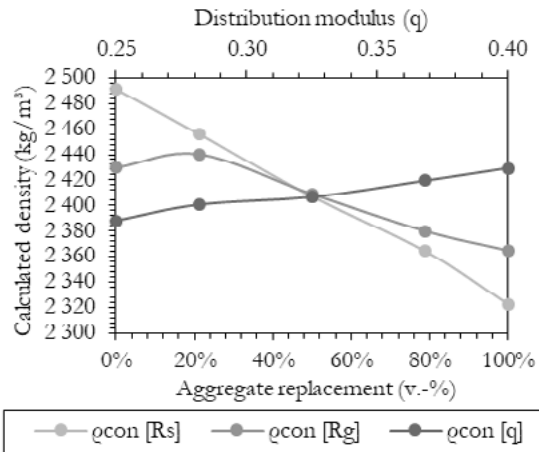
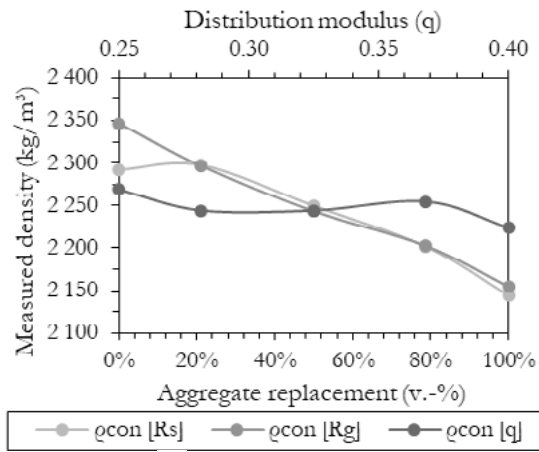Figure 8 R_s, R_g, and q vs. calculated density

Figure 9 R_s, R_g, and q vs. measured density

The measured density of the compacted concrete samples is displayed in Figure 9. The deviation between the calculated and the measured density is a measure for the air content, shown in Figure 10.
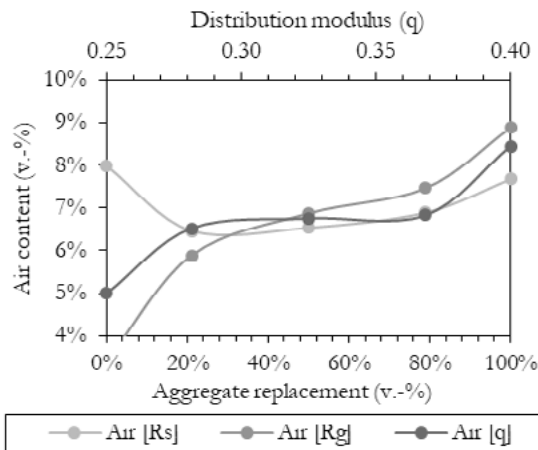

Figure 10 R_s, R_g, and q vs. calculated air content

Prior research and guidelines indicated an air content of 3-9% for ZSC [18,34,48,49]. Except for R_s at 0% and 100%, and q at 0.33, the values are in that range. In contrast to the presented ICT results, the compaction energy applied in practice is larger, in turn resulting in a lower air content closer to the 3-9% range.

4.   Conclusions

Based on the presented results and discussion it can be concluded that for ZSC containing BA:

- pre-saturation of fine and coarse BA reduces the required mixing water correspondingly with 0.23% and 0.39% per percent of aggregate replacement by volume;

- at constant workability (and therefore a constant amount of water in the paste), the addition of both fine and coarse pre-saturated BA increases the total amount of water in the system. This additional water can potentially contribute to hydration by facilitating internal curing at a later stage;

- for constant cement content and workability, increasing the q-value leads to a reduced powder content and therefore a higher binder concentration in the powders, in turn, resulting in a lower water-binder ratio;

- the use of the envelope volume (including porosity and voids) of particles is proposed since the skeletal volume is an unsuitable characteristic for particle packing optimisation with porous materials. With this, the overall density of the concrete is found to decrease with an increase for both fine and coarse aggregate replacement with BA;

- the expected range for air content is only exceeded under specific conditions of the ICT compacted samples and is expected to improve in full scale operation.

Future work will extend the study into the influence of the investigated variables (sand and gravel replacement by MSWI BA and distribution modulus) on the hardened properties (e.g. technical quality, environmental impact, etc.) of the ZSC mixes.

5.   Acknowledgment

6.   References

[1]   CEWEP, Bottom Ash Factsheet, (2015). www.cewep.eu (accessed February 15, 2018).

[2]   CEWEP, Country Report 2012-2013 The Netherlands, 2014. www.cewep.eu.

[3]   CUR-voorschriftencommissie VC89, CUR Aanbeveling 116:2017 - AEC-granulaat als toeslagmateriaal voor beton, (2017) 126.

[4]   P.K. Mehta, P.J.M. Monteiro, Concrete: Microstructure, Properties, and Materials, Fourth, McGraw-Hill Education, New York, Chicago, San Francisco, Athens, London, Madrid, Mexico City, Milan, New Delhi, Singapore, Sydney, Toronto, 2014.

[5]   T. Xu, T. Galama, J. Sathaye, Reducing carbon footprint in cement material making: Characterizing costs of conserved energy and reduced carbon emissions, Sustain. Cities Soc. 9 (2013) 54–61. doi:10.1016/j.scs.2013.03.002.

[6]   E. Tkaczewska, R. Mróz, G. Łój, Coal–biomass fly ashes for cement production of CEM II/A-V 42.5R, Constr. Build. Mater. 28 (2012) 633–639. doi:10.1016/j.conbuildmat.2011.10.022.

[7]   R. Cioffi, F. Colangelo, F. Montagnaro, L. Santoro, Manufacture of artificial aggregate using MSWI bottom ash., Waste Manag. 31 (2011) 281–8. doi:10.1016/j.wasman.2010.05.020.

[8]   X.-G. Li, Y. Lv, B.-G. Ma, Q.-B. Chen, X.-B. Yin, S.-W. Jian, Utilization of municipal solid waste incineration bottom ash in blended cement, J. Clean. Prod. 32 (2012) 96–100. doi:10.1016/j.jclepro.2012.03.038.

[9]   U. Müller, K. Rübner, The microstructure of concrete made with municipal waste incinerator bottom ash as an aggregate component, Cem. Concr. Res. 36 (2006) 1434–1443. doi:10.1016/j.

cemconres.2006.03.023.

[10]   B. Quenee, G. Li, J.M. Siwak, V. Basuyau, Waste Materials in Construction Wascon 2000 - Proceedings of the International Conference on the Science and Engineering of Recycling for Environmental Protection, Harrogate, England 31 May, 1–2 June 2000, Elsevier, 2000. doi:10.1016/S0713-2743(00)80054-9.

[11]   R. Siddique, Use of municipal solid waste ash in concrete, Resour. Conserv. Recycl. 55 (2010) 83–91. doi:10.1016/j.resconrec.2010.10.003.

[12]   S. Sorlini, A. Abbà, C. Collivignarelli, Recovery of MSWI and soil washing residues as concrete aggregates, Waste Manag. 31 (2011) 289–297. doi:10.1016/j.wasman.2010.04.019.

[13]   B. Juric, L. Hanzic, R. Ilić, N. Samec, Utilization of municipal solid waste bottom ash and recycled aggregate in concrete., Waste Manag. 26 (2006) 1436–42. doi:10.1016/j.wasman.2005.10.016.

[14]   R. del Valle-Zermeño, J. Formosa, J.M. Chimenos, M. Martínez, A.I. Fernández, Aggregate material formulated with MSWI bottom ash and APC fly ash for use as secondary building material., Waste Manag. 33 (2013) 621–7. doi:10.1016/j.wasman.2012.09.015.

[15]   A.A. Al-Rawas, A. Wahid Hago, R. Taha, K. Al-Kharousi, Use of incinerator ash as a replacement for cement and sand in cement mortars, Build. Environ. 40 (2005) 1261–1266. doi:10.1016/j.buildenv.2004.10.009.

[16]   J.M. Chimenos, M. Segarra, M.A. Fernández, F. Espiell, Characterization of the bottom ash in municipal solid waste incinerator, J. Hazard. Mater. 64 (1999) 211–222. doi:10.1016/S0304-3894(98)00246-5.

[17]   C.C. Wiles, Municipal solid waste combustion ash: State-of-the-knowledge, J. Hazard. Mater. 47 (1996) 325–344. doi:10.1016/0304-3894(95)00120-4.

[18]   Stutech, Aardvochtig beton, Stutech report No. 22, 's Hertogenbosch, The Netherlands (in Dutch), 2005.

[19]   G. Lee, T.-C. Ling, Y.-L. Wong, C.-S. Poon, Effects of crushed glass cullet sizes, casting methods and pozzolanic materials on ASR of concrete blocks, Constr. Build. Mater. 25 (2011) 2611–2618. doi:10.1016/j.conbuildmat.2010.12.008.

[20]   A.H.M. Andreasen, Ueber die Beziehung zwischen Kornabstufung und Zwischenraum in Produkten aus losen Körnern (mit einigen Experimenten), Kolloid-Zeitschrift. 50 (1930) 217–228. doi:10.1007/BF01422986.

[21]   W.B. Fuller, S.E. Thomson, The Laws of Proportioning Concrete, Trans. Am. Soc. Civ. Eng. (1907).

[22]   J.E. Funk, D.R. Dinger, Predictive Process Control of Crowded Particulate Suspensions: Applied to Ceramic Manufacturing, Kluwer Academic Press, Boston, MA, 1994. doi:10.1007/978-1-4615-3118-0.

[23]   H.J.H. Brouwers, H.J. Radix, Self-Compacting Concrete: Theoretical and experimental study, Cem. Concr. Res. 35 (2005) 2116–2136. doi:10.1016/j.cemconres.2005.06.002.

[24]   X. Wang, K. Wang, P. Taylor, G. Morcous, Assessing particle packing based self-consolidating concrete mix design method, Constr. Build. Mater. 70 (2014) 439–452. doi:10.1016/J.CONBUILDMAT.2014.08.002.

[25]   M. Hunger, An integral design concept for ecological self-compacting concrete, 2010. doi:http://dx.doi.org/10.6100/IR674188.

[26]   M. Hunger, H.J.H. Brouwers, Natural Stone Waste Powders Applied to SCC Mix Design, Restor. Build. Monum. 14 (2008) 131–140. doi:10.1515/rbm-2008-6206.

[27]   R. Yu, P. Spiesz, H.J.H. Brouwers, Mix design and properties assessment of Ultra-High Performance Fibre Reinforced Concrete (UHPFRC), Cem. Concr. Res. 56 (2014) 29–39. doi:10.1016/j. cemconres.2013.11.002.

[28]   R. Yu, P. Spiesz, H.J.H. Brouwers, Development of an eco-friendly Ultra-High Performance Concrete (UHPC) with efficient cement and mineral admixtures uses, Cem. Concr. Compos. 55 (2015) 383–394. doi:10.1016/J.CEMCONCOMP.2014.09.024.

[29]   R. Yu, P. Spiesz, H.J.H. Brouwers, Development of Ultra-High Performance Fibre Reinforced Concrete (UHPFRC): Towards an efficient utilization of binders and fibres, Constr. Build. Mater. 79 (2015) 273–282. doi:10.1016/J.CONBUILDMAT.2015.01.050.

[30]   Q.L. Yu, P. Spiesz, H.J.H. Brouwers, Ultra-lightweight concrete: Conceptual design and performance evaluation, Cem. Concr. Compos. 61 (2015) 18–28. doi:10.1016/J.CEMCONCOMP.2015.04.012.

[31]   R. Yu, D.V. van Onna, P. Spiesz, Q.L. Yu, H.J.H. Brouwers, Development of Ultra-Lightweight Fibre Reinforced Concrete applying expanded waste glass, J. Clean. Prod. 112 (2016) 690–701. doi:10.1016/J. JCLEPRO.2015.07.082.

[32]   D.M.A. Huiskes, A. Keulen, Q.L. Yu, H.J.H. Brouwers, Design and performance evaluation of ultra-lightweight geopolymer concrete, Mater. Des. 89 (2016) 516–526. doi:10.1016/J.MATDES.2015.09.167.

[33]   G. Hüsken, H.J.H. Brouwers, Development of eco earth-moist concrete, 5950 (2009) 97–105.

[34]   G. Hüsken, A multifunctional design approach for sustainable concrete, 2010. doi:10.6100/ IR693348.

[35]   G. Hüsken, H.J.H. Brouwers, On the early-age behavior of zero-slump concrete, Cem. Concr. Res. 42 (2012) 501–510. doi:10.1016/J.CEMCONRES.2011.11.007.

[36]   G. Hüsken, H.J.H. Brouwers, A new mix design concept for earth-moist concrete: A theoretical and experimental study, Cem. Concr. Res. 38 (2008) 1246–1259. doi:10.1016/J.CEMCONRES.2008.04.002.

[37]   B. Quenee, G. Li, J.M. Siwak, V. Basuyau, The use of MSWI (Municipal solid waste incineration) bottom ash as aggregates in hydraulic concrete, Waste Manag. Ser. 1 (2000) 422–437. doi:10.1016/S0713-2743(00)80054-9.

[38]   A. Keulen, A. van Zomeren, P. Harpe, W. Aarnink, H.A.E. Simons, H.J.H. Brouwers, High performance of treated and washed MSWI bottom ash granulates as natural aggregate replacement within earth-moist concrete., Waste Manag. (2016). doi:10.1016/j.wasman.2016.01.010.

[39]   EN 932-1, Tests for general properties of aggregates - Part 1: Methods for sampling, 1996.

[40]   S., Mindness, Young J F, Darwin D., Concrete, 2nd ed., Prentice Hall, Pearson Education, Inc. Upper Saddle River, NJ 07458, 2003.

[41]   EN 933-1, Tests for geometrical properties of aggregates - Part 1: Determination of particle size distribution - Sieving method, CEN, 2012.

[42]   EN 933-2, Tests for geometrical properties of aggregates - Part 2: Determination of particle size distribution - Test sieves, nominal sizes of apertures, CEN, 1995.

ICSBM 2019
ID 151

ICSBM 2019
ID xxx

[43]   D.C. Montgomery, Design and Analysis of Experiments, 2012. doi:10.1198/tech.2006.s372.

[44]   R. Yu, Development of sustainable protective ultra-high performance fibre reinforced concrete (UHPFRC), 2014.

[45]   A. Käppi, E. Nordenswan, Workability of No-Slump Concrete, Concr. Int. 29 (2007) 37–41.

[46]   Invelop oy, Operating Instructions Intensive Compaction Tester model ICT-100R (c0251/C), 2005.

[47]   F. V. Mueller, O.H. Wallevik, Linking solid particle packing of Eco-SCC to material performance, Cem. Concr. Compos. 54 (2014) 117–125. doi:10.1016/J.CEMCONCOMP.2014.04.001.

[48]   D.A. Abrams, Proportioning Concrete Mixtures, in: Proc. 18th Annu. Conv. Am. Concr. Inst., Detroit, Michigan, U.S., 1922: pp. 174–181.

[49]   R. Bornemann, Untersuchung zur modellierung des frisch- und festbetonverhaltens erdfeuchter betone., Struct. Mater. Eng. Ser. 4 (2005).

Influence of the Water- and Foaming Agent Dosage on Hardened Autoclaved Aerated Concrete

C. Straub[a1,b], M.V.A. Florea[b], G. Quercia[a,b,c1], H.J.H. Brouwers[b]

[a] Materials innovation institute (M2i)

[b] Eindhoven University of Technology

[c] TAKTL LLC

Abstract- The most important parameters for the production of Autoclaved Aerated Concrete (AAC) are water-to-powder ratio and foaming agent (Al powder) amount, yet their influence on the green- and final product properties are not sufficiently studied. Here, this influence is thoroughly investigated and quantified, and formulas for the interaction of these parameters are proposed. Moreover, various relations between final AAC properties (thermal conductivity, strength, etc.) and initial mix parameters are derived and explained. The results of this research demonstrate how an optimization of the initial ACC parameters can significantly improve the material behavior.

Keywords: autoclaved aerated concrete, AAC, green body, spread flow, compressive strength, density

1.   Introduction

Autoclaved aerated concrete (AAC) has been known for a long time to be an insulating, lightweight and fire resistant building material [1]. Its advantages compared to other building materials are the possibility of creating monolithic wall structures and its eco-friendliness [2,3]. To further increase its eco-friendliness, new raw materials can be applied. It is a common approach to use alternative materials to extend or improve existing materials. In the case of AAC this idea is implemented already in the original patents [4–6]; for example, the use of fly ash instead of ground quartz is widely applied. There are basically two requirements for the application of new raw materials: a well-developed and optimized standard recipe and the complete characterization of this recipe (including technological parameters like mixing, slurry and green body behaviour, and detailed knowledge about the produced AAC itself).

In literature [1,2,7–22] different ranges for AAC recipes are given. However, details of the raw materials are not provided in most cases, or the formulated recipe is incomplete or not published due to confidentiality or intellectual properties protection issues [2,8,10,17,18,23–31].

For the process and product development of eco- and high performance autoclaved aerated concrete, accurate and complete information on raw materials and their related product performance are vital. The characterization of the produced AAC with substituted raw materials is limited to the final properties [8,10–13,17–22,24–26,32,33], and in these studies the material behaviour before hydrothermal hardening is not investigated. Also in industry, systematic studies are either not conducted, or the available know-how and experience are not published.

Two different AAC products can be compared only if their pore structures, respectively green bodies, are similar. For this hypothesis an adaptation of the recipe, especially of the water and foaming agent

amount, is necessary in case of the application of a replacement material. However, the data providing these important information is not properly documented, in some cases not even the water amount of the mix is provided [20,22,24,25,32], or the phrase "workable" mixtures or similar is used instead [16,19,26,32].

Another novel approach employed in this study is the scale of the moulds. In standards like [34] it is recommended to cut the specimens for the tests from the middle of the produced block, due to the influence of the surface on the texture and hence on the properties. A minimum distance from the mould wall to provide a undisturbed pore structure is 5 cm. Commonly the mould size for AAC castings in research papers [7,8,20,26,28,33,10,11,13,14,16–19] (e.g. 40x40x160 mm³) does not provide sample sizes unaffected by the wall effect.

Correlations between different material parameters were formulated [2,9,10,16,19,21,35], but to the best of the authors' knowledge this is the first time that green parameters are incorporated. Similar research was already conducted on aerated (or surfactant based foamed) concrete [36–38], but aerated concrete and AAC are not comparable materials in the phase of the green body. Similarities occur as well with Al-foamed alkali activated materials [39], whereas the binding process and the intrinsic pH-value are significantly different.

Subsequently, the reference standard recipe needs to be fully characterized. In [1–3,15,40] it is described that a higher water content in the mix leads to a more liquid consistency, higher porosity and lower strength, but an expression of this relation is never given. A model for mix designs is provided on a linear basis in [1], as a guideline for the aimed properties. According to this model, at least 9 different castings are necessary for a rough overview in a small range. The current study investigates these interactions and proposes equations for a more detailed description. The aim is to provide a tool to minimize the number of trial castings. In order to mitigate all these issues, in this study a well-tested recipe developed in an industrial laboratory (provided by HESS AAC systems B.V.) was adopted as a reference standard recipe (Table 1 and Table 2).

In this study, the influence of initial and processing parameters on the final product properties are investigated. Apart from the common hardened properties like raw density and compressive strength, the main focus is on the parameters before autoclaving. This data is used to reveal correlations, which serves for the design of future recipes with other materials.

Another general approach followed for the whole investigation is the hypothesis that an adequate green body can lead to an optimized AAC, while an insufficient green body is unlikely to provide a suitable AAC.

2.   Materials and Methods

2.1   Materials

All materials used for preparing the samples are technical grade and, if not indicated otherwise, match the recommended requirements for AAC production [1,2,15,41] or originated from AAC material suppliers (Table 1). All experiments follow a sand-based reference recipe (provided by HESS AAC Systems B.V., Table 2). Normally, in case of a design of an AAC recipe, the targeted (raw) density is mentioned. In this case the resulting density and its changes was one of the aims of the study. The target raw density range can be roughly given by 500±100 kg/m³.

Table 1: Chemical and physical characteristics of the raw materials.

	Parameter	Quartz	Anhydrite	Cement	Portlandite	Lime
Chemical Analysis (XRF) [mass%]	$Na_2O + K_2O$	0.05	0.37	1.08	0.11	0.27
	MgO	-	1.20	0.96	0.33	0.58
	Al_2O_3	0.85	0.65	4.88	0.13	0.40
	SiO_2	98.6	1.55	15.7	0.30	0.67
	SO_3	-	53.7	3.98	0.05	0.03
	CaO	0.01	38.9	66.5	70.1	95.9
	Fe_2O_3	0.03	0.19	2.48	0.17	0.26
	LOI DIN EN ISO 3262-1	0.26	3.08 (650 °C)	2.38	27.4	1.81
	Phase content (XRD)	Quartz (low)	Anhydrite, gypsum / dolomite	Quartz, C_3S, C_2S, $C_4(AF)$, C_3A	Portlandite, calcite*	Lime, portlandite**
	Specific density [g/cm³]	2.57	2.95	3.12	2.30	3.24
	Supplier	Quarzwerke GmbH	Knauf Gips KG	Cemex	Fels-Werke GmbH	Fels-Werke GmbH
	EN 459-1				CL 90-S	CL 90-Q (R5, P1)
	Product name	SIKRON SF 300	Anhydritstaub	CEM I 42.5 R	WKH 2/4 CL90	11/6

* Calcite content ≈ 15 % (det. by LOI and density) / ** Portlandite content ≈ 10 % (det. by LOI and density), Slaking lime test (EN 459-2): $t_{60°C}$ = 10 min / T_{max} = 75.8 °C

To avoid confusion the naming of the materials was oriented, as far as possible, on their mineral names (IMA List of Minerals). For example the material that is called lime can as well be labelled as quicklime or burnt lime and regarding EN 459-1, the lime could be called CL90 Q, CAS-Number 1305-78-8. Similar synonyms are available for portlandite (hydrated lime, slaked lime, CL90 S, CAS: 1305-62-0). The aluminium powder was obtained from Benda-Lutz Skawina Sp. z o. o. / SunChemical with the specification/trade name Benda-Lutz® 5 6380.

Table 2 : AAC mix composition

Material	Proportion ω [mass%]
Quartz	66.7
Lime	8.3
Cement	20.0
Portlandite	2.5
Anhydrite	2.5
Aluminium	varied
Water	varied

2.2 Methodology

2.2.1 Characterization of raw materials

The analysis of the raw materials was performed as follows: the chemical analysis was performed using an X-Ray Fluorescence device (XRF, PANalytical Epsilon3) with pressed powder tablets; the Loss On Ignition (LOI) was performed in a muffle furnace according to EN ISO 3262-1 at 1000 °C if not indicated otherwise. The phase composition was measured using an X-Ray Diffractometer (XRD, PANalytical X'Pert PRO MPD with CuK$_α$ radiation and an X'Celerator RTMS detector with back loading preparation). The Particle Size Distribution (PSD) was determined using a laser granulometer (Malvern Mastersizer 2000). The specific density of the powders was obtained by a helium pycnometer (Micromeritics AccuPyc II 1340).

2.2.2 Recipe design and mixing

The experiments were performed as follows: after preheating the specific water amount (dependent on the

water-to-powder-ratio, W/P ratio) to 45 °C, it was put in the mixer and stirred at slow speed. Separately, the aluminium powder was manually pre-dispersed with a small part (approximately 100-200 ml) of this water. Quartz and portlandite were successively added and mixed for minimum 60 seconds, in order to ensure homogeneity. The addition of lime, cement and anhydrite was performed within 30 s and then mixing continued for 90 s. Within the last 30 s of the mixing the aluminium powder suspension was added. Within 5 minutes from adding the lime and cement both casting and flow experiments were finished.

The investigated parameters (the influence of the mixing device, the water-to-powder ratio (W/P) and the amount of foaming agent) were varied as follows:

The rotation speed of the mixers were changed while adding the materials. It was tried to keep a constant vortex instead specific rpms.

Water-to-powder ratio: The mass ratio of water to total solids (W/P) was changed between 0.525 and 0.725 in steps of 0.1. Additionally, two extreme mixes with a W/P = 0.425 and 0.825 were made. While the mass of the solids remains unchanged, the water amount was varied. This was done due to the fact that the volume of a mix is more dependent on the foaming agent than on the volume of water or solids.

Foaming agent: The aluminium amount was varied between 0.067 % (mass percent in relation to total solids, ω_{Al}) and 0.1 % in 3 steps.

2.2.4 Hydrothermal treatment

The samples were demoulded the following day and placed directly in the autoclave (autoclave: Maschinenbau Scholz GmbH & Co. KG / steam generator: WIMA ED36). The autoclave was programed as follows: 20 min vacuum (-0.8 bar), heating up to 187 °C / 11 bar within 1.5 hours, holding a plateau of 187 °C / 11 bar for 5 hours, cooling down to 20 °C / 0 bar within 1.5 hours. This test program was chosen to be similar to industrial autoclave cycles [45]. After this treatment, at least 5 cm of each side of the sample were removed by band saw to obtain an undisturbed pore structure (no "wall-effect").

2.2.5 Hardened state analysis

After autoclaving the material was cut for further analysis into 4 cubes (100*100*100 mm³) for raw density (or apparent density) and compressive strength measurements. The polished cubes were oven dried (60°C, forced ventilation) until constant weight. After cooling down to 20 °C the raw density ϱ_{AAC} and the compressive strength σ (FORM+TEST Seidner+Co. GmbH, MEGA 110-200 D-S) were measured. The approach is comparable to the standards [34] and [46]. The thermal conductivity λ was measured using an ISOMET model 2104 heat transfer analyser (Applied Precision), by measuring multiple times on a polished surface.

3.   Results & discussion

3.1   Characterization of raw materials

All materials fulfil the industrial guideline d_{90} < 90 µm (Figure 1). The measured chemical composition, phase content and the suppliers of the materials are listed in Table 1. Normal tap water was used for all the mixes.
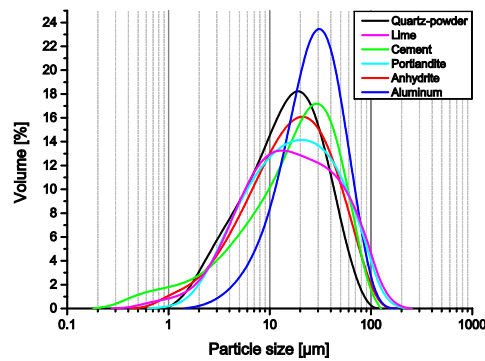
Figure 1: Particle size distribution of the raw materials used.

3.3   Hardened properties

During the autoclave hardening the material will undergo a complete change of its phases and microstructure while keeping the same outer dimensions and macroscopic visible structure.

For the characterization of the produced AAC the raw density ϱ_{AAC}, the compressive strength σ and the thermal conductivity λ were measured.

While the sample with a water-to-powder ratio of 0.425 had already failed during green body preparation, the sample with 0.825 failed during autoclaving. It was necessary to repeat the experiment several times until enough suitable material was accumulated for further analysis. Therefore both mixes are not suitable from the production point of view.

After autoclaving the material showed the following behaviour: the raw density ϱ_{AAC} (Figure 2) of the material is dependent on the water amount as well as on the amount of foaming agent. The range of the samples was within 390 and 570 kg/m³ (the maximum obtained value was 730 kg/m³, but the pore structure was not the typical bubble distribution as it is known for AAC, so this value was not taken into account). The raw density could be expressed as a function of the W/P ratio and the foaming agent amount ω_{Al}, for example:

$$\varrho_{AAC} = G+f^{(W/P)*k} \tag{1}$$

where G represents the asymptote, being a function of the foaming agent amount (the specific formula is similar to this one). The fitting parameters are f (constant with mix design) and k, while the sum G + k remains constant for each mix design (Figure 2).

For the plot in Figure 2 the initial input parameters as production parameters were chosen. From a scientific point of view it might be more suitable to use instead of the W/P the spread flow as expression of the viscosity. However, due to the higher error range of the spread flow a connection of spread flow and raw density are more difficult to obtain.
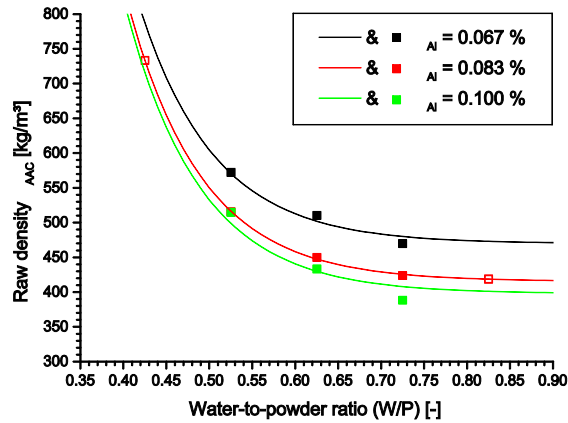
Figure 2: Comparison between the initial water-to-powder ratio (W/P), the foaming agent amount ω_{Al} and the raw density ϱ_{AAC} of the final product. Two-dimensional visualization of the data, with fit according to Eq. (3) (lines).

This result seems to contradict the suggested relation from [1], that stated a linear correlation between the spread flow and the raw density. Due to the short range of investigated densities in [1], an approximation to linear behaviour is valid in practical approaches, especially considering the statistical variation of the values. However, for larger ranges the behaviour is better described in Figure 2.
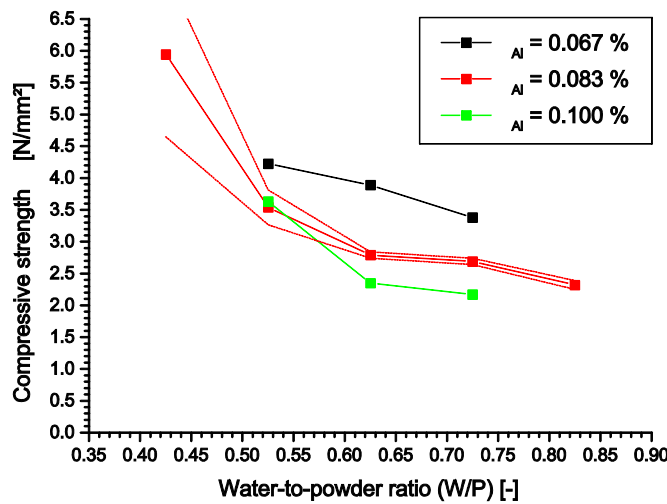

Figure 3: Comparison of the compressive strength σ as function of the water-to-powder ratio (W/P) and the foaming agent amount ω_{Al}. Two-dimensional visualization of the compressive strength. The dotted lines represent the standard deviation of the values for a foaming agent content of 0.083 %.

Together with the raw density, the most common value to describe an AAC is the compressive strength σ (Figure 3). The range of the obtained values is 2.3 - 4.2 N/mm². Due to the fact that the strength is dependent on the raw density, two normalization procedures are known in the industry, the A-Value [2]:

$$\text{A-Value} = \sigma/(\text{const.} * \varrho_{AAC}^2) \tag{2}$$

where σ is the compressive strength [N/mm²], *const.* is 0.016 N/g² and ϱ is the raw density [g/cm³]. This is the original formulation as published in [2], while a variation of it is given in [16]. The unit of the constant is theoretically [(N*cm⁶)/(g²*mm²)], if the A-Value should be dimensionless.

and the compensated compressive strength (CCS) [45]:

$$\text{CCS} = (\sigma/\varrho_{AAC}) * \varrho_{ref} \tag{3}$$

where ϱ_{ref} [kg/m³] is the chosen reference raw density for which the value will be normalized.

While the A-Value approach (Eq. (2)) shows a constant behaviour (within the reported error range, according to literature this is 30 units, [2] respectively 50 units, [45]), the CCS-approach (Eq. (3)) shows a stronger dependency on the W/P ratio and especially the foaming agent amount.

4.   Conclusions

The results presented above are part of a larger study which also takes into account all green properties of the AAC mixes and their relationship with the hardened properties. Additional properties such as thermal conductivity are also studied, together with various mixing parameters and slump flow measurement devices.

The following conclusions can be drawn from the findings presented in this study:

-        It was proven that the investigated parameters, water-to-powder ratio and foaming agent amount, have a critical influence on the final AAC product.

-        In the investigated parameters of the hardened AAC, the water-to-powder ratio is inversely correlated with the foaming agent amount and vice versa. This behaviour could also be observed for the raw density, the compressive strength and the thermal conductivity. It needs to be pointed out that the substitution level of the two ingredients (water and foaming agent) only applies in a quite narrow range within a given mix.

-        If the water-to-powder ratio is too low (in this case lower than 0.525), the flowability of the slurry is affected and a uniform pore structure cannot be obtained. If the water-to-powder ratio is too high (in this case higher than 0.725), a suitable green body can be created, but then material failure occurs during hydrothermal hardening.

-        The compressive strength of the AAC depends on its raw density, while the A-Value provides a more suitable independent value for the comparison of different mixes.

5.   Acknowledgements

6.   References

[1]   S. Reinsdorf, Leichtbeton Band II Porenbetone, VEB Verlag für Bauwesen, Berlin, Germany, 1963.

[2]   S.G. Zürn, Einfluss der Sandminerale auf die Bildung von Calciumsilikathydraten (CSH-Phasen), das Gefüge und die mechanischen Eigenschaften von Porenbetonprodukten Systematische Untersuchungen an synthetischen Sandmischungen mit Übertragung auf Produktionssande, Logos Verlag, Berlin, Germany, 1997.

[3]   S. Röbert, U.a., Silikatbeton Herstellung, Bewertung, Anwendung 2. stark bearbeitete Auflage,

VEB Verlag für Bauwesen, Berlin, Germany, 1987.

[4]   J.A. Eriksson, Verfahren zur Herstellung eines porösen Baustoffes aus Portlandzement, DE000000404677A, 1923.

[5]   J.A. Eriksson, Verfahren zur Herstellung von porösen Baustücken aus Beton, DE000000447194A, 1924.

[6]   J.A. Eriksson, Verfahren zur Herstellung poröser Kunststeine, DE000000454744A, 1924.

[7]   D. Lesueur, F. Mücke, H. Oeinck, U. Peter, C. Pust, F. Verhelst, Impact of quicklime reactivity and origin on autoclaved aerated concrete production, in: 5th Int. Conf. Autoclaved Aerated Concr., Bydgoszcz, Poland, 2011: pp. 101–110.

[8]   F. Matsushita, Y. Aono, S. Shibata, Particles size distribution of quartz sand for AAC production, in: 5th Int. Conf. Autoclaved Aerated Concr., Bydgoszcz, Poland, 2011: pp. 155–162.

[9]   I. Kadashevich, H.J. Schneider, D. Stoyan, Statistical modeling of the geometrical structure of the system of artificial air pores in autoclaved aerated concrete, Cem. Concr. Res. 35 (2005) 1495–1502. doi:10.1016/j.cemconres.2004.10.010.

[10]   A. Alhozaimy, G. Fares, A. Al-Negheimish, M.S. Jaafar, The autoclaved concrete industry: An easy-to-follow method for optimization and testing, Constr. Build. Mater. 49 (2013) 184–193. doi:10.1016/j.conbuildmat.2013.08.024.

[11]   A. Laukaitis, J. Kerien, M. Kligys, D. Mikulskis, L. Lekunait, Influence of mechanically treated carbon fibre additives on structure formation and properties of autoclaved aerated concrete, Constr. Build. Mater. 26 (2012) 362–371. doi:10.1016/j.conbuildmat.2011.06.035.

[12]   T. Mitsuda, K. Sasaki, H. Ishida, Phase Evolution during Autoclaving Process, J. Am. Ceram. Soc. 75 (1992) 1858–1863.

[13]   Y. Song, B. Li, E.-H. Yang, Y. Liu, T. Ding, Feasibility study on utilization of municipal solid waste incineration bottom ash as aerating agent for the production of autoclaved aerated concrete, Cem. Concr. Compos. 56 (2015) 51–58. doi:10.1016/j.cemconcomp.2014.11.006.

[14]   X.Y. Cong, S. Lu, Y. Yao, Z. Wang, Fabrication and characterization of self-ignition coal gangue autoclaved aerated concrete, Mater. Des. 97 (2016) 155–162. doi:10.1016/j.matdes.2016.02.068.

[15]   J.A.H. Oates, Lime and Limestone Chemistry and Technology, Production and Uses, Wiley-VCH Verlag GmbH, Weinheim, Germany, 1998.

[16]   A. Hauser, U. Eggenberger, T. Mumenthaler, Fly ash from cellulose industry as secondary raw material in autoclaved aerated concrete, Cem. Concr. Res. 29 (1999) 297–302. doi:10.1016/S0008-8846(98)00207-5.

[17]   W. Wongkeo, A. Chaipanich, Compressive strength, microstructure and thermal analysis of autoclaved and air cured structural lightweight concrete made with coal bottom ash and silica fume, Mater. Sci. Eng. A. 527 (2010) 3676–3684. doi:10.1016/j.msea.2010.01.089.

[18]   W. Wongkeo, P. Thongsanitgarn, K. Pimraksa, A. Chaipanich, Compressive strength, flexural strength and thermal conductivity of autoclaved concrete block made using bottom ash as cement replacement materials, Mater. Des. 35 (2012) 434–439. doi:10.1016/j.matdes.2011.08.046.

[19]   H. Kurama, I.B. Topçu, C. Karakurt, Properties of the autoclaved aerated concrete produced from coal bottom ash, J. Mater. Process. Technol. 209 (2009) 767–773. doi:10.1016/j.jmatprotec.2008.02.044.

[20]   X. Huang, W. Ni, W. Cui, Z. Wang, L. Zhu, Preparation of autoclaved aerated concrete using copper tailings and blast furnace slag, Constr. Build. Mater. 27 (2012) 1–5. doi:10.1016/j.conbuildmat.2011.08.034.

[21]   C. Karakurt, H. Kurama, I.B. Topçu, Utilization of natural zeolite in aerated concrete production, Cem. Concr. Compos. 32 (2010) 1–8. doi:10.1016/j.cemconcomp.2009.10.002.

[22]   T. Dietz, P. Daschner, Saving of energy and resources in the latest generation of AAC production plants, in: 5th Int. Conf. Autoclaved Aerated Concr., Bydgoszcz, Poland, 2011: pp. 57–62.

[23]   K. Matsui, J. Kikuma, M. Tsunashima, T. Ishikawa, S.Y. Matsuno, A. Ogawa, M. Sato, In situ time-resolved X-ray diffraction of tobermorite formation in autoclaved aerated concrete: Influence of silica source reactivity and Al addition, Cem. Concr. Res. 41 (2011) 510–519. doi:10.1016/j.cemconres.2011.01.022.

[24]   W. Pichór, Properties of autoclaved aerated concretes with cenospheres from coal ash, in: 5th Int. Conf. Autoclaved Aerated Concr., Bydgoszcz, Poland, 2011: pp. 163–170.

[25]   N. Narayanan, K. Ramamurthy, Microstructural investigations on aerated concrete, Cem. Concr. Res. 30 (2000) 457–464. doi:10.1016/S0008-8846(00)00199-X.

[26]   H. Connan, D. Klimesch, A. Ray, P. Thomas, Thermal characterisation of autoclaved cement made with alumina-silica rich industrial waste, J. Therm. Anal. Calorim. 84 (2006) 521–525. doi:10.1007/s10973-005-6674-z.

[27]   K. Matsui, A. Ogawa, J. Kikuma, M. Tsunashima, T. Ishikawa, S. Matsuno, Influence of addition of Al compound and gypsum on tobermorite formation in autoclaved aerated concrete studied by in situ X-ray diffraction, in: 5th Int. Conf. Autoclaved Aerated Concr., Bydgoszcz, Poland, 2011: pp. 147–154.

[28]   J. Kikuma, M. Tsunashima, T. Ishikawa, S. Matsuno, A. Ogawa, K. Matsui, Use of fine particle quartz sand for AAC production : model study by in situ x-ray diffraction and NMR, in: 5th Int. Conf. Autoclaved Aerated Concr., Bydgoszcz, Poland, 2011: pp. 71–77.

[29]   J. Kikuma, M. Tsunashima, T. Ishikawa, S. Matsuno, a. Ogawa, K. Matsui, Development of an in situ X-ray diffraction system for hydrothermal reactions and its application to autoclaved aerated concrete formation, Powder Diffr. 26 (2011) 126–128. doi:10.1154/1.3583565.

[30]   J. Kikuma, M. Tsunashima, T. Ishikawa, S. Matsuno, A. Ogawa, K. Matsui, M. Sato, Effects of quartz particle size and water-to-solid ratio on hydrothermal synthesis of tobermorite studied by in-situ time-resolved X-ray diffraction, J. Solid State Chem. 184 (2011) 2066–2074. doi:10.1016/j.jssc.2011.05.061.

[31]   J. Kikuma, M. Tsunashima, T. Ishikawa, S.Y. Matsuno, A. Ogawa, K. Matsui, M. Sato, In situ time-resolved X-ray diffraction of tobermorite formation process under autoclave condition, J. Am. Ceram. Soc. 93 (2010) 2667–2674. doi:10.1111/j.1551-2916.2010.03815.x.

[32]   K. Laskawiec, J. Malolepszy, G. Zapotoczna-Sytek, Influence of the amount and the kind fly ashes produced of coal combustion in fluidized bed boilers on properties autoclaved aerated concrete ., in: H.-M. Ludwig, H.-B. Fischer, K.A. Bode, C. Beuthan, S. Bähring (Eds.), Proc. 18th Int. Conf. Build. Mater. (Ibausil), Weimar, Weimar, Germany, 2012.

[33]   N.Y. Mostafa, Influence of air-cooled slag on physicochemical properties of autoclaved aerated concrete, Cem. Concr. Res. 35 (2005) 1349–1357. doi:10.1016/j.cemconres.2004.10.011.

[34]   DIN EN 771-4, Berlin, Germany, 2003.

[35]   G. Rausch, J. Baumeister, D. Lehmhus, H. Stanzick, K. Stöbener, M. Wichmann, N. Zimmer, V. Zöllmer, FOAMINAL® Properties Overview and Design Guideline, Bremen, Germany, n.d.

[36]   M. Schauerte, R. Trettin, Neue Schaumbetone mit gesteigerten mechanischen und physikalischen Eigenschaften, in: H.-M. Ludwig, H.-B. Fischer, K.A. Bode, C. Beuthan, S. Bähring (Eds.), Proc. 18th Int. Conf. Build. Mater. (Ibausil), Weimar, Weimar, Germany, 2012.

[37]   J. Pinilla Melo, A. Sepulcre Aguilar, F. Hernández Olivares, Rheological properties of aerated cement pastes with fly ash , metakaolin and sepiolite additions, Constr. Build. Mater. 65 (2014) 566–573. doi:10.1016/j.conbuildmat.2014.05.034.

[38]   J. Jiang, Z. Lu, Y. Niu, J. Li, Y. Zhang, Study on the preparation and properties of high-porosity foamed concretes based on ordinary Portland cement, Mater. Des. 92 (2016) 949–959. doi:10.1016/j.matdes.2015.12.068.

[39]   A. Hajimohammadi, T. Ngo, P. Mendis, J. Sanjayan, Regulating the chemical foaming reaction to control the porosity of geopolymer foams, Mater. Des. 120 (2017) 255–265. doi:10.1016/j.matdes.2017.02.026.

[40]   H. Gundlach, Dampfgehärtete Baustoffe, Bauverlag GmbH, Wiesbaden, Germany / Berlin, Germany, 1973.

[41]   B. Walk-Lauffer, Untersuchung des Einflusses von Sulfaten auf das System CaO-SiO2-Al2O3-K2O-H2O mittels Wärmeflusskalorimetrie und in-situ Neutronenbeugung unter hydrothermalen Bedingungen, Universität Siegen, 2002.

[42]   DIN EN 1015-3, Berlin, Germany, 2004.

[43]   I. Mehdipour, A. Kumar, K.H. Khayat, Rheology, hydration, and strength evolution of interground limestone cement containing PCE dispersant and high volume supplementary cementitious materials, Mater. Des. 127 (2017) 54–66. doi:10.1016/j.matdes.2017.04.061.

[44]   DIN EN 196-3, Berlin, Germany, 1995.

[45]   L. Heinz, Private communication, (2015).

Effect of carbonation on chloride binding behaviors and hydration product formation of metakaolin-ground waste coral blended marine mortars

Y. Wang [1,2], Z. Shui [1], X. Gao [3], Y. Huang [2], R. Yu [1], Q. Song [1,2]

[1] State Key Laboratory of Silicate Materials for Architectures, Wuhan University of Technology, Wuhan 430070, China

[2] School of Materials Science and Engineering, Wuhan University of Technology, Wuhan 430070, China

[3] School of Civil Engineering and Architecture, Wuhan University of Technology, Wuhan 430070, China.

Abstract

The construction of facilities on islands far from mainland is challenged by the lack of raw materials for concrete production. Nowadays, the locally available waste coral is used as concrete aggregate to relieve its dependency of raw materials from mainland, and acceptable hardened behaviors of coral aggregate concrete are achieved. However, waste coral recycled as aggregate can result in significant damage of workability because of porous structure of coral. To ease this adverse effect, the present work recycles waste coral as filler and coupled with metakaolin to prepare marine mortar. The waste coral filler (GWC) is ground from coral waste detritus, during which the pores in coral particles is damaged. Since GWC-metakaolin (MK) based mortars are exclusively used on islands, it can suffer from a heavy chloride attack. In this way, the chloride binding and diffusion behaviors of GWC-MK based mortar should be concerned more. Besides, the blended cementitious materials are normally easier to be carbonated. The resulting calcium hydroxide content reduction and calcium carbonate formation may have certain effects on the hydration production formation and chloride binding of GWC-MK based cementitious materials.

Concerning that, the present work utilized GWC and MK in marine mortar production. The GWC partially replaced cement at 10, 20 and 30 wt.%. MK was used to compensate the GWC addition induced adverse effects on hardened properties of mortar. The replacement ratio of cement with MK was 5 and 10 wt.%. The mortars were cast in 40mm*40mm*160mm steel moulds and cured in lime-saturated water at 20±1 °C. The carbonation-induced modification on chloride binding and hydrate assemblage of hardened mixtures were investigated. Based on the chloride binding capacity and porosity of GWC-MK based mortar, the variation in chloride diffusion of different mortar was explained. The results show that addition of GWC shows no obvious effect on the workability of fresh mixture, but obviously reduces the compressive strength and chloride resistance ability. GWC can involve in the formation of carboaluminate with the aluminum from either clinker or MK to improve the mechanical properties and chloride resistance. Carbonation can further promote carboaluminate formation and convert hemicarboaluminate to monocarboaluminate due to more carbonate available in the system. During chloride exposure, hemicarboaluminate and monocarboaluminate transform to Friedel's salt and meanwhile delayed ettringite formation is favored, but delayed ettringite formation is less remarkable for carbonated samples after chloride exposure. Due to the densification of matrix and improved chloride binding capacity, the chloride diffusion coefficient of GWC mortar is sharply

reduced with MK addition. The mortar with couple use of 20 wt.% GWC and 5 wt.% MK achieves half the chloride diffusion coefficient of plain mortar during a exposure duration of 6 months. And, the even higher amount of MK achieves even lower chloride diffusion coefficient.

Keywords: Carbonation, carboaluminate, Friedel's salt, chloride exposure, delayed ettringite.

1.   Introduction

The shortage of raw materials for concrete production is a longstanding problem for the concrete production on islands far from mainland. This issue is drawing concerns more than ever due to the blooming exploitation of ocean. In tradition, the supply of raw materials for concrete production on the isolated islands is by cargo. However, this mode of transportation takes a long time and sometimes may be a risky option due to the unpredictable weather. Therefore, it is of great significance to find some local alternatives to relieve the dependence of facility construction there on the raw material supplied from mainland.

As commonly known, there is always an abundant deposit of coral reef around tropic islands. During some local engineering works, coral reefs are dug out inevitably and discard as waste nearby. The waste coral reef has the potential to be recycled as concrete ingredients because it is mainly composed of calcium carbonate in the forms of aragonite and calcite [1,2]. The properties of concretes with coral reef utilized as fine aggregate have been investigated and it is found that the properties of coral sand concrete demonstrates acceptable mechanical properties compared to normal river sand concrete [1,3]. As for the durability, recycling waste coral as fine aggregate is reported to improve the chloride resistance compared to river sand concrete [3,4], which was attributed to the denser microstructure of ITZ resulting from the internal curing of porous coral sand [5,6]. The internal curing was reported to obviously reduce the shrinkage of coral aggregate concrete, either [7,8].

Although it can conclude from previous researches that the proper use of waste coral as aggregate does not result in a noticeable degradation of hardened properties of concrete, the waste coral is very porous, the coral aggregate absorbs high amount of mixing water, leading to an obvious increase in superplasticizer dosage to maintain a suitable workability of fresh mixture [2,9,5]. In order to overcome this adverse effect, an alternative method of recycling waste coral as cement filler is proposed [10]. Since the pores in waste coral are seriously destroyed during grinding, the mixing water removed by adsorption of coral materials is prevented and therefore less effect is imposed on the workability of fresh concrete as reported [10]. Another beneficial effect to adopt ground waste coral (GWC) as filler is that less cement is used and the ecological properties of concrete is improved accordingly. However, due to the dilution effect of GWC addition, the mechanical properties of concrete may suffer an obvious declination. One effective manner to limit this drawback is to use alumina-rich pozzolan which benefits the performance of concrete through pozzolanic reaction and carboaluminate formation [11-13].

Metakaolan (MK) is a typical alumina-rich pozzolan, and it extraordinary ability to improve the mechanical properties and form carboaluminate with coral materials has been addressed, indicating that MK is a good candidate to improve the performance of GWC based cement mixtures [10]. However, as a material exclusively used in marine concrete, the chloride binding and diffusion of MK-GWC based marine concrete/mortar under chloride exposure deserves more concern. Besides, since the pozzolan blended cementious materials generally suffer from a high risk of carbonation [14-16], the resulting pH dropping and calcium carbonate generation may show certain effects on the hydration production formation and chloride binding behaviors of GWC-MK based marine mortar. Therefore, more knowledge relating to these issues is needed.

The present work used ground waste coral (GWC) and metakaolin as partial substitution of cement to

prepare marine mortars. The effects of carbonation on hydration production formation and chloride binding capacity were investigated. Besides, the chloride diffusion profile under chloride exposure was also determined to measure chloride diffusion coefficient by fitting with Fick's 2nd law.

2.   Methodology

2.1   Materials

Ordinary Portland cement of grade 42.5, commercial available metakaolin (MK), ground waste coral (GWC) and ISO sand were used to prepare cement mortar. The means particle sizes (by a granulometer) were 12.96 µm for cement, 3.45µm for MK and 8.52µm for GWC. GWC was produced by grinding waste coral detritus in a ball mill. The waste coral detritus was collected from a tropic island on a tropic island. The chemical composition of cementitious materials, X-ray diffraction (XRD) patterns of GWC and Scanning Electronic Scopic (SEM) image of coral detritus can be referred to Ref. [2]. It can be found that the aluminum oxide content in MK is more than 40 wt.% and the GWC mainly consists of aragonite and calcite rich in magnesium. Besides, the SEM image verifies the porous structure of coral materials as already addressed in other Ref. [4,5]. To adjust the workability of fresh mortar mixture, a polycarboxylate superplasticizer (PCE) was used.

2.2   Methods

2.2.1   Sample preparation

Six mortars with water to binder ratio of 0.5 and binder to sand ratio of 1/3 were designed as shown in Table 1. The mass of total binder (cement plus GWC plus MK) has been normalized to 1. The substitution of cement with GWC is 10, 20 and 30 wt.%, whereas that of cement with MK is 5 and 10 wt.% because the further higher amount of MK can result in significantly damage of workability. The fresh mixtures were placed in 40mm*40mm*160mm steel moulds and demoulded at 24 hours. Thereafter, specimens were cured in lime-saturated water at 20±1ºC.

Table 1 Mix proportions of cement mortars

Mix	Cement	GWC	MK	Sand	w/b	PCE
REF	1.00	0	0	3	0.5	0
10C	0.90	0.10	0	3	0.5	0
20C	0.80	0.20	0	3	0.5	0
30C	0.70	0.30	0	3	0.5	0
5M20C	0.75	0.20	0.05	3	0.5	0.001
10M20C	0.70	0.20	0.10	3	0.5	0.002

2.2.2   Porosity and dried bulk density

At the curing age of 6 months, a saturation-drying method was employed to determine the porosity of mortar [17,18]. The mortar samples were firstly saturated with deionized water in a vacuum following the procedures to prepare samples for RCM test according to NT Build 492. Then, the initial weight (m_0, g) and buoyant weight (m_w, g) of saturated samples were measured. Thereafter, the water-saturated samples were dried in an oven at 105 ºC for 2 weeks. In due time, the dry weight (m_d, g) of the samples were measured. In this way, the porosity (p, %) and dried bulk density (ρ_d, g/cm³) of hardened mortars can be calculated following Eqs. (1) and (2) respectively:

$$p = \frac{m_0 - m_d}{m_0 - m_w}$$

$$(1)$$

$$\rho_d = \frac{m_d \cdot \rho_H}{m_0 - m_w}$$

(2)

Here, ρ_H is the density of water, 1.00g/cm^3.

1.1.1 Chloride diffusion profile determined from chloride exposure

At the curing age of 1 month, some mortar prisms were removed from the curing tank and a 40mm*40mm*60mm cuboid was cut off from each one. Thereafter, the five surfaces of remaining part of mortar prisms were coated with epoxy resin with the exception of the newly-cut surface. After the resin was completely dried, the coated samples were saturated with deionized water in a vacuum box, followed by immersing the coated samples in 0.5 M sodium chloride solution with the uncoated surface upward. The exposure solution was refreshed once a month. After 5 months of exposure, the specimens were removed and the resin was scraped down. Then, the specimens were ground layer by layer, perpendicular to the exposed surface (previously uncoated one). Each layer was 4 mm in thickness. The ground powder was dried in a vacuum at $50\,^\circ\text{C}$ for 24 hours. After that, the free chloride content was determined by measuring the water-soluble chloride content in the powder according to Ref. [19,20]. Exactly 4 gram of mortar powder and 40 ml of deionized water were added in a screw-capped vial and homogenized by vibration. After 24 hours of immersion, 5 ml of liquid was pipetted and neutralized with sulfuric acid. After that, it was titrated with 0.02 M silver nitrate with the indicator of potassium chromate to determine the chloride content. In this way, the free chloride in unit volume of mortar in certain layer can be calculated as Eq. (3) shown:

$$X = \frac{8 \cdot C_{Ag} \cdot V_{Ag} \cdot M_{Cl} \cdot \rho_d}{m}$$

(3)

Here:

X the free chloride content in mortar, mg/cm^3 mortar;

C_{Ag} the concentration of silver nitrate, 0.01964 M;

V_{Ag} the consumed volume of silver nitrate, mL;

M_{Cl} the molar mass of chloride, 35.45 g/mol;

ρ_d the dry density of mortar, g/cm^3;

m the mass of mortar powder, 4g;

Fick's 2nd law can be used to describe the non-steady diffusion of chloride in mortar. The equation of Fick's second law can be expressed as:

$$\begin{cases} \dfrac{\partial X}{\partial t} = D \cdot \dfrac{\partial^2 X}{\partial x^2} ; t > 0, x > 0 \\ X(x,t)|_{x=0} = X_s \\ X(x,t)|_{t=0, x>0} = X_0 \end{cases}$$

(4)

The solution of Eq. (4) is Eq. (5):

$$X = (X_0 - X_s) \cdot \frac{2}{\sqrt{\pi}} \cdot \int_0^{\frac{x}{2\sqrt{Dt}}} e^{-\left(\frac{x}{2\sqrt{Dt}}\right)^2} d\frac{x}{2\sqrt{Dt}} + X_s = (X_0 - X_s) \cdot erf\left(\frac{x}{2\sqrt{Dt}}\right) + X_s$$

(5)

Here:

X_s the chloride content of surface layer, mg/cm^3;

X_0 the back ground content of chloride in mortar, mg/cm^3;

D the apparent chloride diffusion coefficient, cm^2/month;

x the depth from the exposed surface, mm;

t the exposure time, month;

Based on Eq. (5), the apparent chloride diffusion coefficient can be determined by fitting the diffusion profile with this equation.

2.2.2 Chloride binding capacity of sound and carbonated mortars

After the mortars were cured in lime-saturated water for 3 weeks, slices with 10mm in thickness were cut from the middle of mortar prims and then stored in a box to initiate the carbonation. The carbonation is carried out under the condition that 20±2 ℃, 70±5 % in relative humidity and 20±3 vol.% in CO_2 concentration. One week later, the slices were removed from the carbonation box, followed by drying in a vacuum oven at 50 ℃ for 24 hours. Thereafter, the slices were ground to powder less than 74 μm in diameter. Then, exact 20g of mortar powder and 30 ml of 0.5 M lime-saturated sodium chloride solution were added in screw-capped vials. The vials were placed on an oscillator and shaken at the frequency of 200 times to avoid sediment. After the mortar powder was exposed for 1 month, 10 ml of exposure solution was pipetted out and diluted to 250 ml with deionized water. Then, 0.02 M sliver solution was used to titrate the chloride in 5 ml of diluted exposure solution with the indicator of potassium chromate, as did in Section 2.3.2. In this way, the chloride bound by per gram of mortar powder can be calculated.

Meanwhile, the chloride binding capacity of samples free of carbonation (cured in lime-saturated water for 4 weeks) was also detected in the same way.

2.2.3 Formation of hydrates

Before and after the test of chloride binding capacity, the mortar powder was examined by Malvern Panalytical Empyrean diffractometer from 8°-28°, 0.01° per step and 2°/min to identify the assemblage of hydrates.

3.   Results and discussion

3.1   Physical properties

Table 2 shows some important basic physical properties of mortars including spread diameter, compressive strength at 56 days, porosity at 6 months and dried bulk density at 6 months. The addition of GWC shows negligible impacts on the workability of fresh mixtures, despite that numerous literatures reported an obvious degradation of workability of coral aggregate concrete due to absorption of mixing water [2,9,5]. This means that the porous structure of coral is significantly destroyed and the mixing water absorption by coral materials is prevented. Meanwhile, a remarked reduction of compressive strength and increase of porosity are also observed. It is ascribed to the dilution effect induced by GWC addition, which results in loose structure of hardened mixture. GWC addition also leads to modest reduction of dried bulk density, probably due to less mixing water chemically bound in GWC blended mortars.

With the addition of MK, the compressive strength of GWC mortar is dramatically improved and porosity is significantly reduced, indicating that a densified microstructure is achieved. One well-known mechanism is that the pozzolanic reaction of MK to form cementitious products. However, another mechanism

exclusively existed in the system with carbonate materials is that the reaction of aluminum from pozzolans with calcium carbonate to from carboaluminate, which densifies the boundaries between carbonate materials and bulk paste [2]. The addition of MK also increases the dried bulk density of mortar. This may be related to the improved packing density and more water bound during hydration.

Table 2 Physical properties of mortars

Mix	Spread diameter	Compressive strength	Porosity	Dried bulk density
	mm	MPa	%	kg/m^3
REF	165	48.3	17.96	2115.1
10C	162	41.5	19.33	2114.8
20C	164	34.0	20.61	2085.4
30C	159	25.4	21.47	2064.3
5M20C	Not measured	46.0	19.54	2085.9
10M20C	Not measured	49.9	17.37	2094.6

3.2 Effect of carbonation on chloride binding capacity

Fig. 1 presents the chloride binding capacity of sound and carbonated samples. It is obvious that the chloride binding capacity of mortars can be reduced with GWC addition due to dilution effect, and improved with MK addition because of additional aluminum supplement. It is also observed that the blended mortars seem to experience a larger reduction in chloride binding capacity after carbonated. As already reported, the blended cement mixtures are easy to be carbonated compared to plain one because less calcium is available for CO_2 to react in blended ones [14-16]. Besides, it is also accepted that the formation of chloroaluminate and chloride adsorption on C-S-H gels can be benefited in the presence of sufficient calcium ions [21-24]. As in this study, the calcium ions in blended mortars can drop faster than plain one during carbonation due to the less calcium hydroxide available in blended samples. As a result, a more remarkable reduction of bound chloride is resulted for blended mortar. This means that for the concrete structures serve in chloride-rich environment, carbonation-induced steel corrosion may be the synergy of pore solution neutralization and bound chlorides reversing to free ones.
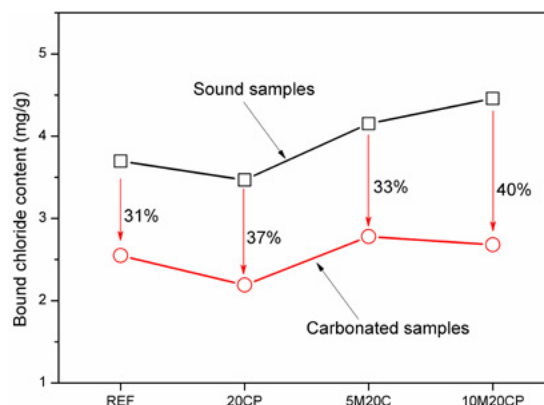

Fig. 1 Chloride binding capacity of sound and carbonated mortars

3.3 Effect of carbonation on phase assemblage

3.3.1 Hydration production before chloride exposure

Fig. 2 illustrates the XRD patterns of sound and carbonated samples before chloride exposure. The assemblage of hydrates is ettringite (Et, $C_6As_3H_{32}$), hemicarboaluminate (Hc, $C_4Ac_{0.5}H_{12}$), monocarboaluminate (Mc, C_4AcH_{11}), calcium hydroxide (CH) and calcite (Cc). It is evident that the addition of GWC improves the formation of Mc, which means GWC can perform the similar reactions to limestone and involve in the formation of carboaluminate [19,25]. After 5 wt.% MK included, the height of Mc diffraction peak almost maintains the same, but the width increases obviously, indicating more Mc formed. With the further addition of MK, a peak corresponding to Hc is generated, which is a type of carboaluminate formed when

reactive calcium carbonate is insufficient. As reported [25], only small fraction of limestone is reacted, probably the surface layer of limestone particles, because of the low solubility of calcite in pore solution. As in this study, although 20 wt.% of GWC can theoretically transform all aluminum in binder to Mc, actually only small fraction of carbonate in the surface layer of GWC particle can be considered as reactive. Thus, the use of 10 wt.% MK can result in formation of Hc.

Comparing to sound samples, the diffraction of CH is significantly reduced in carbonated ones, which is attributed to the reaction between CO2 and CH to form calcite. Besides, it is also observed that the diffraction of Et and Mc of carbonated samples is stronger than that of sound ones. A large r$_{C_4 AsH_{12}}$ literatures have proved that calcite can stabilize Et at the expense of monosulfoaluminate (Ms, $C_4 AsH_{12}$) as shown in Eq. (6) [26,27,11,28]. During carbonation, the formation of calcite is favored and the reaction shown in Eq. (6) is promoted. As a result, Et is further stabilized and stronger diffraction is observed after carbonation. Due to more calcite formed after hydration, more aluminum in MK can react with calcite to form monocarboaluminate, and also more calcite in system favors the transformation from Hc to Mc. The transformation of Hc to Mc is also observed elsewhere for the long-cured cement with alumina-rich pozzolans, which is attributed to the continuous dissolving calcite [11].
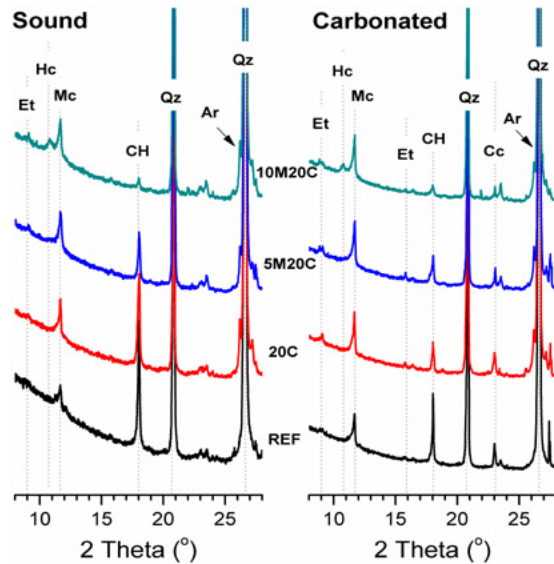
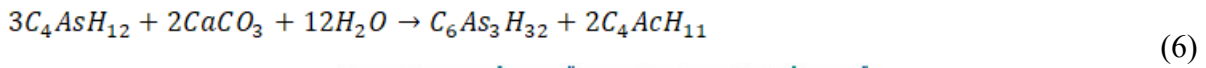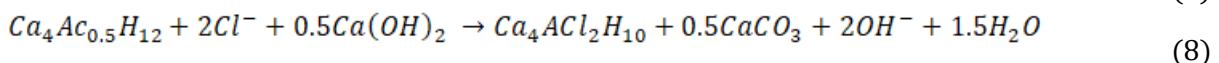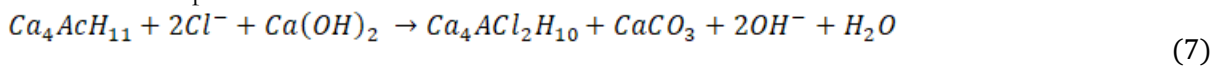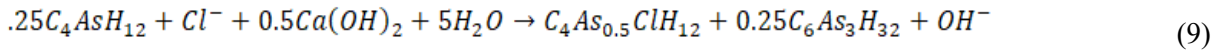$$3C_4 AsH_{12} + 2CaCO_3 + 12H_2O \rightarrow C_6 As_3 H_{32} + 2C_4 AcH_{11}$$

(6)

Fig. 2 XRD pattern of sound and carbonated mortars before chloride exposure (Et: ettringite; Hc: hemicarboaluminate; Mc: monocarboaluminate; CH: calcium hydroxide; Qz: quartz: Cc: calcite; Ar: aragonite)

3.3.2 Hydration production after exposure

Fig.3 illustrates the XRD patterns of sound and carbonated sa$_{C_4 ACl_2 H_{10}}$ chloride exposure. After exposed to chloride solution, Hc and Mc convert to Friedel's salt (Fs, $C_4 ACl_2 H_{10}$) for both sound and carbonated samples, as Eqs. (7) and (8) expressing [10,21]. During these reactions, the carbonates and hydroxyls previously bound in interlayers of Mc and Hc are replaced by chlorides at the expense of CH. However, the carbonated samples have higher ability to form Fs than sound ones. It is ascribed to the fact that less CH is available in carbonated samples for the formation of Fs [19]. The less Fs formed in carbonated samples after chloride exposure results in fewer bound chlorides.

$$Ca_4 AcH_{11} + 2Cl^- + Ca(OH)_2 \rightarrow Ca_4 ACl_2 H_{10} + CaCO_3 + 2OH^- + H_2O$$

(7)

$$Ca_4 Ac_{0.5} H_{12} + 2Cl^- + 0.5Ca(OH)_2 \rightarrow Ca_4 ACl_2 H_{10} + 0.5CaCO_3 + 2OH^- + 1.5H_2O$$

(8)

$$.25C_4AsH_{12} + Cl^- + 0.5Ca(OH)_2 + 5H_2O \rightarrow C_4As_{0.5}ClH_{12} + 0.25C_6As_3H_{32} + OH^- \tag{9}$$

Concomitantly, chloride exposure process increases the diffraction intensity of Et, indicating more Et formed. This phenomenon can be explained by two effects. The first one is that the sulfates in Ms and its solid solution is replaced by chloride, and the released sulfates react with Ms to form delayed Et in return [21]. The relevant reaction is depicted in Eq. (9). The second is that the sulfates previously adsorbed on the C-S-H gels are desorbed during chloride exposure [44-46]. Since chlorides can adsorb on C-S-H gels during exposure, the sulfates previously bound on C-S-H gels will reverse to free ones, and as a result promoting Et formation. It is also observed that after chloride exposure the diffraction of Et in sound mortars increase more remarkably than that in carbonated ones, indicating that sound samples have higher ability to form delayed Et during exposure. This phenomenon can be also attributed to the different amount of CH in sound and carbonated sample. The higher amount of CH can support a constant transformation of Ms to Et as depicted in Eq. 9. For the carbonated mortars, the CH available for the formation of Et is not as much as that in sound ones during chloride exposure. In this way, the reaction depicted in Eq. 9 may be restrained to some extent, and therefore less delayed Et is formed.
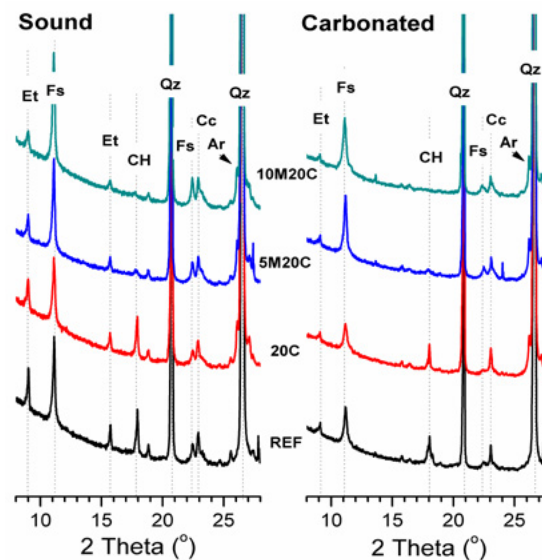

Fig. 3 XRD patterns of sound and carbonated mortars after chloride exposure (Fs: Friedel's salt)

3.4   Chloride diffusion profile and diffusion coefficient

Fig.4 illustrates the free chloride diffusion profiles of mortars after 5 months of chloride exposure. The use of GWC significantly promotes the chloride diffusion by increasing the chloride content and chloride ingress depths in mortar, because the loose structure is achieved with GWC addition as verified in Section 3.1. This means use of GWC in concrete structure is expected to result in higher risk of chloride-induced corrosion of embedded steel bars when serving in a chloride-rich environment.

After 5 wt.% MK is included, the microstructure of GWC blended mortar is densified as already proved in Section 3.1 and chloride diffusion is significantly restrained as a result. It is observed that 5 wt.% MK incorporation in GWC blended mortars achieves lower chloride penetration depth compared to REF sample. The higher amount of MK is found to further benefit the chloride resistance of GWC blended mortar.
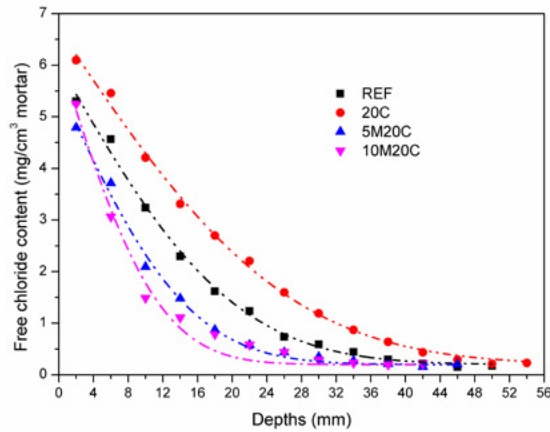
Fig.4 Free chloride profile of mortars after exposed in sodium chloride for 5 months

To further investigate the effect of GWC and MK on chloride diffusion of mortar, the apparent chloride diffusion coefficient is calculated by using Eq. (5) to fit the chloride diffusion profile. Since all the mortars show very similar background of chloride content as shown in Fig.1, the background of chlorides is fixed at 0.20 mg/cm^3 mortar during fitting. The fitted apparent chloride diffusion and chloride concentration in surface layer are shown in Table 3. The chloride diffusion coefficient is almost doubled after 20 wt.% is incorporated. However, the chloride diffusion coefficient is dramatically reduced with MK addition. The chloride diffusion coefficient of GWC blended mortar declines to 1/2 of REF sample for 5 wt.% and 1/3 for 10 wt.% addition. It is accepted that the chloride diffusion in saturated concrete is governed by pore structure and chloride binding capacity [29]. The reduced porosity of GWC blended mortar with MK addition can inhibit chloride diffusion with no doubt. Since MK is an alumina-rich pozzolans, the chloride binding capacity of cement blend can be greatly modified with MK addition. Concerning that, the chloride binding capacity of the mixtures should be evaluated.

As for the free chloride content in surface layer (X_S in Table 3), GWC addition increases and MK addition reduces it. It is related to the porosity of mortars. Since GWC addition increase porosity, more chloride can intrude into the surface layer and improve chloride content. However, although porosity is further reduced with 10 wt.% addition, the chloride concentration of surface layer demonstrates a considerable increase. This phenomenon is probably linked to the carbonation of surface layer of mortar. As mentioned in Sections 3.2 and 3.3, chloride binding of hardened cement mixture is significantly determined from CH available. As a result, the sample with the highest amount of mineral admixtures (namely 10M20C) and therefore the lowest ability to resist carbonation can suffer a higher reduction of bound chloride content due to the excessive declination of CH during carbonation. This indicates that with the gradual carbonation during chloride exposure the large amount of chlorides previously bound in the surface layer of 10M20C can reverse to free ones and increase the free chloride content in surface layer.

Table 3 Chloride diffusion coefficient and chloride content in surface layer of mortar

Mix	D	X_S	R^2
	cm^2/month	mg/cm^3	
REF	25.16	6.02	0.996
20CP	43.19	6.70	0.997
5M20C	13.88	5.58	0.994
10M20C	8.04	6.17	0.982

4.   Conclusions

This work prepares metakaolin (MK)-ground waste coral (GWC) based marine mortars exclusively serving on islands far from mainland. The chloride binding and hydration product formation of sound and carbonated mortar were investigated. The chloride binding capacity and porosity are combined to explain the variation in chloride diffusion behaviors observed in different mortars. Based on the results and discussion, the following conclusions can be drawn:

• GWC can involve in the formation of carboaluminate with the aluminum from either clinker or MK. Carbonation can further promote carboaluminate formation and convert hemicarboaluminate to monocarboaluminate due to more carbonate available in the system;

• During chloride exposure, hemicarboaluminate and monocarboaluminate transform to Friedel'salt and meanwhile delayed ettringite formation is favoured. These transformations are carried out at the expense of calcium hydroxide. Therefore, for the carbonated samples, the formation of Friedel'salt and delayed ettringite can be inhibited to some extent due to less calcium hydroxide available in a carbonated system;

• Addition of GWC imposes negligible influence on the workability of fresh mortar mixture, but harms the mechanical properties and microstructure of hardened mixture due to dilution effect. These degradations can be compensated by MK addition due to the synergy of secondary C-S-H gels and carboaluminate formation.

• Due to the densification of matrix and improved chloride binding capacity of GWC mortar, the chloride diffusion coefficient is sharply reduced with MK addition. The mortar with couple use of 20 wt.% GWC and 5 wt.% MK achieves half the chloride diffusion coefficient of plain mortar during a exposure duration of 6 months. And, the even higher amount of MK achieves even lower chloride diffusion coefficient.

5.   Acknowledgment

6.   Reference

1. Wang QK, Li P, Tian YP, Chen W, Su CY (2016) Mechanical Properties and Microstructure of Portland Cement Concrete Prepared with Coral Reef Sand. J Wuhan Univ Technol 31 (5):996-1001. doi:10.1007/s11595-016-1481-x

2. Wang Y, Shui Z, Gao X, Huang Y, Yu R, Li X, Yang R (2019) Utilizing coral waste and metakaolin to produce eco-friendly marine mortar: Hydration, mechanical properties and durability. J Clean Prod 219:763-774. doi:10.1016/j.jclepro.2019.02.147

3. Cheng SK, Shui ZH, Sun T, Yu R, Zhang GZ, Ding S (2017) Effects of fly ash, blast furnace slag and metakaolin on mechanical properties and durability of coral sand concrete. Appl Clay Sci 141:111-117. doi:10.1016/j.clay.2017.02.026

4. Wang XP, Yu R, Shui ZH, Song QL, Zhang ZH (2017) Mix design and characteristics evaluation of an eco-friendly Ultra-High Performance Concrete incorporating recycled coral based materials. J Clean Prod 165:70-80. doi:10.1016/j.jclepro.2017.07.096

5. Cheng S, Shui Z, Sun T, Yu R, Zhang G (2018) Durability and microstructure of coral sand concrete incorporating supplementary cementitious materials. Constr Build Mater 171:44-53. doi:10.1016/j.conbuildmat.2018.03.082

6. Hu S, Wang F, Ding Q (2005) Interface structure between lightweight aggregate and cement paste. J Chin Ceram Soc 33 (6):713-717. doi: 10.1016/0008-8846(90)90103-5

7. Liu JM, Ou ZW, Mo JC, Chen YZ, Guo T, Deng W (2017) Effectiveness of Saturated Coral Aggregate and Shrinkage Reducing Admixture on the Autogenous Shrinkage of Ultrahigh Performance Concrete. Adv Mater Sci Eng:11. doi:10.1155/2017/2703264

8. Chen F, Zhang G, Ding S, Qing M, Liu K (2016) Experimental study on the performance of coral sand concrete. China Concrete and Cement Products (7):16-21.

9. Wang A, Lyu B, Zhang Z, Liu K, Xu H, Sun D (2018) The development of coral concretes and their upgrading technologies: A critical review. Constr Build Mater 187:1004-1019. doi:10.1016/j.conbuildmat.2018.07.202

10. Wang Y, Shui Z, Huang Y, Sun T, Duan P (2018) Properties of coral waste-based mortar incorporating metakaolin: Part II. Chloride migration and binding behaviors. Constr Build Mater 174:433-442. doi:10.1016/j.conbuildmat.2018.04.076

11. De Weerdt K, Kjellsen KO, Sellevold E, Justnes H (2011) Synergy between fly ash and limestone powder in ternary cements. Cem Concr Compos 33 (1):30-38. doi:10.1016/j.cemconcomp.2010.09.006

12. Nied D, Stabler C, Zajac M Assessing the Synergistic Effect of Limestone and Metakaolin. In, Dordrecht, 2015. Calcined Clays for Sustainable Concrete. Springer Netherlands, pp 245-251

13. Antoni M (2013) Investigation of cement substitution by blends of calcined clays and limestone. PhD, Ecole Polytechnique Fédérale de Lausanne,

14. Barbhuiya S, Chow P, Memon S (2015) Microstructure, hydration and nanomechanical properties of concrete containing metakaolin. Constr Build Mater 95:696-702. doi:10.1016/j.conbuildmat.2015.07.101

15. Kim HS, Lee SH, Moon HY (2007) Strength properties and durability aspects of high strength concrete using Korean metakaolin. Constr Build Mater 21 (6):1229-1237. doi:10.1016/j.conbuildmat.2006.05.007

16. Papadakis VG (2000) Effect of supplementary cementing materials on concrete resistance against carbonation and chloride ingress. Cem Concr Res 30 (2):291-299. doi:10.1016/S0008-8846(99)00249-5

17. Medjigbodo G, Rozière E, Charrier K, Izoret L, Loukili A (2018) Hydration, shrinkage, and durability of ternary binders containing Portland cement, limestone filler and metakaolin. Constr Build Mater 183:114-126. doi:10.1016/j.conbuildmat.2018.06.138

18. Kearsley EP, Wainwright PJ (2001) Porosity and permeability of coamed concrete. Cem Concr Res 31:805-812. doi:10.1016/S0008-8846(01)00490-2

19. Wang Y, Shui Z, Gao X, Yu R, Huang Y, Cheng S (2019) Understanding the chloride binding and diffusion behaviors of marine concrete based on Portland limestone cement-alumina enriched pozzolans. Constr Build Mater 198:207-217. doi:10.1016/j.conbuildmat.2018.11.270

20. Luo R, Cai YB, Wang CY, Huang XM (2003) Study of chloride binding and diffusion in GGBS concrete. Cem Concr Res 33 (1):1-7. doi:10.1016/S0008-8846(02)00712-3

21. Wang Y, Shui Z, Gao X, Huang Y, Yu R, Ling G (2019) Chloride binding behaviors of metakaolin-lime hydrated blends: Influence of gypsum and atmospheric carbonation. Constr Build Mater 201:380-390. doi:10.1016/j.conbuildmat.2018.12.162

22. Shi ZG, Geiker MR, De Weerdt K, Ostnor TA, Lothenbach B, Winnefeld F, Skibsted J (2017) Role of calcium on chloride binding in hydrated Portland cement-metakaolin-limestone blends. Cem Concr Res 95:205-216. doi:10.1016/j.cemconres.2017.02.003

23. De Weerdt K, Colombo A, Coppola L, Justnes H, Geiker MR (2015) Impact of the associated cation on chloride binding of Portland cement paste. Cem Concr Res 68:196-202. doi:10.1016/j.cemconres.2014.01.027

24. Labbez C, Pochard I, Jonsson B, Nonat A (2011) C-S-H/solution interface: Experimental and Monte Carlo studies. Cem Concr Res 41 (2):161-168. doi:10.1016/j.cemconres.2010.10.002

25. Zajac M, Rossberg A, Le Saout G, Lothenbach B (2014) Influence of limestone and anhydrite on the hydration of Portland cements. Cem Concr Compos 46:99-108. doi:10.1016/j.cemconcomp.2013.11.007

26. Lothenbach B, Le Saout G, Gallucci E, Scrivener K (2008) Influence of limestone on the hydration of Portland cements. Cem Concr Res 38 (6):848-860. doi:10.1016/j.cemconres.2008.01.002

27. Bizzozero J, Scrivener KL (2015) Limestone reaction in calcium aluminate cement–calcium sulfate systems. Cem Concr Res 76:159-169. doi:10.1016/j.cemconres.2015.05.019

28. Matschei T, Lothenbach B, Glasser FP (2007) The role of calcium carbonate in cement hydration. Cem Concr Res 37 (4):551-558. doi:10.1016/j.cemconres.2006.10.013

29. Martin-Perez B, Zibara H, Hooton RD, Thomas MDA (2000) A study of the effect of chloride binding on service life predictions. Cem Concr Res 30:1215-1223. doi:10.1016/S0008-8846(00)00339-2

Rejuvenators for High RAP Asphalt Mixes and New Preservation Techniques for Open-Graded Pavements

S.N. Nahar[1,2], F.B. Elzinga[1], B.J. Lommerts[1,*]

[1]Latexfalt bv, P.O. Box 6, 2396 ZG Koudekerk aan den Rijn, the Netherlands, www.latexfalt.com

[2]Department of Civil Engineering and Geosciences, Delft University of Technology, the Netherlands

[*] Author to whom communications should be addressed, bertjan.lommerts@latexfalt.com,

Abstract

The development of a full circular approach regarding road construction materials requires new and fundamental innovations. More in particular the recycling of RAP stemming from open-graded pavements is a challenge as oxidation has progressed significant during the more than a decade of service life of the surface layer, which results in a brittle, glassy material with poor flexibility and limited self-healing properties. Furthermore, these pavements are often produced using polymer modified bitumen and the re-compatibilization of aged binders requires deep insights into oxidation-induced phase behavior effects. In the present paper the option of rejuvenation of high RAP mixes will be reported using pre-blended bitumen with selected rejuvenators. These pre-blended materials are compared to regular soft bitumen, i.e. bitumen with a high maltene content, and other more softening materials. The interaction of rejuvenator blended bitumen with recovered binder obtained from oxidized RAP is studied by means of AFM and rheology. It is demonstrated that a full in-depth rejuvenation and re-compatibilization of the oxidized mastic can be accomplished, which is an important prerequisite for successful high RAP mix design. Dense and open-graded asphalt mixes consisting of at least 50% RAP can be designed without quality and durability implications. Furthermore, the re-compatibilization of aged bitumen is also successfully accomplished in-situ for open-graded or semi-open graded pavements, like porous asphalt and SMA. It has been demonstrated that the newly developed rejuvenating preservation technique for these pavements results in a significant reduction of stone loss and in an increase of the service life of the road of at least 50%. The latter has been determined for numerous pavements treated with the rejuvenator containing bituminous emulsion during a period of over five years, using LCMS monitoring techniques.

Keywords – asphalt recycling, rejuvenation, porous asphalt, road maintenance

1.   Introduction

Durability of bitumen is a concern as bitumen undergoes oxidative ageing during production and service-life of asphalt pavement. Extent of oxidative ageing depends on the molecular make-up of bitumen that can vary depending on nature and source of the crude oil and refining process, environmental condition and mix design (Robertson et al., 1991).

Dutch highway road-network is mostly constructed using porous asphalt due to its numerous advantages; for instance driving comfort resulting from low noise level and less spraying of water during rain fall (The et al., 2016). On the contrary, the life-span of porous asphalt is rather limited. Due to its open structure and high porosity of porous asphalt, bitumen is exposed to ambient oxygen and temperature conditions.

Oxidative ageing causes an increase in molecular interaction within bitumen due to irreversible nature of the chemical reactions that take place during oxidation (Petersen et al, 1984). Oxidative ageing has more severe effect on two-layer porous asphalt, where the top layer is made of polymer modified bitumen.

An obvious change in physical property in oxidized bitumen is seen from its viscosity, stiffness increase and its limited adhesion property. As a result, loss of stones (i.e. raveling) and cracking are observed as main distress mechanisms in porous asphalt. Excessive raveling determines the critical pavement condition (Figure 1) and eventually the end of service life of porous asphalt (Kneepkens et a.l., 2004, The et al., 2016, Lommerts et al., 2016).
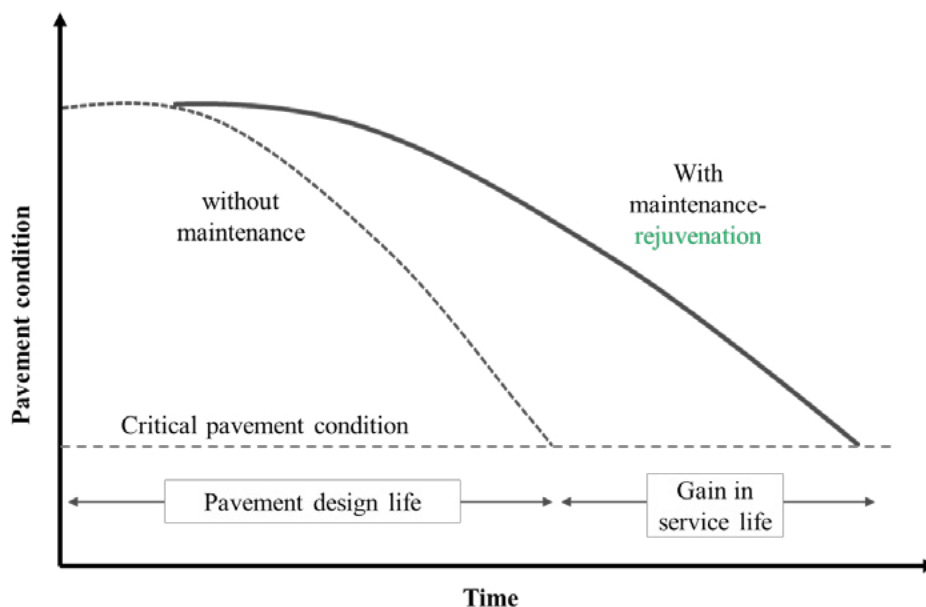

Figure 1: Improvement of pavement service life through rejuvenation.

As a solution to this undesirable effects of ageing of pavement materials, different strategies are implemented in practice. Among them preventive and reconstructive (i.e. recycling) treatments are popular where additive is used to replenish aged binder properties. These additives are commonly known as rejuvenator (Nahar et al., 2014, Lommerts et al., 2016).

At critical pavement condition, the wearing coarse is recycled to construct new asphalt pavement. Recycling of road materials is a common practice in the Netherlands since 1970 in the base asphalt layers with 50% to 70% allowable limit of recycled asphalt pavement (RAP) (Nahar et al,, 2014). In current practices, the contractors are increasing the allowable limit of RAP and also adapting horizontal recycling; recycling of old wearing to new wearing course. Using a rejuvenator will be inevitable to revitalize highly aged, polymer modified bitumen containing wearing course.

Within the scope of this work, rejuvenator is developed with the purpose of restoring the mechanical and adhesive properties of bitumen during recycling and also during pavement maintenance in order to extend the service-life, Figure 1. This paper presents ageing susceptibility of bitumen and the effectiveness of rejuvenator in restoring the intrinsic properties of bitumen after being laboratory aged.

The first part of the paper presents the mechanical property restoration potential of rejuvenator. It is measured by comparing the penetration, softening point and other mechanical properties of neat, laboratory aged bitumen from pressure aged vessel (PAV), rejuvenated bitumen blends and the same system after being aged, as shown in Table-1.

Next part focuses on fundamental property of rejuvenated bitumen like mutual compatibility and phase behavior at the microstructural level. These properties are assessed for neat, aged, rejuvenated bitumens and aged rejuvenated system by using AFM and DSC.

This paper demonstrates methods that can clearly distinguish neat and aged bitumen and can evaluate rejuvenation potential of rejuvenator at fundamental level. The research also present a practical approach for in-situ rejuvenation of highly aged porous asphalt suitable for pavement preservation. This research is useful to predict durability of bitumen, compatibility of rejuvenator in base bitumen and long term performance of rejuvenated bitumen systems.

2.   Materials & Methods

2.1   Material and sample preparation

Bitumen of penetration grade 70/100 from Total refinery is used for this research. The sample is aged in the laboratory using Pressure Ageing Vessel (PAV) for 65 hours at temperature 85°C and pressure 21 bar. Then rejuvenator is blended with aged bitumen to adjust the penetration to its neat value. Following that the rejuvenated binder system is aged again using the same PAV procedure for its investigation on susceptibility to ageing. Mechanical tests are performed with the focus on low and high temperature properties of all the samples. Finally, microstructural and thermal behavior of neat, aged and rejuvenated samples are measured using AFM and DSC technique.

Figure 2: Assessment scheme for evaluation of a rejuvenator.

For AFM study bitumen specimens are prepared by applying approximately 20 mg of sample on the 12-mm AFM sample substrate (i.e. steel disks of 0.5 mm thickness). The specimens are then heated for 30 seconds at 100°C on a heater plate to obtain a smooth bitumen film. Later, in order to have same thermal history for all the specimens, they are conditioned in an oven at 100 °C for 15 minutes. Prior to AFM imaging, the specimens were stored in closed petri dishes at the imaging temperature 21°C for 24 hours.

To perform thermal analysis using DSC, 10mg sample was taken in Tzero aluminium pans and was sealed with hermetic lids that are obtained from TA instruments.

Instrument and operational mode

Atomic Force Microscope (AFM)

Dimension Icon from Bruker AFM was used for this research, Figure 3(a). For AFM imaging, a cantilever with a tip of nominal end radius 8nm is scanned over the sample surface by a piezoelectric scanner. The changes in tip-sample interactions result in deflection of the cantilever which is measured by an optical-lever detection system.

In this research, Tapping-mode AFM was used to characterize the bitumen specimens. In this mode, the probe is driven near to its first resonant frequency. While the probe is scanned across the sample, amplitude is kept constant. In this way the tip maintains an intermittent contact over the sample surface by exerting moderate force that is suitable for bituminous materials.
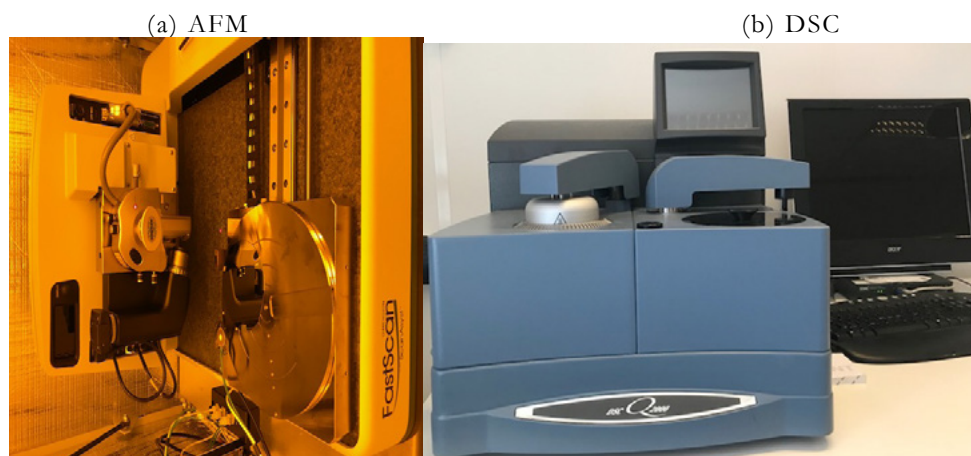
Figure 3: AFM instrumental set-up and operation principle: a) Dimension Icon-AFM set-up b) Differential scanning calorimetry (DSC) set-up from TA instruments.

The oscillating cantilever dissipates different amount of energy as it interacts with material heterogeneity on the sample surface, resulting two major sets of data simultaneously: topography and phase-contrast. Each image type provides specific information with respect to the sample surface. Topography images provide information of relative height of the various features of the material and phase contrast images present relative damping of oscillating cantilever which can again be related to cumulative measure of stiffness and adhesion forces between probe and the sample.

Probe and measuring environment

Cantilever RTESPA from Bruker which have nominal resonance frequency of 300 kHz and spring constant of 40 N/m is used for this research. Probe was scanned by 1 Hz (1 line/s) at ambient condition, 21 °C. Images are collected in 10×10 μm^2 scan size with pixel resolution of 512×512.

Differential Scanning Calorimeter (DSC):

DSC – Q2000 from TA instruments has been used to perform thermal analysis in bitumen (Figure 3b). While a conventional thermal analysis (DSC) is performed in bitumen, it provides a thermogram showing an overlap in endo- and exothermic events. Hence, Temperature modulated (M)-DSC is used to characterize bitumen that can distinguish overlapping thermal events.

In this method, a sinusoidal temperature fluctuation is superimposed over a linear heating or cooling rate. As a result, the sample temperature provides a sinusoidal response and there is a delay between the modulated heat flow and the response of the material. This results in a reversing (i.e. that responds to a change in heating rate) and non-reversing signal. Samples were measured with heating rate of 3 K/min between -90 and 150 °C. Analysis and deconvolution of the reversing and non-reversing signals were done using the TA software.

3.   Results & Discussion

3.1   Mechanical properties

Mechanical tests are conducted in all samples to reveal the high and low temperature performance of materials. A small addition of 4.5% of rejuvenator to PAV aged bitumen could recover penetration and softening point and restore other properties as presented in Table 1.

All mechanical properties confirm recovery of functional properties of bitumen after addition of

rejuvenator. Penetration, softening point and low temperature properties data show that the rejuvenated system is more stable against oxidation compared to neat bitumen system. Low temperature flexibility is improved after adding rejuvenator and this rejuvenated system keeps its flexibility at low temperature after being aged in PAV.

Table 1: Mechanical properties of bituminous systems.

Material properties	Neat bitumen	PAV aged bitumen	Rejuvenated after PAV	Rejuvenated after PAV+additional PAV
Penetration (1/10mm)	79	29	80	46
ΔCp (J/g°C)- DSC	0	0.17	0	0.05
Low temperature properties				
Glass transition temperature T_g (°C)- DSC	-17	-17	-24	-23
Frass breaking point(°C)	-15	-8	-18	-16
High temperature properties				
Softening point; R&B (°C)	45.4	55	47.8	53.6
G' ratio at 60°C (aged/neat bitumen)	1	9.8	3.4	10.7

3.2   Phase behavior of neat, aged and rejuvenated bitumen

Mutual compatibility of the rejuvenator and the base bitumen can be revealed by phase behavior of the system. An incompatibility may induce an additional phase to separate out, if there is a discontinuity in the molecular distribution. This phenomenon can occur in highly aged bitumen as well as in the presence of rejuvenator if it is not fully compatible with the base bitumen. Phase separation characteristics of bitumen in neat state, after oxidation and rejuvenation have been investigated using AFM. Topography and phase images obtained using this technique are presented in Figure 4. Mutual compatibility of the resulted molecular classes after oxidation or addition of rejuvenator can easily be evaluated using this technique.

AFM images in Figure 4 confirm existence of two phase system (i.e. elongated domains and matrix) for all bitumen samples. Two-phase microstructure is a characteristic feature of bituminous materials and has been reported in numerous literature (Nahar et al., 2014, Nahar et al., 2016).

Building blocks of this domains are assumed to be co-association of asphaltene and wax ($\geq$C40) fraction of bitumen (Lesueur et al, 2009, Hofko et al., 2015, Nahar et al, 2016). Asphaltenes are known to self-associate to form an aggregate as inverted micelle of few molecular units and these aggregates mostly tend to flocculate to form a particle of asphaltenes of 2-30nm. These particles have a polar core and an apolar exterior (Yen, 1975). It is speculated that, the apolar exterior may act as an interaction sites for the apolar fraction, such as microcrystalline wax component of bitumen. Thus, these asphaltene particles first may act as a scaffold for the attachment of the wax molecules. While cooling from molten state of bitumen (i.e. a single phase system in terms of mechanical response properties) these domains phase separate following nucleation and growth mechanism (Nahar et al., 2016).
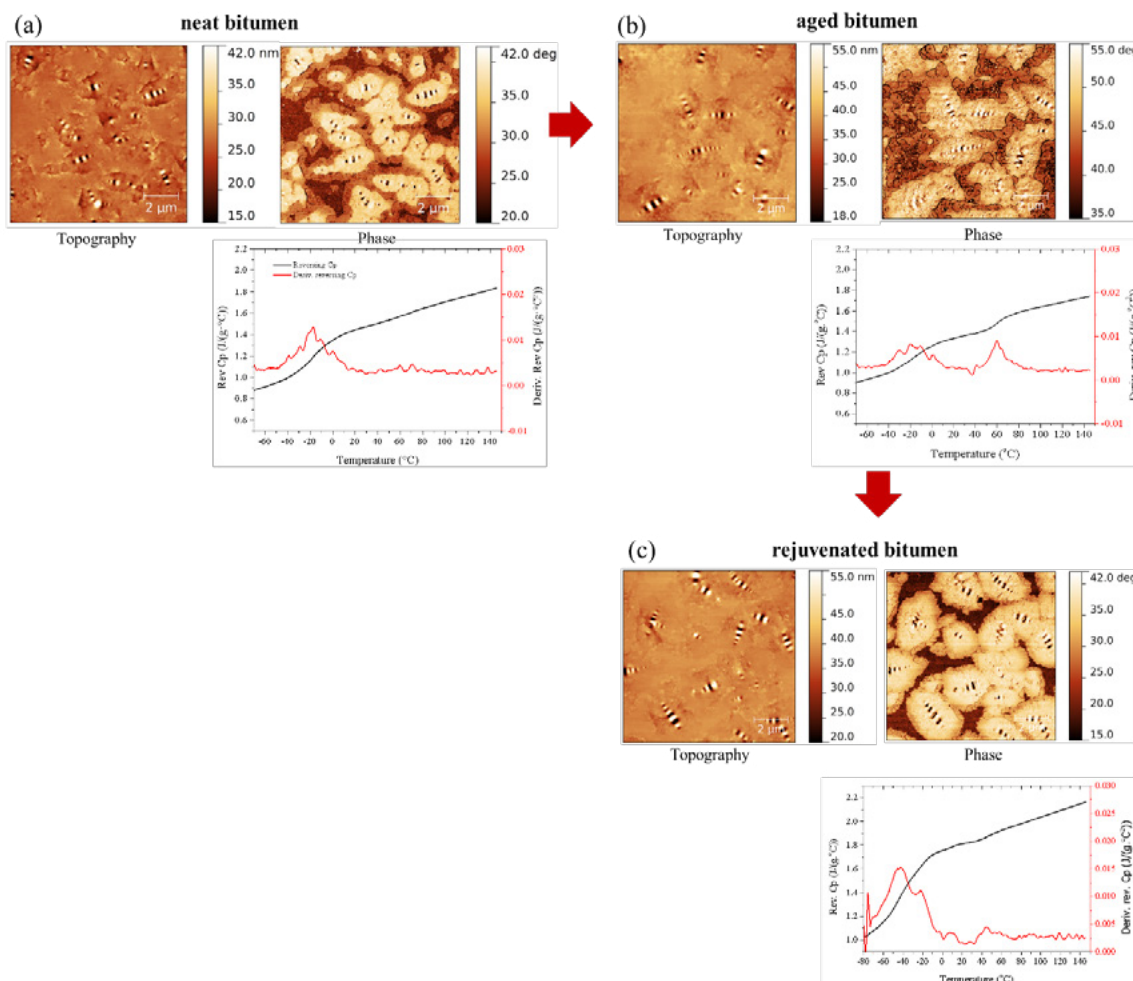
Figure 4: Phase and thermal behavior of (a) neat (b) aged and (c) rejuvenated bitumen.

After PAV ageing, an enhanced agglomeration is observed in the domain phase compared to neat bitumen, Figure 4a and 4b. From the phase image, a significant increase in phase shift is observed in the matrix phase of PAV aged bitumen. Phase images show the cumulative effect of the material property such as stiffness and adhesion of the probe to the material. From controlled nano-mechanical measurement it is known earlier that the phase showing higher phase shift corresponds to a stiffer and less adhesive phase and vice-versa (Nahar et al., 2016). Thus, the phase image also shows the proof of hardening of bitumen at microstructural level as expected after oxidation of bitumen.

During the process of oxidation, mostly polar functional groups, ketones and sulfoxides are formed in bitumen (Petersen, 1984). A characteristic shift from aromatics to resinous components are commonly known to occur in oxidized bitumen (Handle et al., 2017). This result in an increase in molecular interaction and as a consequence more asphaltene tend to agglomerate in oxidized bitumen. This change in physico-chemical property at molecular level translates to its change in mechanical properties showing increase in viscosity and modulus.

The added rejuvenator is compatible with the base bitumen as no foreign phase was observed in the blend. Re-dispersion of the domain phase is also observed through rejuvenation. Rejuvenated bitumen has shown property restoring performance from both the rheological data and microstructural properties of the binders. **Compatibility aspects and thermal behavior of neat, aged and rejuvenated bitumen**

Thermal events like change in specific heat capacity can be detected from the reversing curve from MDSC thermograms. An example of such a thermogram is shown in Figure 5(a) and the results of neat, aged and

rejuvenated bitumens are presented in Figure 4 a, b and c respectively coupled with AFM images.

The thermograms can provide insights on mutual compatibility of the phases in bitumen after oxidation and evaluates compatibility between the pre- blended rejuvenator and the base bitumen. Some useful parameters extracted from the data are glass transition temperature (T_g) of the maltene phase, heat capacity, ΔC_p measured at T_g. After oxidation the T_g shifts to a higher temperature and by rejuvenation again shifts back to neat bitumen state confirming the low temperature flexibility of the material.
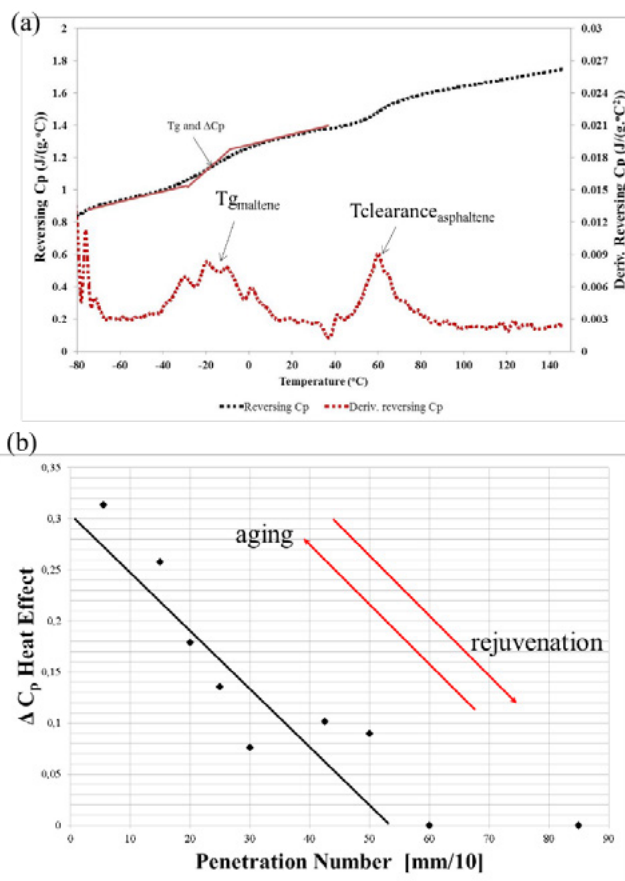

Figure 5: (a) Example of a thermogram showing glass transition and clearance temperature with corresponding ΔCp. (b) Difference in specific heat capacity; ΔCp at clearance temperature can be correlated to oxidation and rejuvenation characteristics of bitumen.

3.3   In-situ rejuvenation technology for preservation of porous asphalt

A novel multi-component emulsion Modimuls® ZV is introduced to the market to preserve open graded porous asphalt. Modimuls® ZV emulsion contains rejuvenating components with different breaking properties which can be sprayed onto the road surface using standard spraying technique. This rapid breaking emulsion is subsequently forced into the open structure by an high pressure jet air flow to facilitate impregnation of the components that can revitalize old oxidized bitumen in porous asphalt. Maintenance of porous asphalt and SMA using this technology has shown evidence to restore the functional properties of asphalt meeting the anti-skid requirements which has been concluded from extensive research on asphalt cores taken from trial sections (The et al., 2016, Lommerts et al., 2016). Some of the pavement surfaces were two-layer open graded asphalt, that were constructed using polymer modified bitumen. Modimuls® ZV technology has been validated by Dutch national roads agency Rijkswaterstaat (RWS) as in-situ rapid pavement maintenance technique to extend the service life of porous asphalt (The et al, 2016). Modimuls® ZV incorporates various functional properties such as good wetting of the internal structure of the open graded asphalt resulting good distribution of the binder. It promotes replenishment of asphalt to restore

viscoelastic and adhesive properties throughout the depth of asphalt. Abrasion tests such as Rotating Surface Abrasion Test (RSAT) are conducted on asphalt cores taken from Modimuls® ZV treated pavement sections of highways A6, A50, A73, A30, A1, A12. The results have shown a significant reduction in stone loss. Using Laser Crack Measurement System (LCMS) monitoring technique, degree of raveling in time has been determined from treated test sections. Treated pavement have been proven to be raveling resistant compared to untreated section. This simulates an increase in service life of more than 5 years (The et al., 2016).

4.   Conclusions

Effectiveness of rejuvenator is evaluated through mechanical and fundamental assessment within the scope of work. From mechanical test results, it is apparent that addition of rejuvenator shows desired property recovery which is comparable to neat bitumen. Mutual compatibility and phase behavior of bitumen and rejuvenated systems have been successfully measured at microstructural level by using AFM and DSC.

The data provides useful information on miscibility of the rejuvenator to the base bitumen and mechanism of rejuvenation. Ageing susceptibility of bitumen and rejuvenated system are also evaluated and compared using the aforementioned techniques. AFM data sets provide insight on phase behavior and microstructure properties. While the durability aspects, low temperature properties of the bituminous systems are understood from ΔCp and T_g value from DSC.

From the overall results, it is concluded that a good rejuvenator is compatible with base bitumen and is resistant to oxidation. The rejuvenation strategy in bitumen has been proposed in Figure 6.
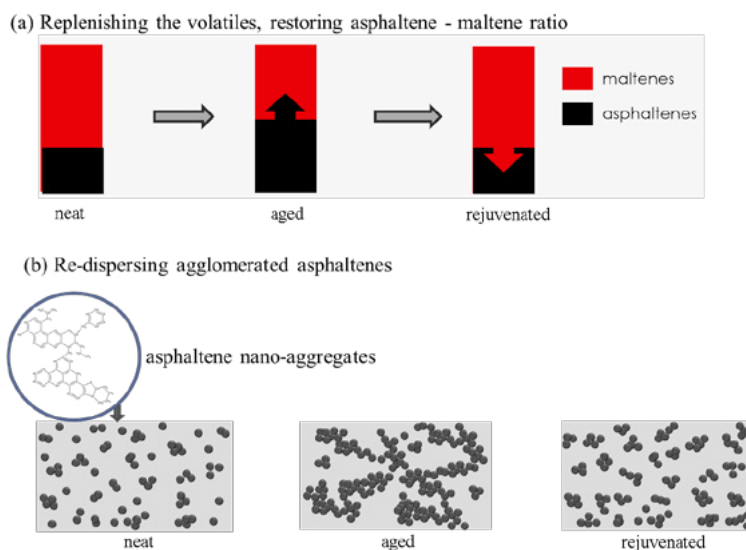

Figure 6: Influence of ageing and rejuvenation through replenishing volatiles and re-dispersion of asphaltene agglomerates.

During the process of ageing some volatiles (i.e. fraction of maltenes) are lost and some functional groups are oxidized in bitumen. This creates a shift in solubility parameter of the molecular fractions within the material and as a result more segregation of molecules occur (Figure 6b). Rejuvenator replenishes the lighter molecular fraction, maltenes and re-disperses the agglomerated molecules of aged bitumen.

Modimuls® ZV is proven as a fast applied, cost effective maintenance technique to extend the service life of porous asphalt. This maintenance technique is applicable to wide range of open graded asphalt, SMA and has the potential to replenish aged polymer modified bitumen. And service life of the open-graded asphalt pavement is demonstrated to extend more than 5 years. In this way the technology contributes to

low carbon foot print in the life-cycle cost of asphalt pavement.

5.   References

1.   Handle F., Harir M., Füssl J., Koyun A. N., Grossegger D., Hertkorn N., Eberhardsteiner L., Hofko B., Hospodka M., Blab R., Schmitt-Kopplin P. and Grothe H., "Tracking Ageing of Bitumen and Its Saturate, Aromatic, Resin, and Asphaltene Fractions Using High-Field Fourier Transform Ion Cyclotron Resonance Mass Spectrometry", *Energy Fuels*, (2017), 31 (5), pp 4771–4779.

2.   Hofko B., Eberhardsteiner L., Füssl J., Grothe H., Handle F., Hospodka M., Grossegger D., Nahar S.N., Schmets A.J.M. and Scarpas A., "Impact of Maltene and Asphaltene Fraction on Mechanical Behavior and Microstructure of Bitumen", *Materials and Structures* (2015), pp. 1–13.

3.   Kneepkens T., van Hoof Th., van Keulen W. and van Gent R.J., "Development of VIA-RAL for Porous Asphalt: more than just research, more pragmatism", *3rd Eurasphalt & Eurobitume Congress* (2004).

4.   Lesueur D., "The colloidal structure of bitumen: Consequences on the rheology and on the mechanisms of bitumen modification", *Advances in Colloid and Interface Science* 145, 42 (2009).

5.   Lommerts B. J., Struik J., Cotiugă I. and van Bochove G., "A New Preservation Technology for Porous Asphalt -a multi-modal, biopolymer stabilized, rejuvenating asphalt emulsion", *6th Eurasphalt & Eurobitume Congress* (2016), proceedings.

6.   Nahar S.N., Schmets A., Schitter G., and Scarpas A. "Quantifying the Thermomechanical Response of Bitumen from Micro-Phase Properties". *Transportation Research Record,* Vol. 2574 (2016), pp. 101-110.

7.   Nahar S.N., Qiu J., Schmets A.J.M., Schlangen E., Shirazi M., van de Ven M. F. C., Schitter G. and Scarpas A., "Turning Back Time: Rheological and Microstructural Assessment of Rejuvenated Bitumen". *Transportation Research Record* (2014), Vol. 2444, pp. 52-62.

8.   Nahar S.N., "Phase separation characteristics of bitumen and their relation to damage-healing". *dissertation*, ISBN 978-94-6186-598-4, pp. 52-62.

9.   Petersen J. C., "Chemical composition of asphalt as related to asphalt durability: state of the art", *Transportation Research Record* (1984).

10.   Robertson R. E., Branthaver J., Plancher H., Duvall J., Ensley E., Harnsberger P., and Petersen J., "Chemical properties of asphalts and their relationship to pavement performance", *Technical Report Strategic Highway Research Program*, National Research Council, (1991).

11.   The P., Voskuilen J., van de Ven M. F. C., "Life-prolonging preventive maintenance techniques for porous asphalt", *6th Eurasphalt & Eurobitume Congress* (2016), proceedings.

12.   Yen T. F., "The role of trace metals in petroleum", *Ann Arbor Science Publishers Inc*, Ann Arbor , 01–30 (1975).